



HAL
open science

Bubble hydrodynamics and mass transfer in complex media

Feishi Xu

► **To cite this version:**

Feishi Xu. Bubble hydrodynamics and mass transfer in complex media. Chemical and Process Engineering. INSA de Toulouse, 2019. English. NNT : 2019ISAT0003 . tel-02918159

HAL Id: tel-02918159

<https://theses.hal.science/tel-02918159>

Submitted on 20 Aug 2020

HAL is a multi-disciplinary open access archive for the deposit and dissemination of scientific research documents, whether they are published or not. The documents may come from teaching and research institutions in France or abroad, or from public or private research centers.

L'archive ouverte pluridisciplinaire **HAL**, est destinée au dépôt et à la diffusion de documents scientifiques de niveau recherche, publiés ou non, émanant des établissements d'enseignement et de recherche français ou étrangers, des laboratoires publics ou privés.



THÈSE

En vue de l'obtention du DOCTORAT DE L'UNIVERSITÉ DE TOULOUSE

Délivré par l'Institut National des Sciences Appliquées de
Toulouse

Présentée et soutenue par

FEISHI XU

Le 19 avril 2019

BUBBLE HYDRODYNAMICS AND MASS TRANSFER IN COMPLEX MEDIA

Ecole doctorale : **MEGEP - Mécanique, Energétique, Génie civil, Procédés**

Spécialité : **Génie des Procédés et de l'Environnement**

Unité de recherche :

LISBP - Laboratoire d'Ingénierie des Systèmes Biologiques et des Procédés

Thèse dirigée par

Nicolas DIETRICH et Gilles HEBRARD

Jury

M. Huai-Zhi LI
M. Mahmoud EL HAJEM
Mme Sylvie GILLOT
M. Olivier BREMOND
Mme Véronique ROIG
M. Arnaud COCKX
M. Gilles HEBRARD
M. Nicolas DIETRICH

Professeur à l'Université de Lorraine
Maitre de conférences/HDR à l'INSA Lyon
Directrice de recherche à l'IRSTEA
Ingénieur Procédés chez SUEZ
Professeure à l'INPT-ENSEEIH/IMFT
Professeur à l'INSA Toulouse
Professeur à l'INSA Toulouse
Maitre de conférences/HDR à l'INSA Toulouse

Rapporteur
Rapporteur
Examinateur
Examinateur
Examinateur
Co-directeur de thèse
Co-directeur de thèse
Directeur de thèse

THÈSE

Présentée

Pour obtenir le titre de

**DOCTEUR DE L'INSTITUT NATIONAL DES SCIENCES APPLIQUÉES DE
TOULOUSE**

École Doctorale MEGEP

Spécialité : Génie des Procédés et de l'Environnement

par

Feishi XU

BUBBLE HYDRODYNAMICS AND MASS TRANSFER IN COMPLEX MEDIA

Soutenue prévue le 19/04/2019 devant le jury composé de :

Huai-Zhi LI	Professeur à l'Université de Lorraine	Rapporteur
Mahmoud EL HAJEM	Maitre de conférences/HDR à l'INSA Lyon	Rapporteur
Sylvie GILLOT	Directrice de recherche à l'IRSTEA	Examineur
Olivier BREMOND	Ingénieur Procédés chez SUEZ	Examineur
Véronique ROIG	Professeure à l'INPT-ENSEEIH/IMFT	Examineur
Arnaud COCKX	Professeur à l'INSA Toulouse	Co-directeur de thèse
Gilles HEBRARD	Professeur à l'INSA Toulouse	Co-directeur de thèse
Nicolas DIETRICH	Maitre de conférences/HDR à l'INSA Toulouse	Directeur de thèse

préparée au Laboratoire d'Ingénierie des Systèmes Biologiques et des Procédés

LISBP-INSA Toulouse - 135, avenue de Rangueil - 31077 Toulouse Cedex 4

Acknowledgement

Firstly, I sincerely thank Prof. Véronique ROIG, the president of thesis' jury, and also extend my sincere gratitude to the reviewers of my dissertation, Prof. Huai-Zhi LI and Dr. Mahmoud EL HAJEM, for your insightful comments and helpful advices to improve and optimize this thesis. Thank you Dr. Sylvie GILLOT and Olivier BREMOND for attending my defence, and I appreciate your kind suggestions in the point of view of industry application.

Secondly, I am extremely grateful to my supervisors. Prof. Gilles HEBRARD, as a leader of the department, you were always willing to spend your precious time to discuss with me and follow my research progress. Your brilliant and global guidance kept my work sailing along the right direction in the scientific sea. Prof. Arnaud COCKX, many thanks for your concern since the first day I joined the TIM7. Your serious attitude well impressed me and your smart suggestions always give me a lot of inspiration for my research. Then I would like to give my special appreciation to Dr. Nicolas DIETRICH who carried me through these three and half years. Your mentorship, motivation and friendship leads me into the area of visualization of gas-liquid mass transfer. Every time when I faced the problems, neither the ones in the lab life nor the ones about the research, you were always the person who helped me out and make me achieve the objective of our research.

Thirdly, thank you all the colleagues in LISBP, especially José MOREAU, Bernard REBOUL, Manon MONTANER for your technique support, and also Claude Le Men for your kind help in camera setting and image post-treatment. Thank you my friends Mei MEI, Zibin NAN, Hui DENG, Ploypailin ROMPHOPHAK for the help in the day of my defence.

The last but not the least, I would like to dedicate this work to my parents who always stand behind me, trusting and supporting me.

Abstract

Bubbly flow is commonly used in chemical and biological processes. In sewage treatment, water aeration is a crucial process where the enhancement of mass transfer rate through the bubble-liquid interface can degrade the pollutants then improve the purification efficiency. The knowledge on the hydrodynamic property and mass transfer of bubble are important since it will give the guideline for selection of the working condition and reactor design in such processes. However, some mechanism of the oxygen mass transfer is still unclear especially for the system with a complex liquid phase thus further investigations are required. For this purpose, this Ph.D. manuscript has carried out an experimental investigation of single air bubbles rising in various polymer solutions which can simulate the property of the sewage. The works can mainly be divided into three parts:

Firstly, with a review of the current visualization techniques for mass transfer, three techniques have been tested for air bubble (equivalent diameter ≈ 1 mm) rising in water including traditional Planar Laser Induced Fluorescent (PLIF, dye: fluorescent resorufin), Fluorescent quenching technique (PLIF with Inhibition, dye: ruthenium complex) and colorimetric techniques (dye: pink resorufin), respectively. The advantages and the limitations of each technique have been summarized depending on their result for characterizing the diffusion and mass transfer.

Secondly, based on images captured by a high-speed camera, the hydrodynamics of the bubble single air bubbles (equivalent diameters: 0.7-7 mm) rising in the polymer solutions (PAAm and Xanthan) have been investigated including the bubble velocity, trajectory, and bubble shape. An innovative model containing the aspect ratio and two shape parameters is proposed and proved to be capable of characterizing the bubble shape from spherical/ellipsoidal to prolate/oblate-tear with good accuracy. Several impacts on bubble deformation and hydrodynamic behavior are then investigated involving the rheological properties of the fluids and different forces exerted on the

bubble which is quantified by multiple dimensionless numbers (e.g. Reynolds number, Eötvös Number, Deborah number). The empirical correlations are obtained for predicting the bubble shape.

Finally, based on PLIF-I technique, the mass transfer and diffusion phenomena in the wake of single air bubbles (equivalent diameter ≈ 1 mm) rising in various aqueous polymer solutions (PAAm and Breox) are investigated. For each fluid medium, liquid-side mass transfer coefficient and the diffusion coefficient are determined and analyzed by considering multiple factors: the rheological properties of the fluid, the concentration of the solute, the hydrodynamics of the bubble, and the contamination effect. The results are compared with cases implemented in non-polymer solutions to clearly identify the characteristics of mass transfer in the polymer media.

Keywords: Mass transfer, hydrodynamics, bubble

Résumé

Les écoulements à bulles sont présents dans beaucoup de processus chimiques et biologiques. Pour le traitement des eaux usées, l'aération de l'eau est un processus crucial dans lequel le transfert de matière à travers l'interface bulle-liquide peut accélérer la dégradation des polluants et améliorer l'efficacité de la purification. La connaissance du comportement hydrodynamique et du transfert de matière est importante car elle fournira des indications précieuses pour la sélection des conditions optimales de fonctionnement et pour la conception du réacteur. Certains mécanismes de transfert de matière restent toutefois encore délicats à comprendre, en particulier dans les milieux complexes, où des investigations supplémentaires sont nécessaires. Cette thèse se consacre à une étude expérimentale pour des bulles d'air isolées en ascension dans diverses solutions de polymères (Breox, Polyacrylamide (PAAm) et Xanthan gum) qui peuvent simuler les propriétés rhéologiques des eaux usées. Les travaux sont divisés en trois parties :

Tout d'abord, en dressant l'état de l'art sur les techniques de visualisation pour le transfert de matière, trois techniques ont été testées pour les bulles d'air (diamètre équivalent ≈ 1 mm) en ascension dans l'eau, notamment la fluorescence induite par plan laser (PLIF, fluorophore: résorufine fluorescente), la PLIF avec inhibition (fluorophore: complexe de ruthénium) et enfin une technique colorimétrique (colorant: résorufine rose). Les avantages et les limites de chaque technique ont été résumés pour caractériser la diffusion et le transfert de matière.

Par la suite, sur la base des images capturées par une caméra haute vitesse, le comportement hydrodynamique des bulles d'air (diamètres équivalents : 0,7 à 7 mm) en ascension dans des solutions de polymères (PAAm et Xanthan) a été étudié, notamment la vitesse, la trajectoire et la forme de la bulle. Un modèle innovant utilisant l'excentricité et deux paramètres de forme est proposé et s'est montré capable de caractériser avec une bonne précision la forme des bulles sphériques, ellipsoïdales et

celles en forme de larme. Plusieurs effets sur la déformation de la bulle et sur le comportement hydrodynamique sont ensuite étudiés, impliquant les propriétés rhéologiques des fluides et les différentes forces exercées sur la bulle qui sont quantifiées par plusieurs nombres sans dimension (ex. nombre de Reynolds, nombre d'Eötvös, nombre de Deborah). Des corrélations empiriques sont aussi obtenues pour prédire la forme de la bulle.

Enfin, appliquant la technique PLIF-I, les phénomènes de transfert de matière et de diffusion dans le sillage de bulles d'air (diamètre équivalent ≈ 1 mm) dans différentes solutions aqueuses de polymères (PAAm et Breox) ont été étudiés. Pour chaque fluide, le coefficient de transfert de matière du côté liquide et le coefficient de diffusion de l'oxygène sont déterminés et analysés en prenant en compte plusieurs facteurs : les propriétés rhéologiques du fluide, la concentration du soluté, l'hydrodynamique de la bulle et l'effet de contamination. Les résultats sont comparés aux cas mis en œuvre dans des solutions non polymères pour identifier clairement les caractéristiques de transfert de matière dans le milieu polymère.

Mots-clés : Transfert de matière, Hydrodynamiques, Bulle

Content

Abstract	I
Résumé	IV
Content	VI
List of figures	X
List of tables	XIX
Nomenclature	XXI
Introduction	1
Chapter 1 Fundamental principles	5
1.1 Principles of gas-liquid mass transfer.....	6
1.1.1 Diffusion coefficient	6
1.1.2 Mass transfer coefficient.....	7
1.1.3 Theories of mass transfer	9
1.2 Gas-liquid mass transfer measurement	15
1.2.1 Classic method	15
1.2.2 Visualization techniques	19
1.3 Rheology principle.....	32
1.3.1 Definition of shear stress, shear rate and viscosity	33
1.3.2 Rheological measurement: principle of rheometer	35
1.3.3 Rheological behavior	37
1.3.4 Viscosity of polymer systems	43
1.3.5 Rheological models.....	45
1.4 Conclusions.....	48
Chapter 2 Material and Methods	50
2.1 Material	51

2.1.1	Polymers to study.....	51
2.1.2	Oxygen indicator (dye).....	60
2.2	Experimental setup.....	64
2.2.1	Column.....	64
2.2.2	Syringe pump.....	65
2.2.3	Nd:YAG laser.....	65
2.2.4	CCD camera.....	66
2.2.5	High-speed camera.....	66
2.2.6	Acquisition system.....	66
2.2.7	Oxygen probe.....	67
2.3	Experimental protocol.....	68
2.4	Methods on bubble hydrodynamics.....	70
2.4.1	Bubble velocity and trajectory.....	70
2.4.2	Bubble shape and size.....	71
2.5	Methods on mass transfer quantification.....	73
2.5.1	Calibration of gray level and dissolved concentration.....	73
2.5.2	Image processing.....	78
2.5.3	Determination of the diffusion coefficient.....	82
2.5.4	Determination of the liquid side mass transfer coefficient.....	86
2.5.5	Error analysis.....	88
2.6	Conclusion.....	90
Chapter 3 Comparison of different visualization techniques (PLIF, PLIF-I and colorimetric techniques).....		93
3.1	State of the arts.....	94
3.1.1	Free bubbly flows.....	94

3.1.2	Plane interface flows.....	97
3.1.3	Taylor flows and confined flows.....	99
3.2	Experiment under controlled conditions.....	101
3.3	Visualization result.....	103
3.3.1	Image of side view.....	103
3.3.2	Image of bottom view.....	105
3.4	Quantification of mass transfer.....	105
3.4.1	Calibration result.....	105
3.4.2	Mass flux.....	108
3.4.3	Diffusion coefficient.....	110
3.4.4	Mass transfer coefficient.....	112
3.5	Summary of advantage and limitation.....	113
3.6	Conclusion.....	114
Chapter 4 Hydrodynamics of the Bubble: Characterization of bubble shapes by parametric equations.....		116
4.1	State of the art.....	117
4.1.1	Bubble shape.....	117
4.1.2	Bubble velocity and drag coefficient.....	121
4.2	Bubble shape characterization and results.....	127
4.2.1	Bubble shape regimes in different solutions.....	127
4.2.2	Characterization with aspect ratio.....	129
4.2.3	Characterization with parametric equations.....	137
4.2.4	Result of shape parameters.....	140
4.2.5	Prediction of bubble shape.....	147
4.3	Result of bubble velocity and drag.....	148

4.3.1	Bubble velocity	148
4.3.2	Drag coefficient	149
4.4	Trajectory characterization and result.....	151
4.4.1	Trajectory fitting model	151
4.4.2	Trajectory result	153
4.5	Conclusion	156
Chapter 5	Mass transfer in polymer fluids.....	158
5.1	State of the art	159
5.1.1	Mass transfer quantification by visualization techniques	159
5.2	Mass transfer visualization and characterization	162
5.2.1	Hydrodynamic result.....	162
5.2.2	Oxygen concentration field in the bubble wake	164
5.2.3	Characterization with Gaussian equation.....	165
5.3	Result of mass transfer quantification.....	167
5.3.1	Mass flux.....	167
5.3.2	Diffusion coefficient	171
5.3.3	Mass transfer coefficient.....	176
5.4	Extension to mass transfer from big bubbles	184
5.5	Conclusion	189
	Conclusion and Perspective	192
	List of publications.....	199
	References.....	201

List of figures

Figure 1-1 The film theory for mass transfer	10
Figure 1-2 Two-film model.....	11
Figure 1-3 Penetration theory for mass transfer	14
Figure 1-4 Gas-liquid mass transfer measurement with a probe in bubble column	16
Figure 1-5 Experimental curve of oxygen concentration against time when air bubbles injected into a column filled with water. Green line: oxygen concentration; Blue triangle: the value of $\ln[CL * -CL/(CL * -C0)]$, Red line: linear regression of the logarithm as a function of time.	18
Figure 1-6. Schematic description of the principle of variant LIF techniques by Jablonski diagram.	21
Figure 1-7. Schematic view of quenching reaction (Eftink, 1991).....	22
Figure 1-8. Relative fluorescence intensity or extinction coefficient variations as a function of pH value. Image from (Lacassagne et al., 2017).....	27
Figure 1-9. Reactions occurring in the “blue bottle” experiment; reproduced from (Anderson et al., 2012).....	30
Figure 1-10. Reduction of resazurin to resorufin by glucose and sodium hydroxide (step[1]). Reduction of resorufin to dihydroresorufin by carbohydrate (step[2]). Reoxidation of dihydroresorufin to resorufin in the presence of oxygen (step[3]).	31
Figure 1-11. Reversible redox reaction of leuco-indigo carmine to keto-indigo carmine with glucose as reducing and oxygen as an oxidizing agent. Colour change (yellow-red-blue) is illustrated in flask experiments. Reproduced from (Krieger et al., 2017)	31
Figure 1-12 I: Two-plate model; II: Laminar flow in the form of planar fluid layers.	33

Figure 1-13 Sensor system of rotational rheometers: I. Concentric cylinder; II. Cone-plate; III. Plate-plate.....	36
Figure 1-14 Different geometries for rheometer. Images from Anton-paar.com.....	36
Figure 1-15 Representation of different rheological behaviors (shear thinning, Newtonian and shear thickening) in a rheogram (I: τ vs γ ; II: μ vs γ).....	38
Figure 1-16 Explanation of shear thinning behavior: structures of polymers at rest and under high shear load.....	39
Figure 1-17 Representation of viscoplasticity in a rheogram (I: τ vs γ ; II: μ vs γ).....	40
Figure 1-18 Example result of the dynamic test for viscoelastic behavior, presented as a sinusoidal function versus time with preset shear strain γ and resulting shear stress τ . The two curves are offset by a phase shift. Figure from (Mezger, 2014).....	41
Figure 1-19 Vector diagram illustrating the relationship between complex shear modulus G^* , storage modulus G' and loss modulus G'' using the phase-shift angle θ . The elastic portion of the viscoelastic behavior is presented on the x-axis and the viscous portion on the y-axis.....	42
Figure 1-20 Typical flow behavior of real fluids of low solids concentration.....	44
Figure 1-21 Non-Newtonian viscosity in polymeric systems of low concentrations, low molecular weight or at temperatures well above the glass transition temperature.....	44
Figure 2-1 Chemical structure of the polymers. I: Breox; II: PAAm; III: Xanthan gum. Images from Lookchem.com.....	52
Figure 2-2 Instruments for the measurement of surface tension and density. I: Tensiometer (Krüss K6, Germany); II: Pycnometer (Blaubrand, Germany).....	54

Figure 2-3 Flow curves of water and Breox solutions. I: shear stress vs shear rate; II: Viscosity vs shear rate.....	56
Figure 2-4 Flow curves of PAAm solutions. I: shear stress vs shear rate; II: viscosity vs shear rate with an example of the fitting curve for PAAm 1.25 wt. % case.	58
Figure 2-5 Flow curves of Xanthan gum solutions. I: shear stress vs shear rate; II: Viscosity vs shear rate with an example of the fitting curve for Xanthan 0.5 wt. % case.....	58
Figure 2-6 Spectrum of the fluorophore (ruthenium complex) expressed in normalized absorption factor (blue line) and normalized emission factor (orange line). Image produced according to the data from Fluorophore.org	61
Figure 2-7 Variation of gray level (12 bits format) for dissolved oxygen concentration between 0 and 3 mg·L ⁻¹ as a function of the dye concentration. Reproduced from (Jimenez, 2013).....	62
Figure 2-8 Spectrum of resorufin expressed in normalized absorption factor (blue line) and normalized emission factor (orange line). Image produced according to the data from Fluorophore.org	64
Figure 2-9 Experimental setup.....	65
Figure 2-10 Evolution of the oxygen concentration in tap water by the oxygen probe (IntelliCAL LDO Probe, HACH®).....	68
Figure 2-11 Ruler	69
Figure 2-12 Sparger	69
Figure 2-13 Example of the trajectory of the bubble. I: Raw images, II: Binary images, III: Trajectory of the bubble.....	71
Figure 2-14 Schematic views of the image processing steps (Example of a bubble rising in 0.5 % wt. Xanthan solution).	72

Figure 2-15 Schematic diagram of the bubble profile (I) and the processing method for the equivalent diameter of the bubble (II).....	72
Figure 2-16 Calibration between grey level and the dissolved oxygen concentration for PLIF-I technique. I: Experimental images under different oxygen concentration; II: calibration curve ($GL_0 = 3267$, $K_{SV} = 0.27 \text{ L} \cdot \text{mg}^{-1}$)	74
Figure 2-17 Impact of the calibration area on the calibration result; I: Concentric calibration area; II&III: Evolution of parameter GL_0 and K_{SV} versus the diameter of the calibration circle.	76
Figure 2-18 Calibration between grey level and the dissolved oxygen concentration for PLIF technique. I: Experimental images under different oxygen concentration; II: calibration curve.....	77
Figure 2-19 Calibration between grey level and the dissolved oxygen concentration for colorimetric technique. I: Experimental images under different oxygen concentration; II: calibration curve.....	78
Figure 2-20 Image processing. I: Raw image of dissolved oxygen concentration field; II: Image after subtracting the background.....	79
Figure 2-21 Image processing. I: Zone without transfer; II: Image after subtracting the background.....	80
Figure 2-22 Image processing. I: Image after applying a threshold; II: Image fitted with the Gaussian model.	81
Figure 2-23 Determination of the diffusion coefficient (N : total number of pixels on the image, N' : number of pixels within area S_{spot} , $[O_2]_i$: oxygen concentration at i pixel).....	85
Figure 2-24 Description of the mass balance domain.....	86
Figure 3-1 Development of mass transfer visualization of freely rising bubbles. Images	

from the indicated authors.95

Figure 3-2. Gas-liquid mass transfer around Taylor bubbles flowing in a meandering millimetric square channel. Reproduced from (Yang et al., 2017b)100

Figure 3-3. Oxidation of leuco-indigo carmine in an FEP tube with 1.6 mm inner diameter. Reproduced from (Krieger et al., 2017)100

Figure 3-4 Recorded images of side view and bottom view.....103

Figure 3-5 Recorded images by different visualization techniques (Side view)103

Figure 3-6 Recorded images by different visualization techniques (bottom view) ...105

Figure 3-7 Examples of calibration result for three visualization techniques (PLIF-I, PLIF, and colorimetric technique).106

Figure 3-8 Examples of concentration field of the dissolved oxygen in bubble wake at the same moment (bottom view).....107

Figure 3-9 Image composition of mass transfer in bubble wake108

Figure 3-10 Corrected images (top) and fitted images (bottom) of the concentration field of the dissolved oxygen in bubble wake.....108

Figure 3-11 Mass flux versus time measured by different techniques (PLIF-I, PLIF, Colorimetric).....110

Figure 3-12 Temporal evolution of the O₂ concentration field at the cross section of bubble wake (left to right: result by PLIF-I, result by PLIF, result by colorimetric, respectively. $\Delta t= 0.67s$)110

Figure 3-13 Evolution of the spot area as a function of time.....111

Figure 3-14 Visualisation result with resorufin as a dye for bigger bubble (**Deq**~3 mm). Left: image by PLIF; Right: image by colorimetric technique.....113

Figure 4-1 Grace Diagram: Shape regimes for bubbles and drops in unhindered gravitational motion through liquids. Image from (Clift et al., 1978).118

Figure 4-2 Bubble terminal velocity in clean water (293.15 K) and contaminated water as a function of the bubble equivalent diameter. Image reproduced by (Guet and Ooms, 2006) from the (Clift et al., 1978).	122
Figure 4-3 Bubble velocity as a function of bubble volume. The fluid is a viscoelastic, shear-thinning polymer solution. The different symbols show experiments recorded at different heights. Image from (Pilz and Brenn 2007)	126
Figure 4-4 Visualization result of the bubble shapes in PAAM solutions of different concentrations	127
Figure 4-5 Visualization result of the bubble shapes in Xanthan solutions of different concentrations	127
Figure 4-6 Shape regime map (namely Grace Map) for bubbles in PAAM and Xanthan solutions (dark gray curves: $\log Mo$; gray spots in the background: typical bubble shape near the corresponding experimental points).....	128
Figure 4-7 Aspect ratio E versus We number in PAAM and Xanthan solutions.....	130
Figure 4-8 Aspect ratio E versus Ta number in PAAM and Xanthan solutions.....	131
Figure 4-9 Aspect ratio E versus the product of $We \cdot Eo \cdot n$ in the PAAM and Xanthan solutions.	134
Figure 4-10 Aspect ratio E versus the product of $We \cdot Ta \cdot n$ in the PAAM and Xanthan solutions.	134
Figure 4-11 Comparison between E from the correlation and E from measurement in PAAM and Xanthan solutions.....	136
Figure 4-12. Schematic diagram of the bubble profile	137
Figure 4-13 Evolution of the shape versus the parameters α and β (I: $E=1$; II: $E=2$).	140
Figure 4-14 Examples of the bubble profiles and the fitting ones by Eq. (6) in PAAM	

(I, III) and Xanthan solutions (II, IV) under different concentrations. (The bubbles are injected by the nozzle with a caliber of 1 mm at a flow rate of 10 μ L/h)..... 142

Figure 4-15 Relationship between the bubble shape parameters (α and β) in both PAAM and Xanthan solutions under various concentrations..... 143

Figure 4-16 The evolution of parameter β in terms of the bubble size (V) and various dimensionless numbers (De , Eo , Re) in PAAM and Xanthan solutions under various concentrations. 145

Figure 4-17 Comparison result between parameter β from correlation (Eq.(4-23)) and β from measurement in PAAM and Xanthan solutions. 147

Figure 4-18 Illustration of correlation equations system for the bubble shape prediction. 148

Figure 4-19 Relationship between bubble rising velocity and bubble size (Deq : 0.7~7 mm) in Xanthan (I) and PAAM solution (II)..... 149

Figure 4-20 Drag coefficient versus Reynolds number for bubbles rising in different solutions. 150

Figure 4-21 Drag coefficient versus Bubble shape parameter β for bubbles rising in different solutions. 151

Figure 4-22 Example of the fitting result of the bubble trajectory ($Deq \approx 5$ mm). I: PAAM 0.1 wt%; II: Xanthan gum 0.1 wt%..... 153

Figure 4-23 Trajectory of the bubbles in different size ($Deq=1-5$ mm) rising in PAAM solutions 154

Figure 4-24 Trajectory of the bubble of different size ($Deq=1-5$ mm) rising in Xanthan solutions 155

Figure 5-1 Examples of corrected images and shapes of a single bubble rising in water, Breox 2.2 wt% and PAAM 0.1 wt% solutions 164

Figure 5-2 Evolution of the values of three parameters A , B , C as a function of time (Example of the PAAm 0.1 wt% case)	166
Figure 5-3 Oxygen concentration field before and after the fitting with Gaussian equation. (Example of PAAm_0.1 wt.%)	167
Figure 5-4. Comparison between flux before fitting and flux after fitting (Example of water case)	168
Figure 5-5 Evolution of the estimated flux as a function of time in different liquids (Water, PAAm and Breox)	170
Figure 5-6 Profile of dissolved oxygen concentration fields in the bubble wake cross sections in Breox solutions ($\Delta t=2/3$ s).....	172
Figure 5-7 Profile of dissolved oxygen concentration fields in the bubble wake cross sections in PAAm solutions ($\Delta t=2/3$ s).....	173
Figure 5-8 Evolution of the spot area as a function of time.....	174
Figure 5-9 Diffusion coefficient versus viscosity in different liquid media	176
Figure 5-10 Stagnant cap model	180
Figure 5-11 Cap angle and contamination on a real bubble.	182
Figure 5-12 Normalized drag coefficient vs stagnant cap angle (Left y-axis); Normalized Sherwood number vs stagnant cap angle (Right y-axis).....	183
Figure 5-13 Visualisation result of the mass transfer of bubbles in different sizes rising in PAAm solutions (1.25 wt. %).	185
Figure 5-14 Visualisation result of the mass transfer of bubbles in different sizes rising in Xanthan gum solution (0.1% wt.).....	185
Figure 5-15 Oxygen concentration field in the wake of bubbles in different sizes rising in PAAm gum solution (1% wt.).....	187

Figure 5-16 Oxygen concentration field in the wake of bubbles in different sizes rising
in Xanthan gum solution (0.1% wt.).....187

List of tables

Table 1-1. Characteristics of the common dyes for fluorescence quenching in mass transfer visualization.....	25
Table 1-2 Characteristics of the common PH-sensitive dyes for mass transfer visualization.	28
Table 1-3. Chemical and physical properties of dyes for colorimetric technique.....	32
Table 1-4 Conversion factors of torque to shear stress K_{SS} and rotational speed to shear rate K_{SR} for different sensor systems.....	37
Table 1-5 Flow curve models applicable for real fluids (p is a parameter).	48
Table 2-1 Surface tension and density of the investigated solutions.	55
Table 2-2 Viscosity of water and Breox solutions at different concentrations	57
Table 2-3. Fitting result of the viscosity of PAAm and Xanthan gum solution by Carreau model.....	59
Table 2-4 Characteristics of ruthenium complex ($C_{36}H_{24}Cl_2N_6Ru \cdot xH_2O$). Data from Sigma-Aldrich.....	61
Table 2-5 Characteristics of the resazurin. Data from Sigma-Aldrich.....	63
Table 2-6 Relation between parameter η and P of Chi-squared distribution.....	84
Table 3-1 Materials and property of the bubble for comparison of three techniques	102
Table 3-2 Result of fluxes before and after fitting for the three techniques	109
Table 3-3 Result of the diffusion coefficient for the three techniques.....	111
Table 3-4 Result of mass transfer coefficient by the three techniques.....	112
Table 3-5 Advantage and limitation of three techniques (PLIF-I, PLIF, colorimetric technique).....	114
Table 4-1 Dimensionless numbers for bubble shape characterization.....	117
Table 4-2. Bibliography of bubble shape characterization	120

Table 4-3 Summary of correlations on the drag coefficient of the gas bubble moving in a quiescent liquid.124

Table 4-4 Correlation results for the bubble aspect ratio with different pairs of dimensionless numbers.132

Table 4-5 Correlation results for the aspect ratio E with Tn number (i.e. $Ta \cdot We \cdot n$)...135

Table 4-6 Approximate models of the profiles of a bubble or droplet: parametric equation and example.137

Table 5-1. Bibliography of the mass transfer quantification of a freely rising bubble by PLIF-I in the past decade160

Table 5-2 Hydrodynamics results of the bubble163

Table 5-3 Results for the diffusion coefficient.....175

Table 5-4 Result of the viscosity and diffusion coefficient for each solution.....176

Table 5-5 Results for the liquid side mass transfer coefficient and the contaminated angle177

Table 5-6 Impact of bubble velocity on the mass transfer179

Table 5-7 Results of normalized drag coefficient and cap angle181

Table 5-8 Results of normalized Sherwood number and rectified cap angle184

Table 5-9 Total transferred mass on the oxygen concentration field188

Table 5-10 Result of the mass transfer coefficient.....189

Nomenclature

Latin letters

A	Parameter of Gaussian equation [$\text{mg}\cdot\text{L}^{-1}$]
a	Specific interfacial area [m^{-1}]
b	Width of the bubble [mm]
c	Height of the bubble [mm]
B	Parameter of Gaussian equation [mm^2]
C	Parameter of Gaussian equation [$\text{mg}\cdot\text{L}^{-1}$]
$[C]$	Concentration of the transfer species [$\text{kg}\cdot\text{m}^{-3}$]
C_i	Concentration of the transfer species in phase i [$\text{kg}\cdot\text{m}^{-3}$]
C_D	Drag coefficient of the bubble [-]
$C_{D,im}$	Drag coefficients for a fully contaminated bubble [-]
$C_{D,m}$	Drag coefficients for a clean bubble [-]
D	Diffusion coefficient [$\text{m}^2\cdot\text{s}^{-1}$]
D_b	Diameter of a bubble [m]
D_{eq}	Equivalent diameter [mm]
E	Aspect ratio
F	Mass transfer rate [$\text{kg}\cdot\text{s}^{-1}$]
F_d	Drag force [N]
F_{O_2}	Oxygen transfer rate [$\text{kg}\cdot\text{s}^{-1}$]
FL	Fluorescence level [-]
G	Gray level [-]
g	Gravity [$\text{m}\cdot\text{s}^{-2}$]
G	Shear modulus [Pa]
GL	Gray level[-]
He	Henry law constant [-]
I	Laser intensity [-]
I_0	Fluorescence intensities without quencher [-]
I_Q	Fluorescence intensities with quencher [-]
J	Flux density [$\text{mg}\cdot\text{m}^{-2}\cdot\text{s}^{-1}$]
K	Flow consistency index [Pa.sn]
K_i	Overall mass transfer coefficient with respect to phase i [$\text{m}\cdot\text{s}^{-1}$]
k	Mass transfer coefficient [$\text{m}\cdot\text{s}^{-1}$]
k_i	Mass transfer coefficient with respect to phase i [$\text{m}\cdot\text{s}^{-1}$]
k_L	Liquid side mass transfer coefficient [$\text{m}\cdot\text{s}^{-1}$]

K_{SV}	Stern-Volmer constant [$L \cdot mg^{-1}$]
l	Length of the bubble [mm]
M	Total transferred of a planar concentration field [$mg \cdot s^{-1}$]
Mo	Morton number [-]
m_{O_2}	Transferred mass by the bubble [mg]
m_i	Mass of the species i [kg]
n	Flow behavior index [-]
$[O_2]$	Oxygen concentration [$mg \cdot L^{-1}$]
$[O_2]_0$	Oxygen concentrations far from the spot center [$mg \cdot L^{-1}$]
$[O_2]^*$	Oxygen concentrations at saturation [$mg \cdot L^{-1}$]
P	Possibility [-]
Q	Quencher concentration [$mg \cdot L^{-1}$]
r	Cylindrical coordinate [mm]
r^2	Determination coefficient [-]
S	Interfacial area [m^2]
S_b	Surface area of the bubble [m^2]
t	Time [s]
t_λ	Relaxation time [s]
U	Rising velocity [$mm \cdot s^{-1}$]
U_x	Oscillating velocity [$mm \cdot s^{-1}$]
U_y	Rising velocity [$mm \cdot s^{-1}$]
V_i	Volume of the object i [m^3]
x	Abscissa of Cartesian coordinates [mm]
X	Abscissa of the spot center [mm]
$x_{i,cal}$	Abscissa by calculation [mm]
$x_{i,exp}$	Abscissa by experiment [mm]
x_C	Half-length of major axis [mm]
y	Ordinate of Cartesian coordinates [mm]
Y	Ordinate of the spot center [mm]
y_A	Length of minor axis [mm]
z	Vertical coordinate [mm]

Greek letters

α	Bubble shape parameter [-]
----------	----------------------------

β	Bubble shape parameter [-]
γ	Shear rate [s^{-1}]
γ	Shear strain [-]
Γ	Gamma function [-]
δ	Thickness of the liquid film [m]
δ_{pixel}	Side length of a single pixel [mm]
ε_G	Gas retention [%]
η	Positive integer parameter [-]
θ	Angle coordinate [$^\circ$]
λ	Noise threshold for image processing [-]
μ	Dynamic viscosity [Pa·s]
ν	Kinematic viscosity [$m^2 \cdot s^{-1}$]
ρ	Density [$kg \cdot m^{-3}$]
σ	Surface tension [$N \cdot m^{-1}$]
τ	Shear stress [Pa]
τ_i	Fluorescence lifetime in state i [ns]
φ_{cap}	Contamination angle [$^\circ$]

Dimensionless numbers

C_D	Drag coefficient, $(2F_d)/(\rho \cdot U_b^2 \cdot S)$
Eo	Eötvös number, $(\rho \cdot g \cdot D_b^2)/\sigma$
Mo	Morton Number, $(g \cdot \mu^4)/(\rho \sigma^3)$
Re	Reynolds number, $(U_b D_b \rho)/\mu$
Sc	Schmidt number, $\mu/\rho D$
Sh	Sheerwood number, $(k \cdot D_b)/D$
Ta	Tadaki number, $Re \cdot Mo^{0.23}$
We	Weber number, $(\rho U^2 \cdot D_b)/\sigma$
Wn	Product of (We, Eo, n)

Subscript

0	Initial concentration or minimum value
*	Saturated concentration or maximum value

<i>dye</i>	Related to dye
<i>G</i>	Related to the gas phase
<i>L</i>	Related to the liquid phase
<i>O₂</i>	Related to the oxygen
<i>Q</i>	In presence of the quencher
<i>m</i>	Mobile
<i>im</i>	Immobile

Introduction

Gas-liquid mass transfer phenomena are of widespread existence in the industry, as well as many chemical and biological processes (see Figure I-1). In the natural environmental systems, detailed climate prediction is still a tough issue due to the unclear mechanism of complex gas-liquid mass transport phenomena across the phase boundary, which poses the main resistances between the oceans and atmosphere (Asher, 2009; Garbe et al., 2008). For wastewater treatment, water aeration is a crucial gas-liquid transfer process for increasing the oxygen dissolution of the water. In spillways or membrane bioreactors, a supply of dissolved oxygen, commonly through an injection of air bubbles, is required to replenish the oxygen consumed by microorganisms for degrading specific pollutants (Roy and Duke, 2000, 2004). This pollutant removal process induces an enhancement of oxygen molecules transporting through the gas-liquid interface. The researches in this area are of prime interest in order to improve purification efficiency (Hébrard et al., 2000, 2009).

The chemical engineering processes such as distillation, solvent extraction and biological reactions like and fermentations oxidations, is primarily defined by mass transfer in the interfacial area between the dispersed phase and the continuous phase (Dani et al., 2007). In these reactors, a component of gas dispersed and absorbed into a continuous liquid. The velocity and efficiency of this process govern the reactors design procedure and operating conditions. A profound understanding and an accurate prediction of mass transfer phenomena are thus essential to improve the performance of gas-liquid reactors. In bioprocessing, gas-liquid mass transfer is extremely important because many processes are aerobic, oxygen must first be transferred from gas bulk through a series of steps onto the surfaces of cells before it can be used (Najafpour, 2006).

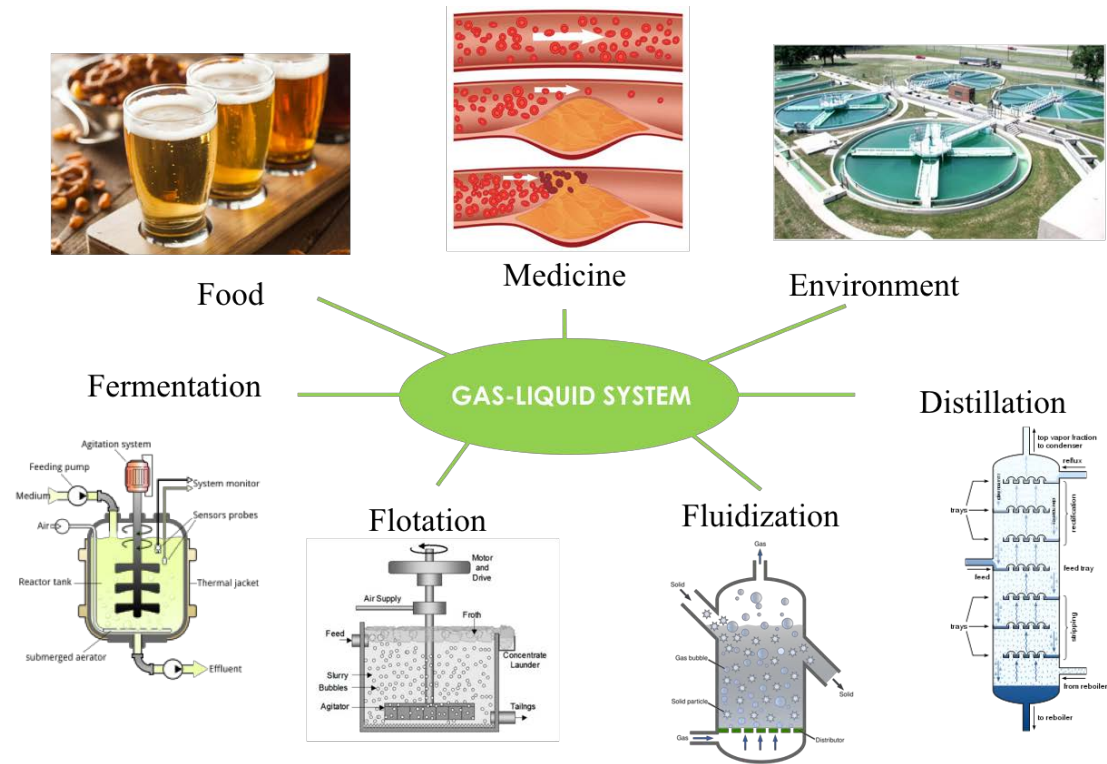


Figure I-1 Gas-liquid systems in the industry and various chemical and biological processes. The image of flotation is from (Kramer et al., 2012).

Different factors occurring at the vicinity of the gas-liquid interface can affect the transfer process in uncertain degrees making the characterization of the mass transfer more complex. These factors consist of the shape and dynamics of the interface, the transported species' Schmidt numbers (momentum diffusion divides mass diffusion), the turbulence characteristics (intensity, size of structures, time scales...), the gas-liquid composition and properties (rheology, contamination, chemical reaction...), operating conditions (temperature...), etc. Nevertheless, it is difficult to isolate a specific parameter and accurately analyze its influence on mass transfer. Due to this challenge, some extent of the mechanism of the gas-liquid mass transfer is still required further investigations including new theoretical analysis and high-prediction numerical or experimental technology.

In the previous work by Jimenez et al., (2013) and Dietrich et al., (2015), mass transfer

in the wake of air bubbles in different non-polymer media (water + glycerol, salt, glucose) has been investigated. However, most liquid media are polymeric fluids in industrial application, especially for wastewater treatment. The purpose of this study is to broaden their work to liquid media more complex. The transfer of oxygen through single air bubble rising in different liquid polymeric solution (Polyacrylamide (PAAm), Breox, and Xanthan gum) is investigated with the visualization technique and the impact induced by the solutions on the mass transfer is discussed. The objective is to isolate a specific factor and accurately analyze its influence on the mass transfer mechanism and to gain insight into the local phenomena of the mass transfer in complex media. The structure of the following content in the thesis is divided into five chapters and they are briefly described below:

Chapter 1 gives the fundamental principle of the gas-liquid mass transfer including the classical theory and definition of the diffusion and mass transfer coefficient. The principle of several visualization techniques and the basis of the rheology is also introduced which are helpful in understanding the following investigation on the mass transfer phenomena and bubble hydrodynamics.

Chapter 2 introduces the material and method which are used for gas-liquid mass transfer investigation. The rheological property of the chemicals, the experimental setup and experiment procedures are presented. The methods for calculating the bubble hydrodynamic properties like rising velocity and diameter are given afterward. The method for mass transfer characterization is then introduced including the calibration, image processing, and the mathematical approaches to determine the two key parameters: diffusion coefficient and mass transfer coefficient.

Chapter 3 compares three visualization techniques: traditional LIF technique (with fluorescent resorufin), fluorescence quenching (with fluorescent ruthenium complex) and colorimetric technique (with pink resorufin). The comparison is based on the result

of the experiments carried out for measuring the mass transfer of a bubble rising in water by the three techniques.

Chapter 4 analyzes the hydrodynamic properties of the bubble rising in various polymer solutions with the data from the experiment. Besides the rising velocity and trajectory, the analysis will focus on the impact of the polymer solution on the bubble deformation.

Chapter 5 determines the diffusion coefficient and liquid-side mass transfer coefficient in each fluid medium and analyzes multiple factors on the mass transfer like the rheological properties of the fluid, the concentration of the solute, and the hydrodynamics of the bubble.

Chapter 1

Fundamental principles

Abstract

In this chapter, the fundamental principles for studying the gas-liquid mass transfer are then presented including the definition of two key parameters (the diffusion coefficient and mass transfer coefficient) and the classic theories that explain the interfacial transfer process. The visualization techniques to measure the mass transfer is introduced after with a literature review of the new visualization techniques in a point of view: reaction-based techniques which can be classified into three different types including quenching reaction, acid-based reaction, and oxidation-reaction. Finally, since the rheological property of the liquid phase has the impact on the bubble hydrodynamics and the mass transfer from bubble to liquid, an introduction of the rheology principle and measurement is given as a basis for the analysis of rheological impact for the following chapters.

1.1 Principles of gas-liquid mass transfer

The principles of gas-liquid mass transfer are presented in the following paragraphs.

1.1.1 Diffusion coefficient

The most common way for mass transfer is diffusion. From a microscopic view, diffusion is caused by random molecular motion (Brownian motion). From a macroscopic view, diffusion is driven by a gradient in chemical potential of the diffusing species. A gradient is a difference in the value of a quantity e.g. concentration, pressure, or temperature with the change in another variable, usually distance. In gas-liquid systems, the cause of diffusion is a concentration gradient of the diffusing component which tends to move the molecules from a region of higher concentration to a region until equilibrium is established as the concentration becomes uniform.

The diffusion process in dilute solutions was approached by Adolf Fick in 1855. He developed the laws of diffusion by means of analogies with Fourier's laws for heat conduction or Ohm's law for electrical conduction (Fick, 1855).

1.1.1.1 Fick's first law

For one-dimensional diffusion in Cartesian coordinates:

$$J = -D \frac{\partial[C]}{\partial x} \quad (1-1)$$

Where:

J is the diffusive flux or the amount of substance that flows through a unit area during a unit time interval [$\text{kg}\cdot\text{m}^{-2}\cdot\text{s}^{-1}$];

D is the diffusion coefficient or diffusivity [$\text{m}^2\cdot\text{s}^{-1}$];

$\partial[C]/\partial x$ is the concentration gradient in x direction with $[C]$ the concentration of the diffusion species [$\text{kg}\cdot\text{m}^{-3}$] and x the position expressed in length [m].

For more dimensions problem, the gradient operator $\vec{\nabla}$ is used and the equation

becomes:

$$\vec{j} = -D\vec{\nabla}[C] \quad (1-2)$$

Where \vec{j} denotes the diffusion flux vector.

1.1.1.2 Fick's second law

Fick's second law predicts how diffusion causes the concentration to change with time. It can be derived from Fick's first law and the mass conservation in the absence of any chemical reactions:

$$\frac{\partial[C]}{\partial t} + \frac{\partial J}{\partial x} = 0 \Rightarrow \frac{\partial[C]}{\partial t} - \frac{\partial}{\partial x} \left(D \frac{\partial[C]}{\partial x} \right) = 0 \quad (1-3)$$

Thus Fick's second law for one-dimensional diffusion can be expressed by the partial differential equation (where t is time [s]):

$$\frac{\partial[C]}{\partial t} = D \frac{\partial^2[C]}{\partial x^2} \quad (1-4)$$

For more dimensions problem, the Laplacian $\vec{\Delta} = \vec{\nabla}^2$ is used and the equation becomes:

$$\frac{\partial[C]}{\partial t} = D \cdot \vec{\Delta}[C] \quad (1-5)$$

In gas-liquid systems, diffusion coefficient can well indicate mass transfer rate for a system in a steady state. However, the diffusion coefficient can only take into account the mass transfer in form of diffusion. In order to estimate the overall transferred mass such as the one by the flow convection, the mass transfer coefficient is defined and is introduced in the following paragraphs.

1.1.2 Mass transfer coefficient

The process of mass transfer across an interface, or across a virtual surface in the bulk of a phase, is the result of a chemical potential driving force. This driving force is more usually expressed in terms of concentrations of the species. The rate of transfer of a

given species depends on some of the physical properties of the system and on the degree of turbulence of the phases involved. In general, the relationship between the flux and these parameters is not easily developed from fundamentals of mass transfer, so that mass transfer coefficients have been defined that lump them all together. These definitions are of the form (Annesini et al., 2017):

$$F = k \cdot S \cdot \Delta[C] \quad (1-6)$$

where

F is the mass transfer rate [$\text{kg} \cdot \text{s}^{-1}$];

k is the mass transfer coefficient [$\text{m} \cdot \text{s}^{-1}$];

S is the interfacial area [m^2];

$\Delta[C]$ is the concentration difference known as a driving force [$\text{kg} \cdot \text{m}^{-3}$].

In the real application, relations for mass transport coefficients are usually given in terms of dimensionless groups:

- **Sherwood Number (Sh)** represents the ratio of the total rate of mass transfer to the rate of diffusive mass transport alone.

$$Sh = \frac{k \cdot l}{D} = \frac{\text{mass transfer rate}}{\text{diffusion rate}} \quad (1-7)$$

where l is a characteristic length of the problem [m].

- **Schmidt Number (Sc)** is a dimensionless number defined as the ratio of momentum diffusivity (viscosity) and mass diffusivity and is used to characterize fluid flows in which there are simultaneous momentum and mass diffusion-convection processes.

$$Sc = \frac{\nu}{D} = \frac{\text{diffusivity of momentum}}{\text{diffusivity of mass}} \quad (1-8)$$

where ν is momentum diffusivity (kinematic viscosity) [$\text{m}^2 \cdot \text{s}^{-1}$].

- **Reynolds Number (Re)** represents the fluid motion conditions

$$Re = \frac{Ul}{\nu} = \frac{\text{inertial forces}}{\text{viscous forces}} \quad (1-9)$$

where U is the velocity of the fluid with respect to the object [$\text{m}\cdot\text{s}^{-1}$].

It can be theoretically proved that the mass transport coefficient can be expressed as a function of Re and Sc :

$$Sh = f(Re, Sc) \quad (1-10)$$

Such a function can be obtained by combining theoretical models (boundary layer, penetration theory, etc.) and correlations of experimental data. For example, for a single spherical particle, a correlation by (Frössling, 1938):

$$Sh = 2 + 0.552 Re^{\frac{1}{2}} Sc^{\frac{1}{3}} \quad (1-11)$$

1.1.3 Theories of mass transfer

1.1.3.1 The Film Theory

The simplest conceptualization of the interfacial transfer process is attributed to Nernst (1904) who postulated that near the interface there exists a stagnant film. This stagnant film is hypothetical since we really don't know the details of the velocity profile near the interface. Nonetheless, such a hypothetical film gives the simplest model of the interfacial region. The steady-state flux across this thin film can be written in terms of the mass transfer coefficient:

$$J = k\Delta[C] \quad (1-12)$$

in which $\Delta[C]$ here refers to the concentration difference between the interface and the bulk.

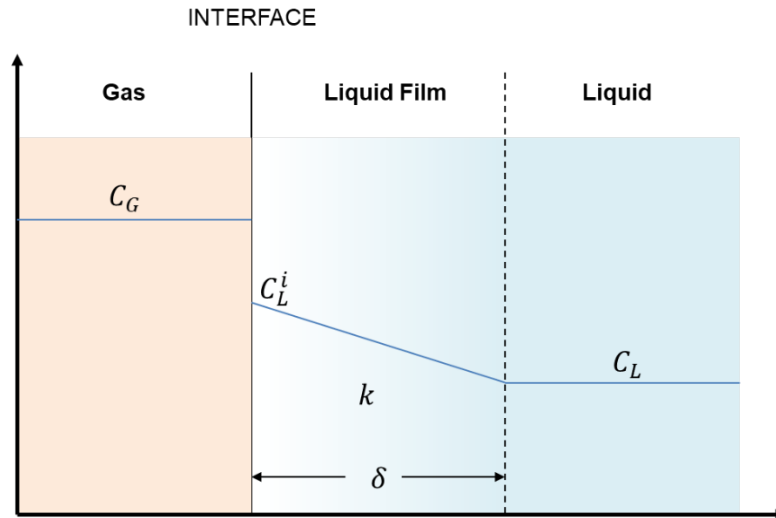


Figure 1-1 The film theory for mass transfer

In dilute solutions, diffusion-induced convection perpendicular to the interface can be neglected. Mass transfer in this film is governed only by molecular diffusion. Therefore, Fick's law describes flux across the film which can also be calculated in terms of the diffusion coefficient (Eq. (1-2)):

$$J = -D \frac{\partial [C]}{\partial x} \approx -D \frac{\Delta [C]}{\delta} \quad (1-13)$$

where δ denotes the thickness of the film.

If we compare Eq. (1-12) and Eq. (1-13), we can find that

$$k = \frac{D}{\delta} \quad (1-14)$$

1.1.3.2 Two-film model

In the study of gas-liquid mass transfer, it is assumed that both phases are separated by an interface and that diffusional mass transfer occurs inside a gas and a liquid film developed at each side of the interface. This representation of the gas-liquid diffusional mass transfer corresponds to the two-film model (Lewis et Whitman, 1924) which is

illustrated in Figure 1-2. In the two-film model, the solute mass transfer firstly diffuses through the gas film and reaches the gas-liquid interface. Then the gas is absorbed and dissolves into the liquid and thermodynamic equilibrium is established. After passing the interface, the solute gas diffuses through the liquid film until it reaches the liquid phase homogenous concentration.

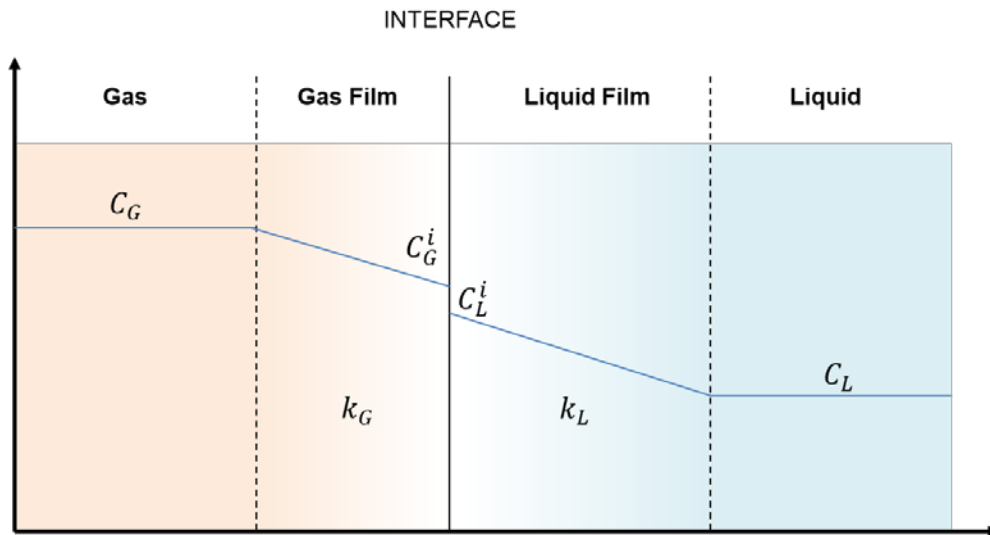


Figure 1-2 Two-film model

According to the two-film model, the following assumptions are made that:

- Outside the film, the concentrations are homogenous (as shown in Figure 1-2: C_G and C_L are the solute concentration in bulk in gas the phase and in the liquid phase, respectively);
- In both films, the gas and liquid films are characterized by film theory. A steady-state flux balance through each film can now be performed. The fluxes are given by:

$$\text{In gas film:} \quad J = k_G(C_G - C_G^i) \quad (1-15)$$

$$\text{In liquid film:} \quad J = k_L(C_L^i - C_L) \quad (1-16)$$

where

k_G is gas-side mass transfer coefficient [$\text{m}\cdot\text{s}^{-1}$];

k_L is liquid-side mass transfer coefficient [$\text{m}\cdot\text{s}^{-1}$];

C_G^i is gas-side solute concentration at the interface [$\text{kg}\cdot\text{m}^{-3}$];

C_L^i is liquid-side solute concentration at the interface [$\text{kg}\cdot\text{m}^{-3}$].

- At the gas-liquid interface, concentrations are in equilibrium according to Henry's law:

$$He = \frac{C_G^i}{C_L^i} \quad (1-17)$$

with He the Henry constant;

However, the concentrations at the interface cannot be measured, so the overall mass transfer coefficients are defined. These coefficients are based on the difference between the bulk concentration in one phase and the concentration that would be in equilibrium with the bulk concentration in the other phase.

In gas film: $J = K_G(C_G - C_G^*) \quad (1-18)$

In liquid film: $J = K_L(C_L^* - C_L) \quad (1-19)$

where

K_G is gas-side overall mass transfer coefficient [$\text{m}\cdot\text{s}^{-1}$];

K_L is liquid-side overall mass transfer coefficient [$\text{m}\cdot\text{s}^{-1}$];

C_G^* is the solute concentration in the gas phase in equilibrium with C_L [$\text{kg}\cdot\text{m}^{-3}$];

C_L^* is the solute concentration in the liquid phase in equilibrium with C_G [$\text{kg}\cdot\text{m}^{-3}$].

The values of C_G^* and C_L^* can be determined by Henry law:

$$He = \frac{C_G^*}{C_L} = \frac{C_G}{C_L^*} \quad (1-20)$$

Combine the Equations (1-15) - (1-21), the overall resistance to mass transfer in the gas and the liquid phase are written as:

$$\frac{1}{K_G} = \frac{1}{k_G} + \frac{He}{k_L} \quad (1-21)$$

$$\frac{1}{K_L} = \frac{1}{k_L} + \frac{1}{He \cdot k_G} \quad (1-22)$$

If the component solubility in the liquid phase is low, the Henry constant (He) is very high. Then the gas-phase resistance is relatively negligible comparing to that of liquid-phase, the mass transfer is generally controlled by the transfer in the liquid side. It means that

$$K_L \approx k_L \quad (1-23)$$

Thus, the mass transfer flux calculated by Eq. (1-19) becomes:

$$J = k_L(C_L^* - C_L) \quad (1-24)$$

1.1.3.3 Penetration theory

To deal with the unsteady state problem, R. Higbie proposed the penetration theory in 1935. The penetration theory is based on the ‘film theory’ with the basic assumptions as follows:

- Unsteady state mass transfer occurs to a liquid element so long it is in contact with the bubbles or other phases;
- Equilibrium exists at the gas-liquid interface;
- Each of the liquid elements stays in contact with the gas for the same period of time.

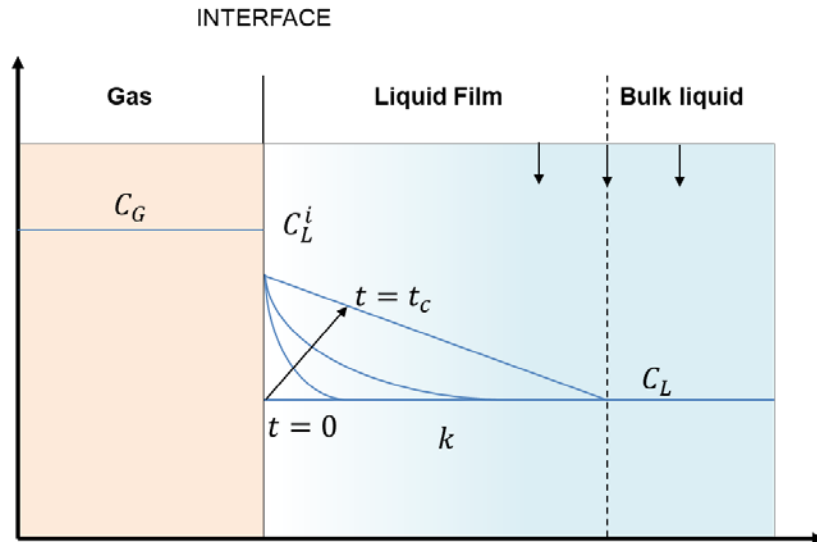


Figure 1-3 Penetration theory for mass transfer

Different from the film theory, the mass transfer rate in the liquid film is no longer a constant. In the beginning, when the liquid elements (eddies) start contacting with the gas-liquid interface, the equilibrium only exists at the interface while in other places of the film the concentration remains equal to the bulk C_L . The mass transfer rate is most important at this moment. Then gas enters and fills in the film during a time interval t_c , the mass transfer rate is decreasing gradually until the concentration equilibrium established. Subsequently, the liquid element is replaced by another one and the same contact process repeats.

The average liquid-side mass transfer coefficient during a contact time interval t_c for a bubble can be obtained from the Fick's second law,

$$k_L = 2 \sqrt{\frac{D}{\pi t_c}} \quad (1-25)$$

1.1.3.4 Surface renewal theory

Considering that the contact time at the interface is probably not the same for all liquid elements arriving at the gas-liquid interface, Danckwert (1951) modified the Higbie's

penetration theory. He stated that a portion of the mass transfer surface is replaced with a new surface by the motion of eddies near the surface and proposed the following assumptions:

- The liquid elements at the interface are being randomly swapped by fresh elements from bulk;
- At any moment, each of the liquid elements at the surface has the same probability of being substituted by a fresh element
- Unsteady state mass transfer takes place to an element during its stay at the interface.

A rate of surface renewal S [s^{-1}] is defined as the fraction of the surface renewed in unit time and the average liquid-side mass transfer coefficient is given by:

$$k_L = \sqrt{DS} \quad (1-26)$$

1.2 Gas-liquid mass transfer measurement

1.2.1 Classic method

A classic method to measure the mass transfer coefficient is carried out in a bubble column (see). The column is filled with the liquid and bubbles are kept injecting from the bottom of the column at a preset constant flow rate. The method is based on the hypothesis of a reactor perfectly mixed for the liquid. It consists of deoxygenating the water (e.g. by degassing with nitrogen or chemical reaction of sodium sulfite in the presence of cobalt ions) and then studying the re-increase of the dissolved oxygen concentration as a function of time.

The mass flux F [$kg \cdot s^{-1}$] transferred from the bubble to the liquid can be deduced from Eq. (1-24):

$$F = J \cdot S = k_L(C_L^* - C_L) \cdot S \quad (1-27)$$

where the interfacial area S equals to the total surface of all the bubble in the column. If divide the flux by the volume of the column, i.e.

$$F/V = k_L(C_L^* - C_L) \cdot S/V \quad (1-28)$$

the term in the left-hand side can be replaced by the time derivative of the dissolve the gas concentration in the liquid, the following equation is obtained:

$$\frac{dC_L(t)}{dt} = k_L \cdot a(C_L^* - C_L(t)) \quad (1-29)$$

with a called the specific interfacial area [m^{-1}] and $k_L \cdot a$ is known as the volumetric oxygen transfer coefficient. Hence by measure the dissolved gas concentration $C_L(t)$ as a function of time and the specific interfacial area a , the mass transfer coefficient k_L can be determined.

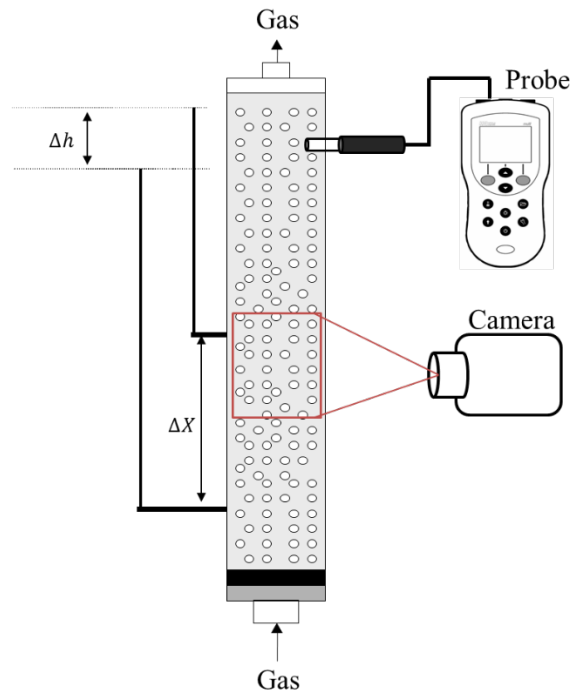


Figure 1-4 Gas-liquid mass transfer measurement with a probe in bubble column

1.2.1.1 Interfacial exchange area

A camera is available to acquire images and measure the size of the generated bubbles. For a single spherical bubble in equivalent diameter D_b , the interfacial area equals to the ratio between the surface area S_b and the bubble volume V_b :

$$a = \frac{S_b}{V_b} = \frac{6}{D_b} \quad (1-30)$$

For bubble swarm, the interfacial exchange area is calculated with the averaged bubble size $\overline{D_b}$ [m] and gas retention for each operating condition ε_G [%], which can be expressed by the following equation (Roustan, 2003):

$$a = \frac{\sum S_{b,i}}{\sum V_{b,i}} = \frac{6\varepsilon_G}{\overline{D_b}(1-\varepsilon_G)} \quad (1-31)$$

For a condition of gas flow and a type of water, the gas retention is determined by using the pressure receptacles arranged along the column (Hébrard, 1995):

$$\varepsilon_G = \frac{\Delta h}{\Delta x} \quad (1-32)$$

The lengths of Δh and Δx are indicated in Figure 1-4.

The size of the bubbles is measured using the video camera provided. When the condition of the flow regime of the gas is established, proceed with the acquisition of images of a number of bubbles. For ellipsoidal bubbles, the equivalent diameter of each bubble is determined by considering the width (b) and the height (c) of the bubble:

$$D_b = \sqrt[3]{c b^2} \quad (1-33)$$

The mean value of the equivalent diameters D_b is then determined as the characteristic value of the bubble population.

1.2.1.2 Dissolved gas concentration

The dissolved gas concentration in the liquid is measured with a probe placed at the top

of the column. The concentration values are recorded every constant time interval, i.e. $C_L(t)$.

The integration of Eq. (1-29) gives:

$$\ln\left(\frac{C_L^* - C_L(t)}{C_L^* - C_0}\right) = -k_L a \cdot t \quad (1-34)$$

where C_0 is gas concentration at $t = 0$ [$\text{kg}\cdot\text{m}^{-3}$] and C_L^* is the saturated concentration after injected bubbles for a long time. By plotting the curve of $\ln\left(\frac{C_L^* - C_L(t)}{C_L^* - C_0}\right)$ as a function of time, the volumetric oxygen transfer coefficient $k_L a$ equals to the slope of the linear part of the curve. An example of the experimental curve is shown in Figure 1-5 for air bubble dissolved in water. Finally, divide the volumetric oxygen transfer coefficient by the interfacial exchange area, the mass transfer coefficient k_L is obtained.

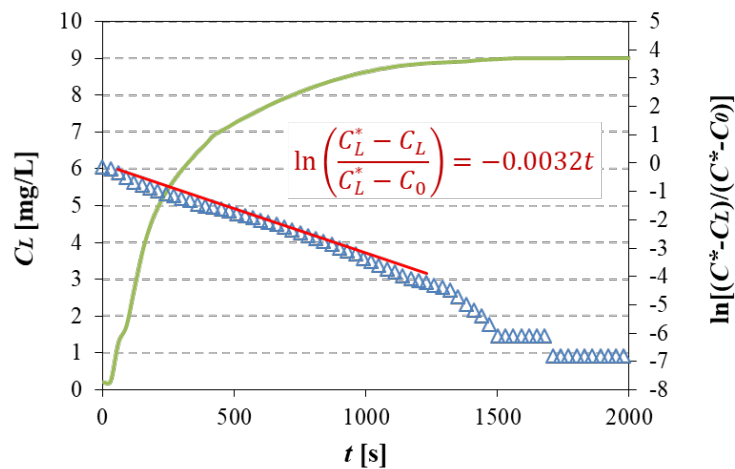


Figure 1-5 Experimental curve of oxygen concentration against time when air bubbles injected into a column filled with water. Green line: oxygen concentration; Blue triangle: the value of $\ln[(C_L^* - C_L)/(C_L^* - C_0)]$, Red line: linear regression of the logarithm as a function of time.

1.2.2 Visualization techniques

The mass transfer measured by the classic method is global or averaged value for the whole gas-liquid system. In order to get a deeper understand of the mass transfer phenomenon, getting access to the local mass transfer like the mass transfer in the bubble wake or even near the bubble surface is necessary. However, the thickness of the boundary layer on the liquid side which controls the gas transfer process is common in the millimeter or even micrometer scale. Due to this rigorous propriety, an extremely high resolution of experimental visualization is required. With the development of the experimental technique in the past several decades, various researches have been conducted to characterize, visualize and quantify gas-liquid mass transfer phenomena. The main techniques are based on probes or microprobes (Chu and Jirka, 1992; Jamnongwong et al., 2010; Riethues et al., 1986), holographic interferometry (Ma et al., 1999; Wylock et al., 2011), colorimetric technique (Dietrich and Hébrard, 2018; Kováts et al., 2017) and laser-induced fluorescence (LIF) technique (Butler et al., 2016, 2018; Crimaldi, 2008; Hanyu and Saito, 2010; Lacassagne et al., 2017, 2018; Valiorgue et al., 2013). The main drawback of using microprobes is that they are invasive and their presence could disrupt the fluid motions that are responsible for the concentration fluctuations. LIF is thus created in the late 1960s (Tango et al., 1968). If the laser is in the form of a plane, then it is called Planar Laser Induced Fluorescence (PLIF), fluorescence induced by a laser plane. The pioneer study was conducted by (Hanson et al., 1990) for gas combustion. PLIF has rapidly extended to study the mixing and dispersion of fluorescent tracers in liquid and gaseous flows. Compared to the probe technique, the LIF techniques which is mainly carried by using soluble fluorescent dye (fluorophore) and optical equipment, have the advantages of no flow disturbance, quick response time and high optical resolution, and capacity to elucidate the profile near the boundary with its limited thickness (Herlina and Jirka, 2004). In addition, it can be combined quite easily with other optical methods that can provide simultaneous

measurements of flow velocity and temperature (e.g. LIF-PIV (Charogiannis et al., 2015)).

1.2.2.1 Traditional PLIF technique

For traditional PLIF technique, the measurement is based on the linearity between the fluoresced light and the concentration of fluorophore in the weak excitation regime (Crimaldi, 2008). It is known that, under weak excitation condition (excitation intensity I much smaller than the saturation intensity of the dye), the relationship between fluorescence level FL and local concentration of the dye C_{dye} has the simplified relationship:

$$FL \propto I \cdot C_{dye} \quad (1-35)$$

where I can be assumed constant (Anderson et al., 2010; Golnabi and Razani, 2007). Thus using a multi-pixel light sensitive sensors (CMOS or CCD), one can record the fluorescence signal and thus determine the corresponding instantaneous concentration field. The traditional PLIF requires the transported species itself play as a role of fluorophore which is hard to realize for most gas-liquid species. Therefore, several variants of PLIF technique appears with the respective personalized name: PLIF-I (PLIF with Inhibition (Jimenez et al., 2013)), 2T-LIF (Two-tracer LIF, (Kováts et al., 2017)), LIF/HPTS (Huang and Saito, 2015), BPLIF (Blocked PLIF, (Lacassagne et al., 2017)), I_{PH}^R -PLIF (Ratiometric pH-sensitive-inhibited (Lacassagne et al., 2018)), DeLIF (Dual Emission LIF, (Someya et al., 2005)), etc. Different from traditional PLIF techniques, the fluorophore is here pre-mixed homogeneously into the liquid. Fluorescence of this kind of dye under monochromatic excitation can be affected by the presence of a flow-passive scalar (concentration of a chemical species, pH value, temperature...) (Figure 1-6). Then the value of this scalar can be deduced from the change of fluorescence intensity once a previous calibration is done that fluorescence intensities are measured for several preset values of the scalar.

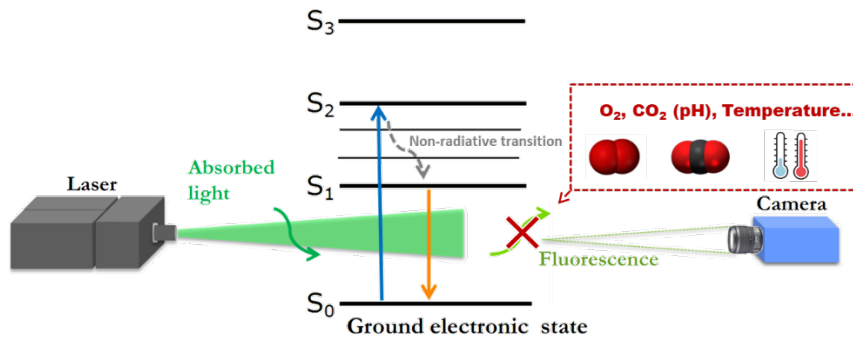


Figure 1-6. Schematic description of the principle of variant LIF techniques by Jablonski diagram.

Several excellent reviews have been made focusing on LIF techniques (Crimaldi, 2008; Rüttinger et al., 2018), however, they mixed the traditional PLIF techniques with variant PLIF techniques even though they are theoretically different. To the author's knowledge, most of the variant PLIF techniques are essentially based on the reaction between the dissolved scalar (e.g. gas molecules) and the soluble dye molecules. Therefore, the following content contributes to review the techniques other than traditional LIF in a different point of view: reaction-based techniques. Three different types of techniques for gas-liquid mass transfer visualization will be discussed which are based on the quenching reaction, acid-based reaction, and oxidation-reaction, respectively.

1.2.2.2 Quenching-based techniques

The first technique is an extension of the LIF technique based on the quenching phenomena of the fluorescence. The combination of fluorescence intensity measurements with the effect of fluorescence quenching for gas concentration measurements in liquids was first introduced by (Vaughn and Weber, 1970). As oxygen has been known as an excellent quencher (Jimenez et al., 2013), Wolff et al. (Wolff et al., 1991) introduced primarily LIF quenching technique to visualize O_2

concentration near a gas-liquid interface. Many following researchers (Asher and Litchendorf, 2009; François et al., 2011a; Herlina and Jirka, 2004; Kapoustina et al., 2015) have continued to work on the same subject by studying the absorption of O₂. In a quenching experiment, the ability of some molecules called “quenchers” to inhibit the fluorescence dye is considered. The quenching reaction can be depicted as the following figure:

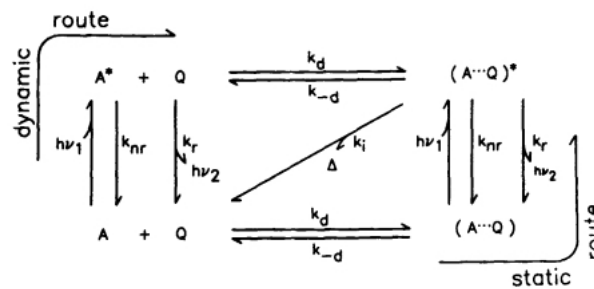


Figure 1-7. Schematic view of quenching reaction (Eftink, 1991)

In the absence of quencher, the fluorophore A, which is excited by absorption of a photon (e.g. from a laser source), will jump to a higher electronic energy level A*. Then A* can return to the ground state by the non-radiative way with a rate constant k_{nr} and by emitting a photon (fluorescence) with the radiative rate k_r . The fluorescence lifetime τ_0 is defined as:

$$\tau_0 = \frac{1}{k_r + k_{nr}} \quad (1-36)$$

When the quencher Q is added to the system, additional reactions are possible which lead to a more rapid return of excited states back to ground states. As shown in the figure, the reactions can be divided into a dynamic process and static process.

Dynamic process: the excited A^* may collide with Q , with a diffusional rate constant

k_d to form an excited-state encounter complex, $(A \cdot Q)^*$. If Q is in fact a quencher, then such $(A \cdot Q)^*$ complexes will undergo an internal fluorescence quenching reaction, with a rate constant k_i .

Static process: the quencher may also form a ground state complex, $(A \cdot Q)$, by encountering the ground state of A . Such a complex may also absorb a photon to directly populate the excited-state encounter complex, $(A \cdot Q)^*$. The internal quenching reaction may then proceed immediately after excitation.

When measuring the fluorescence lifetime with a quenching effect, only the dynamic route should take into account because the static process can usually be regarded to be instantaneous. Thus the lifetime is given by the following relationship:

$$\tau_Q = \frac{1}{k_r + k_{nr} + k_q Q} \quad (1-37)$$

where k_q the quenching rate constant, is defined as:

$$k_q = \frac{k_i k_d}{k_i + 1/\tau_0 + k_{-d} + k_d Q} \quad (1-38)$$

For a strong quencher, the internal quenching rate k_i is much larger than the other rates, thus it can be assumed that $k_q = k_d$.

Regarding the fluorescence lifetime is proportional to fluorescence intensity, the dynamic quenching process is expressed as the Stern-Volmer relationship:

$$\frac{\tau_Q}{\tau_0} = \frac{I_Q}{I_0} = \frac{1}{1 + K_{SV} Q} \quad (1-39)$$

where $K_{SV} = k_q \tau_0$ is the Stern–Volmer constant, and I_Q and I_0 the fluorescence intensities in the presence and absence of quencher, respectively. The parameters I_0 and K_{SV} of the Stern–Volmer equation can be easily determined by a calibration process by measuring several I_Q values under the different preset concentration of quenchers.

In PLIF quenching experiments, the most important material is the fluorescence dye, which is called fluorophore. The performance of the fluorophore used will affect directly the results of mass transfer quantification. Primary factors that govern the suitability of a fluorophore include an absorption spectrum that is compatible with available laser excitation, a large separation between absorption and emission spectra (Stokes shift), and high quantum efficiency to maximize signal. In considerations of quenching, the crucial factor is fluorescence sensitivity to the presence of quencher, or more concretely, decrease the degree of the fluorescence with quencher concentration. Other elements include susceptibility to photobleaching by the excitation source, solubility to liquid, and the price which is also considered in continual experiments.

The most common dyes for quenching reaction are pyrene butyric acid (PBA) (CAS: 3443-45-6) and some ruthenium complexes which are sensitive to the presence of O₂. Vaughn and Weber (Vaughn and Weber, 1970) demonstrated that pyrenebutyric acid (PBA) in solution provides an excellent indicator for dissolved oxygen concentration. PBA has been used to measure oxygen concentration in biological substances and tissues. The fluorescence lifetime for PBA is unusually long: in water solution at room temperature, it is approximately 165 ns when unperturbed. Dissolved oxygen quenches the fluorescence of PBA, reducing the lifetime to 65 ns in oxygen-saturated water. The fluorescence emission has a band from 370 to 430 nm. An absorption band from 310 to 345 nm makes a nitrogen laser ~337.1 nm an appropriate excitation source.

Table 1-1. Characteristics of the common dyes for fluorescence quenching in mass transfer visualization.

Dye	Formula	Molecular Weight [g/mol]	λ_{abs} peak [nm]	λ_{em} peak [nm]	Water solubility	Price [€/g]
PBA	C ₂₀ H ₁₆ O ₂	288.34	310-345	375-425	YES	110.5
Ruthenium complex a	C ₇₂ H ₄₈ C ₁₂ N ₆ O ₈ Ru	1297.16	521	631	NO	32000
Ruthenium complex b	C ₇₂ H ₄₈ N ₈ O ₆ Ru	1222.27	532	670	NO	3000
Ruthenium complex c	C ₃₆ H ₂₄ Cl ₂ N ₆ Ru. xH ₂ O	712.59+18x	499	582	YES	143

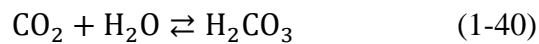
- PBA: pyrene butyric acid
- Ruthenium complex a: tris (4,7-diphenyl-1,10-phenanthroline) ruthenium(II)bis(perchlorate)
- Ruthenium complex b: Ru(4; 7 diphenyl-1; 10 phenanthroline)₃(NO₃)₂
- Ruthenium complex c: tris(1; 10-phenanthroline)ruthenium(II) chloride hydrate
- The price information is from Sigma-Aldrich.
- The information for each dye is from the reference of (Roy and Duke, 2004; Walker and Peirson, 2008), (Dani et al., 2007), (Jimenez, 2013), respectively.

According to the literature, it's proved that the ruthenium complex is also a typical quenching fluorescence dye which has strong inhibition performance in the presence of oxygen molecules. In the work of (Dani et al., 2007), several ruthenium complexes were tested and one dye named was retained (ruthenium complex a). But the price of this product is certainly a limiting factor (32 Euros/mg) for large scale applications. Another ruthenium complex (ruthenium complex b), are developed in Laboratory of Physics and Chemistry of Nano-Objects (LPCNO, France) and subsequently adopted by Francois et al. (François et al., 2011b, 2011a) and Jimenez et al. (Jimenez et al., 2013). A test of this dye showed excellent inhibition propriety: with this dye (concentration of 25mg/L), a variation of 1000 gray levels (12 bits image) was achieved with dissolved oxygen of 0-3 mg/L in liquid medium (Jimenez, 2013). Besides, the price of this dye is also a favorable advantage which costs 10 times cheaper than the previous one. On the other hand, these above two dyes are difficult to dissolve directly in water that makes the addition of material (e.g. ethanol) is necessary to improve their

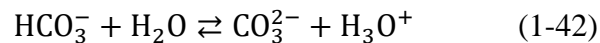
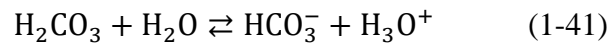
solubility. More recently, (Kück et al., 2010, 2012) investigated the mass transfer of the oxygen or air bubble by using a new fluorescence dye (ruthenium complex c). Despite weaker sensibility to the oxygen (than ruthenium complex b), this dye is soluble in the water and it is sufficient for quantifying the oxygen concentration. The details on each dye refer to Table 1-1.

1.2.2.3 Acid-based techniques

The second extension of LIF techniques is based on an acid reaction. It relies on the fact that after CO₂ dissolution into water, aqueous carbon dioxide interacts with water to form carbonic acid through the reaction:



Carbonic acid then dissociates into hydrogen carbonate HCO₃⁻, and hydrogen carbonate into carbonate CO₃²⁻ through the successive acid-base equilibria (Lacassagne et al., 2017):



As the H₃O⁺ ions are produced, the water is acidified leading to a decrease of pH value which can be indicated by the fluorescent pH sensitive dyes adding to the liquid. The change in the pH level is expected to correspond with the change in the fluorescent intensity. An example of the fluorescence intensity variations as a function of pH is shown in Figure 1-8. The dissolved CO₂ concentration thus can be deduced from the gray level of the recorded fluorescent images.

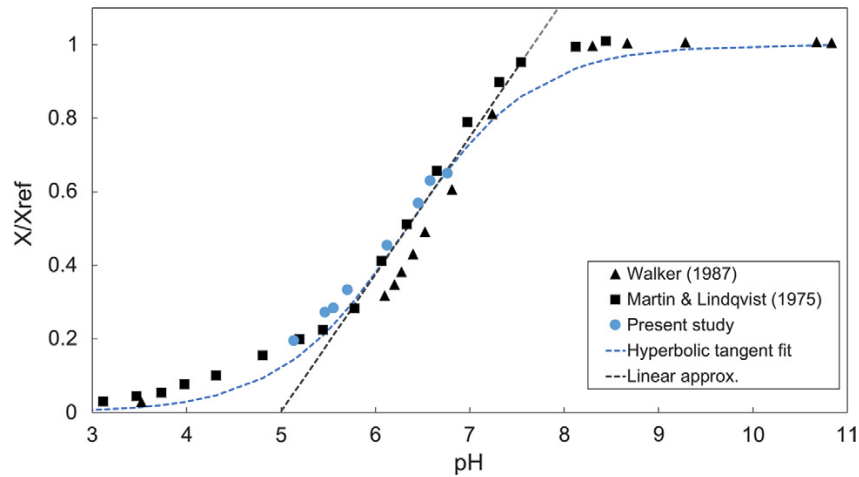


Figure 1-8. Relative fluorescence intensity or extinction coefficient variations as a function of pH value. Image from (Lacassagne et al., 2017).

Fluorescein (CAS: 2321-07-5), rhodamine dyes and HPTS (8-hydroxypyrene-1,3,6-trisulfonic acid) (CAS: 27928-00-3) are mainly used for CO₂ quantification which depended on the variation of pH value of the solute caused by a chemical reaction at the interface (Woodrow and Duke, 2001). Fluorescein (i.e. fluorescein sodium) has peak absorption near 490 nm (enabling efficient excitation with the 488 nm line of an argon-ion laser), peak emission near 510 nm, and has relatively low sensitivity to temperature changes (Crimaldi, 2008). Fluorescein is sensitive to pH and fluoresces when the pH reaches a certain threshold value. Typically, the fluorescence is off when the pH < 4 and maximum fluorescence occurs at pH = 7. At pH > 7, the fluorescence is constant. In the region pH < 7, the intensity is strongly dependent on the pH of the solution. Another common category of fluorescence dye is Rhodamine dyes. Rhodamine 6G (CAS: 989-38-8) which is not pH-independent shows an unstable property due to the quenching phenomenon. The dye is highly resistant to photobleaching (Larsen and Crimaldi, 2006). It's not suitable for quantifying the mass transfer. On the contrary, the fluorescence of Rhodamine B (CAS: 81-88-9) is sensitive to changes in pH. Its fluorescence is virtually independent of pH over the range 3-11.

Moreover, its outstanding temperature sensitivity can be exploited to use LIF for temperature measurements. But it should be mentioned that Rhodamine B is quite toxic and may have acute and chronic health effects in case of skin or eye contact. An alternative dye, Rhodamine WT (CAS: 37299-86-8), its spectral properties are quite similar to those of Rhodamine B and are much more soluble and reportedly much less toxic than Rhodamine B. The application of this dye for quantifying the mass transfer is scarce and more research is needed to approve its properties.

Table 1-2 Characteristics of the common PH-sensitive dyes for mass transfer visualization.

Dye	Formula	Molecular Weight [g/mol]	λ_{abs} peak [nm]	λ_{em} peak [nm]	Water solubility	Price [€/g]
Fluorescein	$\text{C}_{20}\text{H}_{10}\text{Na}_2\text{O}_5$	376.27	490	515	YES	0.437
HPTS	$\text{C}_{16}\text{H}_7\text{Na}_3\text{O}_{10}\text{S}_3$	524.39	455	510	YES	84.8
Rhodamine B	$\text{C}_{28}\text{H}_{31}\text{ClN}_2\text{O}_3$	479.01	550	590	YES	49.5
Rhodamine 6G	$\text{C}_{28}\text{H}_{31}\text{N}_2\text{O}_3\text{Cl}$	479.01	525	555	YES	81.5
Rhodamine WT	$\text{C}_{29}\text{H}_{29}\text{ClN}_2\text{Na}_2\text{O}_5$	566.98	550	590	YES	-

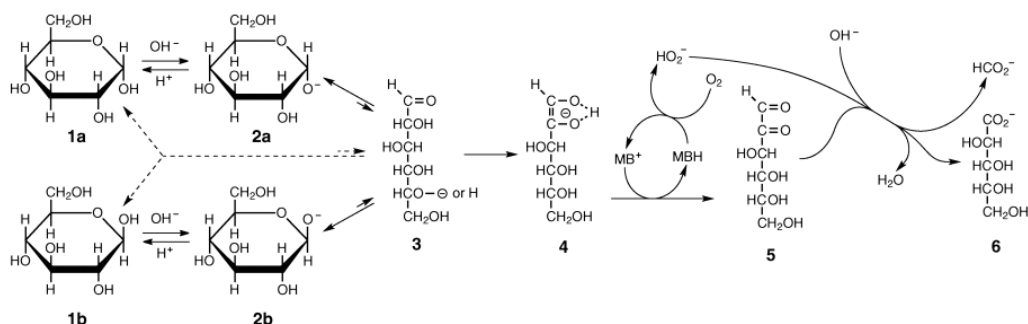
- HPTS: 8-hydroxypyrene-1,3,6-trisulfonic acid
- The price information is from Sigma-Aldrich.
- The information for each dye is from the reference of (Crimaldi, 2008), (Huang and Saito, 2015, 2017b, 2017a), (Shao et al., 2012), (Crimaldi, 2008), (Alm eras et al., 2016), respectively.

It should be noticed that the laser-based visualization technique for a gas-liquid system always has two main drawbacks: interface reflections and heterogeneous excitation intensity due to Beer-Lambert absorption. An improvement has been made by using a so-called “two-color” method (Coppeta and Rogers, 1998). The principle is to make the fluorescent light emitted at two different wavelengths while the one emitted light for quantification and the other one used as a reference. Dividing the first wavelength intensity field by the second one, the heterogeneous excitation effects are corrected,

since the excitation intensity is common to both fluoresced wavelengths. This improvement can be realized by a pair of fluorescent dyes or a single dye excited by the same laser. Both ways have been adopted by some researchers if we called them “Two dyes - two color” method (Fenner and Stephan, 2017; Hlawitschka et al., 2017; Kováts et al., 2017, 2018; Someya et al., 2005) and “One dye – two color” method (Bruchhausen et al., 2005; Lacassagne et al., 2018). The later one is less chemically intrusive since they only require the addition of one chemical component instead of two inside the fluid. However, as for two dyes system, the dye has to be wisely chosen to avoid spectral conflicts.

1.2.2.4 Redox-based techniques

Among the literature about oxidation and reduction reactions in colorimetric methods, methylene blue (Piccione et al., 2017), resazurin (Dietrich et al., 2013) and leuco-indigo carmine (Krieger et al., 2017) were mainly applied to investigate mass transfer and concentration fields. The methylene blue (MB^+) is widely known in “blue bottle” experiments. It’s performed with glucose and sodium hydroxide. After the initial dissolution and agitation, the solution is blue. Then MB^+ was reduced by glucose to its leuco-form, MBH, producing a colorless solution. When the solution is shaken in contact with air, it results in oxidation of MBH by O_2 back to blue MB^+ . The oxidation and reduction reaction of prepared solution can be repeated several circles, shown in Figure 1-9. But the rate of oxygen consumption of methylene blue (several seconds, (Anderson et al., 2012)) is relatively lower compared to that of another redox dye, resazurin (several milliseconds, (Dietrich et al., 2013)).



^a1a, α -D-glucopyranose; 1b, β -D-glucopyranose; 2a, α -D-glucopyranosyloxy anion; 2b, β -D-glucopyranosyloxy anion; 3, open chain form of glucose; 4, enediolate anion; 5, D-arabino-hexos-2-ulose (glycosulose, open chain form); 6, D-arabinonate anion; MB⁺, methylene blue; MBH, methylene white; HO₂⁻, hydroperoxide anion; HCO₂⁻, formate anion.

Figure 1-9. Reactions occurring in the “blue bottle” experiment; reproduced from (Anderson et al., 2012).

As Figure 1-10 shows, resazurin (blue and not fluorescent), is reduced to resorufin (pink and highly fluorescent), which is further reduced to dihydroresorufin (colorless and not fluorescent). These reactions are catalyzed by the presence of glucose and sodium hydroxide. The related stoichiometry of reactions is given from equations (1-43) to

(1-45). The change of color results from reversible oxidation (fast) and reduction (slow) reactions between resorufin (pink) and dihydroresorufin (colorless). Resazurin solution has one of the highest values known of Kreft's dichromaticity index (Kreft and Kreft, 2009), which could obtain a large range in perceived color change. resazurin \rightarrow resorufin (1-43)



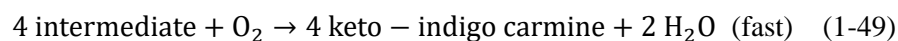
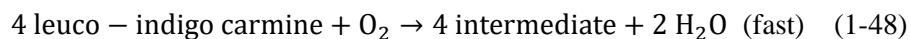
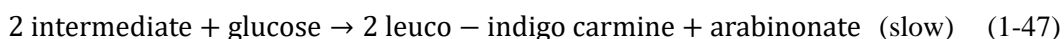
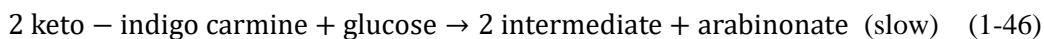


Figure 1-10. Reduction of resazurin to resorufin by glucose and sodium hydroxide (step[1]). Reduction of resorufin to dihydroresorufin by carbohydrate (step[2]). Reoxidation of dihydroresorufin to resorufin in the presence of oxygen (step[3]).

As shown in Figure 1-11, In the presence of glucose in an alkaline environment, Keto-indigo carmine (blue) is first reduced to anionic radical intermediate (red) and further to leuco-indigo carmine (yellow). The reaction rates of reductions and oxidations are slow (several minutes) and fast (a few milliseconds) respectively. And specific stoichiometry of reactions is given in Eq. (1-46) to (1-49). Unlike the dichromatism properties hold by methylene blue and resazurin, indigo carmine performs two distinct color changes (i.e., yellow-red-blue) during consecutive oxidation reaction.



Figure 1-11. Reversible redox reaction of leuco-indigo carmine to keto-indigo carmine with glucose as reducing and oxygen as an oxidizing agent. Colour change (yellow-red-blue) is illustrated in flask experiments. Reproduced from (Krieger et al., 2017)



More complicated systems involved enhancement effects by chemical reaction on the mass transfer have also been studied in recent years. (Paul et al., 2018) well reviewed three main groups of chemical systems applied in bubbly flows: (1) Cu/O₂ complexes; (2) Fe/O₂ complexes; (3) Fe/NO systems.

A summary of dyes based on the colorimetric method for mass transfer is depicted in Table 1-3.

Table 1-3. Chemical and physical properties of dyes for colorimetric technique

Dye	Chemical formula	Molar mass [g·mol ⁻¹]	Water solubility [g·L ⁻¹] at 25 °C	Price [€g ⁻¹]
Methylene blue	C ₁₆ H ₁₈ N ₃ ClS	319.85	43.60	1.99
Resazurin	C ₁₂ H ₇ NO ₄	229.19	1.00	16.00
Indigo carmine	C ₁₆ H ₈ N ₂ Na ₂ O ₈ S ₂	466.36	10.00	0.98
Bromothymol blue	C ₂₇ H ₂₈ Br ₂ O ₅ S	624.38	Sparingly soluble (10-33.3)	7.35
Phenol red	C ₁₉ H ₁₄ O ₅ S	354.38	0.77	5.25

1.3 Rheology principle

As discussed in Section 1.2, in a gas-liquid system, the main resistance for the mass transfer is from the liquid phase. The flow properties of complex media like polymer fluid will affect the rate of the mass transfer. In order to characterize this impact, a rheological analysis of the fluid is necessary. Rheology is the science used to describe

and assess the deformation and flow behavior of materials. The term rheology was coined by Eugene C. Bingham in 1920 from a suggestion by his colleague, Markus Reiner (Reiner, 1964). The term was inspired by the Greek aphorism: *πάντα ῥεῖ* (panta rhei) meaning that "everything flows". Rheology connects the knowledge from material science and fluid mechanics. It applies to substances that have a complex microstructure, such as muds, sludges, suspensions, polymers and other glass formers (e.g., silicates), as well as many foods and additives, bodily fluids (e.g., blood) and other biological materials or other materials that belong to the class of soft matter such as food.

1.3.1 Definition of shear stress, shear rate and viscosity

The fundamental rheological parameters are defined by the two-plate model (see Figure 1-12-I). The upper plate with the area A [m²] is set in motion by the (shear) force F [N] then the resulting displacement x [m] and velocity u [m·s⁻¹] is measured. The lower plate is stationary $u = 0$. Between the plates, there is the distance h [m], and the sample is sheared in this shear gap.

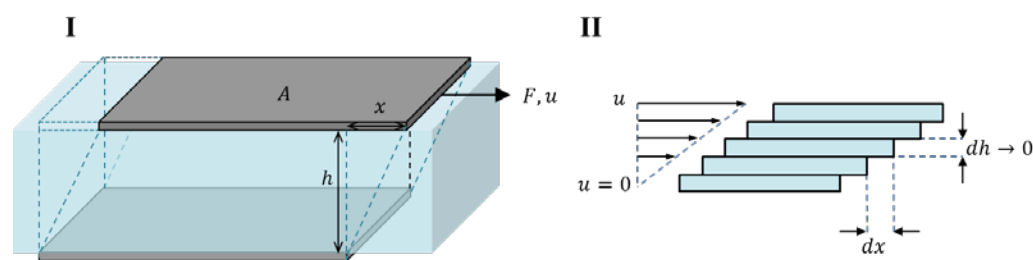


Figure 1-12 I: Two-plate model; II: Laminar flow in the form of planar fluid layers.

The fluid in the gap performed a laminar shear flow. It is assumed that the following shear conditions are occurring:

1. The material can be imagined in the form of adjacent layers of infinitely thin thickness. (see Figure 1-12-II)

2. The sample shows adhesion to both plates without any wall-slip effects.
3. There is no turbulent flow, i.e. no vortices are appearing and there is no transfer of matter between the various layers.

The real geometric conditions in rheological measuring systems are not as simple as in the Two-Plates-Model. However, if a shear gap is narrow enough, the necessary requirements are largely met and the definitions of the following rheological parameters can be used.

The ratio of the shear force P to the unit surface A is called shear stress τ [Pa]:

$$\tau = \frac{P}{A} \quad (1-50)$$

The ratio of the displacement x of a layer to the thickness h of the layer is named shear strain or deformation γ :

$$\gamma = \frac{x}{h} \quad (1-51)$$

The velocity gradient (see Figure 1-12-II) is called the shear velocity or shear rate $\dot{\gamma}$ [s^{-1}]:

$$\dot{\gamma} = \frac{dy}{dt} = \frac{u}{h} \quad (1-52)$$

For all flowing fluids, the molecules have relative motion between one another that is always combined with internal frictional forces. This process will perform as resistance to gradual deformation by external shear stress. ‘Viscosity’ is defined to quantify the level of this resistance for fluids.

According to the two-plate model, viscosity can be conceptualized as quantifying the frictional force that arises between two adjacent layers of fluid that are in relative motion. The ratio between shear stress τ and shear rate $\dot{\gamma}$ is defined as dynamic viscosity μ [$\text{Pa}\cdot\text{s}$]:

$$\mu = \frac{\tau}{\dot{\gamma}} \quad (1-53)$$

Divide the dynamic viscosity by the density of fluids ρ [$\text{kg}\cdot\text{m}^{-3}$], the kinematic viscosity ν [$\text{m}^2\cdot\text{s}$] is defined:

$$\nu = \frac{\mu}{\rho} \quad (1-54)$$

1.3.2 Rheological measurement: principle of rheometer

In order to measure the rheological properties of fluids, a viscometer or a rheometer is used which can be grouped into two main types: tubular rheometer and rotational rheometer. Compared with a tubular rheometer, the rotational rheometer is popular since regarding its advantages like wider shear range, small volume sample required, operation with continuous rotation and rotational oscillation, capability for viscoelasticity measurement etc.

In rotational rheometer, a sample of fluid is filled into the narrow gap of the sensor system which always consists of a rotator called geometry and a stationary plate or container. The sensor systems can be classified into three categories: cylinder, cone-plate, and plate-plate (see Figure 1-13). Moreover, for the same sensor system, commercial rotational rheometers can also employ a wide range of geometries for viscosity and flow behavior measurement (see Figure 1-14).

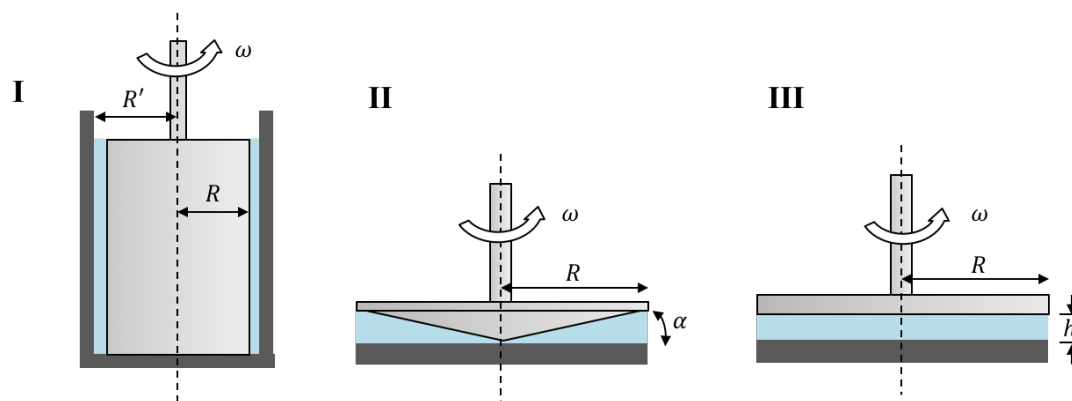


Figure 1-13 Sensor system of rotational rheometers: I. Concentric cylinder; II. Cone-plate; III. Plate-plate.



Figure 1-14 Different geometries for rheometer. Images from Anton-paar.com

The measurement with rotational rheometers can be carried out in one of two operation modes:

1. Rotation with controlled shear rate (CSR): A rotational speed (angular velocity) is preset which in the sensor system filled with a sample causes a shear rate. The torque required for achieving and maintaining the desired shear rate is the viscosity-proportional parameter.
2. Rotation with controlled shear stress (CSS): According to the reversed principle, here a torque (shear stress) is preset and the resulting movement (deformation) i.e. the resulting angular velocity (shear rate) is measured.

Conversion of torque into the shear stress and rotational speed into the shear rate is via conversion factors which depend on the geometries. The shear stress is proportional to

the torque M [N·m] and to a characteristic geometry factor identified as K_{SS} (shear stress factor):

$$\tau = K_{SS} \cdot M \quad (1-55)$$

High torque means also high shear stress. Large values of A stand for small sensors.

The shear rate $\dot{\gamma}$ is proportional to the rotational speed (angular velocity ω [rad]) and proportional to the geometry factor K_{SR} (shear rate factor):

$$\dot{\gamma} = K_{SR} \cdot \omega \quad (1-56)$$

High angular velocity means also high shear stress. High K_{SR} values stand for very small gaps. The conversion factors for different systems are listed in Table 1-4.

Table 1-4 Conversion factors of torque to shear stress K_{SS} and rotational speed to shear rate K_{SR} for different sensor systems.

	Cylinder	Cone-plate	Plate-plate
K_{SS}	$\frac{1}{2\pi R^2 h}$	$\frac{3}{2\pi R^3}$	$\frac{2}{\pi R^3}$
K_{SR}	$\frac{2R'^2}{R'^2 - R^2}$	$\frac{1}{\alpha}$	$\frac{R}{h}$

1.3.3 Rheological behavior

Viscosity values are not constant values as they are affected by many conditions. The fluids have different flow behavior under shear even at constant temperature. We can use a rheogram or flow curves to represent these rheological behaviors. There are two ways to plot the flow curves:

1. Shear stress as a function of shear rate (τ vs $\dot{\gamma}$);

2. Viscosity as a function of shear rate (μ vs $\dot{\gamma}$), applying the law of viscosity, each measuring viscosity is calculated with Eq. (1-53), which is called apparent viscosity.

We can classify the fluids into different types depending on rheological behavior as follows and their flow curves plotted in Figure 1-15.

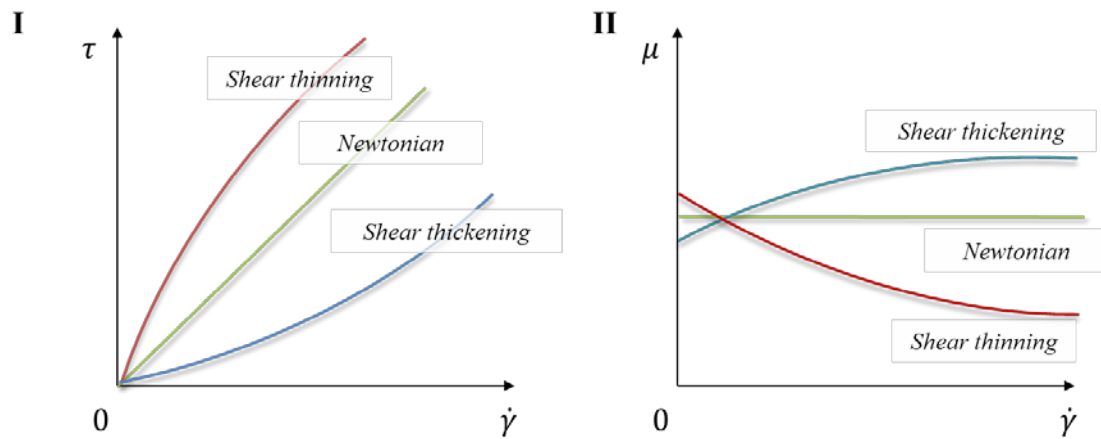


Figure 1-15 Representation of different rheological behaviors (shear thinning, Newtonian and shear thickening) in a rheogram (I: τ vs $\dot{\gamma}$; II: μ vs $\dot{\gamma}$)

1.3.3.1 Newtonian fluids

Newtonian fluids (or: Ideally viscous fluids) is a fluid in which that the measured viscosity of the fluids is independent of the shear rate (Figure 5.2, line 1). That means the viscosity is a constant and the shear stress are linearly proportional to the shear rate. Typical materials from this group include water, mineral oil, salad oil, solvents such as acetone, glycerol, benzene, etc. All the other fluids are called the non-Newtonian fluids since their viscosity depends on the shear rate.

1.3.3.2 Shear thinning

Shear-thinning behavior (or: pseudoplasticity) is characterized by decreasing viscosity with increasing shear rates (Figure 5.2, line 2). Typical materials that show this behavior are coatings, glues, shampoos, polymer solutions, and polymer melts. Since viscosity is shear-dependent, it should always be given with the shear condition. The

shear thinning phenomenon is generally considered to be the result of microscale structural rearrangements within the fluid, or the organization of microspheres into hexagonally packed structures that slide over each other more easily (i.e. exhibit lower viscosity, a schematic explanation for polymers is given in Figure 1-16) than at lower shears where randomly organized particles collide frequently

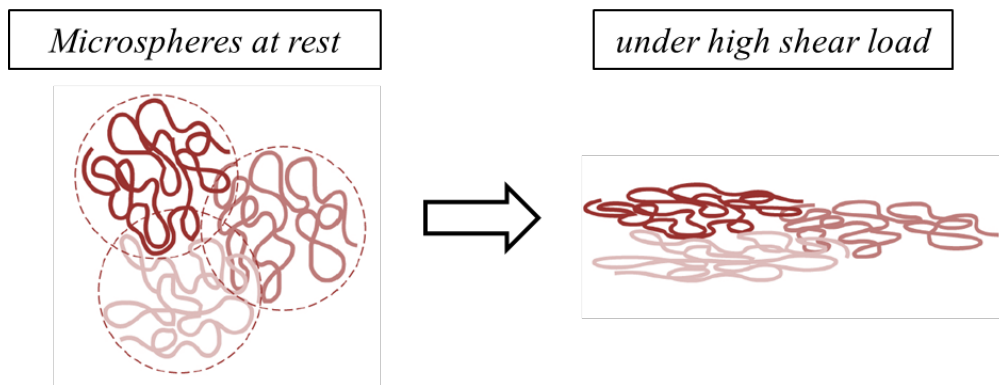


Figure 1-16 Explanation of shear thinning behavior: structures of polymers at rest and under high shear load

1.3.3.3 Shear-thickening

Shear-thickening (or: dilatant flow behavior) means increasing viscosity with increasing shear rates (Figure 5.2, line 3). Materials that typically display such behavior include highly filled dispersions, such as ceramic suspensions (casting slurries), starch dispersions, plastisol pastes that lack a sufficient amount of plasticizer, dental filling masses (dental composites) as well as special composite materials for protective clothing (Mezger, 2014). This behavior is rare and occurs in concentrated slurries when the increment of the shear rate leads to the formation of clusters that rigidify the suspension structure. If the suspension is composed of associative polymers, an increase in shear forces favors the polymer interactions resulting in a more solid structure.

1.3.3.4 Viscoplasticity (yield stress behavior)

Some non-Newtonian fluids behave like a solid under the application of small stresses but flow like liquids once the applied stress exceeds a critical value called the yield stress. This initial solid behavior is commonly explained by the presence of strong inter-particle forces (Van-Der-Waals forces) or an interconnected three-dimensional network of suspended aggregates. Particularly, if the shear rate is directly proportional to the amount by which the applied shear stress exceeds the yield stress, the fluid is called Bingham plastic. Examples of yield stress materials encountered daily include blood, mayonnaise, toothpaste, gelled products, paint, and concrete (Hammad, 2015).

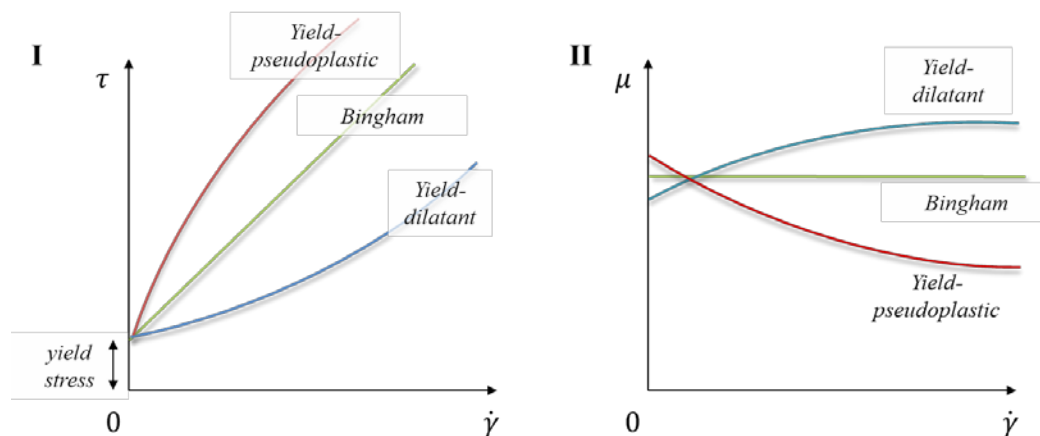


Figure 1-17 Representation of viscoplasticity in a rheogram (I: τ vs $\dot{\gamma}$; II: μ vs $\dot{\gamma}$)

1.3.3.5 Viscoelasticity

Viscoelasticity is the property of materials that exhibit both viscous and elastic characteristics when undergoing deformation. In the 1830s, a French engineer, Louis Vicat, had noticed that bridge cables continued to elongate over time even though under constant load, a viscoelastic phenomenon known as creep. Under the preset shear stress,

a viscoelastic material exhibit time-dependent strain as well as an elastic behavior explained by the ability to store part of the mechanical energy supplied to the fluid as elastic energy in inter-particle bonds for instance (Seyssiecq et al., 2003). Consequently, when the material is later released, this stored energy acts as a driving force for reforming the original structure that a partial elastic recovery is observed.

For the characterization of viscoelastic fluids, dynamic testing is implemented. An oscillatory (sinusoidal) deformation (stress or strain) is applied to a sample and then the material response (strain or stress) is measured. An example result is shown in Figure 1-18. It is observed that the sinusoidal curves of the preset shear stress and the measuring strain show a time lag for the response signal. This lag is called the phase shift θ . This shift angle is always between 0° and 90° while $\theta = 0^\circ$ for ideally elastic deformation behavior and $\theta = 90^\circ$ for ideally viscous flow behavior.

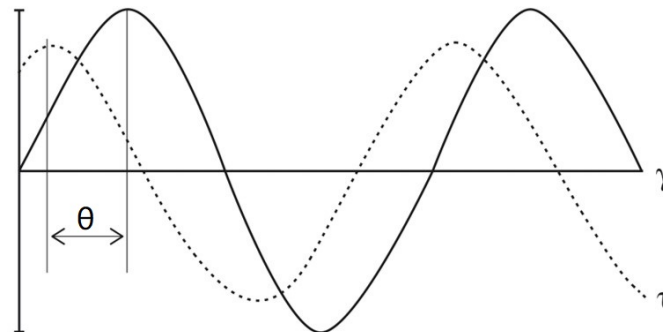


Figure 1-18 Example result of the dynamic test for viscoelastic behavior, presented as a sinusoidal function versus time with preset shear strain γ and resulting shear stress τ . The two curves are offset by a phase shift. Figure from (Mezger, 2014)

By analogy to Hooke's Law, the shear modulus G [Pa] is defined as shear stress dividing shear strain:

$$G = \frac{\tau}{\gamma} \quad (1-57)$$

For a viscoelastic material, we define a complex shear modulus G^* as the overall

resistance to deformation of the materials:

$$G^* = G' + iG'' \quad (1-58)$$

with

- G' is the elastic (storage) modulus to quantify the elasticity and the ability of the material to store energy;
- G'' is the viscous (loss) modulus to quantify the ability of the material to dissipate energy.

The absolute value of G^* can be calculated from the dynamic test:

$$|G^*| = \frac{\tau^*}{\gamma^*} \quad (1-59)$$

where τ^* and γ^* is the amplitudes of the shear stress τ and strain amplitude γ , respectively. In the dynamic test. The relation between G^* and G' (or G'') is represented in Figure 1-19. Thus, the following equations can be obtained:

$$\text{Storage modulus:} \quad G' = |G^*| \cos \theta \quad (1-60)$$

$$\text{Loss modulus:} \quad G'' = |G^*| \sin \theta \quad (1-61)$$

The ratio between G' and G'' is called the loss factor or damping factor:

$$\tan \theta = \frac{G''}{G'} \quad (1-62)$$

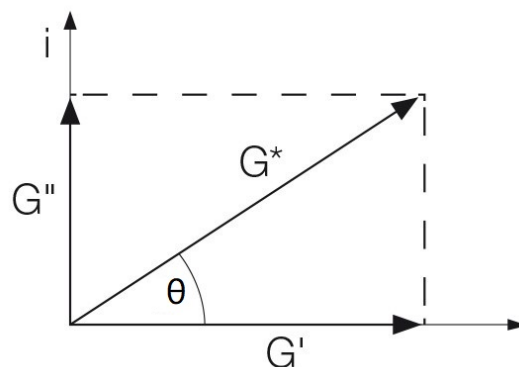


Figure 1-19 Vector diagram illustrating the relationship between complex shear modulus G^* , storage modulus G' and loss modulus G'' using the phase-shift

angle θ . The elastic portion of the viscoelastic behavior is presented on the x -axis and the viscous portion on the y -axis.

Viscous behavior of a viscoelastic material brings the energy loss that makes it different from an ideal elastic material. This energy loss is always in the form of heat energy arises from the internal friction between the molecules and particles in a flowing fluid. This loss of energy is also called energy dissipation. Viscoelastic liquids have a higher loss modulus than storage modulus $G'' > G'$. Examples of viscoelastic materials are amorphous polymers, semi-crystalline polymers, biopolymers and even the living tissue and cells.

1.3.4 Viscosity of polymer systems

The main classes of flow behavior discussed in Section 1.3.3 are observed if the flow curve is measured over limited ranges of shear rate. Generally, most real fluids will exhibit behavior conforming to more than one flow classification over a shear rate range wider than two or three decades.

As an example, Figure 1-20 shows the general shapes of flow and viscosity curves on logarithmic scales for a typical fluid of low solids concentration. These curves indicate that at low shear rates the viscosity is constant while at high shear rates the viscosity is again constant, but at a lower level. Between these two extremes, sometimes known as the first and second Newtonian regions, the viscosity decreases as the shear rate increases. The viscosities in the first and second Newtonian regions are referred to as the zero-shear viscosity, and the infinite shear viscosity

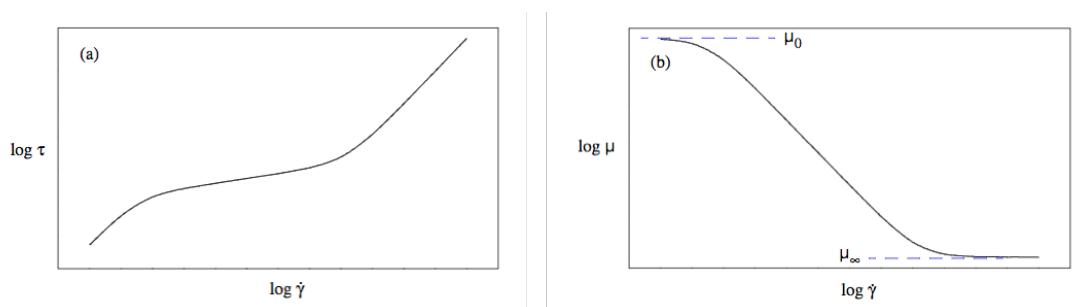


Figure 1-20 Typical flow behavior of real fluids of low solids concentration

For polymeric systems of low concentrations, low molecular weights or at temperatures well above the glass transition temperature, the typical variation of viscosity with shear rate as a function of concentration, molecular weight or temperature is shown in Figure 1-21.

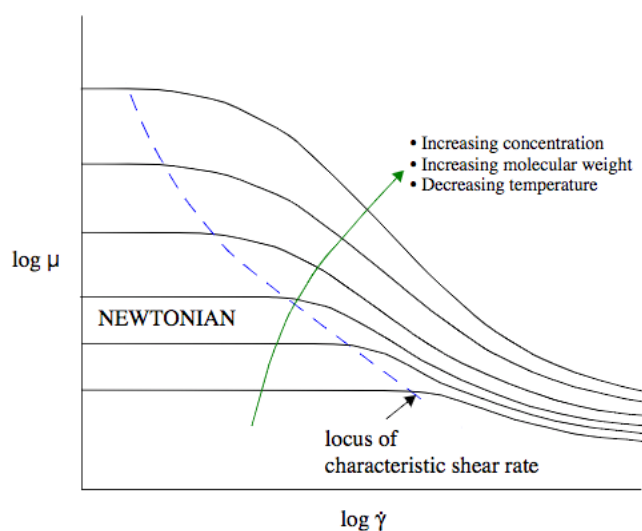


Figure 1-21 Non-Newtonian viscosity in polymeric systems of low concentrations, low molecular weight or at temperatures well above the glass transition temperature.

As the concentration or molecular weight is increased or the temperature is decreased, both the zero and infinite shear viscosities increase and the change in the zero-shear viscosity is much greater than that for infinite shear viscosity. The characteristic shear rate, where the viscosity begins to decrease with increasing shear rate and the behavior

of the fluid is no longer Newtonian, decreases with increasing concentration or molecular weight or with decreasing temperature.

It should be noted that some polymer solutions can be shear-thickening caused by shear-induced entanglement and agglomeration at high shear rates, and gels may show yield stress.

1.3.5 Rheological models

The non-Newtonian viscosity curve or flow curve data obtained from viscometric measurements under steady-state shear can be described mathematically in terms of rheological models (constitutive equations) and are amenable to curve fitting. The general form of a rheological model is fitted over a relevant shear rate range to the flow curve or viscosity curve by least-squares regression analysis so that a specific rheological model can be obtained. This specific equation is then used for material characterization or engineering design applications. The rheological model for Newtonian fluids contains just one constant. Many models have been proposed to describe non-Newtonian flow behavior of fluids, although the majority of these are of little value for engineering design applications and serve more as theoretical analyses. However, there are several well-established models used widely in the prediction of fluid rheology. The most common models are introduced as follows.

1.3.5.1 Newtonian Model

This is the simplest of all flow curve models and is given by

$$\tau = \mu_N \dot{\gamma} \quad (1-63)$$

With μ_N being the Newtonian viscosity.

1.3.5.2 Power Law Model

The power law, also known as the Ostwald-de-Waele model, is commonly utilized due to its validity and simplicity (Chhabra, 2010). The experimental results of the shear flow test were fitted by nonlinear regression to the model, presented as a power-law relationship between the shear stress and the shear rate:

$$\tau = K\dot{\gamma}^n \quad (1-64)$$

where:

K is the flow consistency index [$\text{Pa}\cdot\text{s}^n$];

n is the flow behavior index (dimensionless).

This equation describes Newtonian behavior when $n = 1$, shear-thinning behavior when $n < 1$ or shear-thickening behavior when $n > 1$. On a log - log plot, the model is represented by a straight line with a slope of n .

1.3.5.3 Bingham Model

For a yield stress material, the Bingham model is introduced which is similar to the Newtonian model by adding yield stress. This model is described by

$$\tau = \tau_{yield} + \mu_B\dot{\gamma} \quad (1-65)$$

Where τ_{yield} is called Bingham yield stress and μ_B is the constant Bingham plastic viscosity.

1.3.5.4 Herschel-Bulkley Model

This model, combining the Bingham model and the power law model, is a generalized form to describe the viscoplastic behavior. The law equation is given by

$$\tau = \tau_{yield} + K\dot{\gamma}^n \quad (1-66)$$

This equation describes Bingham plastic behavior when $n = 1$, yield shear-thinning behavior when $n < 1$ or yield shear-thickening behavior when $n > 1$ (See Figure 1-17).

1.3.5.5 Carreau Model

For real fluids as discussed in Section, the flow curve has more than one flow behavior. It thus needs a more common model that is valid over the complete range of shear rates. To fit the flow curves shown in Figure 1-20, the four parameters Carreau model is introduced. For cases where there are significant variation from the power-law model i.e. at very high and very low shear rates, it becomes essential to incorporate the values of viscosity at zero shear, μ_0 and at infinite shear, μ_∞ into the formulation.

$$\frac{\mu - \mu_\infty}{\mu_0 - \mu_\infty} = [1 + (t_\lambda \cdot \dot{\gamma})^2]^{\frac{n-1}{2}} \quad (1-67)$$

Where,

μ_0 is the viscosity at the zero shear rate [Pa.s];

μ_∞ is the viscosity at the infinite shear rate [Pa.s];

t_λ is the relaxation time [s] related to the viscoelasticity of the fluids;

n is the power index.

There are also other models which have been proved valid for specific types of fluids.

Some of them are shown in Table 1-5 with their application:

Table 1-5 Flow curve models applicable for real fluids (p is a parameter).

Model	Equation	Application
Carreau-Yasuda	$\frac{\mu - \mu_{\infty}}{\mu_0 - \mu_{\infty}} = [1 + (t_c \dot{\gamma})^p]^{\frac{n-1}{p}}$	Molten polystyrene
Eyring	$\frac{\mu - \mu_{\infty}}{\mu_0 - \mu_{\infty}} = \frac{\operatorname{arcsinh}(p\dot{\gamma})}{p\dot{\gamma}}$	Napalm, 1% nitrocelulos in 99% butyl acetate
Cross	$\frac{\mu - \mu_{\infty}}{\mu_0 - \mu_{\infty}} = \frac{1}{1 + p\dot{\gamma}^n}$	aqueous polyvinyl acetate dispersion, aqueous limestone suspension
Sisko	$\mu = \mu_{\infty} + p\dot{\gamma}^{n-1}$	Lubricating greases
Ellis	$\mu = \frac{\mu_{\infty}}{1 + p\tau^{n-1}}$	0.6% w/w carboxymethyl cellulose; (CMC) solution in water, poly(vynil chloride)

1.4 Conclusions

The study on the gas-liquid mass transfer is of great significance since it existed widely in industry and realizing the control of the mass transfer rate is very critical for many chemical and biological process. Diffusion, as a most common form of mass transfer, is characterized by the Fick's law by analogy with the heat transfer. A diffusion coefficient is defined to quantify the transport rate of the molecules driven by a gradient in chemical potential of the diffusing species. Beside diffusion, the rate of transfer of a given species depends also on some of the physical properties of the system and on the degree of turbulence of the phases involved. Thus another key parameter, the mass transfer coefficient is then proposed to estimate the entire mass transfer. Based on the utilization of these two parameters, the interfacial transfer process is conceptualized by various theories of which the most classic consists of the film theory, penetration theory, and surface renewal theory. With the development of the equipment, many efforts then

have implemented by means of the experimental investigation. The classic experiment is mainly carried out by microprobes but it could only get knowledge of the gas concentration in several fix positions and their presence could disrupt the fluid motions that are responsible for the concentration fluctuations. To overcome this difficulty, new techniques by using optical instruments and soluble dyes are carried out which is capable to visualize and quantify local gas-liquid mass transfer. The representative techniques are reviewed in the point of view: reaction-based techniques which can be classified into three different types including quenching reaction, acid-based reaction, and oxidation-reaction.

Regarding the rheology, the fluids have different flow behavior (e.g. shear thinning, viscoelasticity, etc.) according to the evolution of their response strain (or shear stress) to the applied shear rate. These behaviors can be described mathematically by rheological models. The rheological principle is used to fit the flow curves of the investigated fluids in our study (Chapter 2) and to analyze the result of the bubble hydrodynamics (Chapter 4).

Chapter 2

Material and Methods

Abstract

This chapter introduces the materials and methods used in the study. Three aqueous polymer solutions (Brex, Polyacrylamide, and Xanthan gum) are used as the liquid media which are close to those of fluids present in wastewater treatment or chemical industries. The physical properties of the three polymer solutions are measured especially for their rheological properties. Two types of dye (ruthenium complex and resorufin) are used as the oxygen indicator for different techniques, i.e. Planar-Laser Induced Fluorescence (PLIF), PLIF with Inhibition (PLIF-I), and colorimetric technique. Then, the experimental setup is shown schematically with specific parameters for each instrument following by the experimental protocols for each technique. The methods for calculating the bubble rising velocity and size are given afterward. Finally, for mass transfer characterization, the content consists of the calibration method, image processing, and the mathematical approaches to determine the two key parameters: diffusion coefficient and mass transfer coefficient. A discussion on the error analysis is also involved.

2.1 Material

2.1.1 Polymers to study

The advancements of industry have brought extensive use of a wide range of rheologically complex materials, e.g., polymeric solutions and melts, suspensions, mixtures, oil products, fiber-forming substances, etc. Such complex materials are often used in conditions of the gas-liquid flow regime. There are many applications and manufacturing processes where a continuous phase has complex rheological properties, e.g., purification of polymeric sewage in water treatment process, gas removal from polymeric solutions or melts in the production of film, chemical fibers, and other polymeric materials production, transport of gas-oil mixtures, boiling of high-molecular-weight solutions etc. (Levitsky and Shulman, 1995)

As the objective of our research is to study the mass transfer process in such complex media, three water-soluble polymers are chosen for experiments:

- Breox (Polyethylene-polypropylene glycol, $\text{HO}\cdot(\text{C}_2\text{H}_4\text{O})_m\cdot(\text{C}_3\text{H}_6\text{O})_n\cdot\text{H}$, BREOX[®] 75 W 55000, BASF SE, CAS: 9003-11-6)
- PAAm (Polyacrylamide, $(\text{C}_3\text{H}_5\text{NO})_n$, Sigma-Aldrich, CAS: 9003-05-8)
- Xanthan gum $((\text{C}_{35}\text{H}_{49}\text{O}_{29})_n$, Sigma-Aldrich, CAS: 11138-66-2)

Breox is a block co-polymer of ethylene glycol and propylene glycol. The high viscosity and low volatility of this product make it very suitable neat for high-temperature lubrication. Breox synthetic fluids provide the base for an extensive range of applications from high-performance industrial lubricants to process aids in food and pharmaceuticals. The aqueous solution of Breox is a Newtonian fluid.

PAAm is a polymer formed from acrylamide subunits. PAAm is versatile and used worldwide to improve commercial products and processes, such as the flocculation of solids in a liquid, and to enhance oil recovery. The average molecular weight of commercial polyacrylamide ranges from approximately 2×10^3 to as high as 15×10^6

g/mol. These large molecules of PAAm greatly influence the products' properties as a flocculent and rheology control agent (Kreiba, 2000). The aqueous solution of PAAm is one of the most common non-Newtonian fluids and is widely used as the investigated agent in much laboratory research.

Xanthan gum is a polysaccharide produced by the fermentation of glucose, sucrose, or lactose and is commonly used as a food thickening agent or to stabilize suspensions and emulsions (Davidson, 1980). Xanthan gum is highly soluble in both cold and hot water with relatively high viscosity. One of the most remarkable properties of Xanthan gum is its ability to produce a large increase in the viscosity of a liquid when added in very small quantities, of the order of 0.5% in most foods. Xanthan solutions are pseudoplastic or shear thinning (see Chapter 1). This means that their viscosity decreases at a higher shear rate, whether from mixing, shaking or even chewing, and once the shear forces are removed, the solutions will thicken up again.

Chemical structure of these three studies polymers is depicted in Figure 2-1.

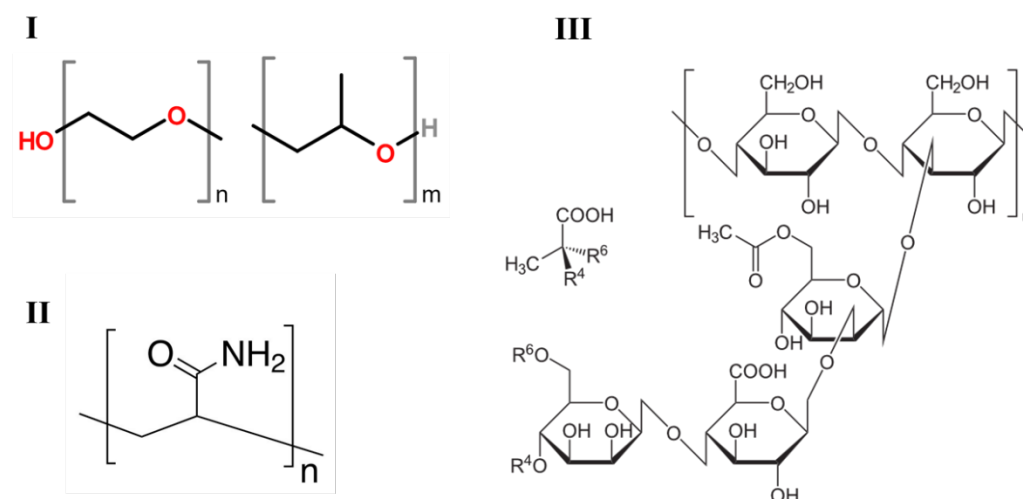


Figure 2-1 Chemical structure of the polymers. I: Breox; II: PAAm; III: Xanthan gum. Images from Lookchem.com

The reason for choosing these polymers is that their aqueous solutions have a similar property close to those of fluids present in wastewater treatment or chemical industries

and have been widely investigated by many researchers that can give sufficient reference information to our study (Aguirre et al., 2017; Butler et al., 2018; Cao et al., 2016; Jung et al., 2016; Xie et al., 2017).

2.1.1.1 Preparation of polymeric solutions

Polymer solutions must be prepared with care. Special effort should be expended to ensure complete, homogeneous dissolution. In this research, the raw materials (polymers) are in form of dry fine powders. They are dissolved into the deionized water to prepare the solutions at different concentrations:

- PAAm (0.1%, 0.25 %, 0.5%, 1%, 1.25 % wt.)
- Breox (2%, 5.5% 9.1% wt.)
- Xanthan gum (0.1 %, 0.25 %, 0.5% wt.)

The concentration is expressed in mass fraction defined as the mass of the solute m_s dividing the total mass of the solution m_{total} :

$$wt\% = \frac{m_{solute}}{m_{total}} \quad (2-1)$$

In order to prepare the solutions of mass m_{total} at objective concentration $wt\%$, the procedure can be divided into the following steps:

1. Clean and dry glassware (beaker, flask), taking care to ensure that no residues remain;
2. Weigh the mass of the solute (polymer) which equals to $m_{total} \times wt\%$;
3. Take a flask on the weighing scale and add the solvent (deionized water) until the mass of the solvent equals to $m_{total} * (1 - wt\%)$;
4. Move part of the solvent from the flask into a beaker and put the beaker on a magnetic stirrer;
5. Starting stirring the solvent in the beaker then add the solute slowly into the beaker.
6. The solution in the beaker is pre-stirred for 6 hours then move the stirred solutions from the beaker to the bulk solvent in the flask;

7. Keep stirring the solutions in the flask for 24 hours to make sure the solute is dissolved and well mixed with the solvent.

The preparation is implemented at the room temperature (293.15 K) controlled by an air conditioner. Once the solution is prepared, it is used immediately and conserved no more than one week.

2.1.1.2 Surface tension and density of the solutions

The surface tension of the experimental solutions is measured using a tensiometer (Krüss K6, Germany, see Figure 2-2-I). The principle is based on Du Noüy ring method that a platinum ring is immersed in the sample and slowly withdrawn by lowering the liquid (du Noüy, 1925). As the ring is withdrawn, the surface tension causes the wire to twist and its deflection is indicated on a scale which is calibrated for the surface tension. The result of the measurement is indicated accurately to 0.5 mN/m.

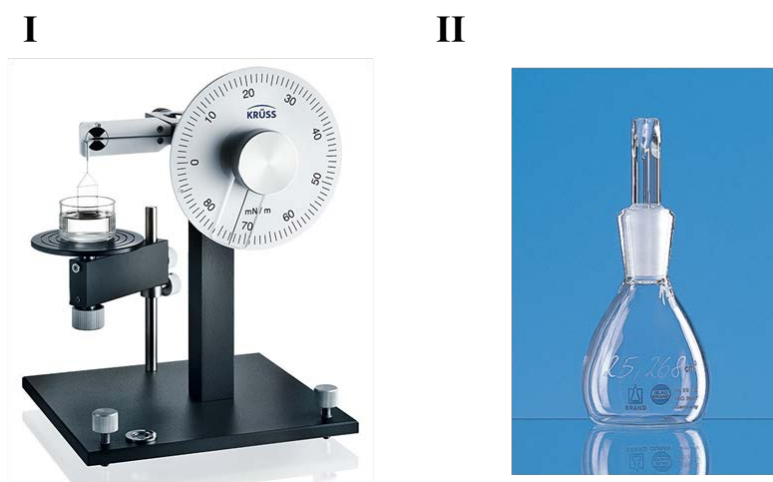


Figure 2-2 Instruments for the measurement of surface tension and density. I: Tensiometer (Krüss K6, Germany); II: Pycnometer (Blaubrand, Germany)

The density of the solutions is measured with a pycnometer or density bottle (Blaubrand, Germany, see Figure 2-1-II) which is a glass bottle of an accurately calibrated volume. Each density bottles are individually adjusted. The nominal capacity specified to 0.001

cm³ is indelibly engraved on each bottle. During the measurement, the bottle is filled with the sample liquid carefully and the weight of the filled bottle is determined with the mass balance. Subtract the mass of the empty bottle gives the mass of the sample. Then the density is calculated from the ratio of mass and the volume of the liquid which is engraved on the bottle

The measurement of the surface tension and density is implemented at the reference temperature of 293.15 K. For each concentration, multiple samples are tested and the average result is given in Table 2-1. Compared with the water, it is found that the addition of the polymer as a solute will slightly increase the density and reduce the surface tension. For the same type of the polymer, this impact will be enhanced with higher solute concentration.

Table 2-1 Surface tension and density of the investigated solutions.

Composition	Concentration (wt%)	σ [mN/m]	ρ [kg/m³]
Water	-	72	998
Breox	2.00 %	65	999
	5.50 %	63	1007
	9.10 %	61	1013
PAAm	0.1 %	69	999
	0.25 %	67	999
	0.5 %	66	1001
	1 %	65	1003
	1.25 %	65	1004
Xanthan	0.1 %	69	999
	0.25 %	67	1000
	0.5 %	66	1001

2.1.1.3 Viscosity of the solutions

Most polymer fluids are non-Newtonian fluids that have complex rheological

properties like shear-thinning, shear thickening, viscoelastic etc. (Chapter 1). It is believed that this property has an impact on bubble hydrodynamics and mass transfer (Levitsky and Shulman, 1995; Shulman and Levitskiy, 1992). It is thus important to measure the rheological properties. For this purpose, the viscosities of the solutions are tested with a rotational rheometer (Hakke Mars III, Germany) under 20 °C. The plate-plate sensor system (i.e. Hakke P35) and the measurement are carried out in operation modes of rotation with controlled shear rate (CSR). Pure water is also tested as a reference.

For Breox and water, their flow curves are measured with the shear rate ranging between 0.1 s^{-1} to 1000 s^{-1} . The results are plotted in Figure 2-3. It can be seen that their shear stress is proportional to the shear rate and the viscosity is independent with the shear stress. That indicates the Breox solutions are Newtonian fluids. It can also be found that the viscosities of Breox solutions increase at higher solute concentrations. The viscosity of Breox solutions at different concentrations is given in Table 2-2. For each concentration, multiple samples are tested and the error values in Table 2-2 refers to the standard deviation of the data.

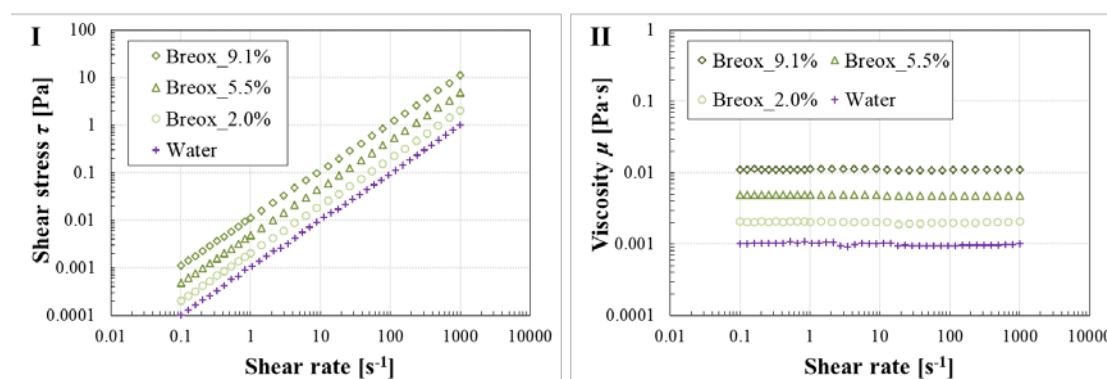


Figure 2-3 Flow curves of water and Breox solutions. I: shear stress vs shear rate; II: Viscosity vs shear rate.

Table 2-2 Viscosity of water and Breox solutions at different concentrations

Solutions [wt]	μ [mPa·s]
Water	1.0 ± 0.03
Breox_2.0%	2.0 ± 0.03
Breox_5.5%	4.8 ± 0.04
Breox_9.1%	11.1 ± 0.11

For PAAm and Xanthan gum solutions, their flow curves are measured with the shear rate ranging between 0.01 s^{-1} to 10000 s^{-1} . The results are plotted in Figure 2-4 and Figure 2-5, respectively. It is also found that, at a given concentration, the viscosities of PAAm and Xanthan solutions both approach a Newtonian plateau at very low and very high shear rates where the viscosities become constant. Between the plateau, PAAm and Xanthan gum solutions both have the apparent shear thinning property that the viscosity decreases at higher shear rates. However, the shear thinning range is wider for Xanthan ($0.1 \sim 100 \text{ s}^{-1}$ in shear rate) than the PAAm solution ($0.1 \sim 1000 \text{ s}^{-1}$ in shear rate). Xanthan solutions are more viscous than the PAAm solutions at low shear rates ($<10 \text{ s}^{-1}$). For example, at a shear rate of 1 s^{-1} , all viscosities of PAAm solutions are below $0.1 \text{ Pa}\cdot\text{s}$ while the value of Xanthan is much higher.

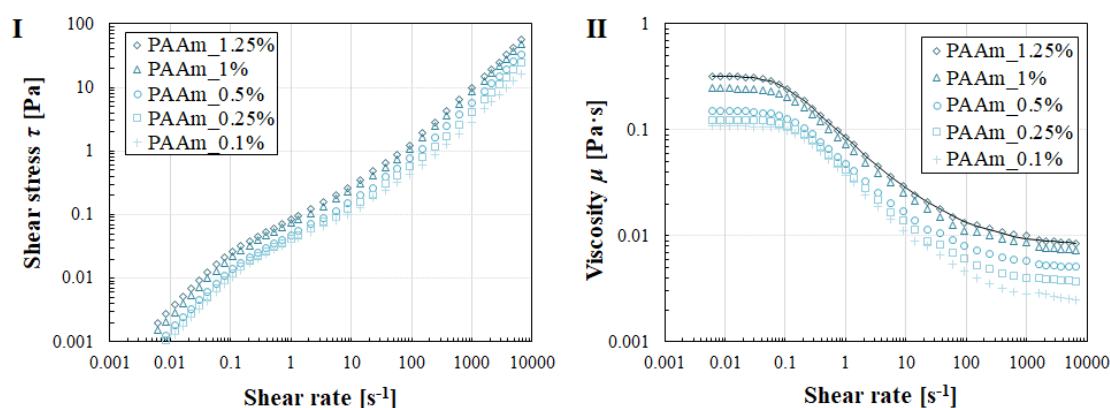


Figure 2-4 Flow curves of PAAm solutions. **I:** shear stress vs shear rate; **II:** viscosity vs shear rate with an example of the fitting curve for PAAm 1.25 wt. % case.

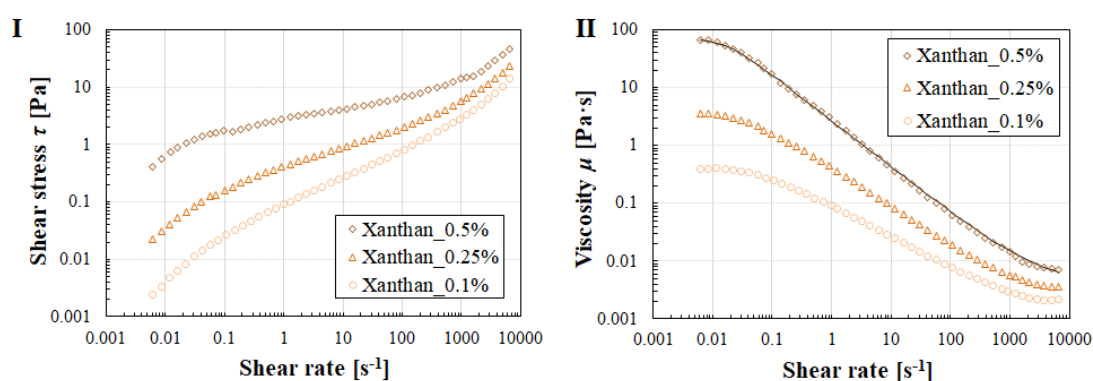


Figure 2-5 Flow curves of Xanthan gum solutions. **I:** shear stress vs shear rate; **II:** Viscosity vs shear rate with an example of the fitting curve for Xanthan 0.5 wt. % case.

As introduced in Chapter 1, the viscosities of Newtonian fluids cannot be given as a specific value. Instead, the rheological models are proposed to characterize the flow curves. Regarding the flow curves obtained for PAAm and Xanthan, Carreau model (Byron Bird and Carreau, 1968; Carreau et al., 1968) is suitable for the fluids with shear thinning property and Newtonian plateau at extreme shear rates. Nonlinear regression is carried out in Matlab software (Curve Fitting Toolbox) to fit experimental data of the viscosity with the Carreau model:

$$\frac{\mu - \mu_{\infty}}{\mu_0 - \mu_{\infty}} = [1 + (t_{\lambda} \dot{\gamma})^2]^{\frac{n-1}{2}} \quad (2-2)$$

With four parameters:

- μ_0 is the viscosity at the zero shear rate [Pa·s];
- μ_{∞} is the viscosity at the infinite shear rate [Pa·s];
- t_{λ} is the relaxation time [s];
- n is the flow behavior index (dimensionless) related to the shear thinning level

For each concentration, multiple samples are tested then fitted with the Carreau model. The averaged result of the four parameters is given in Table 2-3 and the relative deviation of each parameter is within 10%.

Table 2-3. Fitting result of the viscosity of PAAM and Xanthan gum solution by Carreau model

Composition	Concentration (wt)	μ_0 [mPa·s]	μ_{∞} [mPa·s]	t_{λ} [s]	n	r^2
PAAM	0.1%	108.6	2.6	5.91	0.38	0.95
	0.25%	124.5	3.6	6.77	0.40	0.95
	0.5%	150.1	4.8	8.19	0.42	0.97
	1%	246.3	7.0	9.18	0.42	0.97
	1.25%	318.6	8.0	11.86	0.43	0.99
Xanthan	0.1%	360.0	1.0	15.12	0.47	0.97
	0.25%	3600.0	2.0	26.11	0.33	0.96
	0.5%	69000.0	4.0	59.26	0.20	0.98

To evaluate the fitting quality of the model, we usually use the coefficient of determination in statistics, denoted r^2 . The coefficient of determination is defined as the proportion of the variance in the dependent variable that is predictable from the independent variable(s). Its value ranges from 0 to 1 that 0 means the dependent variable cannot be predicted from the independent variable and 1 means the model can

predict without error.

In our case, if the viscosities are marked $\mu_1, \dots, \mu_i, \dots$, each associated with a predicted (or modeled) value $\mu_1', \dots, \mu_i', \dots$, the coefficient of determination can be calculated by the following equation:

$$r^2 = 1 - \frac{\sum_i (\mu_i - \mu_i')^2}{\sum_i (\mu_i - \bar{\mu})^2} \quad (2-3)$$

with $\bar{\mu}$ the mean value of the measured viscosity. The value of the coefficient of determination for each concentration is also given in Table 2-3. All the r^2 values are large than 95% indicating the fitting model is reasonable. In detail, the fitting quality is better for more concentrate solutions.

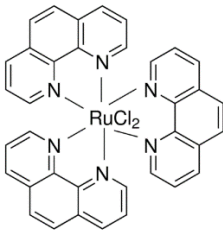
2.1.2 Oxygen indicator (dye)

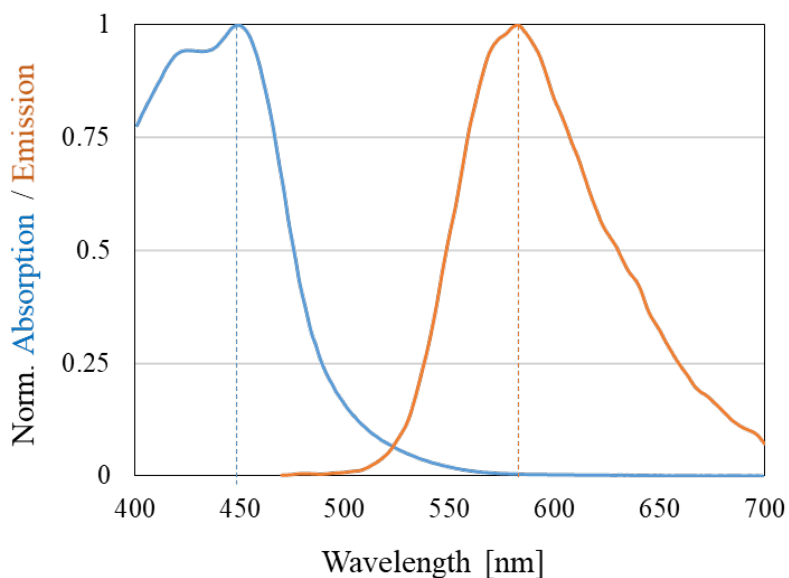
Three techniques are used in the study to visualize the mass transfer, i.e. Planar-Laser Induced Fluorescence (PLIF), PLIF with Inhibition (PLIF-I), and colorimetric technique (Chapter 1). The oxygen concentration is indicated by different dissolved dyes: ruthenium complex for PLIF-I and resorufin for the colorimetric technique and the PLIF technique.

2.1.2.1 Ruthenium complex

As discussed in Chapter 1, different fluorescence dyes have been listed and compared. In this study, a type of ruthenium complex is adopted as a fluorescence dye and its characteristics are given in Table 2-4 with its spectrum is shown in Figure 2-6. The dye is easy to dissolve in water and has a large separation between absorption and emission spectra (Stock shift). It has also been proven sensitive to the presence of the oxygen molecule (Kück et al., 2010, 2012).

Table 2-4 Characteristics of ruthenium complex (C₃₆H₂₄Cl₂N₆Ru·xH₂O). Data from Sigma-Aldrich

Name	Dichlorotris(1,10-phenanthroline)ruthenium(II) hydrate	
Formula	C ₃₆ H ₂₄ Cl ₂ N ₆ Ru·xH ₂ O	Structure: 
Appearance	Orange powder	
Supplier	Sigma-Aldrich	
CAS	207802-45-7	
Molar mass	712.59 g·mol ⁻¹	
Water solubility	Yes	
Peak absorption wavelength	449 nm	
Peak emission wavelength	582 nm	
Price	188 € g ⁻¹	

**Figure 2-6 Spectrum of the fluorophore (ruthenium complex) expressed in normalized absorption factor (blue line) and normalized emission factor (orange line). Image produced according to the data from Fluorophore.org**

Compared with the one used by (Jimenez et al., 2013), the main advantage of the dye considered in this study is its direct solubility in water that it does not require extra material to make dissolve thus brings smaller influence on the mass transfer phenomenon. The fluorescence efficiency is tested for different concentrations of dye

(Jimenez, 2013) by comparing the difference of the gray levels when dissolved oxygen concentration varies from 0 mg·L⁻¹ to 3 mg·L⁻¹. The result is depicted in Figure 2-7 where the variation of the gray level is plotted as a function of the concentrations of dye. It is found that when the concentration of the dye passes a critical value (~75 mg·L⁻¹), the fluorescence efficiency no longer increases. Thus the concentration of dye is set at 75 mg/L to guarantee fluorescence efficiency and economy. Before each experiment, the dye will add into the polymer solutions and blend together for 1 hour for well mixing.

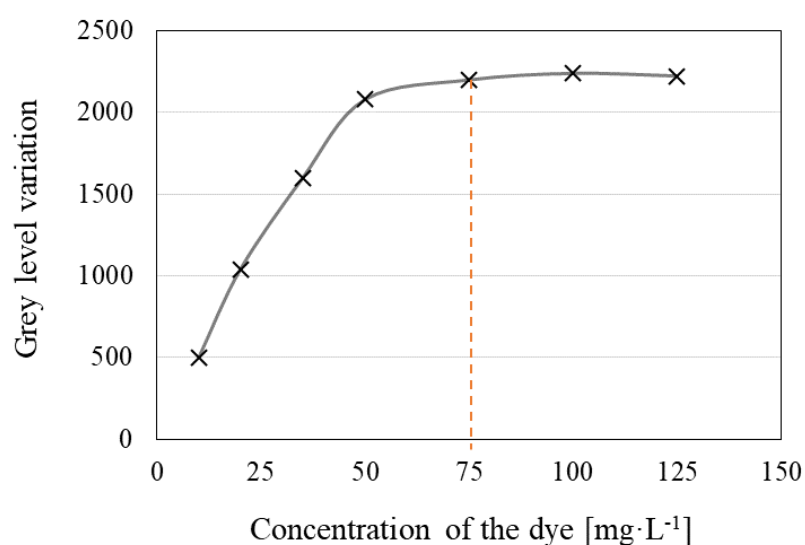
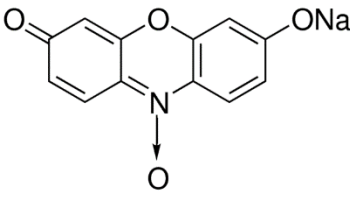


Figure 2-7 Variation of gray level (12 bits format) for dissolved oxygen concentration between 0 and 3 mg·L⁻¹ as a function of the dye concentration. Reproduced from (Jimenez, 2013).

2.1.2.2 Resazurin (resorufin)

Another dye used in this research is resazurin and its characteristics are given in Table 2-6. Resazurin is a phenoxazin-3-one dye which has been widely employed for testing bacterial or yeast contamination in biological fluids and milk, and also identifying the semen quality by colorimetry since the 1950s (Erb and Ehlers, 1950).

Table 2-5 Characteristics of the resazurin. Data from Sigma-Aldrich

Name	7-Hydroxy-3H-phenoxazin-3-one-10-oxide	
Formula	$C_{12}H_6NNaO_4$	<p style="text-align: center;">Structure:</p> 
Appearance	black powder	
Supplier	Sigma-Aldrich	
CAS Number:	62758-13-8	
Molar mass	$251.17 \text{ g}\cdot\text{mol}^{-1}$	
Water solubility	Yes	
Peak absorption wavelength	572 nm	
Peak emission wavelength	583 nm	
Price	30 €g^{-1}	

The dye solution is prepared with $100 \text{ mg}\cdot\text{L}^{-1}$ in the presence of sodium hydroxide (VWR, USA, CAS: 1310-73-2) and D-glucose anhydrous (Fischer Scientific, USA, CAS: 50-99-7), both diluted at $20 \text{ g}\cdot\text{L}^{-1}$. Under this condition, the corresponding enhancement factor equals to 1.03, which means that the enhancement effect of the colorimetric reaction on the diffusion could be negligible (Yang et al., 2017a).

According to the principle of the colorimetric technique (Chapter 1), when resazurin dissolves in water, it reacts with the water and it is reduced to resorufin which has a pink color. In fact, these pink resorufin molecules play a role as an oxygen indicator. On the other hand, it is known that resorufin is also highly fluorescent. This property makes it can also be used as a dye for PLIF technique. The spectrum of the resorufin is shown in Figure 2-8.

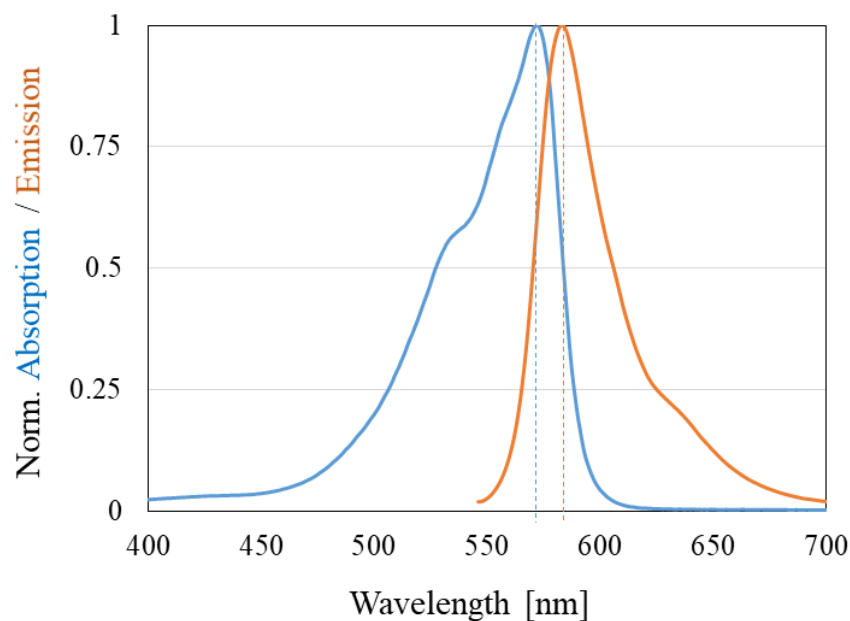


Figure 2-8 Spectrum of resorufin expressed in normalized absorption factor (blue line) and normalized emission factor (orange line). Image produced according to the data from Fluorophore.org

2.2 Experimental setup

To implement the three techniques (PLIF, PLIF-I, and colorimetric technique), the experimental setup, depicted in Figure 2-9, is based on the dual camera system (François et al., 2011a). The experimental system is placed in a thermostatic environment (293.15 K) controlled by an air conditioner and under atmospheric pressure. The specific parameters of each instrument are introduced as follows:

2.2.1 Column

The glass column made of PMMA (Poly (methyl methacrylate)) has a dimension of $100 \times 100 \times 300 \text{ mm}^3$. A stainless steel needle (calibers $\approx 0.5\text{-}1 \text{ mm}$) is inserted into the column through a hole located 20 mm above the bottom of the column. The needle is used for bubble injection that the bubble is pushed out from the tip of the needle when the other side of the needle connects to a syringe pump.

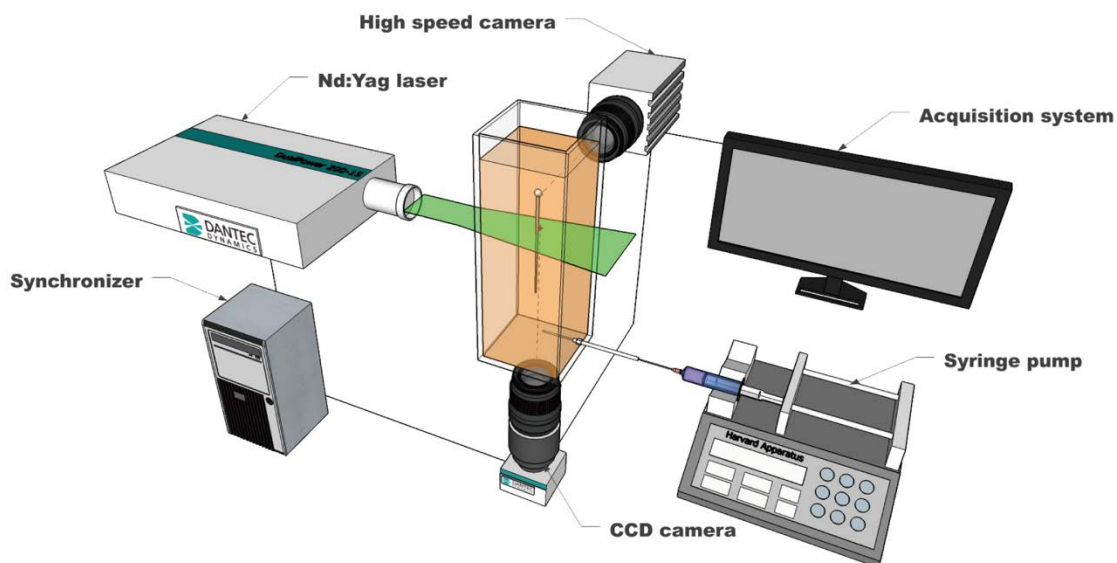


Figure 2-9 Experimental setup

2.2.2 Syringe pump

A syringe pump (Harvard Apparatus PHD 22/2000 Programmable, USA) is used for the purpose of bubble generation. A syringe pump is a small, positive-displacement pump used to gradually transfer precise volumes of fluid. In this study, a syringe of volume 20 mL is installed on the pump. A pusher block driven by a stepper motor pushes against the plunger of the secured syringe for infusion. The pump's stepper motor is precisely turned by a lead screw threaded through a pusher block so that the infusion rate can be precisely controlled. In order to generate isolated bubbles, the infusion rate is set as small as $1 \mu\text{L}\cdot\text{h}^{-1}$. When the stepper motor turns in the opposite direction, the pusher block will pull syringe plunger and the syringe will be refilled.

2.2.3 Nd:YAG laser

A laser sheet is generated by a Nd:Yag laser (Dantec Dynamics Dualpower 200-15, France) and set about 100 mm above the needle. The high-intensity laser ($2\times 200 \text{ mJ}$)

emits light with a wavelength of 532 nm which is located between the peak absorption wavelength and peak emission wavelength of the dye (see Figure 2-6). It enables the excitation of the dye with a frequency of 15Hz. It should notice that for the colorimetric technique, the laser is not necessary.

2.2.4 CCD camera

When the bubble rises in the column, the images of the fluorescence in the wake of the bubble are recorded by a Charge-Coupled Device (CCD) camera (Dantec Dynamics Flowsense CM). The camera is put under the column and focused on the laser sheet. A microlens (105 mm f/8, Canon) with an extension tube (36 mm) is applied to greater the magnification of the investigated area. The length scale is calibrated with a ruler and image area in real distances is about $10 \times 10 \text{ mm}^2$. A 570 nm high-pass filter is also placed in front of the lens to block the laser light. The CCD camera is synchronized to the laser so 15 images are acquired every second in forms of 12 bits and 2048×2048 pixels of resolution. For each bubble, the time is set to 0 when the first picture containing the transferred mass is taken.

2.2.5 High-speed camera

A high-speed camera (Photron SA3, Japan) is placed orthogonally to the first camera, next to one lateral side of the column. It is used to capture the hydrodynamics of the bubble such as the velocity, shape, and trajectory of the bubble at a rate of 2000 fps. The images are in 8 bits format with a resolution of 1024×1024 pixels. The length scale is calibrated with a ruler and image area in real distances is about $30 \times 30 \text{ mm}^2$. The backlight provided by a lighting board facing to the camera.

2.2.6 Acquisition system

The images from the two cameras are then transferred to the acquisition system, which consists of two professional software packages (DynamicStudio 4.0 / Photron Fastcam

Viewer (PFV2)). They can realize simple image treatment such as color filtration, length calibration etc. For further processing, the acquired images are exported in .TIF format and treated with the Matlab software. The detail on the image processing is present in Section 2.5.2.

It should be noticed that the above experimental setup is for characterizing the mass transfer in the bubble wake. To visualize the mass transfer near the bubble interface, the laser sheet can be changed to be vertical and the positions of the two cameras may be switched. The detail is introduced in Chapter 3.

2.2.7 Oxygen probe

Except for the instrument depicted in Figure 2-9, an oxygen probe is usually used during the experiment for calibration or monitoring the oxygen concentration as a reference. The probe system is composed of a portable meter and an optical probe (HQd Digital Meter & IntelliCAL LDO Probe, HACH®). This IntelliCAL LDO is a product of luminescence-based LDO technology (DeGraff and Demas, 2005) providing precise and accurate measurements at a wide range oxygen concentration.

The HQd Meter provides a continuous measurement mode which is to measure automatically in a selected time interval, 10 seconds in the experiments. The data is saved in the internal inventory of the meter and available for further export. A test of the probe is carried out to measure the oxygen concentration in water and the result is stable proving good reliability of probe (see Figure 2-10).

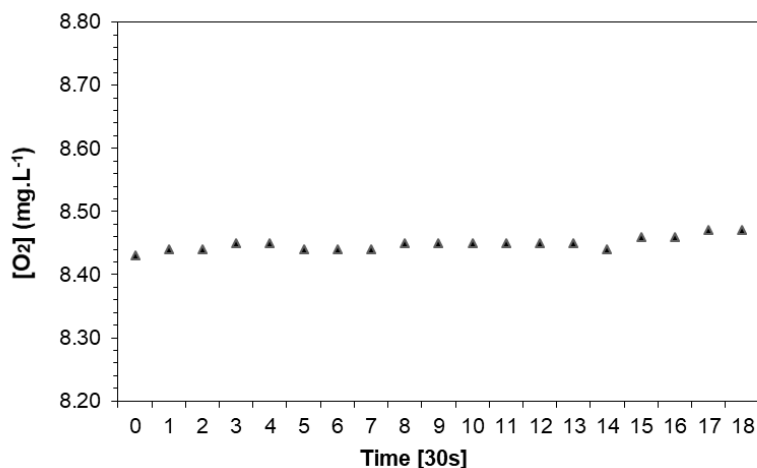


Figure 2-10 Evolution of the oxygen concentration in tap water by the oxygen probe (IntelliCAL LDO Probe, HACH®)

2.3 Experimental protocol

With the equipment introduced above, the general procedure of the experiment can be divided into the following steps. It should notice that different from the laser techniques (PLIF and PLIF-I) several steps are not necessary for the colorimetric technique including laser adjustment and the process to deoxygenate and re-oxygenate the solution.

- 1. Fill the column** Gently pour 2L of the investigated fluid (polymer solution + fluorophore) into the column. Remove the small bubbles adhered to the wall of the column until the fluid looks clear and homogeneous.
- 2. Adjust the cameras** Launch the syringe pump to generate bubble regularly then adjust the position of the two cameras until the bubbles can appear or pass at the center of the image. Stop the pump.

3. Calibrate with ruler

Insert a home-made ruler (see Figure 2-11) into the liquid which is composed of two rulers being perpendicular to each other. Adjust the high-speed camera to focus on the vertical ruler and the CCD camera focus on the horizontal ruler. An image for length calibration is then caught by each camera.

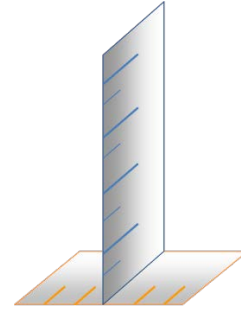


Figure 2-11 Ruler

4. Adjust the laser (only for laser techniques: PLIF and PLIF-I)

Launch the laser (with very low power) to have a horizontal laser sheet. Then adjust the height of the laser until the laser is coplanar with the horizontal ruler. Stop the laser.

5. Deoxygenate the solution (only for PLIF-I techniques)

Inject the nitrogen bubbles using a sparger (see Figure 2-12) into the column to deoxygenate the solution until the dissolved oxygen concentration become close to 0. After the deoxygenation, it needs to wait for the solution being still again. The oxygen concentration is monitored and recorded by the probe.

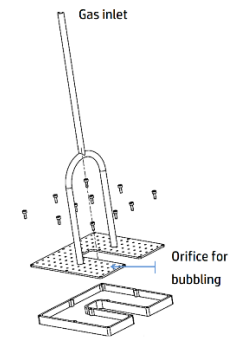


Figure 2-12 Sparger

6. Take reference images

Launch the laser again and use the cameras to take images of the investigated area. The image record by the CCD refers to the initial oxygen concentration $[O_2]_0$ while the image by high speed camera can be used as the reference image for removing the background.

7. Inject a single bubble

Launch the syringe pump to generate a single bubble. Turn on cameras then the high-speed camera captures the movement of the rising bubble while the CCD synchronized with the laser take images of the mass transfer in the wake of the bubble. Stop the camera and save the images. To

visualize a new bubble, it should repeat from step 5.

8. Re-oxygenate the solution (only for PLIF-I techniques)

In order to calibrate the oxygen concentration versus gray level on the image, inject the air bubbles using a sparger to oxygenate the solution. Choose several reference concentration (e.g. 3, 5, 7...mg·L⁻¹) including saturated concentration $[O_2]^*$ and for each concentration, use the CCD to take the 100 fluorescence images of the investigated area. The calibration process is discussed in Section 2.5.1.

9. Purge and clean

Drain the column and clean it with the ethanol several times to avoid the remains that may bring impact on the next measurement.

2.4 Methods on bubble hydrodynamics

2.4.1 Bubble velocity and trajectory

The hydrodynamic properties of the rising bubble are obtained from the sequence of images recorded by the high-speed camera. An example of the experimental images is shown in Figure 2-13-I where the profiles of the rising bubble recorded at 7 different moments are depicted on the same image. Depending on the bubble velocity, hundreds of frames are saved to characterize the rising process of the bubble. To calculate the velocity of the bubble, on each frame containing the bubble profile is converted to binary images (Figure 2-13-II showing 7 frames). Then the centroid (x_i, y_i) of the bubble in each frame is recognized and processed in Matlab software. Plot the centroids of the bubble on a coordinate plan will give the trajectory of the bubble (see Figure 2-13-III)

The distance between the centroids in two successive frames divided by the time interval Δt (1/2000 s) gives the velocity of the bubble:

Horizontal velocity
$$U_x = \frac{x_{i+1} - x_i}{\Delta t} \quad (2-4)$$

Rising velocity

$$U_y = \frac{y_{i+1} - y_i}{\Delta t} \quad (2-5)$$

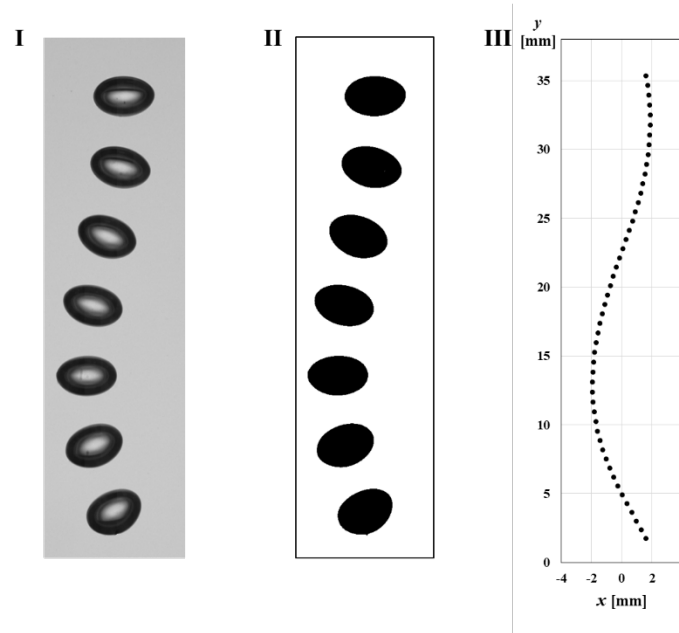


Figure 2-13 Example of the trajectory of the bubble. **I: Raw images, II: Binary images, III: Trajectory of the bubble**

2.4.2 Bubble shape and size

The raw images recorded from the experiment cannot be used directly for the bubble shape investigation. A Matlab image processing procedure is implemented to extract the bubble profile from the raw images. The specific steps are displayed in Figure 2-14. Firstly, a reference image concerning the background, which is taken before the passage of the bubble, is subtracted from the raw image (Figure 2-14-I). The image thus obtained is then transformed into a binary image (Figure 2-14-II) on which the bubble is depicted by a black spot after the background noise is removed. Since the bubble usually slants while rising in the liquid, a rotation is implemented to situate the major axis of the bubble along the vertical direction and fitted the coordinate system. The bubble contour (Figure 2-14-IV) is finally extracted by recognizing the boundary of the

bubble spot (Figure 2-14-III).

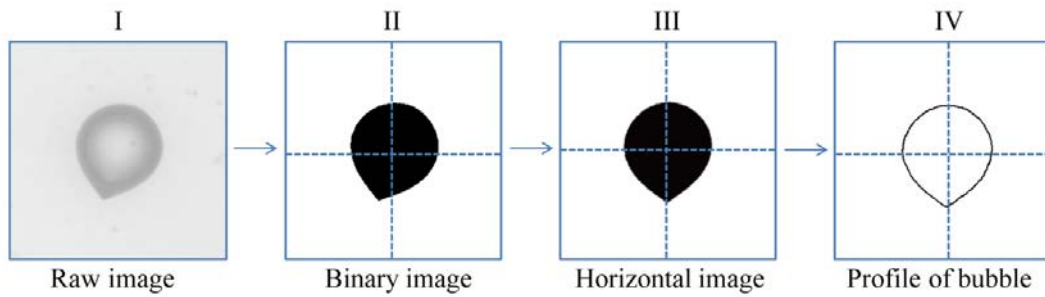


Figure 2-14 Schematic views of the image processing steps (Example of a bubble rising in 0.5 % wt. Xanthan solution).

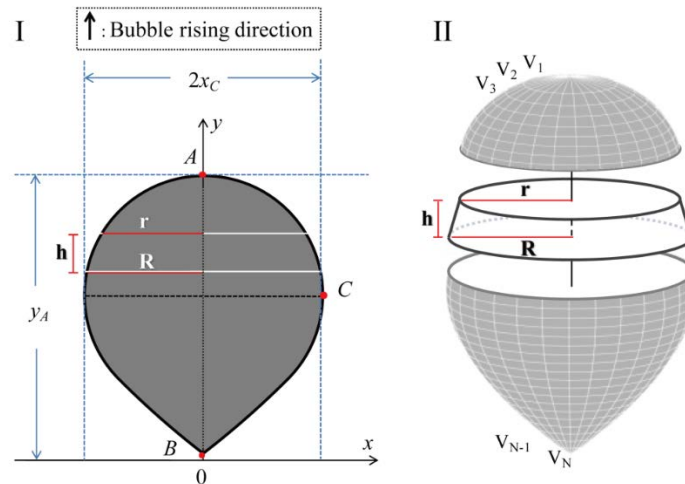


Figure 2-15 Schematic diagram of the bubble profile (I) and the processing method for the equivalent diameter of the bubble (II).

As shown in Figure 2-15-I, the images obtained from the experiment were two-dimensional bubble profiles. The aspect ratio of the bubble is defined as the ratio between the minor axis (width of the bubble: $2x_C$) and the major axis (length of the bubble: y_A) of the bubble profile:

$$\text{Aspect ratio: } E = \frac{2x_C}{y_A} \quad (2-6)$$

With respect to the bubble equivalent diameter, a reconstruction of the three-

dimensional bubble is implemented (see Figure 2-15-II) by supposing that the bubble shape is axisymmetric with the minor axis of the bubble profile. Then the solid bubble is divided into a set of small circular conical frustums. For each frustum, the lateral surface area S_i and the volume V_i are defined as follows:

$$S_i = \pi(R + r)\sqrt{(R - r)^2 + h^2} \quad (2-7)$$

$$V_i = \frac{1}{3}\pi h(R^2 + r^2 + Rr) \quad (2-8)$$

where R and r the radius of the lower and upper cross-sections, respectively, and h is the height of the frustum. These three variables can be directly obtained from the bubble profile recorded by the high-speed camera. The surface area of the bubble is the sum of the lateral surface area of all the small frustums:

$$\text{Surface area:} \quad S_b = \sum_{i=1}^N S_i \quad (2-9)$$

Similarly, the equivalent diameter can be calculated from the total volume of all the small frustums:

$$\text{Equivalent diameter:} \quad D_{eq} = \sqrt[3]{\frac{6 \sum_{i=1}^N V_i}{\pi}} \quad (2-10)$$

2.5 Methods on mass transfer quantification

2.5.1 Calibration of gray level and dissolved concentration

The mass transfer in the bubble wake is recorded by the CCD camera. To enable the quantification of the mass transfer, a calibration is necessary to establish the relationship between the gray level on the image and the actual dissolved oxygen concentration.

2.5.1.1 Calibration for PLIF-I technique

As present in Chapter 1, according to the theory of (Stern and Volmer, 1919), the fluorescence level is directly related to the quencher concentration in the liquid. In our experiment, the fluorescence level can be replaced by the gray level on the image and the quencher concentration equals to the dissolved oxygen concentration $[O_2]$. Hence, (1-39) can be transformed into the following equation:

$$\frac{1}{GL} = \frac{1}{GL_0} + \frac{K_{SV}}{GL_0} [O_2] \quad (2-11)$$

where GL and GL_0 are the gray levels in the presence and absence of oxygen, respectively. It can be seen that the reciprocal of the gray level is proportional to the dissolved oxygen concentration. Thus, for the calibration, images of the fluorescence area are taken in the condition of different dissolved oxygen concentrations (see Section 2.3: re-oxygenate the solutions). An example of the calibration figure depicting the gray level according to the oxygen concentration is given in Figure 2-16 along with gray level images related to the experimental points. The experimental points are fit with Eq. (2-11) and the fitting curves have good linearity (see Figure 2-16-II).

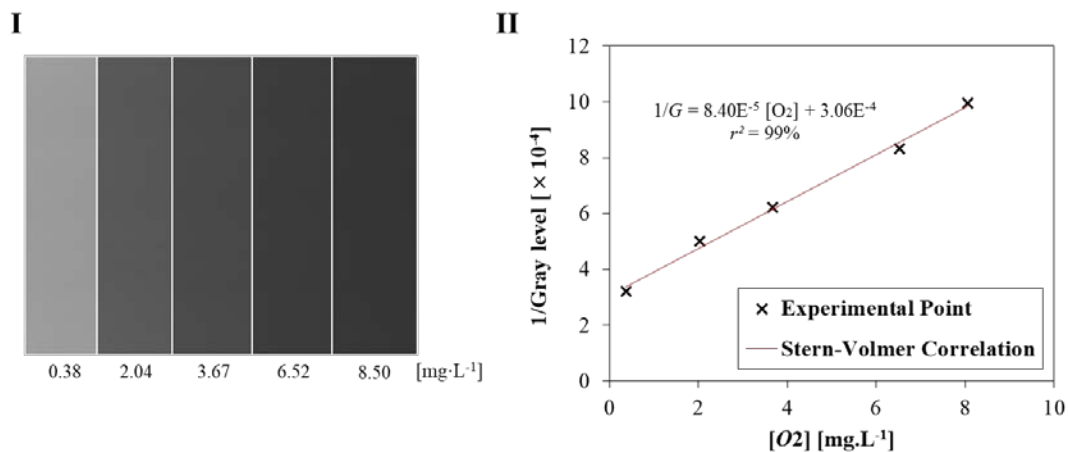


Figure 2-16 Calibration between grey level and the dissolved oxygen concentration for PLIF-I technique. I: Experimental images under different oxygen concentration; II: calibration curve ($GL_0 = 3267$, $K_{SV} = 0.27 \text{ L} \cdot \text{mg}^{-1}$)

The calibration for each tested fluid is performed individually. The specific values of the parameter GL_0 and K_{SV} depend on the concentration of the dye and setting of the equipment including the laser intensity, the aperture and shutter speed of the camera. Exclusively, the calibration area will also alter the calibration result. To verify this impact, the calibration is carried out for areas of a series of concentric circles. As shown in Figure 2-17, the parameters GL_0 and K_{SV} are calculated for the calibration area within each circle. It can be seen that when the calibration area reduces, the values of GL_0 decrease (see Figure 2-17-I) since the bright zone near the image edge is removed. On the other hand, the values of K_{SV} does not have great variation but it becomes more stable for a smaller calibration area (Figure 2-17-II).

It should notice the above calibration is implemented based on the data of the averaged gray level within the calibration area. For higher precision, the “pixel to pixel” calibration method (Valiorgue et al., 2013) may be used instead to calibrate for each pixel. A test by this technique is done and the parameter GL_0 and K_{SV} are calculated for all pixel within the circles. The result is in Figure 2-17 where the standard deviation of GL_0 and K_{SV} is depicted with the error bar. It can be seen that when the calibration area is small enough, the deviation of the calibration result is moderate (e.g. within a 200×200 pixels area, the gray level variation is less than 10 degrees for 12 bits image). Regarding the “pixel to pixel” calibration is time-consuming and requires a lot of computation resource, we use an averaged calibration within the circle of 200×200 pixels.

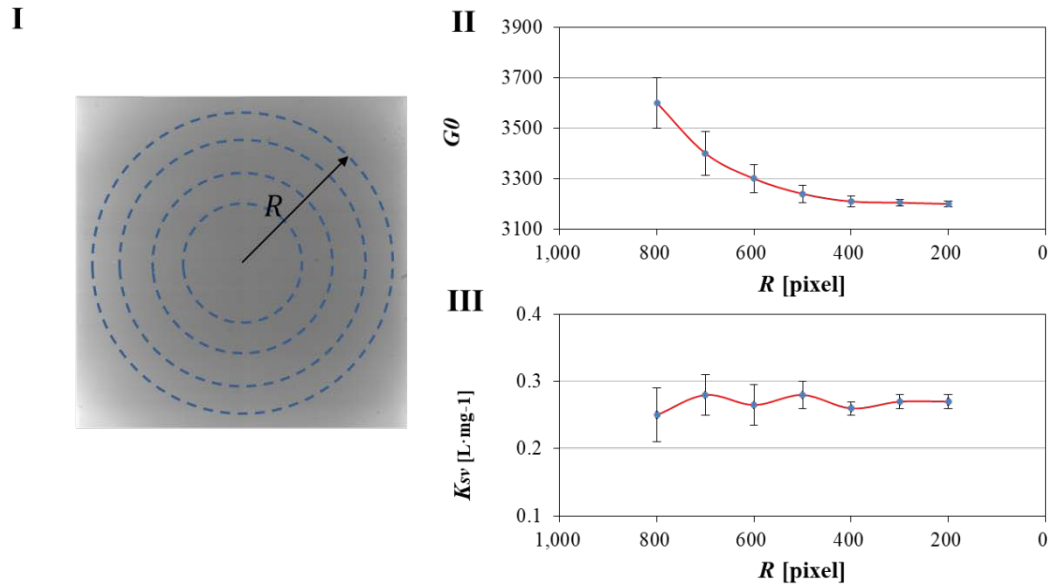


Figure 2-17 Impact of the calibration area on the calibration result; I: Concentric calibration area; II&III: Evolution of parameter GL_0 and K_{SV} versus the diameter of the calibration circle.

2.5.1.2 Calibration for PLIF technique

For the PLIF technique with the dye of resazurin, the calibration measurement is similar to the one for colorimetric but adding a laser facing to the camera. The 100 fluorescence images are taken for each resazurin solutions (0, 40, 70 and 120 mg·L⁻¹).

Regarding that the amount of the fluorophore (resorufin: product from the oxidation of the resazurin) is proportional to the consumed oxygen (Eq. (2-13)), and based on the principle of traditional PLIF technique (Chapter 1), the following relation can be driven:

$$GL \propto I \cdot [O_2] \quad (2-12)$$

with I a constant depend on the laser intensity. An example of the calibration curve between the averaged gray level GL and the local oxygen concentration $[O_2]$ is shown in Figure, so that the mass transfer can be quantified in the experiment.

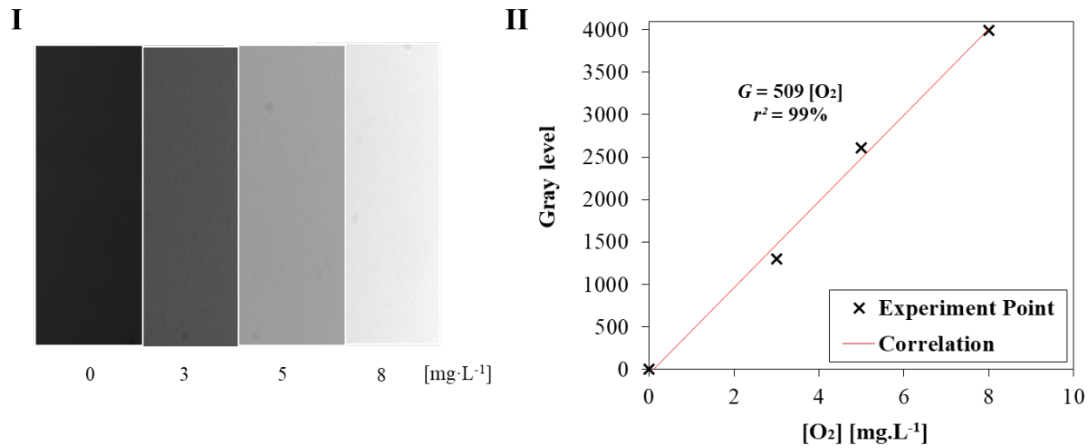


Figure 2-18 Calibration between grey level and the dissolved oxygen concentration for PLIF technique. I: Experimental images under different oxygen concentration; II: calibration curve

2.5.1.3 Calibration for colorimetric technique

According to the oxidation reaction expressed in Chapter 1, when there is a sufficient amount of resazurin to react with all the oxygen transferred, the number of moles of dissolved oxygen can be deduced from the number of moles of resazurin, as

$$n_{O_2 \text{ transferred}} = n_{O_2 \text{ reacted}} = \frac{n_{\text{resazurin}}}{2} = \frac{n_{\text{resorufin}}}{2} \quad (2-13)$$

Therefore, for the calibration process, resazurin solution of different concentrations has been prepared: 0, 40, 70 and 120 mg·L⁻¹ which refer to the concentration of oxygen: 0, 3, 5, 8 mg·L⁻¹. They are saturated with oxygen from the air in order to reach their highest intensity of pink (or their highest value of grey level on the acquired image) then added in

For each concentration, about 100 pictures without bubbles are recorded and calculated their averaged gray level. Then a linear relationship between the gray level and the transferred oxygen concentration is found, enabling the quantification of the mass transfer.

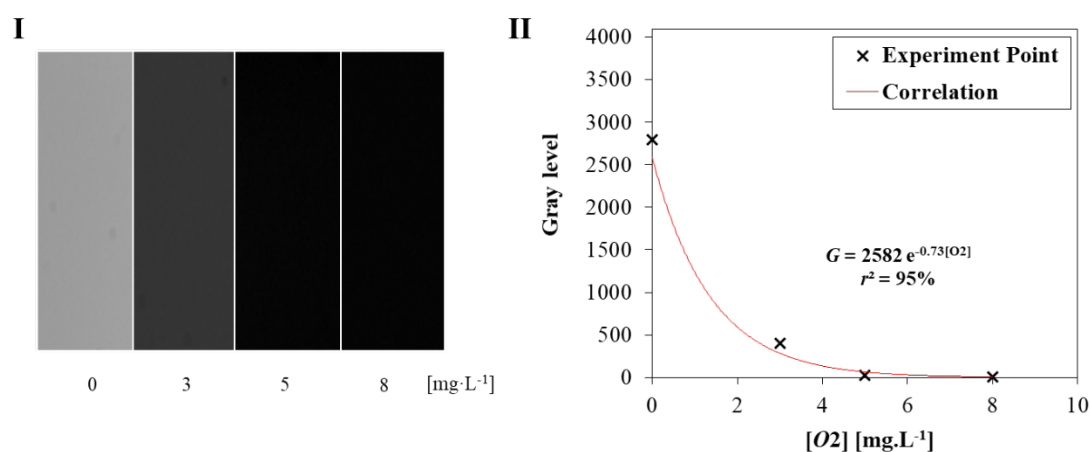


Figure 2-19 Calibration between grey level and the dissolved oxygen concentration for colorimetric technique. I: Experimental images under different oxygen concentration; II: calibration curve

2.5.2 Image processing

Using the calibration curve, the experimental images can be converted to the dissolved oxygen concentration fields where the mass transfer can be presented as a circular spot (for small bubbles with $D_{eq} \sim 1$ mm, see Figure 2-20-I). It is obvious that there is a lot of noise on the image and the background is not homogeneous that can dramatically distort the results. These noise may be induced by various possible sources during the experiment such as laser instability, photobleaching (Axelrod et al., 1976), Beer-Lambert absorption (Mayerhöfer et al., 2016). In order to improve the image quality for further investigation, an image processing procedure is implemented using Matlab software. It should be noted that the images presented in Figure 2-20 have a resolution of about 200×200 pixels as the border is removed from the original 1024×1024 pixels image. The laser illuminates from the right-hand side to the left.

2.5.2.1 Step 1: Subtract the background

The process consists of, first, subtracting the background image from the raw image. The background image is a reference image corresponding to the average of 50 images

taken just before the bubble passing. After the subtraction, the concentration difference between the right-hand side and the left is reduced (Figure 2-20-II).

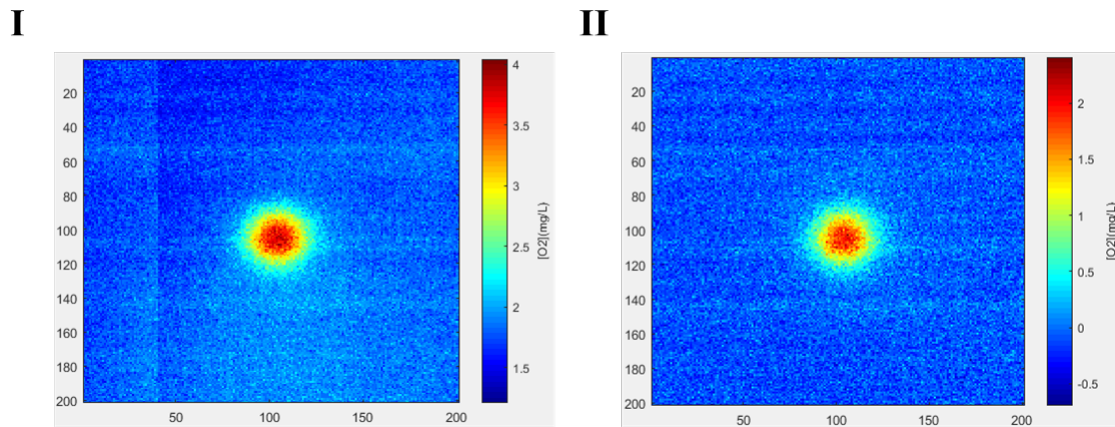


Figure 2-20 Image processing. I: Raw image of dissolved oxygen concentration field; II: Image after subtracting the background.

2.5.2.2 Step 2: Shift all the values of the image

After the subtraction, the background value is still different from zero and some values are even negative. The probability distribution of oxygen concentration at the zone without transfer (Figure 2-21-I) is plotted (Figure 2-21-II). It is found that the background values follow a normal distribution:

$$f([O_2]) = \frac{1}{\sigma\sqrt{2\pi}} e^{-\frac{([O_2]-\mu)^2}{2\sigma^2}} \quad (2-14)$$

where μ is the mean value of data and σ is the estimated standard deviation.

Obviously, most of the background concentration is between $-0.4 \text{ mg}\cdot\text{L}^{-1}$ and $0 \text{ mg}\cdot\text{L}^{-1}$, and the mean value μ of the background concentration is negative. To fix this distortion, shift all the values of the image (including the mass transfer zone) to make the mean of background concentrations (without transfer) become $0 \text{ mg}\cdot\text{L}^{-1}$. Then the majority of the background value will be between $-0.2 \text{ mg}\cdot\text{L}^{-1}$ and $0.2 \text{ mg}\cdot\text{L}^{-1}$. (see Figure 2-21-II bubble line)

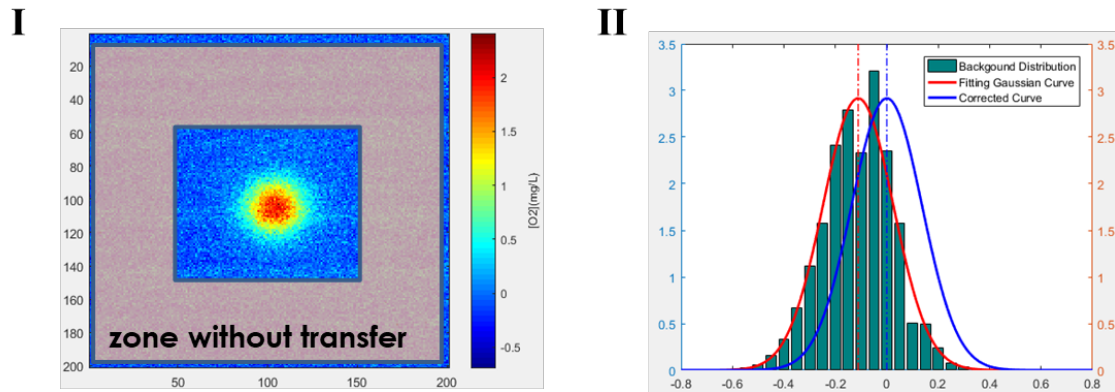


Figure 2-21 Image processing. I: Zone without transfer; II: Image after subtracting the background.

2.5.2.3 Step 3: Apply a threshold

After the previous step, there are still some negative values. Thus, a threshold λ is then set as defined in Eq. (2-16) to eliminate the influent of background noise and determine the boundary between the background of the image and the transferred mass by the bubble:

$$\begin{aligned} \text{For } [O_2] \geq \lambda \times \sigma_{st}, \quad [O_2] \\ \text{For } [O_2] < \lambda \times \sigma_{st}, \quad [O_2] = 0 \end{aligned} \quad (2-15)$$

$$\lambda \in \{0, 1, 2, 3, 4, 5\}$$

where σ_{st} is the estimated standard deviation of the distribution of oxygen concentrations of the image background obtained from the Section 2.5.2.2. The choice of the threshold factor is crucial since it directly affects the quantification of the total amount of the oxygen diffusion. Depending on the image quality, the threshold factor is chosen for each image to minimize the noise and maximize the spot of mass transfer. For most cases, a threshold factor of 3 is high enough (Jimenez et al., 2013). The image after applying a threshold is shown in Figure 2-22-II.

2.5.2.4 Step 4: Oxygen field fitting

In previous studies (Dietrich et al., 2015; François et al., 2011a), it was found that, for quasi-spherical bubbles, the diffusion spot is circular and presented a Gaussian profile. Thus a fitting model is proposed for the diffusion spot which will facilitate the further mass transfer quantification (Section 2.5.4). So the oxygen concentration $[O_2]$ on the pixel (x, y) is estimated by:

$$[O_2](x, y) = A \exp \frac{-(x-X)^2 + (y-Y)^2}{B} + C \quad (2-16)$$

where A, B are the parameters representing the properties of a Gaussian distribution, C is the mean value of the residual noise on the image, and (X, Y) is the center of the spot. With the Fminsearch solver (Matlab software), these five parameters are determined by minimizing the error between the measured value $[O_2]$ and the value from Eq. (2-16). For initialization, the parameters were set as follows:

- Initialization of A : Maximum value of $[O_2]$ on the spot
- Initialization of B : Variance of the Gaussian by placing on a fixed line passing through the center of the spot
- Initialization of C : Minimum value of $[O_2]$ on the spot
- Initialization of (x, y) : Coordinates of the maximum $[O_2]$

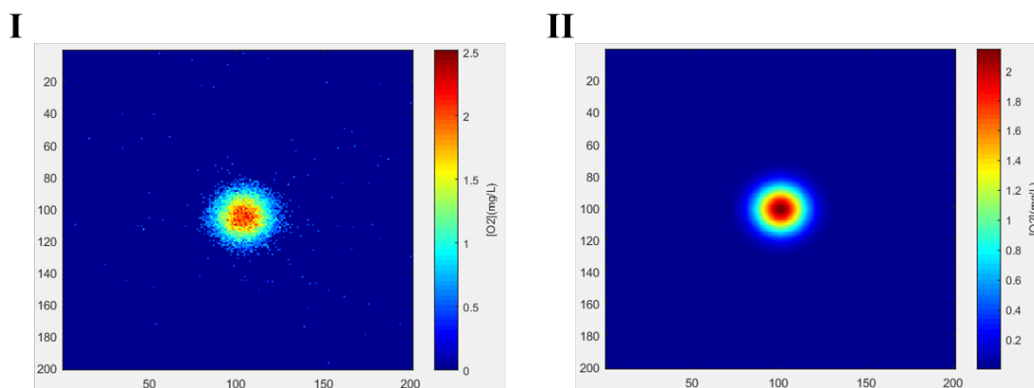


Figure 2-22 Image processing. I: Image after applying a threshold; II: Image fitted with the Gaussian model.

The fitted oxygen concentration field is shown in Figure 2-22-I. After the fitting process, the concentration in the bulk of the image, which does not contain the transfer spot, is uniform. Thus the real oxygen concentration field can be expressed by the following equation, where the noise term C is removed. The detail on the parameters A , B , and C are discussed in greater detail in Chapter 5.

$$[O_2](x, y) = A \exp \frac{-(x-X)^2+(y-Y)^2}{B} \quad (2-17)$$

2.5.3 Determination of the diffusion coefficient

According to the diffusive regime presented in Crank (1979), the diffusion coefficient D can be calculated with the experimental images. The concentration $[O_2]$ is expressed in this problem as the amount of diffusing oxygen per unit area of the image. The instantaneous concentration at a position (x, y) on the cross-section of the bubble wake (bubble spot) is given by:

$$[O_2](x, y, t) = \frac{M}{4\pi Dt} \exp\left(\frac{-(x^2+y^2)}{4Dt}\right) \quad (2-18)$$

where M is defined as the total amount of substance diffusing from a point source on an infinite plane surface, by performing the integration

$$M = \int_{-\infty}^{\infty} \int_{-\infty}^{\infty} [O_2] dx dy \quad (2-19)$$

At a fixed time t , for a bubble spot with area S , the oxygen concentration field could be expressed as:

$$\iint_S [O_2](x, y) dx dy = \iint_S \frac{M}{4\pi Dt} \exp\left(\frac{-(x^2+y^2)}{4Dt}\right) dx dy \quad (2-20)$$

For a quasi-circular spot of radius R , the Eq. (2-20) could be expressed in the polar coordinate:

$$\iint_S [O_2](\theta, r) dx dy = \int_0^{2\pi} d\theta \int_0^R \frac{M}{4\pi Dt} \exp\left(\frac{-r^2}{4Dt}\right) r dr \quad (2-21)$$

With

$$w = \frac{r^2}{2Dt} \quad (2-22)$$

It remains:

$$\iint_S [O_2](\theta, r) dx dy = \int_0^{\frac{R^2}{2Dt}} \frac{1}{2} \exp\left(\frac{-w}{2}\right) dw \quad (2-23)$$

In the other hand, according to the probability theory, the probability density $f(w)$ of Chi-squared distribution in k freedom degrees can be written as:

For $w > 0$:

$$f(w) = \frac{\left(\frac{1}{2}\right)^{\frac{k}{2}}}{\Gamma\left(\frac{k}{2}\right)} w^{\frac{k}{2}-1} \exp\left(\frac{-w}{2}\right) \quad (2-24)$$

Otherwise

$$f(w) = 0 \quad (2-25)$$

with Γ the gamma function (Weisstein, 2002). In our study, the freedom degrees k is 2 (θ and r) and definitely $w > 0$ (Eq. (2-22)). Therefore, the Eq. (2-24) becomes:

$$f(w) = \frac{1}{2} \exp\left(\frac{-w}{2}\right) \quad (2-26)$$

Comparing the forms of Eq. (2-23) and Eq. (2-26), the following equation can be derived:

$$\frac{\iint_S [O_2](x,y) dx dy}{M} = \int_0^{\frac{R^2}{2Dt}} f(w) dw \quad (2-27)$$

It could provide the feasibility to determine the diffusion coefficient D from the proprieties of chi-squared distribution. It is known that in the case of $k = 2$, the cumulative distribution function of chi-squared distribution has a simple form:

$$P[w \leq \eta | w \sim \chi^2] = \int_0^\eta f(w) dw \quad (2-28)$$

$$= 1 - e^{-\eta/2} \quad (2-29)$$

where P the probability in case $w \leq \eta$ and w is distributed according to Chi-squared

law. An example of values of P versus η is given in Table 2-6.

Table 2-6 Relation between parameter η and P of Chi-squared distribution

η	P
1	0.3995
2	0.6321
3	0.7769
4	0.8647
5	0.9179
6	0.9502

Substituting Eq. (2-29) into Eq. (2-27), the relationship between the diffusing oxygen concentration field and probability property of chi-squared distribution is given by the following equation (Xu et al., 2017):

$$\frac{\iint_{S_{spot}} [O_2](r, \theta) r dr d\theta}{M} = 1 - e^{-\frac{\eta}{2}} \quad (2-30)$$

where M and $[O_2](r, \theta)$ are the total transferred mass and the oxygen concentration on the circular spot plan. The right-hand term of Eq. (2-30) denotes the cumulative possibility $P(\eta)$ of a chi-squared distribution of 2 degrees of freedom with a positive integer parameter η . From Eq. (2-30), it is deduced that, once the value η is fixed, the ratio between the oxygen diffusing within the area S and the total transferred mass M will stay constant. Since the mass transfer in the vertical direction is already neglected, the total transferred mass, M , on the cross-section of the bubble wake is also constant and the diffusion is assumed to occur only in the fluorescence plane. Therefore, the area S_{spot} will expand when the oxygen diffuses from the spot center to the surroundings. Obviously, the speed of expansion depends on the diffusion coefficient.

For the quasi-circular spot of radius R , the area, S_{spot} , is given as (Xu et al., 2017):

$$S_{spot} = \pi R^2 = 2\pi\eta Dt \quad (2-31)$$

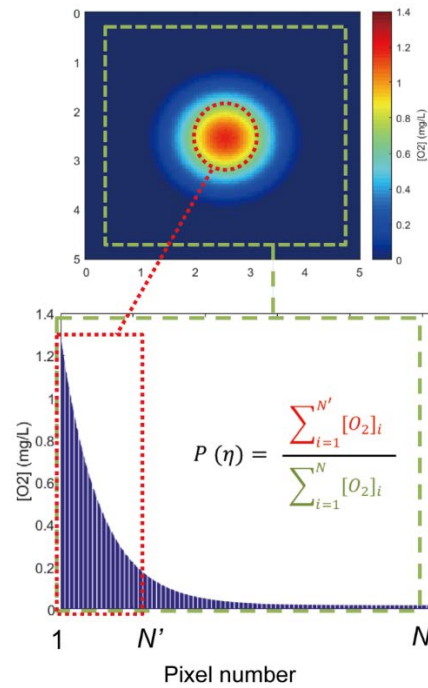


Figure 2-23 Determination of the diffusion coefficient (N : total number of pixels on the image, N' : number of pixels within area S_{spot} , $[O_2]_i$: oxygen concentration at i pixel)

The area S_{spot} can be obtained from a processed image from which the noise has been removed (expressed by Eq. (2-17)). As depicted in Figure 2-23, the following steps were implemented:

- 1) Choose η and calculate $P(\eta)$;
- 2) Sort the concentrations in all the pixels N in descending order;
- 3) Sum all the oxygen concentrations (indicated by green color);
- 4) Perform a cumulative sum to achieve the proportion $P(\eta)$ of the total concentration (indicated by red color);
- 5) Count the number of pixels N' forming this cumulative sum;
- 6) Multiply the number by the surface of a single pixel δ^2 to obtain S_{spot}

From Eq. (2-31), for constant D and a chosen η , the area, S_{spot} , expands linearly with time t . The speed of expansion is related to the slope of the curve $S_{spot}-t$ and the diffusion coefficient D can thus be determined. The result of diffusion is discussed in

Chapter 5.

2.5.4 Determination of the liquid side mass transfer coefficient

With the dissolved oxygen concentration field, mass transfer can be quantified. The mathematical approach used to calculate the mass transfer coefficient is based on a previous study by Francois et al. (François et al., 2011a). It is assumed that, when the bubble has passed far enough from the investigated plane (fluorescence plane in this study), the effect induced by the bubble passing or the convection can be neglected. Thus the total flow rate of mass transfer from the bubble can be approximated as:

$$F_{O_2} = \frac{dm_{O_2}}{dt} \quad (2-32)$$

with m_{O_2} the mass of oxygen transferred by the bubble.

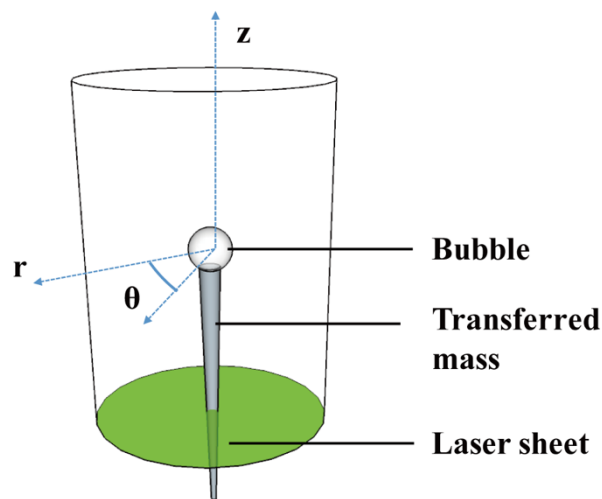


Figure 2-24 Description of the mass balance domain

Mass transfer can then be tracked by the oxygen accumulation in the distant wake. Under a cylindrical coordinate system (r, θ, z) , as depicted in Figure 2-24, the

accumulation term can be written in volume V as:

$$\begin{aligned}
 F_{O_2} &= \frac{dm_{O_2}}{dt} = \lim_{\Delta t \rightarrow 0} \frac{m_{O_2}(t+\Delta t) - m_{O_2}(t)}{\Delta t} \\
 &= \lim_{\Delta z \rightarrow 0} \frac{\iint_{V(z)}^{V(z+\Delta z)} [O_2](r, \theta, z) dV}{\int_z^{z+\Delta z} dz / U_b} \quad (2-33)
 \end{aligned}$$

Away from the bubble, the variation of the oxygen concentration $[O_2](r, \theta, z)$ in the z direction can be neglected compared with the variation along the r direction, which implies $[O_2](r, \theta, z) = [O_2](r, \theta)$. Thus Eq. (2-33) can be simplified as:

$$\begin{aligned}
 F_{O_2} &= \lim_{\Delta z \rightarrow 0} \frac{\int_z^{z+\Delta z} dz \iint [O_2](r, \theta) r dr d\theta}{\int_z^{z+\Delta z} dz / U_b} \\
 &= U_b \iint [O_2](r, \theta) r dr d\theta = U_b \cdot M \quad (2-34)
 \end{aligned}$$

where M is defined as the total mass transferred on the infinite cross-section in the bubble wake. In the study, this cross-section refers to the investigated plane where the fluorescence occurs and the dissolved oxygen concentration field (containing the diffusion spot) is recorded by the camera.

In the general case, whatever the shape of the diffusion spot, the transferred mass, M , [$\text{mg} \cdot \text{m}^{-1}$] can be calculated simply as the sum of the oxygen concentrations $[O_2]_i$ in all pixels on the experimental image:

$$M = \sum [O_2]_i \delta_{pixel}^2 \quad (2-35)$$

where δ_{pixel}^2 is the area of a square pixel [m^2].

If the spot is circular, the concentration field on the image is assumed to have a Gaussian distribution. As already presented in Section 2.4.2, the concentration field can be fitted by Eq. (2-16). Thus the transferred mass M can be calculated directly as follows:

$$M = \pi AB \quad (2-36)$$

Based on the knowledge of M and the bubble rising velocity U_b , the flow rate F_{O_2} can

be obtained (Eq. (2-34)). Then the flux density J_{O_2} can be deduced using the bubble surface area S (Eq. (2-9)) and, finally, the liquid side mass transfer coefficient k_L is equal to the flux density or flux J_{O_2} [$\text{mg}\cdot\text{s}^{-1}\cdot\text{m}^{-2}$] divided by the driving force ($[O_2]_{sat} - [O_2]_{bulk}$):

$$J_{O_2} = \frac{F_{O_2}}{S_b} \quad (2-37)$$

$$k_L = \frac{J_{O_2}}{[O_2]^* - [O_2]_0} \quad (2-38)$$

where $[O_2]^*$ and $[O_2]_0$ are the oxygen concentrations at saturation and far away from the mass transferred by the bubble, respectively. These two values are determined using an optical oxygen probe (see Section 2.3) for each liquid investigated.

2.5.5 Error analysis

Based on the method to calculate the diffusion and mass transfer, the error and the uncertainty of the measured result is defined and estimated by the following methods:

2.5.5.1 General rule for combination of errors:

For a function $Z = f(X_1, X_2, X_3, \dots, X_N)$, assuming the variables in the equation are uncorrelated, it has:

$$\ln Z = \ln f(X_1, X_2, X_3, \dots, X_N) \quad (2-39)$$

$$\frac{dZ}{Z} = \frac{\partial \ln f}{\partial X_1} dX_1 + \frac{\partial \ln f}{\partial X_2} dX_2 + \frac{\partial \ln f}{\partial X_3} dX_3 + \dots + \frac{\partial \ln f}{\partial X_N} dX_N \quad (2-40)$$

Thus the uncertainty can be defined:

$$\frac{\Delta Z}{Z} \approx \sqrt{\left(\frac{\partial \ln f}{\partial X_1} \Delta X_1\right)^2 + \left(\frac{\partial \ln f}{\partial X_2} \Delta X_2\right)^2 + \left(\frac{\partial \ln f}{\partial X_3} \Delta X_3\right)^2 + \dots + \left(\frac{\partial \ln f}{\partial X_N} \Delta X_N\right)^2} \quad (2-41)$$

2.5.5.2 Error of image fitting

The experimental oxygen concentration field is fit by a Gaussian equation, the error is defined as the difference between the measured value $[O_2]_i$ and the fitting value $[O_2]_{i,fit}$ in all the fitting area (200×200 pixels in this study):

$$err = \sum_i |[O_2]_{i,fit} - [O_2]_i| \quad (2-42)$$

The relative error:

$$err\% = \frac{\sum_i |[O_2]_{i,fit} - [O_2]_i|}{\sum_i [O_2]_i} \quad (2-43)$$

2.5.5.3 The uncertainty of diffusion coefficient D

In our study, according to Eq. (2-31), the diffusion coefficient D is obtained by the function:

$$D = \frac{S_{spot}}{2\pi\eta t} \quad (2-44)$$

So the uncertainty of D is:

$$\frac{\Delta D}{D} = \sqrt{\left(\frac{\Delta S_{spot}}{S_{spot}}\right)^2 + \left(2\pi\eta \frac{\Delta t}{t}\right)^2} \quad (2-45)$$

Regarding that the uncertainty of the time is generally negligible, this expression can be simplified by only considering the impact of S_{spot} . As the S_{spot} is calculated by counting the number of pixels (Section 2.5.3), it can be assumed that the deviation of S_{spot} should be within the area of a single pixel (δ^2):

$$\frac{\Delta D}{D} = \frac{|\Delta S_{spot}|}{S_{spot}} = \frac{\delta^2}{S_{spot}} \quad (2-46)$$

Moreover, as shown in Fig. 13, we have one value S_{spot} for each recording moment. So if there is N recording moments, the final uncertainty of D should be equal to the average:

$$\frac{\Delta D}{D} = \frac{1}{N} \sum_{i=1}^N \frac{\delta^2}{S_{spot,i}} \quad (2-47)$$

2.5.5.4 The uncertainty of diffusion coefficient k_L

According to Section 2.4.3, the mass transfer coefficient k_L is obtained by the function:

$$k_L = \frac{U_b AB}{D_{eq}^2 ([O_2]_{sat} - [O_2]_{bulk})} \quad (2-48)$$

So the uncertainty of D is:

$$\frac{\Delta k_L}{k_L} = \sqrt{\left(\frac{\Delta A}{A}\right)^2 + \left(\frac{\Delta B}{B}\right)^2 + \left(\frac{\Delta U_b}{U_b}\right)^2 + 4 \left(\frac{\Delta D_{eq}}{D_{eq}}\right)^2 + \left(\frac{\Delta [O_2]}{[O_2]_{sat} - [O_2]_{bulk}}\right)^2} \quad (2-49)$$

- ΔA and ΔB can be obtained from the image fitting process as their variation in the interval $[\text{err}, (1 + 5\%)err]$;
- ΔU_b and ΔD_{eq} can be determined from the hydrodynamics result of the bubble;
- $\Delta [O_2]$ depends on the accuracy of the oxygen probe

2.6 Conclusion

The material and method used in this research are introduced in the chapter.

Firstly, three different polymers are chosen since they are very common and have a wide application in the industry. The aqueous solutions of the polymers are prepared carefully and their physical properties are measured. Compared with the water, it is found that the addition of the polymer as a solute will slightly increase the density and reduce the surface tension. According to the result measured by the rotational rheometer, the Breox solutions are Newtonian fluids. The PAAm and Xanthan solutions are non-Newtonian fluids that they both have a shear thinning property under the shear rate between 0.1 s^{-1} and 100 s^{-1} . In this range, the investigated Xanthan gum solutions are more viscous than the PAAm ones.

Secondly, three techniques are used in the study to visualize the mass transfer, i.e. Planar-Laser Induced Fluorescence (PLIF), PLIF with Inhibition (PLIF-I), and colorimetric technique. The experimental setup and procedure for different techniques are basically the same except that the colorimetric technique is carried out without the laser. The column is filled with the polymer solution mixed with the dye (ruthenium complex or resorufin). Once a single bubble is injected, the images of mass transfer and the movement of the bubble are captured by the two-camera system (CCD+high speed camera).

Analyzing the images acquired by a high-speed camera, the bubble velocity and trajectory can be obtained by recognizing the centroid of each frame. For calculating the bubble size, a three-dimensional bubble is reconstructed and divided into small circular truncated cones. The bubble surface area and volume equal to the sum of these small cones. Then the equivalent diameter of the bubble can be deduced from the volume.

On the other hand, the image from the CCD camera is used for mass transfer characterization. To enable the quantification of the mass transfer, a calibration is necessary to establish the relationship between the gray level on the image and the actual dissolved oxygen concentration. The calibration processes are carried out by taking images for several solutions at preset oxygen concentrations then the calibration curve is obtained based on the principle of each technique. Using the calibration curve, the experimental images can be converted to the dissolved oxygen concentration fields where the mass transfer can be presented as a circular spot. After the image processing by Matlab software, the noise and background impact are removed and the concentration field can be used for mass transfer characterization.

Finally, the methods for calculating the diffusion coefficient and mass transfer coefficient are introduced. To calculate the diffusion coefficient, the chi-squared probability density function is introduced to describe the diffusing oxygen concentration field. It is found that the ratio between the oxygen diffusing within the

specific area S_{spot} and the total transferred mass M refers to the diffusion coefficient. The diffusion coefficient D can thus be determined from the slope of the curve S_{spot} as a function time. To calculate the mass transfer coefficient, it is assumed that, when the bubble has passed far enough from the investigated plane (fluorescence plane in this study), the effect induced by the bubble passing or the convection can be neglected. Thus the oxygen is transferring only within the cross-section of the bubble wake and the transferred mass equals to the sum of the oxygen concentrations in all pixels on the experimental image. With the bubble velocity and surface area of the bubble, and the driving force measured by the probe, the mass transfer coefficient can be determined.

Chapter 3

Comparison of different visualization techniques (PLIF, PLIF-I and colorimetric techniques)

Abstract:

In this chapter, the visualization techniques are reviewed according to their application to different systems. In order to compare the representative techniques, three sets of experiments are conducted to characterize the local mass transfer and the diffusion around a single air bubble (with equivalent diameters ~ 1 mm) rising in water by using PLIF (with fluorescent resorufin), PLIF-I (with ruthenium complex), and colorimetric techniques (with pink resorufin), respectively. It aims at comparing these three techniques and figuring out their advantages as well as their limitations. The comparison is divided into two parts: the visualization and the quantification of the mass transfer. The discussion focuses on the image quality, the equipment requirement, the accuracy of quantification result including the mass flux, diffusion coefficient, and mass transfer coefficient. This chapter provides a guideline for choosing the visualization technique to accurately visualize and characterize the local mass transfer in gas-liquid systems.

3.1 State of the arts

As presented in Chapter 1, most of the modern visualization techniques for gas-liquid mass transfer are based on the addition of the indicator (fluorescence dye or colorimetric dye) into the liquid phase. According to the principle of these techniques, they can be classified into the traditional PLIF technique, variant PLIF technique, and the colorimetric technique. These techniques have been adapted for use with a wide variety of gas-liquid contacting conditions, including bubbly flows, flows across the planar interface and Taylor flows/ confined flows. Their application to different flow systems is introduced as follows.

3.1.1 Free bubbly flows

In several industrial processes (bubble column reactor, stirred tank, etc.), the gas phase usually appears as a form of bubble swarms or isolated bubble because of their high interfacial area for gas-liquid mass transfer (Colombet et al., 2011). The visualization techniques provides an efficient tool to characterize this transferring process for different type of gas: air (Bouche et al., 2013; Fedrizzi and Soria, 2014; Jimenez et al., 2013; Moghaddas et al., 2002), oxygen (François et al., 2011a; Kück et al., 2010) and carbon dioxide (Hanyu and Saito, 2010; Stöhr et al., 2009; Yamamoto et al., 2008). The examples of the visualization result are shown in Figure 3-1.

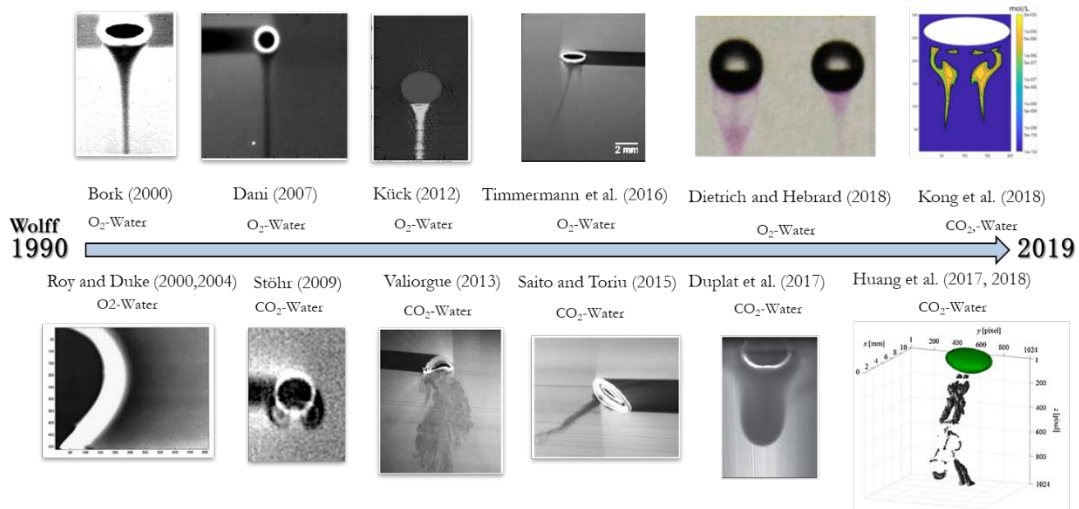


Figure 3-1 Development of mass transfer visualization of freely rising bubbles. Images from the indicated authors.

A series of representative researches have been implemented which apply visualization techniques to bubble in recent decades. (Roy and Duke, 2000) measured dissolved oxygen concentration gradients in water near the surface of an air bubble. An expansion of their study to the surface in surfactant-contaminated water was made in 2004. (Bork et al., 2005) investigated the impact of local phenomena on mass transfer from single bubbles and bubbles rising under swarm conditions with the bubble diameter and the viscosity as variation parameters by using quenching reaction. (Dani et al., 2007) measured oxygen concentration fields in solution in an aqueous liquid. (Stöhr et al., 2009) visualized the gas-liquid mass transfer and wake structure of rising bubbles using acid-based LIF. The technique was applied to freely rising bubbles which perform rectilinear, oscillatory or irregular motions. The resulting LIF image sequences reveal the evolution of characteristic patterns in the near and far wake of the bubbles and further allow the estimation of bubble size and rise velocity. (Kück et al., 2010, 2012) investigated the impact of local phenomena on mass transfer from single free-rising gas bubbles with and without a superimposed chemical reaction using LIF and PIV. (Jimenez et al., 2013) worked on the transferring ellipsoidal bubble and indicated the influence of the bubble diameters and liquid composition (glycerol, salt, glucose) on

the flux density. (Bouche et al., 2013) implemented an experimental study of the mixing of a passive scalar of very low diffusivity in a homogeneous swarm of inertial bubbles rising in a thin gap. The in-plane local mass of dye is measured by using a two-dye PLIF technique that has been adapted to fix the problem of multiple light reflections at the bubble interfaces. (Valiorgue et al., 2013) evaluated the influence of extinction coefficient variations on CO₂ concentration measurement for a test case in the wake of a free rising bubble. (Nagami and Saito, 2013) discussed the enhancement of the transition of the bubble motion from 2D to 3D by combining the liquid-phase motion obtained through PIV/LIF measurement and the bubble wake motion captured through the LIF method with dye HPTS, under both conditions in which the initial bubble formation and the bubble motion were considered to be the same. Considering the oxygen concentration fields appear symmetric with a 3D Gaussian profile forming a concentric, rounded gradient of oxygen with the maximum concentrations at the center of the spot. In the study of (Saito and Toriu, 2015a), the authors used experimental results from highly precise measurements of bubble volume to clarify the instantaneous mass-transfer coefficients of a zigzagging CO₂ bubble. The zigzagging motion and surface oscillation, as well as the CO₂ dissolution (mass transfer) process from the bubble to the surrounding liquid, were 3-dimensionally and simultaneously visualized, by using two high-speed cameras and mirrors and the LIF/HPTS method. Based on the similar configuration, (Huang and Saito, 2015, 2017b, 2017a) discussed the influences of gas-liquid interface contamination on the bubble motions, bubble wakes, and mass transfer process based on the reconstruction of three-dimensional bubble wakes in the purified water and contaminated water. (Timmermann et al., 2016) investigated the influence of bubble collisions on the local concentration field at well-defined conditions and the influence of a superimposed sodium sulfite reaction on the concentration field after bouncing. Using a high-speed PIV/LIF system combined with shadowgraphy, the local and temporal evolution of the CO₂ chemisorption in aqueous NaOH solution in a cylindrical bubble column is investigated (Kováts et al., 2017) and compared with the simulation result (Hlawitschka et al., 2017). Focus on the convective mass transfer

contribution, (Kong et al., 2018) used fluorescein as a dye to studying the case of a millimetric CO₂ bubble which is suspended under a substrate and dissolved into pure liquid water. Based on the reduction of the colorimetric indicator (resorufin) in presence of oxygen, (Dietrich and Hébrard, 2018) estimated the liquid-side mass transfer coefficient around a freely rising bubble and the result proved that the colorimetric technique has the potential of providing new and detailed insights into the spatiotemporal dynamics of mass transfer of rising gas bubbles. According to these studies in the literature, the techniques by using the soluble fluorescent or colorimetric dyes and optical equipment, are proved be efficient to visualize the local mass transfer from the bubble in high resolution.

3.1.2 Plane interface flows

In multi-phase unit operations, such as distillation and absorption processes in packed towers, the liquid phase often occurs as a film (0.1-1mm) on a planar surface. The visualization techniques can be used for film thickness, velocity measurements, free-surface temperature, as well as for concentration field measurements in liquids (Kapoustina et al., 2015). The method can be adapted to measurements in stagnant as well as in moving liquids on smooth and textured surfaces.

The exploratory study carried out in the last decade of the 19th century, while (Wolff and Hanratty, 1994) implemented the method based on the oxygen quenching to measure the 1D concentration profiles of oxygen in a stratified air-water flow with smooth and wavy interfaces. The oxygen quenching method was then expended to 2D measurement by (Duke and Hanratty, 1995) who studied the oxygen absorption at a wavy air-water interface. In succession, (Lee, 2002) and (Schladow et al., 2002) applied the 2D LIF technique in a deep water tank (0.6 m) to quantify the oxygen transfer driven by natural convection. The 2D spatial variations of oxygen concentration were measured instantaneously in water body. The work of (Woodrow and Duke, 2001),

which provided technical guidance for the following research, applied PLIF-I technique to the study of oxygen transfer across an unsheared flat and wave air-water interface, with employing a two-dimensional adaptive filter and a near-interface correction for optical blurring. Its optical set-up and image processing technique was adopted by (Herlina and Jirka, 2004), in whose work the interaction between oxygen absorption into liquids and bottom shear-induced turbulence was investigated in a grid-stirred tank. The LIF technique enabled visualization as well as quantification of planar concentration fields of the dissolved oxygen near the air-water interface.

Previous LIF investigations have been limited to reporting dissolved oxygen concentration profiles to within 200 μm of the air-water interface, restricting reliable results to relatively low gas flux experiments. By careful consideration of optical distortions and the design of the UV laser sheet, (Walker and Peirson, 2008) achieved reliable measurements of the dissolved oxygen profile to within 28 μm of the surface in wind-wave tank. An application of PLIF-I to a flat air-liquid interface in Hele-Shaw cell ($5*5*0.2\text{cm}^3$) was performed by (Jimenez et al., 2012b, 2012a) with a new configuration of the high-resolution optical systems. More recently, a study is carried out by (Kapoustina et al., 2015), in which the impact of a single pyramidal microstructure on mass transfer into the film flow is examined. By comparing the results to liquid film flow over a smooth surface, the enhancement of oxygen transport into liquid film flows by placing microstructures onto a plane surface was clearly visualized. (Kim et al., 2016) visualized gas diffusion process between the gas-liquid interface and measure a diffusion coefficient of dissolved oxygen in water by using a microscale UV-LED-induced phosphorescence method. The mass transfer between air and water was visualized qualitatively in a Y-shaped microchannel and the diffusion coefficient was measured quantitatively. In the study of (Lacassagne et al., 2017), the mass transfer was characterized and used to acquire simultaneous measurements of velocity and dissolved CO_2 concentration in thin sub-layer under at a flat air-water interface. A complex combination of injection and renewal events was observed on the

instantaneous concentration fields.

3.1.3 Taylor flows and confined flows

Taylor flows were widely studied due to its performances in terms of both heat and mass transfer, its regularity, stability, and operability in a large operating domain. (Dietrich et al., 2013) first proposed the colorimetric technique (with resorufin) to investigate mass-transfer in Taylor flow. A conversion from grey value maps to equivalent oxygen concentrations and mass transfer model was established, presenting the local characterization of gas-liquid mass transfer. In addition, (Yang et al., 2017a) considered the possibility of enhancement of gas-liquid mass transfer by this oxygen colorimetric reaction. With the determination of kinetics constant and diffusion coefficients by colorimetric methods, Hatta number and enhancement factor were deduced, and there is no enhancement of the gas-liquid mass transfer by this extremely fast oxygen reaction. As for the non-invasive and instantaneous advantages, (Yang et al., 2016) further investigated the mass transfer contribution of bubble formation stage to the overall process. The liquid side mass transfer coefficients at the moment right-after pinch-off stage and 14 times away from bubble inlet are obtained and compared, which demonstrates that the contribution of bubble formation stage to overall mass transfer is reasonably large. Furthermore, Yang et al. (Yang et al., 2017b) studied the mass transfer intensification in square meandering channel, illustrated in Figure 3-2. (Kováts et al., 2018) compared methylene blue and resazurin systems used in a helically-coiled tube, which shows better performance in resazurin system due to the larger difference of time constants in terms of oxidation and reduction process.

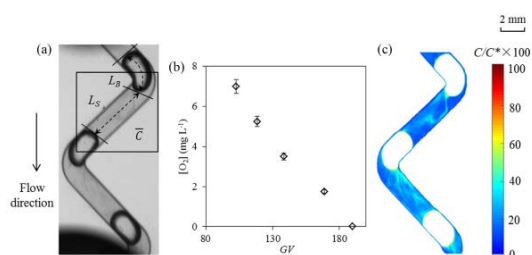


Figure 3-2. Gas-liquid mass transfer around Taylor bubbles flowing in a meandering millimetric square channel. Reproduced from (Yang et al., 2017b)

(Krieger et al., 2017) utilized leuco-indigo carmine to visualize local mass transfer and concentration distributions. Because of the existing of the anionic radical intermediate state, chemical selectivity was also investigated. Overlap of three different indigo carmine colors may result in multiple colors, shown in Figure 3-3. Therefore, the isolation of each indigo carmine in the calibration procedure is achieved by imaging processing technique and UV/Vis spectrometer methods.

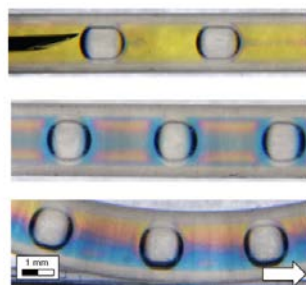


Figure 3-3. Oxidation of leuco-indigo carmine in an FEP tube with 1.6 mm inner diameter. Reproduced from (Krieger et al., 2017)

In more complicated system of the combined mass transfer process and chemical reaction, (Kastens et al., 2017) reported oxygen concentration fields and wake structures around a Taylor bubble and compared the obtained wake structures with that using PIV-LIF technique. (Butler et al., 2016, 2018) first investigated the mass transfer

of a Taylor oxygen bubble by means of PLIF-I technique and deduced the oxygen concentration based on Stern-Volmer relations by the ruthenium fluorescence intensities. By using two groups of PLIF-I images, namely O₂ and N₂ as the gas phase, they successfully corrected the scattered light by gas phase in O₂ images through N₂ images as references. They have separated mass transfer coefficients between film to bubble, film to slug and bubble cap to slug, which widens to short slugs with the contribution of liquid films.

In confined 2D Hele-Shaw cells, bubbles were largely flattened by narrow gaps and confined to move only in two degrees of freedom. Unlike the adopted method of Butler, (Bouche et al., 2013) using two fluorescent dyes (i.e., Fluorescein Sodium and Rhodamine WT) to remove the light reflections caused by the gas interface. (Alméras et al., 2016) further analyzed the fluctuations of concentration. (Roudet et al., 2017) estimated the total mass transfer rate using Sherwood number and Péclet number and compared the mass transfer rate in the films with total mass transfer. (Felis et al., 2018) investigated the oxygen mass transfer and local oxygen concentration around a rising bubble and compared the equivalent oxygen concentration obtained by resazurin with that by Cu/O₂ complexes.

3.2 Experiment under controlled conditions

In order to compare the visualization techniques, three sets of experiments are conducted to characterize the local mass transfer and the diffusion around a single air bubble rising in water by using PLIF (with fluorescent resorufin), PLIF-I (with ruthenium complex), and colorimetric techniques (with pink resorufin), respectively. As presented in Chapter 2, the experimental setup for three techniques is basically the same except that the colorimetric technique does not need the laser.

All the experiments are carried out under the controlled conditions, i.e. with the same

needle (~ 0.7 mm of inner diameter) and same flow rate ($2 \mu\text{m}\cdot\text{h}^{-1}$) for bubble injection, at 293.15K of temperature and under atmospheric pressure. The injected bubbles have good reproducibility with the bubble size (~ 1 mm), shape (ellipsoidal) and trajectory (linear) that we can assume that each of the single bubbles examined is identical. The details of the materials and property of the bubbles in the experiments are given in Table 3-1.

It should be noticed that the presence of the dye brings a small impact on the fluid property. Especially for cases with resazurin, the extra chemical (NaOH and Glucose) will increase a bit the viscosity of the liquid compared with the measured result in pure water (see Chapter 2)

Table 3-1 Materials and property of the bubble for comparison of three techniques

	PLIF-I	PLIF	Colorimetric
Liquid-Gas	Deionized water + Air bubble		
Dye	Ruthenium Complex 75 mg/L	Resazurin 100 mg/L (+ NaOH 20 g/L+ Glucose 20 g/L)	
σ [mN·m ⁻¹]	72	75	
ρ [kg·m ⁻³]	1000	1004	
μ [mPa·s]	1.003	1.100	
Diameter of bubble	1.25 ± 0.04 mm		
Ratio aspect of bubble	1.13 ± 0.02		
Velocity of bubble	295 ± 10 mm/s		
Re	368 ± 20		

3.3 Visualization result

With the experimental configuration displayed in Chapter 2, the mass transfer in the wake of the bubble can be visualized from two directions: side view and bottom view (see Figure 3-4).

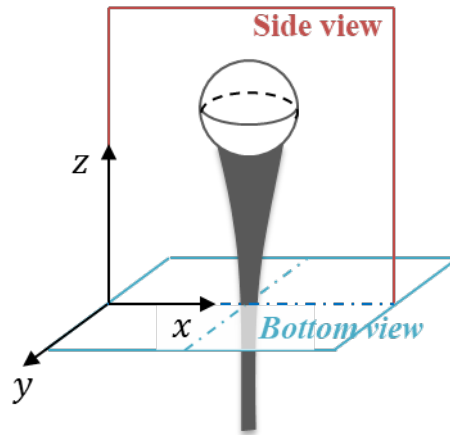


Figure 3-4 Recorded images of side view and bottom view

3.3.1 Image of side view

The images recorded by different visualization techniques from the side view are shown in Figure 3-5.

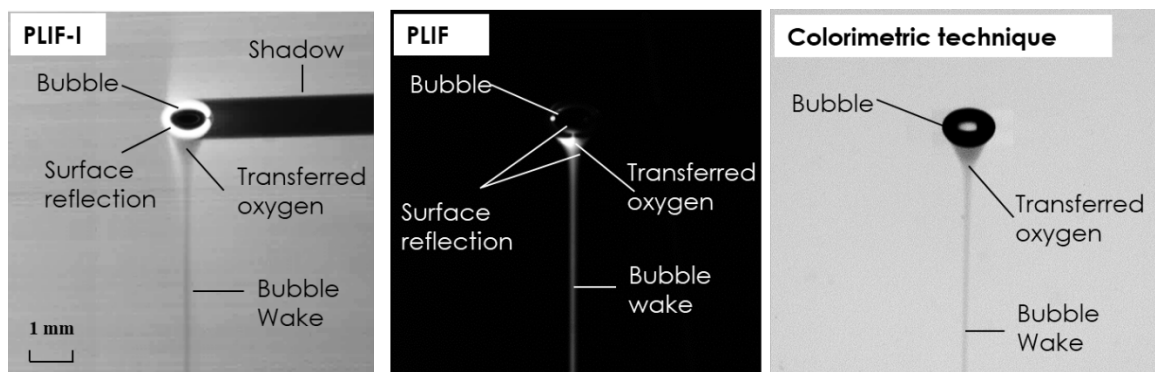


Figure 3-5 Recorded images by different visualization techniques (Side view)

On the image by PLIF-I and the colorimetric technique, the mass transfer zone is dark in a bright background which is contrary to the images by PLIF. Some observation can be obtained:

(1) For the side view, the images by the laser techniques (either PLIF or PLIF-I) suffer the reflection problem around the bubble surface.

(2) A white ring around the bubble interface is visualized as well as the bubble shadow on the PLIF-I image. That makes the boundary of the bubble difficult to recognize. Moreover, the reflection also has an impact on the mass transfer area near the bubble surface, especially for the part facing the laser (left part on the image). Along the laser direction, the effect is reducing but still cannot be neglected.

(3) For the PLIF image, the fluorescence effect is quite strong that the light around the bubble surface is relatively weaker than that in the bubble wake. The reflection exists at the transfer interface making the recorded gray level in this area much higher than the real value induce.

(4) On the other hand, the local mass transfer by the colorimetric technique is quite clear without the reflection issue. This property makes the colorimetric suitable for tracking the mass transfer even near the gas-liquid interface.

(5) Far from the bubble surface, all of the three methods can visualize the mass transfer properly.

Due to the reflection problem of the laser techniques, there is a lack of information near the bubble surface thus it is difficult to precisely quantify the mass transfer with images of the side view. On the contrary, without the reflection problem, the colorimetric technique can be used to calculate the mass transfer coefficient (Dietrich and Hébrard, 2018).

3.3.2 Image of bottom view

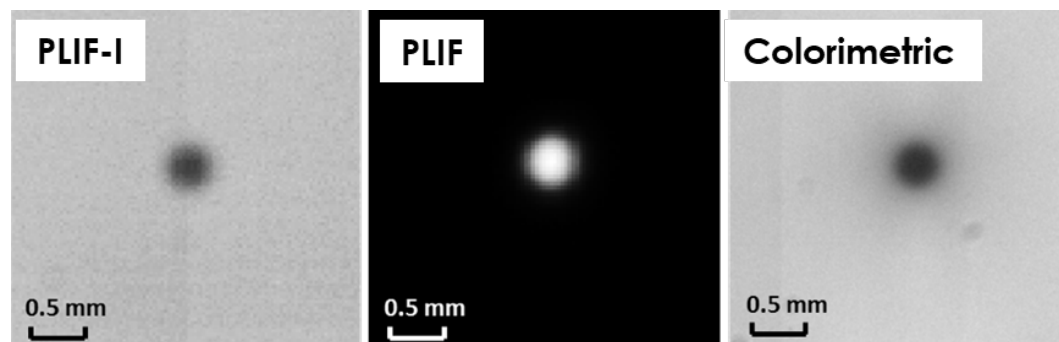


Figure 3-6 Recorded images by different visualization techniques (bottom view)

To avoid the reflection around the bubble caused by the laser flash, the camera is put under the column to record the mass transfer in one cross-section of the bubble wake far from the passed bubble. From the bottom view, there is a good contrast between the mass transfer 'spot' and the background. The transferred mass (dissolved oxygen) concentrates at the spot center and becomes dispersed near the boundary of the spot. Among the three images, the quality of the one by PLIF seems better with the clear background (totally black) due to the aforementioned different indicated color of the mass transfer (white). The mass transfer can be quantified with the images of bottom view for all the three techniques.

3.4 Quantification of mass transfer

3.4.1 Calibration result

The relationship between the real oxygen concentration and the recorded gray level on the images are established by the calibration process (see Chapter 2). The examples of the calibration results for the three techniques are shown in Figure 3-7. It can be seen that all of the three curves represent monotonic functions leading to a reasonable calculation of the oxygen concentration. Among the three curves, the one for PLIF is

linear that the gray level increases with higher oxygen concentration. For the other two curves (PLIF-I and colorimetric technique), the gray levels go downward sharply showing that the dye is sensitive for lower oxygen concentration ($[O_2] < 4 \text{ mg}\cdot\text{L}^{-1}$) but when the oxygen concentration gets higher, the variation of the gray level is relatively small. In most of our study, the oxygen concentration in the bubble wake is small within a reasonable calibration range.

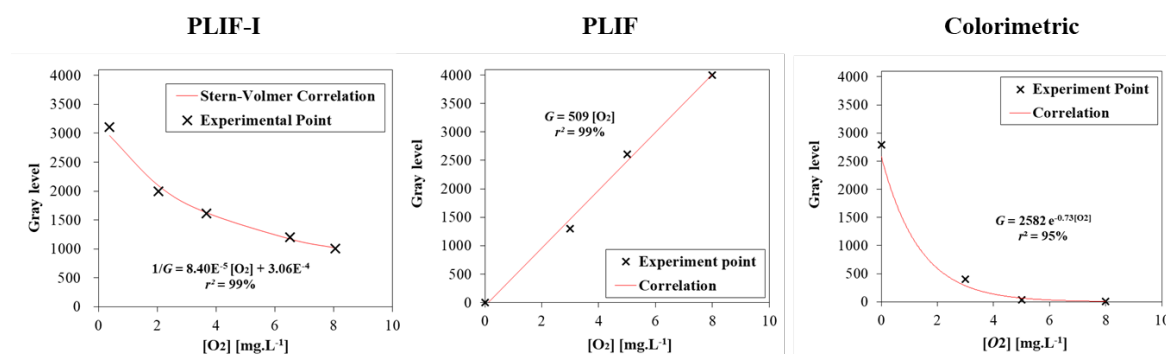


Figure 3-7 Examples of calibration result for three visualization techniques (PLIF-I, PLIF, and colorimetric technique).

Regarding the sensitivity of calibration, when dissolved oxygen concentration varies from 0 mg to 8 mg·L⁻¹, the change of grey level for the three techniques (PLIF-I, PLIF, Colorimetric technique) are 2000, 4000 and 2500 levels. Under our investigated configuration, the resorufin is more sensitive to the oxygen concentration when used as a fluorescent dye than when used as a colorimetric dye and also better than cases by the ruthenium complex. This property leads to better contrast between the mass transfer and the background which discussed in following sections.

In addition, the calibration curve of the colorimetric technique is not linear which is different from the result carried out in the microchannel (Yang et al., 2016). That is because while the camera takes images from the bottom of the column, the thickness of the image area is no longer negligible. The calibration in our case is actually implemented for a volume instead of a thin plan, thus the Beer–Lambert absorption will decrease the gray level especially for the solution with high concentration of the dye.

With the calibration curve, the gray level is converted to the oxygen concentration, and the concentration field of the dissolved oxygen in the bubble wake is plotted in Figure 3-8. It can be seen that the noise of the background on the PLIF image is less significant compared with the other two images, which is consistent with the result from the side view in Figure 3-6. The noise of the background on PLIF-I image is relatively significant that it needs a large threshold (defined in Chapter 2) for PLIF-I to eliminate the noise impact from the background.

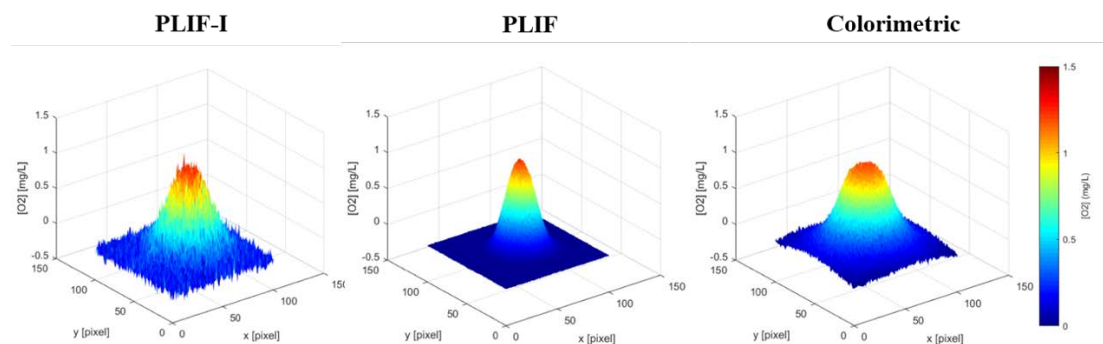


Figure 3-8 Examples of concentration field of the dissolved oxygen in bubble wake at the same moment (bottom view).

Different from the result by PLIF and PLIF-I technique, the background concentration is much higher than zero for the result by the colorimetric technique. It should be noticed that the gray level (mass transfer) recorded on the images by these three techniques are not exactly the same (see Figure 3-9). Since only a slice plane is lightened by the laser sheet, the results by PLIF and PLIF-I display exactly the mass transfer in the concerning cross-section. For colorimetric technique, the whole column is illuminated by the backlight thus the camera not only records the information in the focal plane but also the front and the rear ones due to the depth of field of the camera. Its results refer to the superposition of the mass transfer in a series of continuous cross sections. It thus probably brings the deviation to the mass transfer estimation.

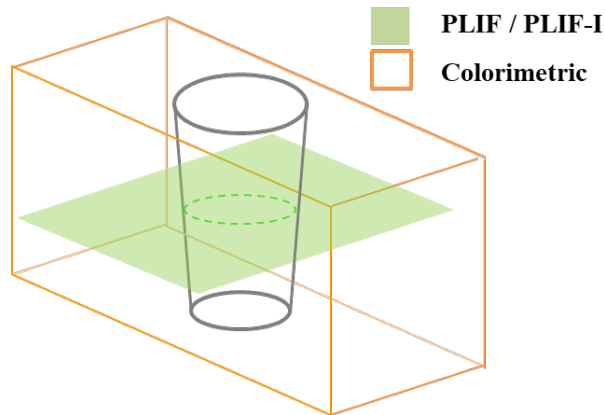


Figure 3-9 Image composition of mass transfer in bubble wake

3.4.2 Mass flux

After the image processing, the background noise is removed and the image quality is improved. The corrected images of the oxygen field then are fitted with the 2D Gaussian equation (See Section 2.5.2.4). The results are shown in Figure 3-10.

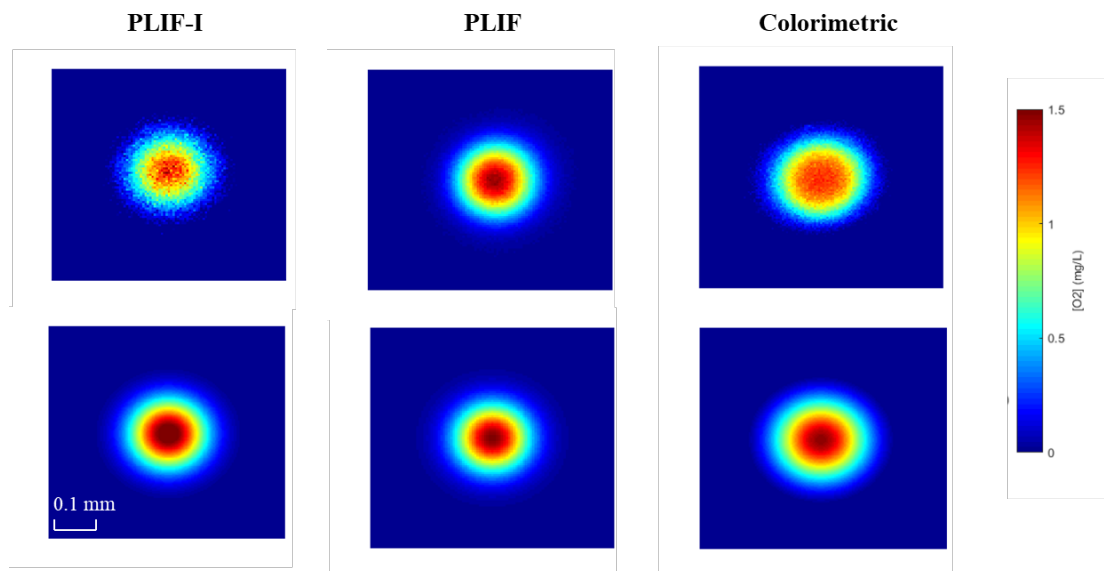


Figure 3-10 Corrected images (top) and fitted images (bottom) of the concentration field of the dissolved oxygen in bubble wake.

The fitting errors for all the three techniques are within 5% validating the fitting Gaussian equation. By summing the oxygen concentration in each pixel of the image area (Section 2.5.4), the fluxes before and after the fitting are given in Table 3-2. The PLIF technique has the best fitting result regarding its good quality of the raw images.

Table 3-2 Result of fluxes before and after fitting for the three techniques

	Flux before fitting [mg·s ⁻¹ ·m ⁻²]	Flux after fitting [mg·s ⁻¹ ·m ⁻²]	Fitting error [%]
PLIF-I	3.53 ± 0.10	3.70	< 5%
PLIF	3.43 ± 0.03	3.45	< 1%
colorimetric	3.35 ± 0.08	3.45	< 3%

The oxygen concentration field in the bubble wake is obtained for each recording moment (every 1/15 second), the temporal evolution of the mass flux can be obtained. The result is shown in Figure 3-11. As introduced in Chapter 2, for a small bubble with linear trajectory, the mass transfer in the bubble wake far from the passed bubble is dominated by diffusion since the vertical convection induced by the bubble can be neglected. The mass transfer executes a two-dimensional diffusion that means the total flux on the image should be conservative as a function of time.

It can be seen that after the variation for the first several images due to the convection of the bubble, the fluxes measured by the three techniques tend to be constant versus time. For PLIF and colorimetric cases, the fluxes are basically stable but the total flux is a bit smaller than the one by PLIF-I. This flux decrease may be related to the presence of the extra chemicals (NaOH and Glucose) which brings the impact on the liquid properties (Table 3-1).

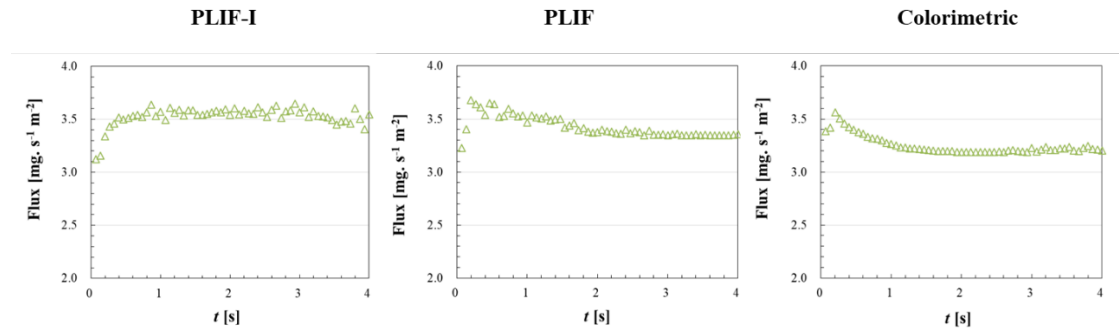


Figure 3-11 Mass flux versus time measured by different techniques (PLIF-I, PLIF, Colorimetric).

3.4.3 Diffusion coefficient

If we plot the fitted oxygen concentration along a line passing the spot center, we can see the distribution of the oxygen concentration has a Gaussian profile. Based on this temporal evaluation of the oxygen profile in the bubble wake, we can characterize the diffusion process (see Figure 3-12). It can be seen that the dissolved oxygen is concentrated on the spot center then is diffusing gradually to the surrounding to make the concentration on the area more homogeneous.

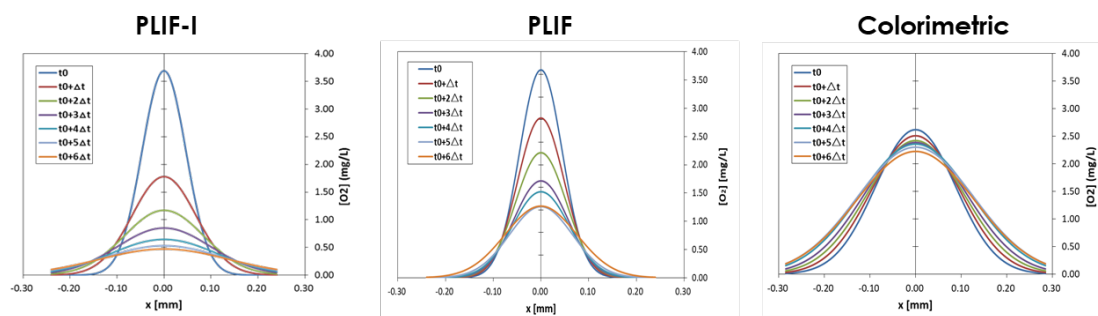


Figure 3-12 Temporal evolution of the O₂ concentration field at the cross section of bubble wake (left to right: result by PLIF-I, result by PLIF, result by colorimetric, respectively. $\Delta t = 0.67s$)

With the method introduced in Chapter 2, the area of the mass transfer spot expands as a function of time with a rate related to the diffusion coefficient ($\eta = 1$):

$$S_{spot} = \pi R^2 = 2\pi Dt \quad (3-1)$$

The evolution of the spot area for the three techniques is plotted in Figure 3-13. For all the three techniques, the curves of S_{spot} have a good linearity versus time so the diffusion coefficient can be calculated with the slope of the curve.

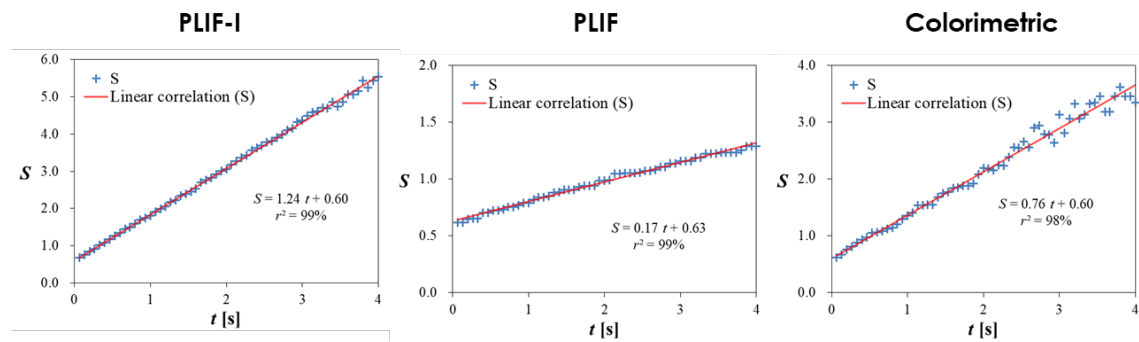


Figure 3-13 Evolution of the spot area as a function of time

Table 3-3 Result of the diffusion coefficient for the three techniques

	Slope of $S_{spot} - t$	r^2	D [$\times 10^{-9} \text{ m}^2 \cdot \text{s}^{-1}$]
PLIF-I	1.24	99%	1.97
PLIF	0.17	99%	0.27
colorimetric	0.76	98%	1.20

The diffusion coefficient for PLIF-I, PLIF and colorimetric are $2 \times 10^{-9} \text{ m}^2 \cdot \text{s}^{-1}$, $0.27 \times 10^{-9} \text{ m}^2 \cdot \text{s}^{-1}$, and $1.20 \times 10^{-9} \text{ m}^2 \cdot \text{s}^{-1}$, respectively. In view of the aforementioned technical problem, the PLIF with resazurin and colorimetric technique have distortion on diffusion coefficient estimation. The reason is that these two techniques are based on the tracking of a different molecule (resorufin) and not oxygen. The mathematical

approach is based on the conservative flux (see Section 2) which may also bring the error for the result by PLIF with resazurin and colorimetric technique. In contrast, the result by PLIF-I is consistent with the literature (Kück et al., 2010), proving more accurate for the quantification of the diffusion.

3.4.4 Mass transfer coefficient

With the fluxes obtained from the images (Section 3.4.3), the mass transfer coefficient can be estimated by dividing the driving force from the flux J_{O_2} . In our cases, the saturated concentration $[O_2]^*$ is closed to $9 \text{ mg}\cdot\text{L}^{-1}$. For PLIF-I technique, the bulk concentration $[O_2]_0$ is $0.2 \text{ mg}\cdot\text{L}^{-1}$ measured after the deoxygenation of the liquid. For the technique with resazurin (PLIF and colorimetric technique), the oxygen is totally consumed or reacted before the experiment, so the $[O_2]_0$ is supposed to be $0 \text{ mg}\cdot\text{L}^{-1}$.

$$k_L = \frac{J_{O_2}}{[O_2]^* - [O_2]_0} \quad (3-2)$$

The result of the mass transfer coefficients are given in Table 3-4. Regarding the underestimated flux, the value determined by PLIF and colorimetric technique with resazurin is a bit smaller than that of by PLIF-I. Despite this, all the values are consistent with the literature (Roustan, 2003) indicating all these three techniques can be used for quantifying the mass transfer.

Table 3-4 Result of mass transfer coefficient by the three techniques

	k_L [$\times 10^{-4} \text{ m}\cdot\text{s}^{-1}$]
PLIF-I	4.01 ± 0.010
PLIF	3.81 ± 0.005
Colorimetric	3.61 ± 0.008

3.5 Summary of advantage and limitation

The advantage and limitation of each technique are summarized in the following table. All three techniques can be used for tracking the mass transfer to some extent. When resorufin (from resazurin) used as a pink dye, the colorimetric technique can even visualize the mass transfer near the bubble surface. When it is used as a fluorescent dye, the image by PLIF technique have good contrast between the mass transfer area and pure black background. This property makes the resorufin useful for the visualization of the mass transfer in a more complex structure that is induced by bigger bubbles (Figure 3-14).

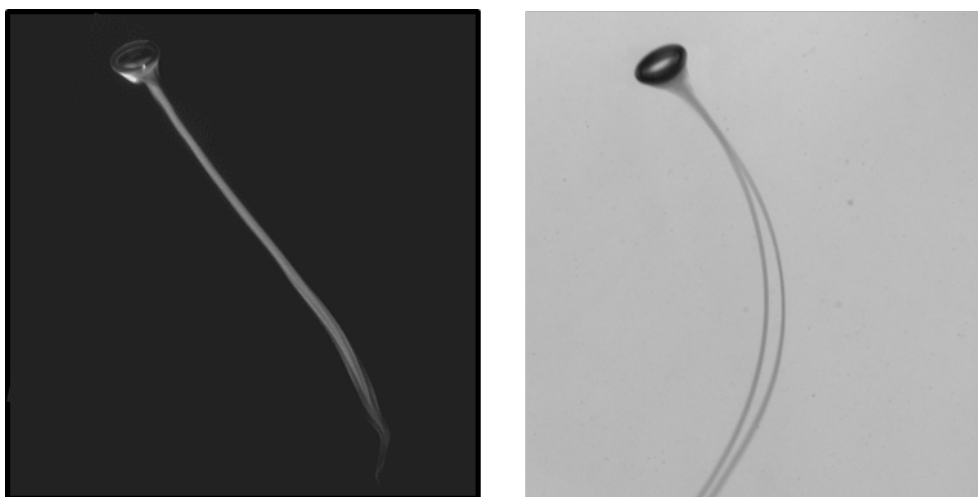


Figure 3-14 Visualisation result with resorufin as a dye for bigger bubble ($D_{eq} \sim 3$ mm). Left: image by PLIF; Right: image by colorimetric technique.

For the quantification of the mass transfer, PLIF-I technique can give a reasonable result for diffusion coefficient and mass transfer coefficient while the other two technique with resazurin cannot correctly characterize the diffusion process due to the reaction mechanism. Another limitation for the PLIF and colorimetric technique is that the oxygen indicator resazurin should be used together with extra chemical (NaOH and glucose) which will bring impact on the investigated fluid. Except in the water case, the impact is still not clear in other liquid media. For the above reason, the PLIF-I

technique is selected for the following study to characterize the mass transfer in polymer solutions (Chapter 5).

Table 3-5 Advantage and limitation of three techniques (PLIF-I, PLIF, colorimetric technique)

	Advantage <input checked="" type="checkbox"/> and limitation <input checked="" type="checkbox"/>
PLIF-I	<ul style="list-style-type: none"> <input checked="" type="checkbox"/> Track mass transfer in the wake far from the surface <input checked="" type="checkbox"/> Accurate quantification of flow flux <input checked="" type="checkbox"/> Characterize the diffusion <input checked="" type="checkbox"/> Reflection at the bubble surface <input checked="" type="checkbox"/> Significant noise in the background <input checked="" type="checkbox"/> Shadow of the bubble
PLIF	<ul style="list-style-type: none"> <input checked="" type="checkbox"/> Track mass transfer in the wake far from the surface <input checked="" type="checkbox"/> Less noise in the background <input checked="" type="checkbox"/> Cannot characterize the diffusion of oxygen <input checked="" type="checkbox"/> Reflection at the bubble surface <input checked="" type="checkbox"/> Extra chemical
Colorimetric technique	<ul style="list-style-type: none"> <input checked="" type="checkbox"/> Track mass transfer even near the bubble <input checked="" type="checkbox"/> No reflection near the bubble <input checked="" type="checkbox"/> Cannot characterize the diffusion of oxygen <input checked="" type="checkbox"/> Complex composition of the recorded image <input checked="" type="checkbox"/> Extra chemical

3.6 Conclusion

Three different visualization techniques PLIF-I (with ruthenium complex), (PLIF (with fluorescent resorufin), and colorimetric techniques (with pink resorufin)) are compared focusing on their application to characterize the mass transfer around a single bubble

rising in water. The PLIF and colorimetric technique with resazurin are both effective for tracking the local mass transfer. However, under our investigated condition, there is a small distortion to quantify the oxygen transferred fluxes by these two techniques due to the presence of the extra chemicals (NaOH and Glucose). Moreover, they cannot be used to quantify oxygen diffusive process as oxygen is consumed. Actually, these two techniques are based on the tracking of a different molecule (resorufin) instead of the oxygen molecule. Concerning the colorimetric technique, it is also less precise due to that its image contains the mass transfer not only on the target cross-section but also on the lower and the upper ones. Regardless of the relatively rigorous treatment to remove the noise in the image background, PLIF-I is more accurate for the quantification of the diffusion coefficient and mass transfer coefficient. For the above reason, the PLIF-I technique is selected for the following study to characterize the mass transfer in polymer solutions. This chapter provides a guideline for choosing a visualization technique to accurately visualize and characterize the local mass transfer in gas-liquid systems for measuring a flux or a diffusion coefficient.

Chapter 4

Hydrodynamics of the Bubble: Characterization of bubble shapes by parametric equations

Abstract

The bubble-liquid mass transfer is closely related to the bubble rising velocity and the bubble shape which affects the interfacial area for the mass transfer. An investigation on the bubble hydrodynamics is thus important. In this chapter, based on the experiment of single air bubbles (with equivalent diameters: 0.7-7 mm) rising in the polymer solutions (PAAm and Xanthan), the hydrodynamics of the bubble are investigated including the bubble velocity, trajectory and bubble shape. The discussion will focus on the bubble shape. An innovative model containing the aspect ratio (E) and two parameters (α, β) is proposed and proved to be capable of characterizing the bubble shape from spherical/ellipsoidal to prolate/oblate-tear with good accuracy. Several impacts on bubble deformation are then investigated involving the rheological properties of the fluids and different forces exerted on the bubble which is quantified by multiple dimensionless numbers (e.g. Reynolds number, Eötvös Number, Deborah number). Within a wide range ($-9 < \log Mo < 3$, Mo : Morton number), the empirical correlations are obtained for the aspect ratio and the bubble shape parameters. Together with the shape model, a complete system is set up for bubble shape characterization and prediction that will provide new ideas for future studies on bubble hydrodynamics.

4.1 State of the art

4.1.1 Bubble shape

Gas bubbles rising in acquiescent liquids are widespread in industries such as oil extraction, wastewater treatment, and bioreactors. For these applications, the knowledge of bubble shape is important since it is directly related to hydrodynamic behavior (e.g. terminal velocity, drag, surface area) and can influence the mixing level and the efficiency of energy, mass, and momentum transfer.

The observed shapes of individual bubbles in free motion in Newtonian fluids have been well investigated and can be divided mainly into three categories: spherical, ellipsoidal, and spherical-cap or ellipsoidal-cap (Chhabra, 2006). In the absence of wall effects, it is generally agreed that the shape of a freely rising bubble in a stagnant liquid are dominated by buoyancy, inertial force, surface tension, viscous force and the physical properties of the continuous phase (Clift et al., 1978), which are governed by the magnitudes of the dimensionless numbers (listed in Table 4-1). The dimensionless numbers in Table 4-1 are defined in a simplified form assuming that the mass density of the liquid is far greater than that of gas in a bubble-liquid system. In fluid mechanics, Re gives a measure of the ratio of inertial forces to viscous forces and consequently quantifies the relative importance of these two types of forces for given flow conditions. On the other hand, We is often useful in analyzing fluid flows where there is an interface between two different fluids, especially for multiphase flows such as bubble rise in liquids. It can be thought of as a measure of the relative importance of the fluid's inertia compared to its surface tension. The quantity is useful in analyzing the formation of droplets and bubbles. The Morton number Mo , is also used together with the Eötvös number (Eo) to characterize the shape of bubbles or drops moving in a surrounding fluid or continuous phase.

Table 4-1 Dimensionless numbers for bubble shape characterization

Eötvös Number	$Eo = \frac{\rho g D_{eq}^2}{\sigma}$	$\frac{\text{Buoyancy}}{\text{Surface tension}}$
Reynolds Number	$Re = \frac{\rho U D_{eq}}{\mu}$	$\frac{\text{Inertia}}{\text{Viscous Force}}$
Weber Number	$We = \frac{\rho U^2 D_{eq}}{\sigma}$	$\frac{\text{Inertia}}{\text{Surface tension}}$
Morton Number	$Mo = \frac{g \mu^4}{\rho \sigma^3}$	Fluid properties
Tadaki Number	$Ta = Re \cdot Mo^{0.23}$	/

(Grace et al., 1976) have proposed a generalized graphical correlation or the so-called “Grace diagram” (see Figure 4-1) that delineates the shapes of bubbles in Newtonian fluids, which provides a guideline for the further studies on the bubble shape (Anwar, 2013; Hua et al., 2008; Yu et al., 2011).

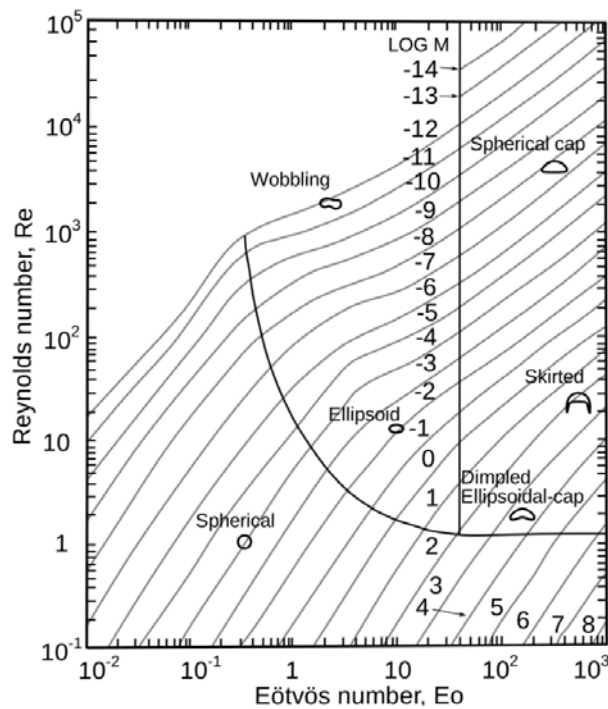


Figure 4-1 Grace Diagram: Shape regimes for bubbles and drops in unhindered gravitational motion through liquids. Image from (Clift et al., 1978).

On the other hand, although numerous studies deal with bubbles rising in non-

Newtonian media, only a few of them have discussed and analyzed the bubble shape. (Böhm et al., 2014; Frank et al., 2003, 2012; Hassan et al., 2007, 2010; Zhang et al., 2010). It is generally agreed that non-Newtonian fluids have complex rheological properties (e.g. shear thinning, viscoelasticity, etc.) leading to a variety of bubble shapes, such as teardrop or elongate bubbles (Dekée and Chhabra, 1988; Dekée et al., 1986; Funfschilling and Li, 2006).

To quantitatively characterize the bubble shape, many researchers used the aspect ratio or eccentricity i.e. the ratio between the lengths of the major and minor axes of the bubbles. Some related research and correlations found in the last decade are listed in Table 4-2. Pioneering work by (Moore, 1959) and (Tadaki and Maeda, 1961) theoretically correlated the aspect ratio of the bubble with the Weber number and original Tadaki number ($Ta = Re.Mo^{0.23}$), respectively. Their correlation were modified and improved for small inertial effects (Taylor and Acrivos, 1964) and became applicable to clean and contaminated bubbles (Fan and Tsuchiya, 1990; Vakhrushev and Efremov, 1970; Wellek et al., 1966) for a large range of Morton numbers (Raymond and Rosant, 2000). More recently, many researchers have begun to realize that, for fluids with high viscosity, no single dimensionless number (Eo , We , or Ta number) is suitable to predict the bubble deformation. Therefore, more dimensionless numbers have been used and many empirical models have been built to fit the results of the new experiments or numerical simulations (Kelbaliyev and Ceylan, 2007; Legendre et al., 2012; Raymond and Rosant, 2000; Sugihara et al., 2007). For instance, (Liu et al., 2015) suggested that, in highly viscous fluids, the bubble shape is dramatically affected by the viscosity and the effects of We number should be considered along with Re number. However, the aspect ratio suffers from the shortcoming of being unable to characterize the details of shape or irregular forms (e.g. a cap bubble and an ellipsoidal bubble would have the same aspect ratio). A few researchers have tried to use other parameters to characterize the bubble deformation. (Myint et al., 2007) introduced a distortion factor to quantify the asymmetry between the upper and lower parts of the bubble divided by the major axis. Another study, by Yan and Zhao (Yan and Zhao, 2016), used the bubble

circularity, defined as the ratio of the circumference of an equivalent circle to that of the real bubble projection. Although some valuable conclusions have been drawn from the previous work, most of the expressions mentioned above could only handle quasi-ellipsoidal bubbles. For a bubble with a more complicated contour (e.g. cap, teardrop), it is clear that neither the ratio aspect nor the circularity can properly capture or predict the bubble shape.

Table 4-2. Bibliography of bubble shape characterization

AUTHOR	LIQUID	SHAPE	CORRELATION
(Tadaki and Maeda, 1961)	Sodium chloride/glycerol aqueous solution	Spherical Ellipsoidal Cap	$E^{-\frac{1}{3}} = \begin{cases} 1 & Ta < 2 \\ 1.14Ta^{-0.176} & 2 < Ta < 6 \\ 1.36Ta^{-0.28} & 6 < Ta < 16.5 \\ 0.62 & 16.5 < Ta \end{cases}$ $Ta = Re \cdot Mo^{0.23}$
(Sugihara et al., 2007)	Water	Spherical Ellipsoidal	$E = 1 + \frac{9}{64}We + \frac{0.04We^2}{(3.7 - We)^{0.5}}$
(Myint et al., 2007)	Glycerol aqueous solution	Spherical Ellipsoidal Cap	$E = \frac{1}{1 - 0.0487Ta - 0.0289Ta^2}$ $\gamma = 0.957 + 0.008Eo + 0.002Eo^2$ $\gamma = \frac{2b_2}{b_1 + b_2} \quad Ta = Re \cdot Mo^{0.23}$ <p>b_1, b_2 : distances from the major axis to the bottom and the top of the shape, respectively</p>
(Kelbaliyev and Ceylan, 2007)	Glycerol aqueous solution	Spherical Ellipsoidal	$E = \frac{1 + \frac{\lambda_v}{2}We}{1 - \lambda_v We}$ $\lambda_v = \frac{1}{12} \left(1 - \frac{3}{25} \frac{We}{Re} \right)$ $1.1 \times 10^{-5} < Mo < 7$
(Dong et al., 2010)	Ionic liquids (Newtonian fluids)	Ellipsoidal	$E = 1 + 0.0184 \times (Re \cdot Eo)^{0.671}$

(Li, 2011)	CMC	Spherical Ellipsoidal Prolate Cap	$E = 0.9585 + 0.0357Wn^{0.8958}$ $Wn = We \cdot Eo \cdot n$
(Legendre et al., 2012)	Glycerol aqueous solution	Spherical Ellipsoidal Cap	$E = \frac{1}{1 - \frac{9}{64} \left[\frac{We}{1 + 0.2Mo^{0.1}We} \right]}$ $4.6 \times 10^{-6} < Mo < 7$
(Liu et al., 2015)	Glycerol aqueous solution	Spherical Ellipsoidal Skirted	$E = 0.9914 + 0.1147 \times Re^{0.3841} \times We^{0.5678}$
(Yan and Zhao, 2016)	Glycerol aqueous solution	Spherical Ellipsoidal Cap	$C = 4\pi S/P^2$ $\sqrt{C} = \frac{1}{0.9943 + 0.0007 \times Re^{0.6626} \times We^{0.1197}}$ $1 < Re < 3041, 0.0002 < We < 8.6$
(Aoyama et al., 2016)	Glycerol aqueous solution	Spherical Ellipsoidal	$E = [1 + 0.016 \times Eo^{1.12} \times Re]^{0.388}$ $0.0032 < Re < 130, 0.042 < We < 29$

Therefore, in this chapter, a new model using the parametric equations is proposed to directly depict the complete outline or profile of the bubble. Experiments will be implemented to study individual air bubbles of different sizes (D_{eq} : 0.7-7 mm) rising in stagnant non-Newtonian fluids (aqueous solution of PAAm or Xanthan gum) by means of high-speed photography and image post-processing technologies. The objective mainly aims to investigate the overall impact (including the different dimensionless numbers and the rheological properties of the fluid) on the bubble shape.

4.1.2 Bubble velocity and drag coefficient

The velocity of the bubble rising in a fluid is one of the most fundamental and important issues in multiphase flow problems. The bubble velocity not only affects the residence time of the bubble in the liquid phase but also affects the interaction between the

bubbles and the turbulence characteristics of the liquid phase around the bubble, thereby affecting the transfer process between phases and the performance of the device.

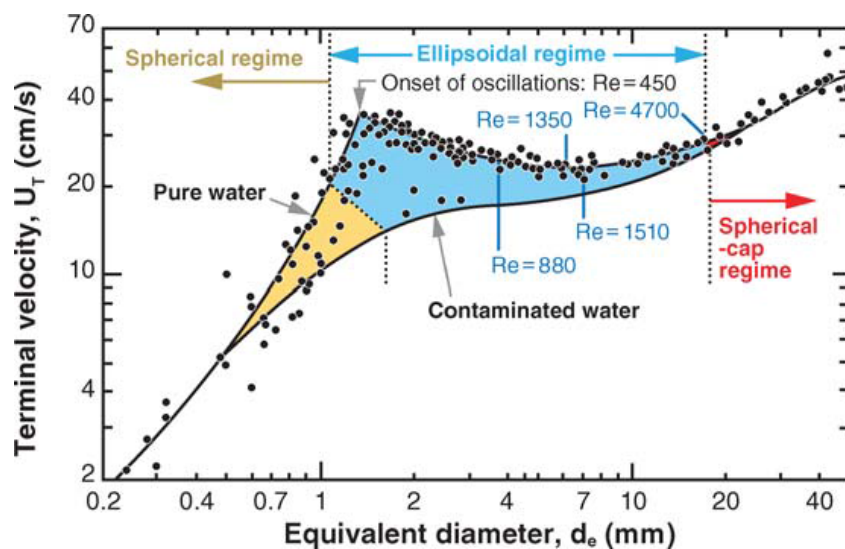


Figure 4-2 Bubble terminal velocity in clean water (293.15 K) and contaminated water as a function of the bubble equivalent diameter. Image reproduced by (Guet and Ooms, 2006) from the (Clift et al., 1978).

Experimental results on the rise velocity of single bubbles in an infinite medium of water have been collected from various experimental studies in (Clift et al., 1978) (Figure 4-2). Because gravity is the dominant force for large bubbles, the bubble terminal velocity increases with the equivalent diameter of the bubble. The terminal velocities in clean and contaminated liquids are different for a given equivalent bubble diameter. This is due to the changes in bubble shape with the contamination level, which in turn affects the equivalent drag-force coefficient (Guet and Ooms, 2006; Tomiyama et al., 2002).

The drag coefficient is a dimensionless number that quantifies the drag or resistance of an object in a fluid environment and can be used to indirectly indicate the velocity of the bubble. The drag coefficient is defined as:

$$C_D = \frac{2F_d}{\rho_L \cdot U^2 S_{ref}} \quad (4-1)$$

Where

- F_d is the drag force, which is by definition the force component in the direction of the flow velocity [N];
- ρ_L is the density of the fluid [$\text{kg} \cdot \text{m}^{-3}$];
- U is the flow speed of the object relative to the fluid [$\text{m} \cdot \text{s}^{-1}$]
- S_{ref} is the reference area [m^2]; For a bubble S_{ref} equals to the projection area of a cross section perpendicular to the bubble moving direction.

When the bubble rises freely in the liquid and reaches a steady state, the buoyancy and drag force on the bubble should be equal. According to the force balance:

$$(\rho_L - \rho_G)g \cdot V = \frac{1}{2} C_D \cdot \rho_L \cdot U^2 S_{ref} \quad (4-2)$$

With V the volume of the bubble and ρ_G the density of the gas. Supposing $\rho_L \gg \rho_G$, the drag coefficient has a form as:

$$C_D = \frac{1}{3} \frac{\pi \cdot g \cdot D_{eq}^3}{U^2 S_{ref}} \quad (4-3)$$

In particular, for a spherical bubble of diameter D_{eq} , $S_{ref} = \frac{1}{4} \pi \cdot D_{eq}^2$ and the drag coefficient equals:

$$C_D = \frac{4}{3} \frac{g \cdot D_{eq}}{U^2} \quad (4-4)$$

Simultaneously, the bubble reaches its terminal velocity:

$$U = \sqrt{\frac{4}{3} \frac{g D_{eq}}{C_D}} \quad (4-5)$$

Hence, the terminal bubble velocity is an increasing function of the bubble diameter and decreases with the increase of the bubble drag coefficient.

The early expression of the drag coefficient is mainly derived by theoretical derivation. Hadamard and Rybczynski deduced the drag coefficient for creeping flow (or Stokes flow, $Re \ll 1$) (Hadamard, 1911). Because the Reynolds number is low, they ignore

the inertial force and obtains the expression of the drag coefficient on the Reynolds number:

$$C_D = \frac{8}{Re} \left(\frac{2+3\frac{\mu_g}{\mu_l}}{1+\frac{\mu_g}{\mu_l}} \right) \quad (4-6)$$

If the gas viscosity μ_l is much higher than μ_g , the equation can be simplified to:

$$C_D = \frac{16}{Re} \quad (4-7)$$

Based on Hadamard's model, (Mei et al., 1994) proposed a drag coefficient correlation with a wider range of Reynolds numbers ($1 < Re < 200$).

$$C_D = \frac{16}{Re} \left(1 + \frac{Re}{8+0.5(Re+3.315Re^{0.5})} \right) \quad (4-8)$$

Many following researchers have used theoretical derivation or semi-empirical correlation to obtain many dimensionless calculations for drag coefficients (Kelbaliyev and Ceylan, 2007; Li et al., 2012; Rodrigue, 2001, 2002, 2004; Sun et al., 2015; Yan et al., 2017; Zhang et al., 2008). Some of these correlations are summarized in Table 4-3.

Table 4-3 Summary of correlations on the drag coefficient of the gas bubble moving in a quiescent liquid.

Author	Correlation	Validated range	Studied solutions
(Hadamard, 1911)	$C_D \approx \frac{16}{Re}$	$Re \ll 1$	Newtonian fluids
(Mei et al., 1994)	$C_D = \frac{16}{Re} \left(1 + \frac{Re}{8 + 0.5(Re + 3.315Re^{0.5})} \right)$	$1 < Re < 200$	Newtonian fluids
(Dewsbury et al., 1999)	$C_D = \frac{16}{Re} (1 + 0.173Re^{0.657}) + \frac{0.413}{1 + 16300Re^{-1.09}}$	$10^{-1} < Re < 10^3$	CMC
(Margaritis et al., 1999)	$C_D = \frac{16}{Re} (1 + 0.173Re^{0.657}) + \frac{0.413}{1 + 16300Re^{-1.09}}$ $C_D = 0.95$	$Re < 60$ $Re > 60$	Various polysaccharidesin solution

(Rodrigue, 2001)	$C_D = \frac{16}{Re} [1 + 0.018 (\frac{3}{4} C_D Re^2)^{8/9} Mo^{1/9}]^{3/4}$	$10^{-2} < Re < 10^4$	Various viscous fluids
(Kelbaliyev and Ceylan, 2007)	$C_D = \frac{8}{Re} [1 + \frac{1}{1 - 0.5(1 + 250Re^5)^{-2}}]$ $C_D = \frac{16}{Re} [1 + (\frac{Re}{1.385})^{12}]^{1/55} + \frac{8}{3} \frac{Re^{4/3} Mo^{1/3}}{24(1 + Mo^{1/3}) + Re^{4/3} Mo^{1/3}}$	$0.1 < Re < 0.5$ $Re > 0.5$	Various viscous fluids
(Zhang et al., 2008)	$C_D = \frac{16}{Re} (1 + 0.12Re^{0.6})$	$10^{-1} < Re < 10^3$	CMC, PAAS, XG, HEC
(Li et al., 2012)	$C_D = \frac{16}{Re} (1 + 0.43Re^{0.44})(1 + 3.868n^{0.7528}(1 - E))^{0.6810}$	$10^{-1} < Re < 10^2$	CMC
(Sun et al., 2015)	$C_D = 1.12 \times \frac{24}{Re} (1 + 0.173Re^{0.675})$ $C_D = 0.813 \times \frac{24}{Re} (1 + 24Re^{-1.125})$ $C_D = 1.07 \times \frac{24}{Re^{0.825}} (-1 + 0.037Re^{0.825})$	$Re < 10$ $10 < Re < 100$ $Re > 100$	XG

For non-Newtonian fluids, some researchers have proposed that the apparent viscosity of the fluid replaces the viscosity term in the dimensionless number, so that the bubble drag coefficient correlation for Newtonian fluids is equally applicable to non-Newtonian fluids (Dewsbury et al., 1999; Zhang et al., 2008). Nevertheless, (Dziubiński et al., 2003) experimentally studied the bubble velocity in non-Newtonian fluids, and comment that using such a generalized Reynolds number resulting from the power-law model of the liquid cannot obtain high accuracy of correlation of the drag coefficient. It is believed that this may be related to the complex rheological properties of non-Newtonian fluids and the deformation of bubbles. To this end, several researchers have directly studied the drag effect by directly taking into account the parameters that characterize the rheological properties of non-Newtonian fluids, like flow index n in the power-law model and the relaxation time constant t_λ in the Carreau model (Chhabra, 2010; Rodrigue, 2004).

Another special property for the bubble velocity in Non-Newtonian fluid is that, when the free rise velocity of a bubble is measured as a function of its size, a discontinuity

could be observed in terminal velocity at a critical bubble size (see Figure 4-3). (Wild et al. 2003) cited this phenomenon as an example of the complex behavior of bubbles, and (Chhabra, 2006) described the discontinuity as one of the most striking effects associated with bubble motion in non-Newtonian fluids. More recently, (Zenit and Feng, 2018) explain this velocity jump as a result of the increase of the extension and shear rates around the bubble.

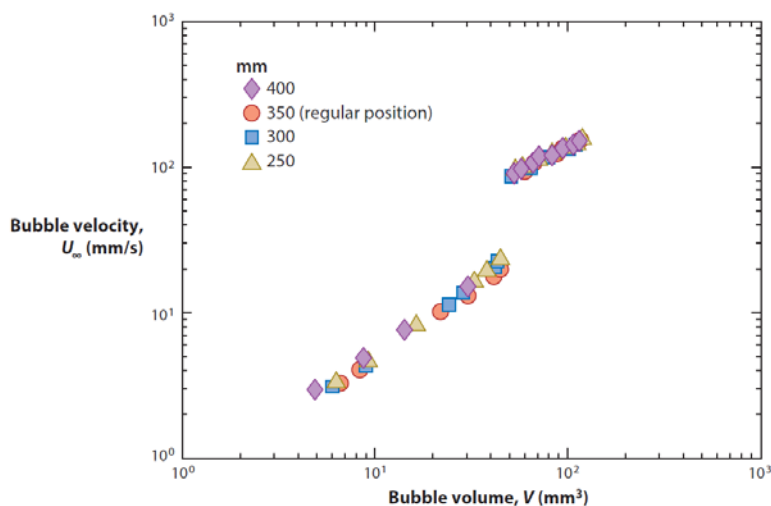


Figure 4-3 Bubble velocity as a function of bubble volume. The fluid is a viscoelastic, shear-thinning polymer solution. The different symbols show experiments recorded at different heights. Image from (Pilz and Brenn 2007)

Nevertheless, there are conflicting reports in the literature on the existence of a discontinuity in the free rise velocity of small bubbles in non-Newtonian fluids. While a number of investigators have observed a discontinuity (Fraggedakis et al., 2016; Legendre et al., 2012; Liu et al., 2015; Soto et al., 2006), others have not, and in some cases, the experiments conducted in the same polymer solutions have given contradictory results (Amirnia et al., 2013; Dekée and Chhabra, 1988; Dekée et al., 1986; Funfschilling and Li, 2006). Further investigation is required to give rise to such a phenomenon.

4.2 Bubble shape characterization and results

4.2.1 Bubble shape regimes in different solutions

As introduced in Chapter 2, the projections of the bubbles rising in different polymer solutions (i.e. both PAAM and Xanthan solutions) are captured by the high-speed camera. The examples of raw images are shown in Figure 4-4 and Figure 4-5, for the PAAM solution and Xanthan solution, respectively.

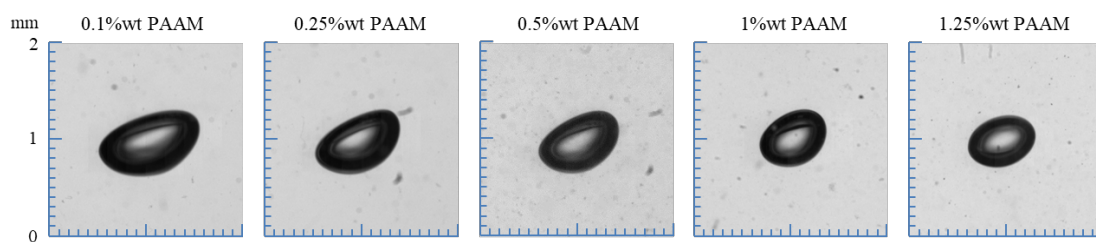


Figure 4-4 Visualization result of the bubble shapes in PAAM solutions of different concentrations

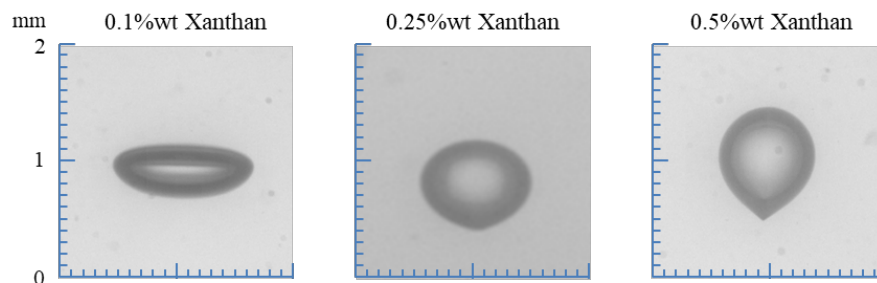


Figure 4-5 Visualization result of the bubble shapes in Xanthan solutions of different concentrations

The resulting bubble shapes in different polymer solutions are shown as bubble shape regime map, namely so-called Grace Map, in Figure 4-6. This bubble shape regime map is plotted in terms of the dimensionless Re , Eu numbers and $\log Mo$ (dark gray curves), which can be calculated as defined in Table 4-1, and the corresponding typical bubble shapes (gray patterns in the background) extracted from the raw images are also

depicted near the corresponding experimental points.

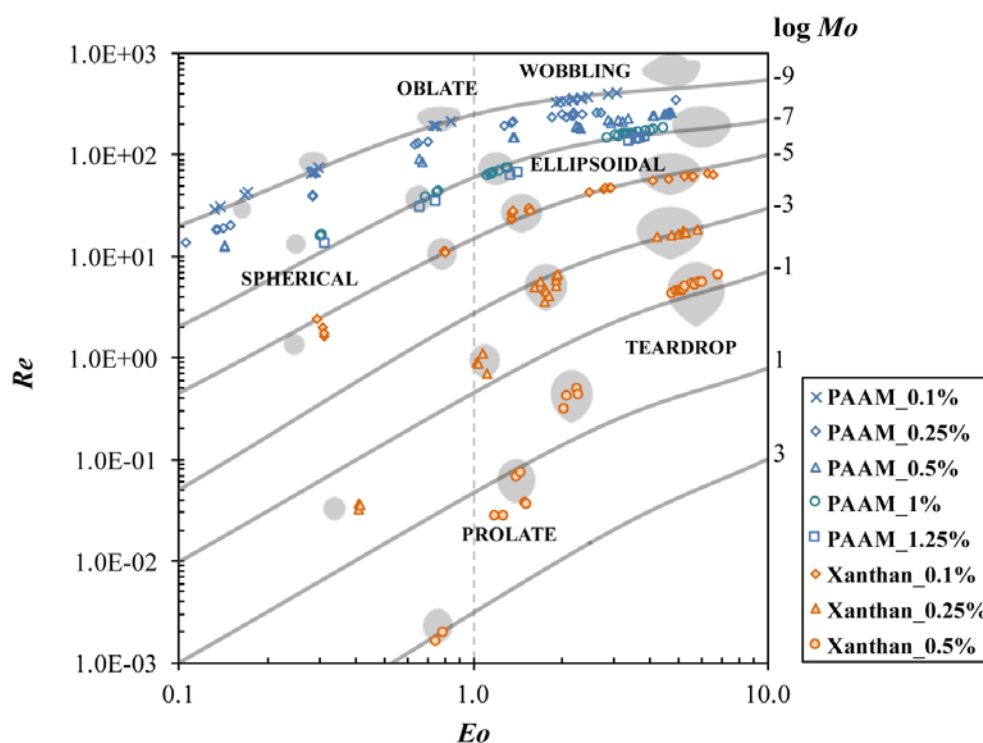


Figure 4-6 Shape regime map (namely Grace Map) for bubbles in PAAM and Xanthan solutions (dark gray curves: $\log Mo$; gray spots in the background: typical bubble shape near the corresponding experimental points).

In PAAM solutions, the range of Mo number is relatively small ($-9 < \log Mo < -7$) within the concentration range of study (0.1%-1.25 wt. %). The data covers the spherical bubble and the ellipsoidal bubble regimes. When increasing Eo and Re , the bubble becomes bigger and the shape changes from spherical to ellipsoidal. Regarding the concentration of the solution, it can be seen that the Re increases in a dilute solution, making the bubble become more oblate and even causing wobbling due to the strong surface oscillation.

In Xanthan solutions, the range of Mo number is larger ($-9 < \log Mo < 3$) in the concentration range investigated (0.1%-0.5 wt. %). The data covers not only the spherical and ellipsoidal bubbles but also the prolate and teardrop ones. A similar

tendency is found for the bubble deformation as in the PAAm solutions. In particular, the cusp appears for high Eo number ($Eo > 1$) and becomes more significant with the increase of the solution concentration or at lower Re number. Under this condition, the bubble is also elongated vertically, which is uncommon in Newtonian fluids.

Compared with the Grace map given by (Clift et al., 1978) for bubble shapes in Newtonian fluids, the intervals of the spherical bubble and the ellipsoidal bubble regimes in the present study are consistent when $Re > 1$. However, the bubble shapes are invariably spherical when $Re < 1$, which are contrary to those in non-Newtonian fluids. In fact, in non-Newtonian fluids, as the bubble velocity could be extremely low due to the complex rheological properties of the solution, relatively smaller values of Re number should be considered, namely Re ranging from 0.001 to 1 in this study. Within this range, the prolate bubble and teardrop bubble can also be visualized while the spherical bubble appears only for low Eo number ($Eo < 1$).

4.2.2 Characterization with aspect ratio

Many correlation expressions are available to calculate the aspect ratio E with dimensionless numbers, which are summarized in Table 4-2. By analyzing E in function of a single dimensionless number, the fitting results are found to be better when using We and Ta , while the results are very scattered with Re and Eo . Figure 4-7 and Figure 4-8 show the comparison of the experimental data and predicted ones by the existing correlations from the literature adopting We and Ta , respectively.

From Figure 4-7, it can be seen that, overall, the aspect ratio of the bubble is nearly constant at the beginning and then increases sharply for higher We number, which indicates that the bubble tends to be more oblate once the inertial force is stronger than the surface tension. In the PAAM solutions, where viscosity is relatively low, the stable bubble shape can be maintained for a wide range of $We < 0.5$ and the experimental points can be fitted by the correlation of (Legendre et al., 2012) considering different Mo numbers. The curve predicted by another empirical correlation from Sugihara et al. (Sugihara et al., 2007) reaches the upper boundary of the experimental points where the

results of PAAM_0.1% wt. are situated, which suggests that this correlation, obtained for the case of water, is not suitable for the fluid of higher viscosity. On the other hand, the aspect ratio of the bubble has more variation in Xanthan solutions. For $We < 0.001$, the aspect ratio begins to decrease slightly, which is consistent with the appearance of the prolate shape in Figure 4-6. This decrease is more significant for a higher concentration of the solute. Neither of the correlations from the literature can characterize this law of change.

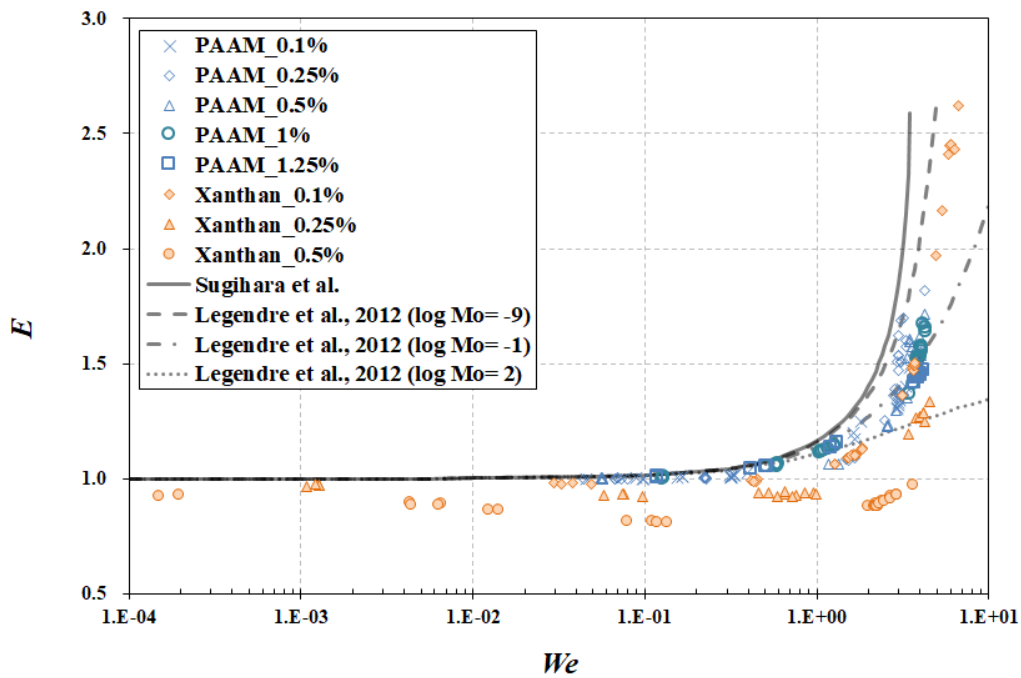


Figure 4-7 Aspect ratio E versus We number in PAAM and Xanthan solutions.

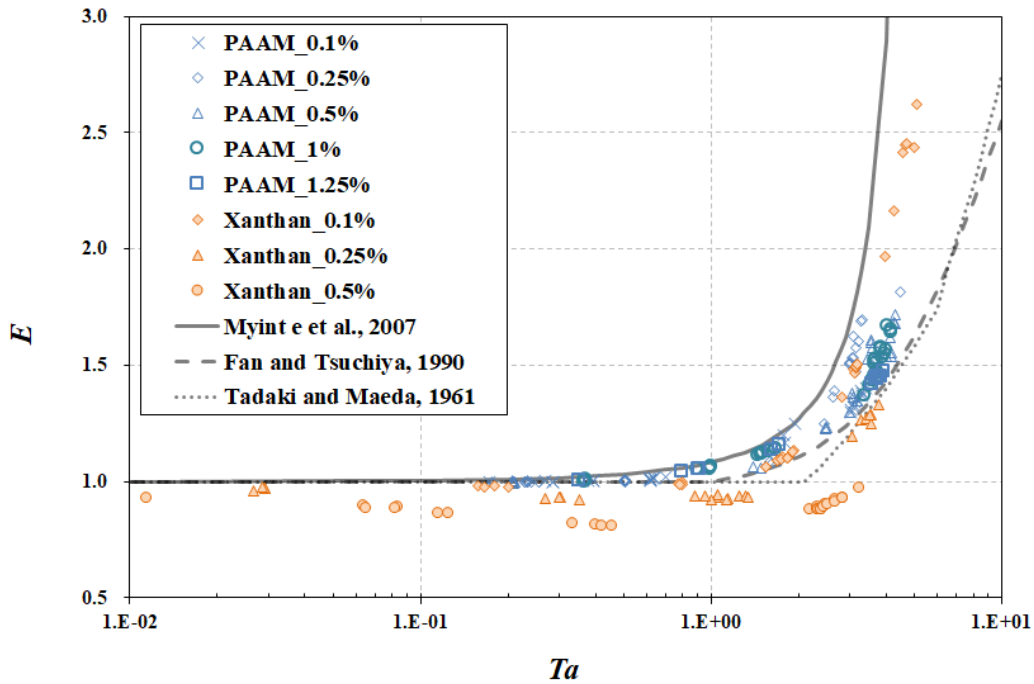


Figure 4-8 Aspect ratio E versus Ta number in PAAM and Xanthan solutions.

The impact of the Ta number on the aspect ratio E is investigated in Figure 4-8, where Ta number is related to the inertial force, the viscous force and the fluid properties. A similar tendency is found indicating that the increase of the aspect ratio is due to the dominant inertial force. The correlations by (Myint et al., 2007) and (Fan and Tsuchiya, 1990) approach the upper and lower bounds, respectively, of the data of the PAAM cases. The pioneering correlation by (Tadaki and Maeda, 1961) shows a bias when Ta number is close to 2. For Xanthan solutions, it seems that the existing correlations are not useful, as all of them overestimate the aspect ratio for bubbles under small Ta numbers.

The limits of the application of a single dimensionless number to characterize the bubble deformation are revealed. As listed in Table 4-2, several correlations have been found in recent years (Aoyama et al., 2016; Dong et al., 2010; Kelbaliyev and Ceylan, 2007; Liu et al., 2015), which use pairs of dimensionless numbers, such as (We, Re) and (Eo, Re) . These correlations were tested and used to calculate the aspect ratio with the

experimental data in this study. It is found that the correlation proposed by the literature (Aoyama et al., 2016; Dong et al., 2010; Kelbaliyev and Ceylan, 2007; Liu et al., 2015) all underestimate the aspect ratio, especially for larger bubble ($D_{eq} > 5$ mm) with a deviation of more than 15% between E calculated from the correlation and E from measurement in PAAM and Xanthan solutions. Since their correlations were obtained from an experiment using other fluids, it can be supposed that the coefficient in their equations should be modified for the non-Newtonian fluids. Liu et al. (Liu et al., 2015) proposed the following form of a function to predict the aspect ratio of the bubble:

$$E = a + b \cdot N_1^c N_2^d \quad (4-9)$$

with four fitting coefficients (a , b , c , d) and two chosen dimensionless numbers (N_1 , N_2). To verify this two-number model, the two numbers chosen among Re , EO , We and Ta are combined for the fitting of Eq. (4-9). The coefficients are optimized for each pair of dimensionless numbers and the deviation between the predicted aspect ratio and the measured one is calculated; it is denoted by the determination coefficient or r^2 . The fitting results are given in Table 4-4. Unfortunately, whichever combination of two dimensionless numbers is used, the error is significant, indicating that the prediction model is not suitable for the current study, namely for non-Newtonian fluids.

Table 4-4 Correlation results for the bubble aspect ratio with different pairs of dimensionless numbers.

	We, Re	We, Eo	We, Ta	Eo, Ta	Eo, Re	Re, Ta
a	0.9692	0.9824	0.9875	0.9745	0.9568	0.9634
b	0.003689	0.006974	43.87	0.004287	0.001096	0.002787
c	1.774	4.886	28.72	-1.851	1.402	0.6045
d	0.6143	-2.075	-36.48	5.67	1.117	2.252
r^2	61.43 %	76.65 %	65.7 %	79.58 %	68.47 %	69.56 %

Regarding the above analysis, it seems that the correlation developed for the Newtonian fluid is not applicable to the non-Newtonian case. Given the complexity of the non-Newtonian fluid, a parameter that can characterize the special rheological property, such as the shear thinning property of the fluid, should be introduced. It was mentioned in the introduction that one of the previous studies by (Li, 2011) adopted a so-called dimensionless number: $Wn = We \cdot Eo \cdot n$, which additionally considers the rheological factor n (flow behavior index of the Carreau model, see Section 2.1.1.3). Li's correlation containing the Wn number was tested and compared with our data. The result is plotted in Figure 4-9. It can be seen that the experimental points are still widely scattered and the curve of Li's correlation underestimates the majority of our data. So, the Wn number cannot properly predict the aspect ratio of our cases. That is probably due to that the Wn number contains the Eo number, which has been found to lack correlation with the aspect ratio. Since Ta is better correlated with the aspect ratio (Figure 4-9-II), it seems reasonable to replace the Eo number by the Ta number. Therefore, the evolution of the aspect ratio versus the product of We , Ta and n was investigated and the result is shown in Figure 4-10.

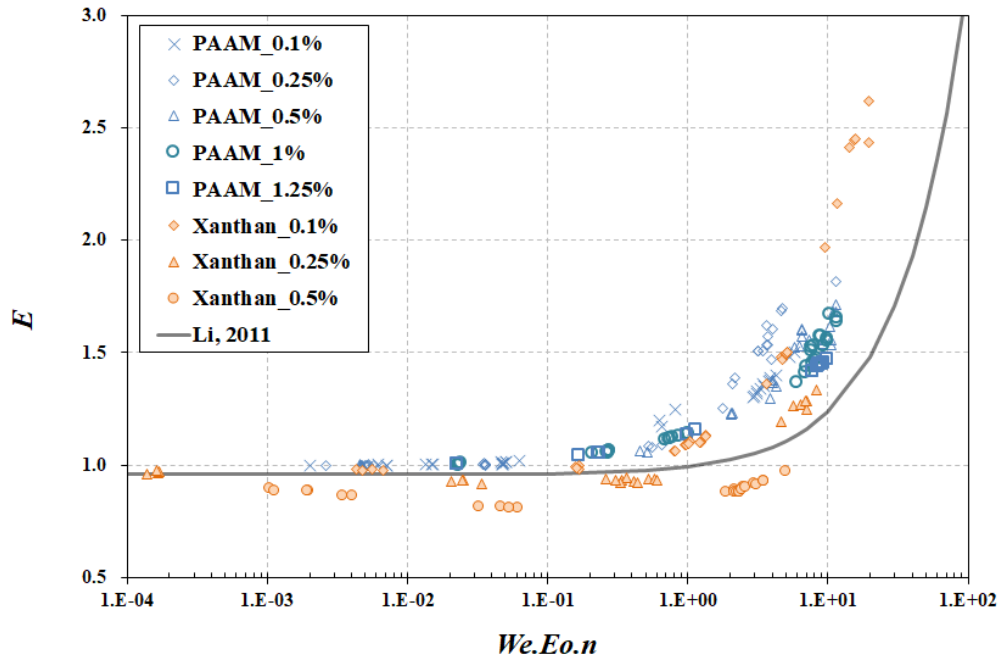


Figure 4-9 Aspect ratio E versus the product of $We \cdot Eo \cdot n$ in the PAAM and Xanthan solutions.

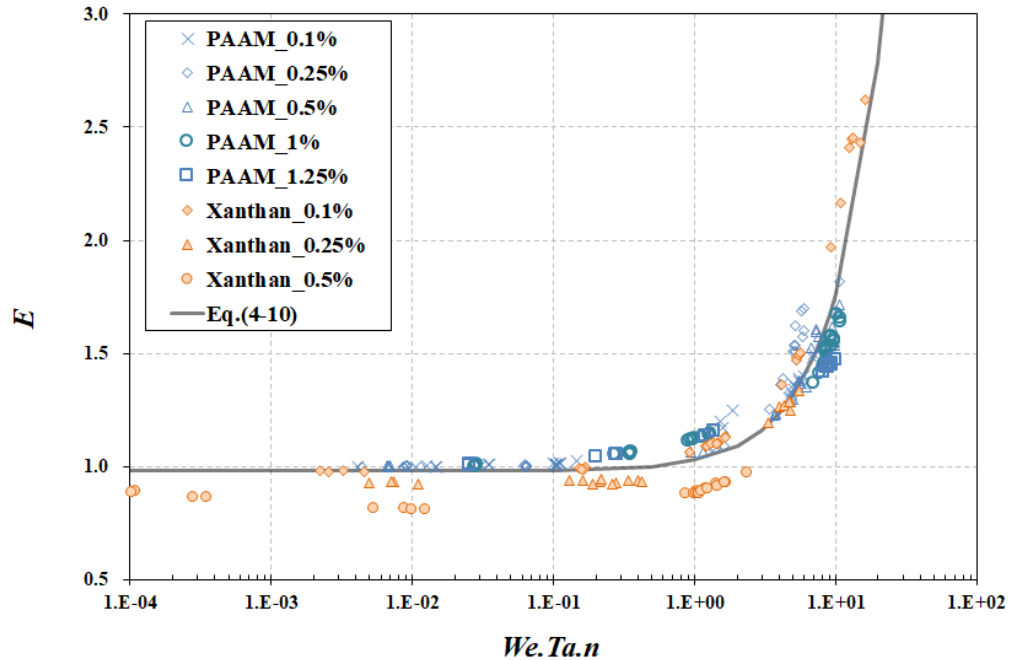


Figure 4-10 Aspect ratio E versus the product of $We \cdot Ta \cdot n$ in the PAAM and Xanthan solutions.

Although there is still some deviation for Xanthan at concentrations lower than 0.5% wt, the fitting quality is significantly improved. It can be derived that a more accurate correlation for predicting the aspect ratio could be developed based on Eq. (4-9). For this purpose, three modified prediction functions are listed below. Inspired by Wn number, the product of $(We \cdot Ta \cdot n)$ is denoted ' Tn '.

$$Tn = We \cdot Ta \cdot n \quad (4-10)$$

$$E = a + b \cdot Tn^c \quad (4-11)$$

$$E = a + b \cdot Tn^{(c \cdot n + d)} \quad (4-12)$$

$$E = a + (b \cdot n + c) \cdot Tn^{(d \cdot n + e)} \quad (4-13)$$

where a , b , c , d , and e are the fitting coefficients.

In the range investigated in this study ($-9 < \log Mo < 3$), the fitting results are shown in Table 4-5.

Table 4-5 Correlation results for the aspect ratio E with Tn number (i.e. $Ta \cdot We \cdot n$).

	Eq. (4-11)	Eq.(4-12)	Eq.(4-13)
a	0.98	0.97	0.96
b	0.0049	0.06	0.45
c	1.204	-1.17	-0.11
d	-	1.75	-3.38
e	-	-	2.62
r^2	86.7 %	91 %	96.3 %

From Eq. (4-11) to Eq. (4-13), the correlation functions become more complicated by giving more importance to the rheological index n and the fitting quality is significantly improved. This indicates the importance of considering the rheological properties when studying the bubble shapes in non-Newtonian fluids. The aspect ratios calculated by

Eq. (4-11) - Eq. (4-13) are compared with the result of Li's model in Figure 4-11.

It can be seen that, by adopting Tn instead of Wn , the fitting quality is improved with respect to Li's correlation and also much better than the results listed in Table 4-2, in which the aspect ratio was predicted without considering the rheological index n . The reason for the good fitting agreement is assumed to be that the Tn number contains multiple influencing factors, including the inertial force (We , Ta), surface tension (We), viscous force (Ta), fluid properties (Ta) and rheology (n).

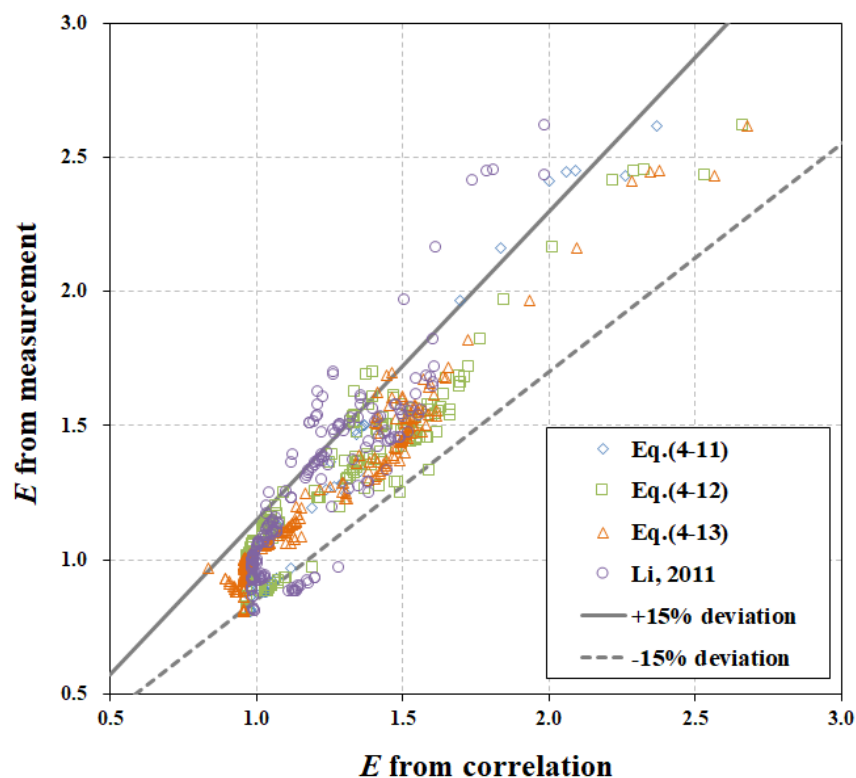


Figure 4-11 Comparison between E from the correlation and E from measurement in PAAM and Xanthan solutions.

To sum up, in the non-Newtonian fluid, the bubble shape is more sensitive to external conditions than that in Newtonian fluids. It is possible for the aspect ratio of the bubble to be smaller than 1 in non-Newtonian fluids, giving the appearance of an elongated bubble. Although the aspect ratio is still mainly related to the inertial force (for big

oblate bubbles), simply considering one factor or one dimensionless number is insufficient to predict it. The aspect ratio of the bubble depends not only on the different forces applied to the bubble but also on the rheological properties of the fluid.

4.2.3 Characterization with parametric equations

4.2.3.1 Definition

The profiles of the bubbles in cross-section (x - y) are recorded by the camera (Figure 4-12). It would be interesting if these profiles could be described by simple parametric equations. There are several well-known shapes, such as teardrop, simple folium and piriform, which give rise to approximate models of the profiles of a bubble or droplet. Their parametric equations are given with examples in Table 4-1.

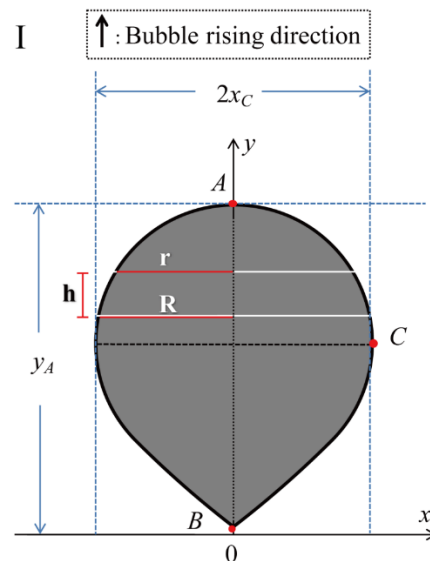

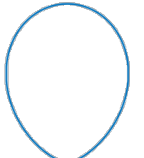



Figure 4-12. Schematic diagram of the bubble profile

Table 4-6 Approximate models of the profiles of a bubble or droplet: parametric equation and example.

Teardrop	$\begin{cases} x = a \sin t \left(\sin \frac{t}{2} \right)^n \\ y = a \cos t \end{cases}$	$a=1$ $n=3$ $t \in [-\infty, +\infty]$	
Simple folium	$\begin{cases} x = ty \\ y = \frac{a}{(1+t^2)^2} \end{cases}$	$a=1$ $t \in [-\infty, +\infty]$	
Piriform	$\begin{cases} x = \frac{a^2}{b} \cos^3 t \sin t \\ y = a \cos^2 t \end{cases}$	$a=1$ $b=1$ $t \in [-\infty, +\infty]$	

Based on the equations listed in Table 4-6, a new method is proposed to characterize the bubble shape by parametric equations. The interpretation is given as below:

$$\begin{cases} x(t) = \frac{2x_C t}{1+t^2} \\ y(t) = \frac{y_A}{[1+\alpha t^2]^\beta} \end{cases} \quad t \in [-\infty, +\infty] \quad (4-14)$$

$$E = \frac{2x_C}{y_A} \quad (4-15)$$

where:

- α, β are two parameters describing the bubble shape;
- E is the aspect ratio;
- $2x_C$ is the length of the minor axis of the bubble profile depicted in Figure 4-12;
- y_A is the length of the major axis of the bubble profile depicted in Figure 4-12;
- t is a numerical variable range between negative and positive infinity.

4.2.3.2 Determination of parameter α, β from the images

Since the value of y_A and $2x_C$ can be obtained directly by measurement, an optimization can be performed to determine the values of α and β . Supposing that the edge of the

bubble profile can be divided into N points, the coordinates of point i ($x_{i,exp}$, $y_{i,exp}$) on the experimental image are defined. By arbitrarily proposing a pair of values (α , β) we have, from Eq. (4-14):

$$t_i = \sqrt{\frac{1}{\alpha} [(y_{i,exp}/y_A)^{-\frac{1}{\beta}} - 1]} \quad (4-16)$$

By substituting t_i in Eq. (4-14), the calculated abscissa $x_{i,cal}$ can be obtained:

$$x_{i,cal} = \frac{2x_c t_i}{1+t_i^2} \quad (4-17)$$

The values of the parameters α and β are optimized by minimizing the sum of the difference at all points between the abscissa calculated with Eq. (4-14) and the one from the experiment:

$$|x_{i,cal} - x_{i,exp}| \quad (4-18)$$

The difference is then compared to the equivalent diameter and the relative deviation of the fitting result is defined as follow:

$$err = \frac{|x_{i,cal} - x_{i,exp}|}{N.D_{eq}} \quad (4-19)$$

4.2.3.3 Influence of the parameters on bubble profiles

Regarding Eq. (4-14) & (4-15), the bubble shape could be characterized by the parameters, α , β , and the aspect ratio, E . To investigate their impacts on the shapes, the evolution of the bubble shape in function of α and β is represented in Figure 4-13 where the profiles of the bubbles are shown for aspect ratio $E=1$ (Figure 4-13-I) and $E=0.5$ (Figure 4-13-II). Within the investigated experimental conditions, it could be observed that the profile is sensitive to both α and β . The value of α can change the position of the major axis (horizontal) of the bubble profiles. When the value of β is fixed (e.g. $\beta=1$) and α increases (e.g. $\alpha=0.5-2.5$), the major axis is moving from near the top of the bubble to the bottom of the bubble. On the other hand, β is related to the appearance

of the cusp. Herein, the bubble deformation can be roughly summarized as follows:

- For $\beta < 0.6$, there is a clear cusp at the bottom of the bubble. The typical inverted teardrop shape appears at a high value of α . (e.g. Figure 4-13-I: $\alpha=2.5, \beta=0.4$).
- For $0.6 < \beta < 0.8$, the shape profile becomes progressively rounded at the bottom and the cusp gradually disappears as the value of β increases.
- For $0.8 < \beta < 1$, there is no longer a cusp and the profile becomes more and more rounded. The quasi-ellipsoidal bubble appears at this interval. In particular, the circular profile (spherical bubble) and the perfectly elliptical profile (ellipsoidal bubble) appear when the value α and β are both equal to 1. Their difference comes from the change of the aspect ratio value.
- For $\beta > 1$, the bottom of the profile tends to be flat. The typical cap shape appears when the values of α and β are both high enough. (e.g. Figure 4-13-II: $\alpha=1.5, \beta=1.5$)

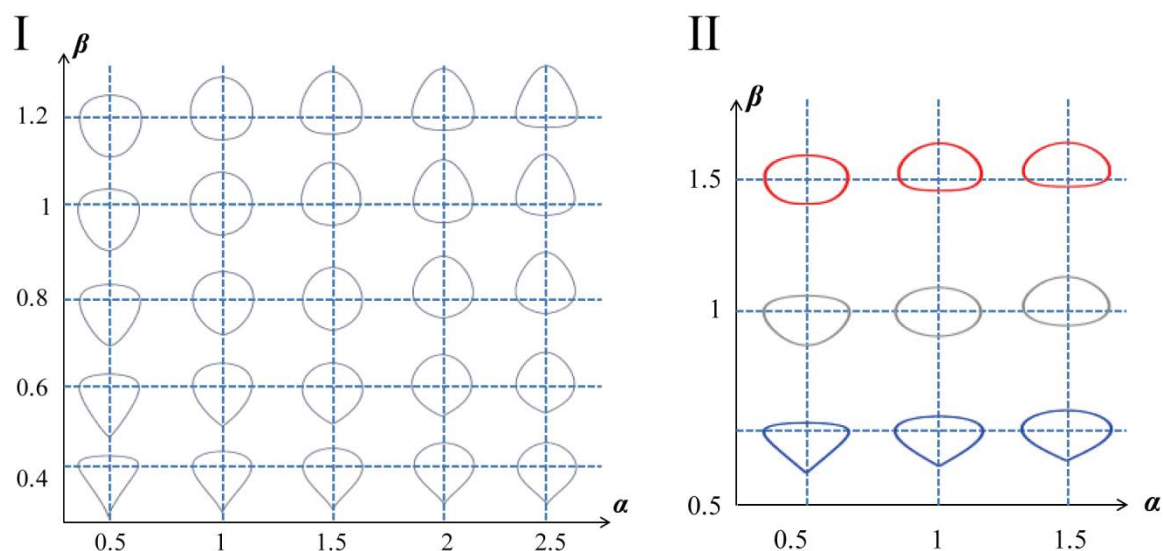


Figure 4-13 Evolution of the shape versus the parameters α and β (I: $E=1$; II: $E=2$).

4.2.4 Result of shape parameters

4.2.4.1 Fitting result

To better analyze the bubble shape, the bubble profile is fitted by the parametric models introduced. Two typical fitting results, chosen for single bubbles in Xanthan and PAAm

solutions, respectively, are shown in Figure 4-14-I & II, where the black dots are the contour points of the original bubble extracted by Matlab and the red line is the fitting contour with the values of α and β indicating alongside. It can be seen that whether the bubble has a teardrop or ellipsoidal shape, the deviation between the experimental points and the fitting points is small. In fact, the deviation defined in Eq. (4-19) obtained by measurement is in a magnitude smaller than 3%. To ensure the validity of the bubble characterization result, fitting data with an error of more than 2% was eliminated. An example of the averaged fitting results of the bubble shapes in both PAAm and Xanthan solutions under different concentrations are given in Figure 4-14-III & IV. It can be observed that under the same operational condition for bubble generation (i.e. the size of nozzle and the air flow rate), the sizes and shapes of bubbles depend on the type and concentration of the solutes (i.e. PAAm and Xanthan). In addition, the evolution of the bubble shapes given by the model is consistent with the original bubble shapes depicted in Figure 4-6.

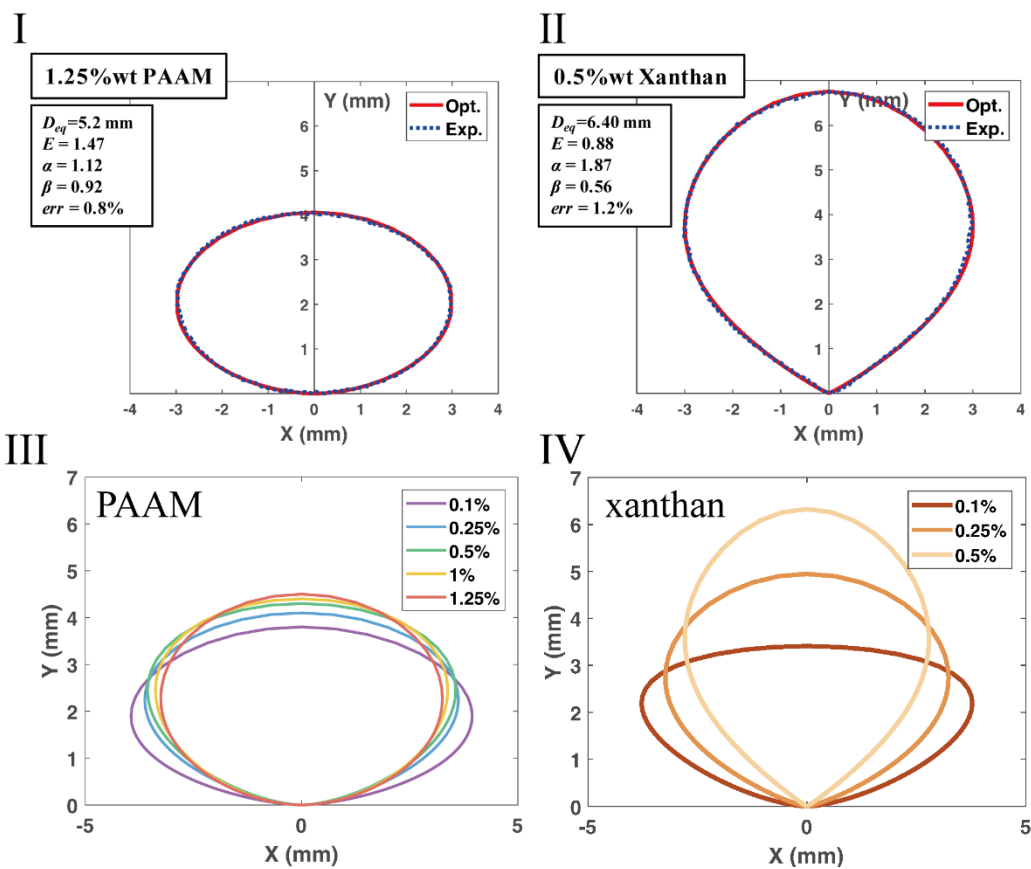


Figure 4-14 Examples of the bubble profiles and the fitting ones by Eq. (6) in PAAm (I, III) and Xanthan solutions (II, IV) under different concentrations. (The bubbles are injected by the nozzle with a caliber of 1 mm at a flow rate of 10 μ L/h).

It can be seen from Figure 4-14-III & IV that in PAAm solution, the size of the bubble slightly changes, while the shape becomes more and more rounded for higher concentrations, namely, from an oblate bubble to a general ellipsoidal bubble. In contrast, in Xanthan solutions, the major axis of the bubble increases as the concentration of Xanthan increases, as well as the bubble deforms from an oblate ellipsoid to an oblate teardrop and then turns to an average teardrop.

4.2.4.2 Relationship between parameters α and β

For a single bubble, a pair of parameters (α , β) could be obtained from the fitting result. Thus the shape of the bubble can be depicted by using these two parameters. In Figure 4-15, the relationship between the bubble shape parameters (α and β) are depicted for bubbles in PAAm and Xanthan solutions. The corresponding bubble profiles (light gray outline) are also displayed at the positions of values α and β . In this figure, the delicate changes of bubble shape can be visualized and quantified, which is difficult to achieve simply by using the aspect ratio. For PAAm solutions, the data are concentrated in the range of $1 < \alpha < 1.2$ and $0.8 < \beta < 1$, suggesting that the bubble is spherical or ellipsoidal, while, for the Xanthan solution, the range of these two parameters is much larger. As the parameter α increases, the value of β decreases gradually. As interpreted in Section 2.4.2, the cusp of the bubble appears when $\beta < 0.6$ and it becomes sharper or pointed when β continues to decrease. The result of the Xanthan cases shows good agreement with this evolution.

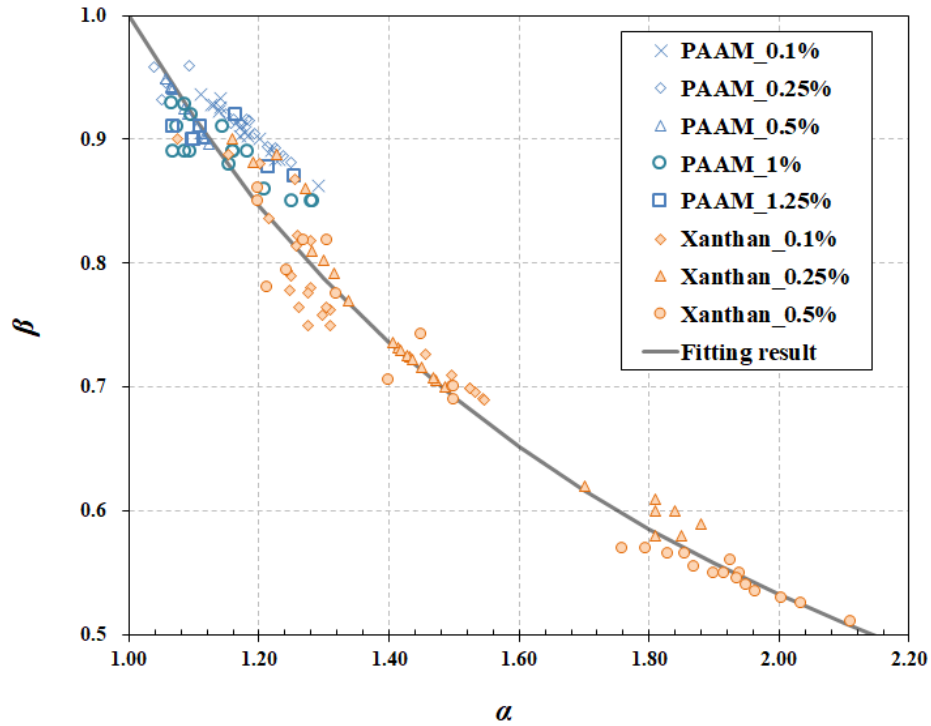


Figure 4-15 Relationship between the bubble shape parameters (α and β) in both PAAm and Xanthan solutions under various concentrations.

The relationship between α and β could be correlated by a power-law function, which is expressed as below:

$$\alpha^{0.85} \beta = 1 \quad (4-20)$$

In the range investigated in this study ($-9 < \log Mo < 3$), the accuracy of this correlation is acceptable, with a determination coefficient $r^2 > 95\%$. It can be seen from Figure 4-15 that the curve of Eq. (4-20) passes the point $(\alpha, \beta) = (1, 1)$, which indicates a perfect spherical bubble (or an ellipsoidal bubble when $E \neq 1$). Thanks to Eq. (4-20), it is possible to characterize the bubble shape with only one parameter (either α or β). In the next section, only the parameter β is taken into consideration.

4.2.4.3 Correlation of parameters

It can be known from Section 4.2.4 that the aspect ratio E roughly describes the bubble

shape while the parameter α and β characterize the details of bubble deformation in both PAAm and Xanthan solutions. As mentioned in the introduction that a lot of research has been carried out for predicting the aspect ratio E for bubbles in different liquids, we will focus on the discussion of the bubble shape parameter β .

Depending on the value of β , bubble shape changes from ellipsoidal (without cusp tail) to teardrop (with cusp tail). Some existed research attempts to explain the appearance of the cusp tail theoretically and most of the authors support the reason that the majority of non-Newtonian fluids are composed of long-chain molecules and possess viscoelasticity (Barnett et al., 1966; Zenit and Feng, 2018). To quantify the elasticity of the fluid, the Deborah number is utilized to compare the response of the fluid to the characteristic time of the motion:

$$De = \frac{t_\lambda U y}{D_{eq}} = t_\lambda \dot{\gamma} \quad (4-21)$$

With t_λ the relaxation time of the Carreau model (Eq. (2-2)).

For our operating conditions, shear rates can be estimated from the processed experimental data: rising velocity U and equivalent diameter of the bubble D_{eq} (Dietrich, 2008):

$$\dot{\gamma} = \frac{U}{D_{eq}} \quad (4-22)$$

The method to calculate U and D_{eq} is presented in Sections 2.3.

Since the cusp could now be quantified by the parameter β , we can study this problem experimentally by analyzing the evolution of β in terms of the bubble size (V) and various dimensionless numbers (De , EO , Re), shown as in Figure 4-16.

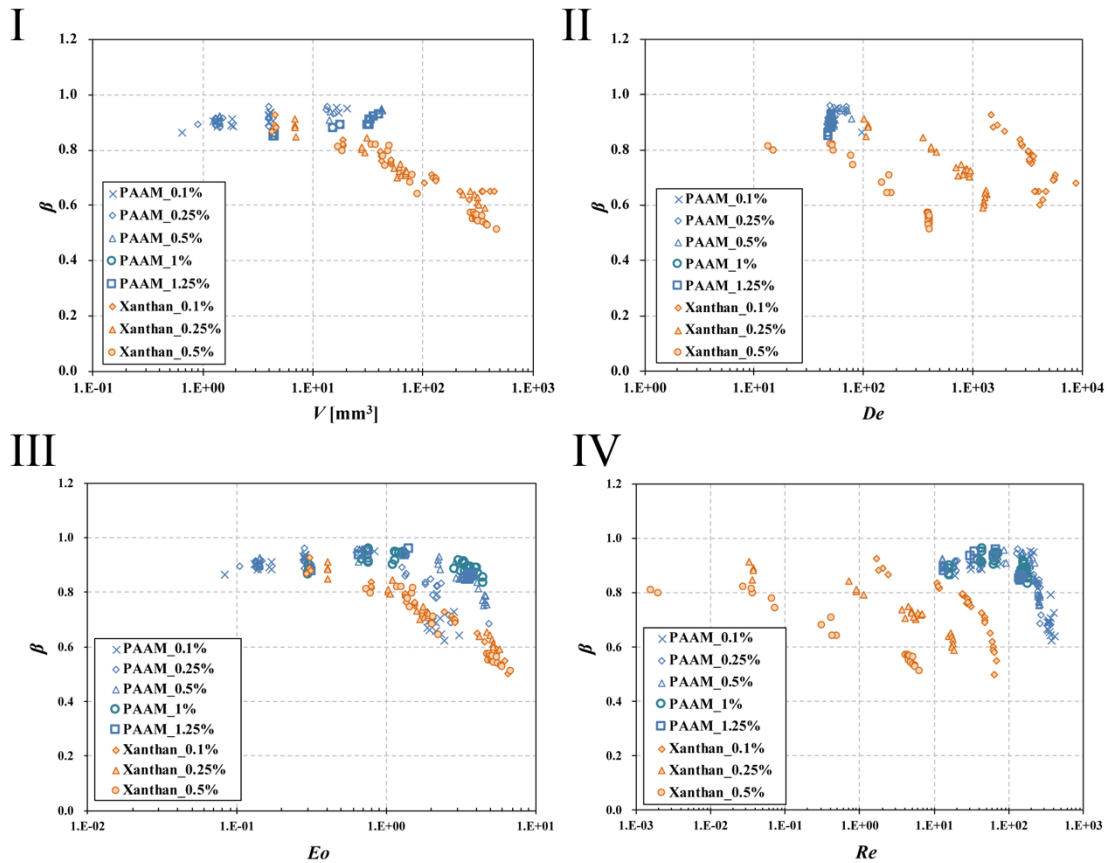


Figure 4-16 The evolution of parameter β in terms of the bubble size (V) and various dimensionless numbers (De , Eo , Re) in PAAM and Xanthan solutions under various concentrations.

It can be obtained from Figure 4-16 that:

(1) for larger bubbles, the velocity of the bubble increases then the bubble begins to deform and becomes less rounded when the contribution of inertial force and buoyancy is stronger than the surface tension and viscous force.

(2) β decreases with higher viscoelasticity of the solution in most investigated range except for some PAAM which are relatively less elastic. If the bubble moves too fast, the liquid cannot fill the space in the rear of the bubble immediately. Hence this space is still occupied by the gas and pressed by the long-chain liquid molecule from the side, leading to a little cusp tail forming in the rear of the bubble.

(3) In the evolution of $\beta-De$ and $\beta-Re$, the evolution of the value β under three concentrations is quite dispersed. This result might be caused by the different shear-thinning level of the solutions as the shear-thinning property is also a reason

for the deformation of the bubble (Warshay et al., 1959).

The data in Figure 4-16 are too scattered for a general law to be obtained. Hence multiple influencing factors are considered instead of one. By analogy with the analysis of aspect ratio, the investigation was carried out for the evolution of β with different pairs of dimensionless numbers as well as the shear-thinning property which can be roughly quantified by the power index n . After testing several functions, the following correlation was proposed to fit the experimental data:

$$\beta = n - 0.11De^{0.19}Eo^{0.11} + 0.80 \quad (4-23)$$

This equation is correlated to the result depicted in Figure 4-16 as β decreases monotonically with high De , Eo numbers and the shear-thinning levels. The comparison between parameter β predicted by Eq. (4-23) and the experimental ones is shown in Figure 4-17. It can be seen that, in the range used for this study ($-9 < \log Mo < 3$), the prediction quality of parameter β in both PAAm and Xanthan solutions is satisfied. Relatively large deviation appears at high values of β due to the wobbling of the bubble when rising in thin PAAm solution. The fitting result has a coefficient of determination (R^2) higher than 95%.

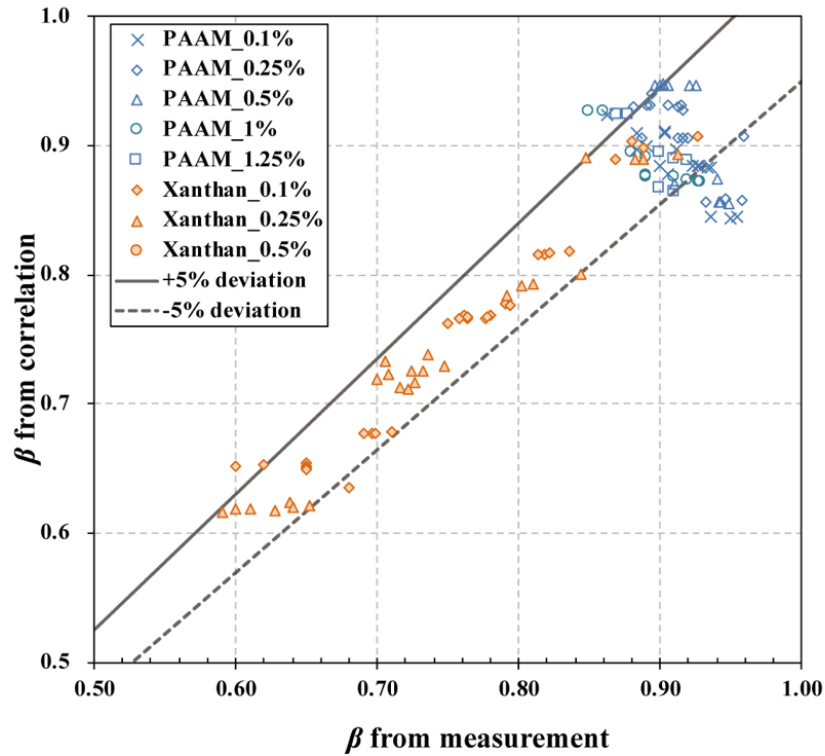


Figure 4-17 Comparison result between parameter β from correlation (Eq. (4-23)) and β from measurement in PAAM and Xanthan solutions.

4.2.5 Prediction of bubble shape

In summary, with Eq. (4-14) & (4-15) to describe the bubble shape, Eq. (4-13) for aspect ratio E , Eq. (4-23) for predicting parameter β and Eq. (4-20) for the relationship between α and β , a complete system could be established for investigating or predicting the bubble shape in non-Newtonian fluids. As shown in Figure 4-18, the aspect ratio of the bubble and the parameter β can be estimated using multiple dimensionless numbers and the flow behavior index n . The other shape parameter α could be calculated by the correlation between α and β . The values of E , α , and β are then substituted into the bubble shape equations and finally, the bubble profile can be predicted.

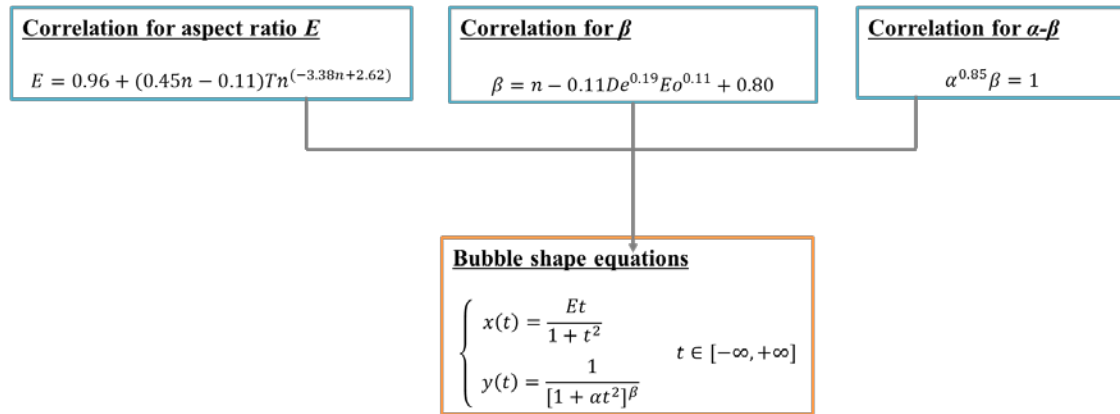


Figure 4-18 Illustration of correlation equations system for the bubble shape prediction.

4.3 Result of bubble velocity and drag

4.3.1 Bubble velocity

Concerning the bubble terminal velocity, as shown in Figure 4-19, it first increases with the bubble size then tends to be constant when the bubble size gets bigger. Although the velocity curves at different concentrations differ more from each other for Xanthan solutions, this evolution and the final constant velocity do not depend on the type of solution or the concentration of the solute. It could be derived that, in a highly viscous Xanthan solution, the bubble rises much more slowly and needs to attain the final constant velocity in a bigger size. In particular, it exists a remarkable difference between the velocity curves of the three lower concentrations of PAAm solutions and those of the two higher concentrations. It could be explained that, in the dilute PAAm solutions (0.1%- 0.5% wt), the bubble shape is less stable with surface oscillation, which leads to the reduction of the viscosity around the bubble due to the shear thinning property. On the other hand, when a bubble is rising in a concentrated enough PAAm solution (1%-1.25% wt), the surface oscillation no longer exists due to the stable bubble shape. The bubble thus encounters more resistance and its velocity is much slower. Moreover, there is no evident velocity discontinuity under our experimental conditions indicating that the bubble terminal velocity could be less influenced by the bubble shape

deformation (from ellipsoidal to inverted teardrop). This continuity is consistent with the literature (Amirnia et al., 2013; Funfschilling and Li, 2006), in which the same behavior of rising bubbles was found in Xanthan solutions and PAAm solutions.

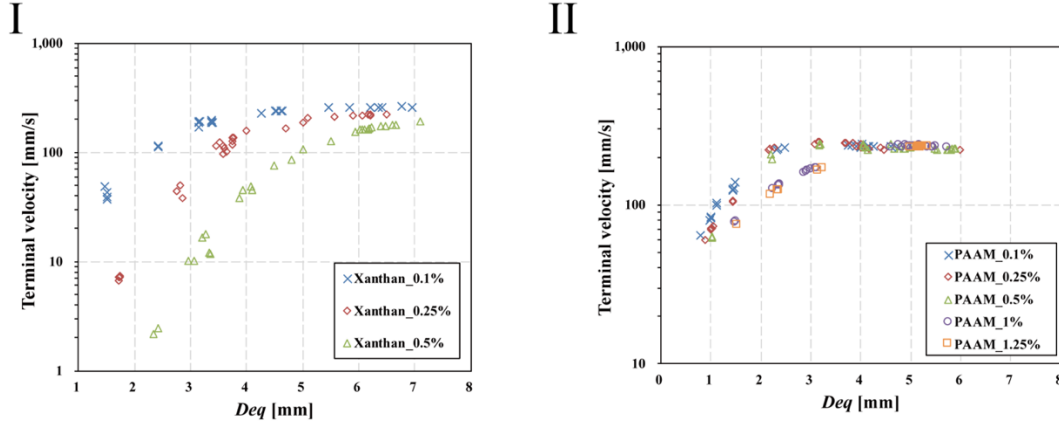


Figure 4-19 Relationship between bubble rising velocity and bubble size (D_{eq} : 0.7~7 mm) in Xanthan (I) and PAAm solution (II).

4.3.2 Drag coefficient

According to the mass balance (Section 4.1.2), the drag coefficient of the bubble equals to

$$C_D = \frac{1}{3} \frac{\pi \cdot g \cdot D_{eq}^3}{U^2 A} \quad (4-24)$$

Where A refers to the area of a cross section perpendicular to the bubble moving direction. This area can be calculated from the width of the bubble $2x_c$ (Figure 4-12)

$$A = \pi x_c^2 \quad (4-25)$$

Thus the expression of drag coefficient becomes

$$C_D = \frac{1}{3} \frac{g \cdot D_{eq}^3}{U^2 x_c^2} \quad (4-26)$$

With the Eq. (4-26), the drag coefficient is calculated for bubbles rising in different solutions. The result is plot as a function of Reynolds number which is estimated with

the viscosity from the Carreau model (Section 2.1.1.3). It shows that the drag coefficient decreases when $Re < 10$ then tend to be constant for higher Reynolds number. This tendency is clear especially for the cases of Xanthan gum solutions which have a wide range of Reynolds. Regarding the concentration of the solute, it seems that drag coefficient slightly increases for more concentrated Xanthan gum solution. This is supposed to relate to the elasticity of the solution. For PAAM solutions which have smaller variation of the elasticity (depending on the relaxation time in the the Carreau model), this impact is relatively negligible in the figure. The result is compared to several existed correlation model. Our result has a better consistence for smaller Reynolds number with a value close to $16/Re$. For $Re > 30$, the drag coefficient become a constant value close to 1 while all the depicted correlation has underestimated the value.

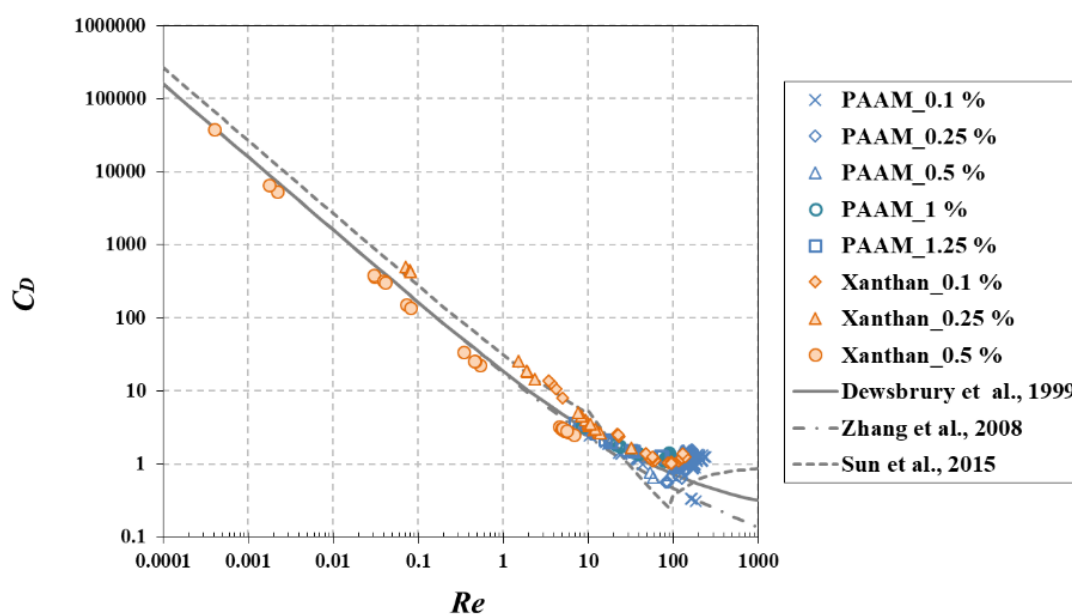


Figure 4-20 Drag coefficient versus Reynolds number for bubbles rising in different solutions.

Besides the property of the solution, the bubble shape itself can affect the drag. To

investigate this impact, the drag coefficient is plotted as a function of the shape parameter β . The result is shown in Figure 4-21. Since the bubble shape is not stable in dilute solutions, the data only refers to the case PAAm (1-1.25 wt. %) and Xanthan gum (0.1-0.5 wt.%). The result shows that for all the cases, the drag coefficient increases with a higher value of the parameter β . As discussed in Section 4.2.3, a higher value β leads to a more rounded bubble and small β leads to the bubble with a pointed tail or the teardrop shape. It is known that the teardrop shape is much more streamlined than the spherical one. That can explain the drop of the drag for a lower value of the parameter β .

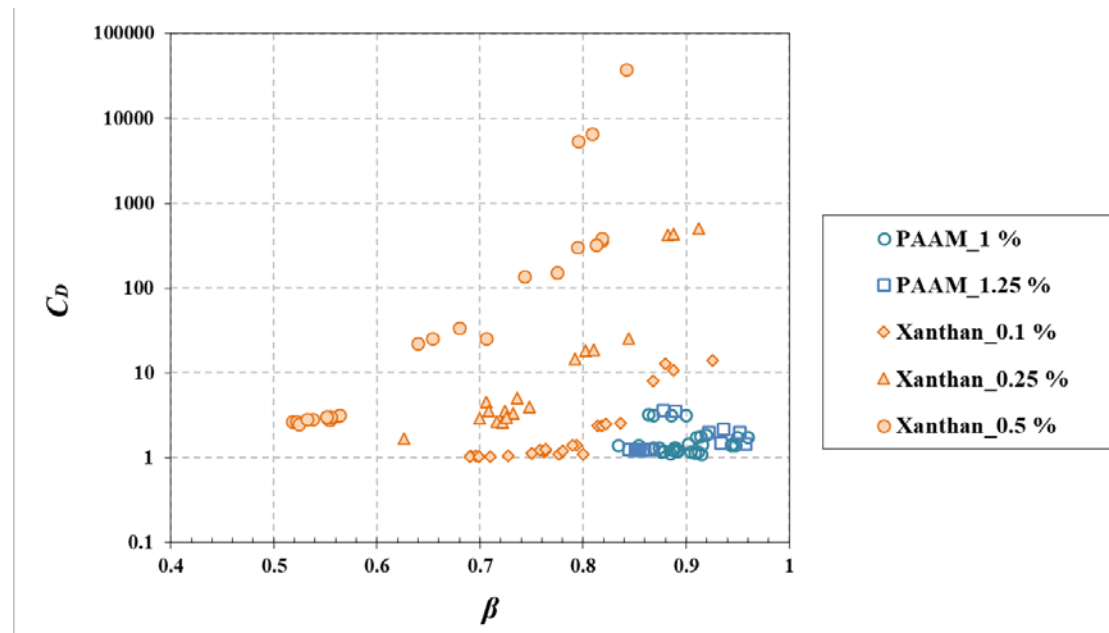


Figure 4-21 Drag coefficient versus Bubble shape parameter β for bubbles rising in different solutions.

4.4 Trajectory characterization and result

4.4.1 Trajectory fitting model

As introduced in Chapter 2, the centroid of the bubble in each recording frame is

recognized and processed in Matlab software. Plot the centroids of the bubble on a coordinate plan will give the trajectory of the bubble.

To characterize the trajectory of the bubble, the following equation is defined:

$$x = A \sin(B \cdot y + C) + D \quad (4-27)$$

where (A, B, C, D) are four fitting parameters and (x, y) is the coordinate of the bubble centroid. The fitting for this trigonometric function is implemented by using a nonlinear regression solver `Fminsp` in Matlab software.

Thus the period of the oscillation can be defined as:

$$T = \frac{2\pi}{B} \quad (4-28)$$

The example of the fitting result is shown in Figure 4-22 for a bubble with an equivalent diameter of 5 mm rising in most dilute concentrations (0.1%). It can be seen that for such a big bubble, the bubble in PAAm exhibits a zigzag motion while the bubble in Xanthan solution has a linear path. Both results are well fitted with a determination coefficient r^2 high than 98%.

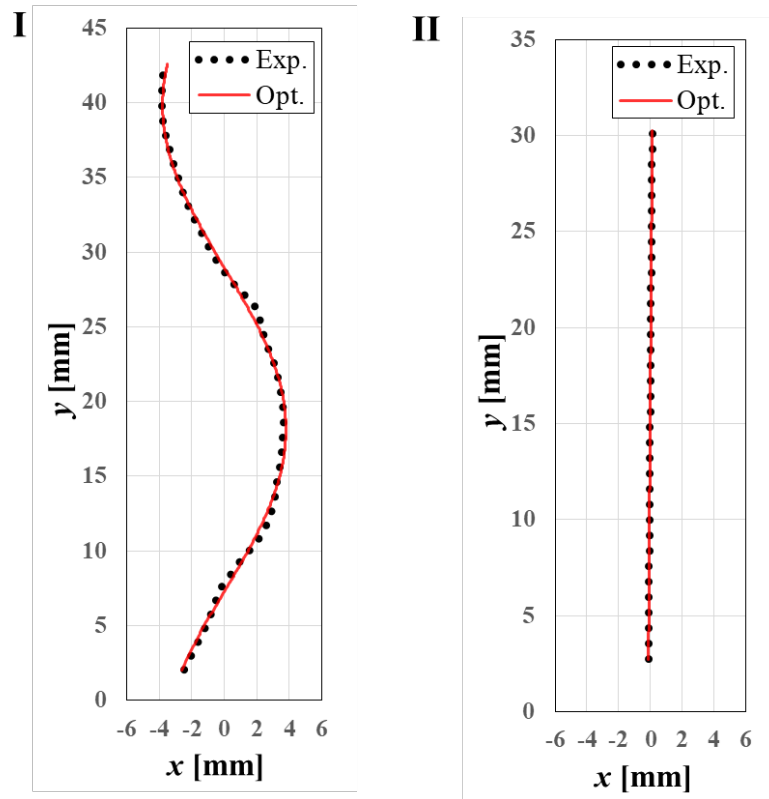


Figure 4-22 Example of the fitting result of the bubble trajectory ($D_{eq} \approx 5$ mm). I: PAAm 0.1 wt%; II: Xanthan gum 0.1 wt%

4.4.2 Trajectory result

In PAAm solutions, for the bubble with an equivalent diameter smaller than 1.5 mm, the bubble is rising approximately linear. When the bubbles become bigger, a zigzag path is visualized. The trajectory of the bubble of different size rising in PAAm of various concentration is depicted in Figure 4-23. It is found that for dilute solutions (concentration of 0.1 wt. % - 0.25 wt. %) there is no an evident tendency between the trajectory and the bubble size. This is due to the variation of the bubble shape which leads to the complex flow condition around the bubble. On the other hand, when the bubble rises in concentrated solutions (concentration of 0.5 wt. % and 1 wt. %), it can be seen that the oscillation period of the trajectory is increasing for bigger bubbles. If the solute concentration continues to increase (1.25%), the liquid gets more vicious, the

impact of the bubble size on the trajectory reduces. Regarding the impact of the bubble shape on the trajectory, the spherical bubbles have more linear trajectory than the ellipsoidal bubbles which rise in a zigzag path.

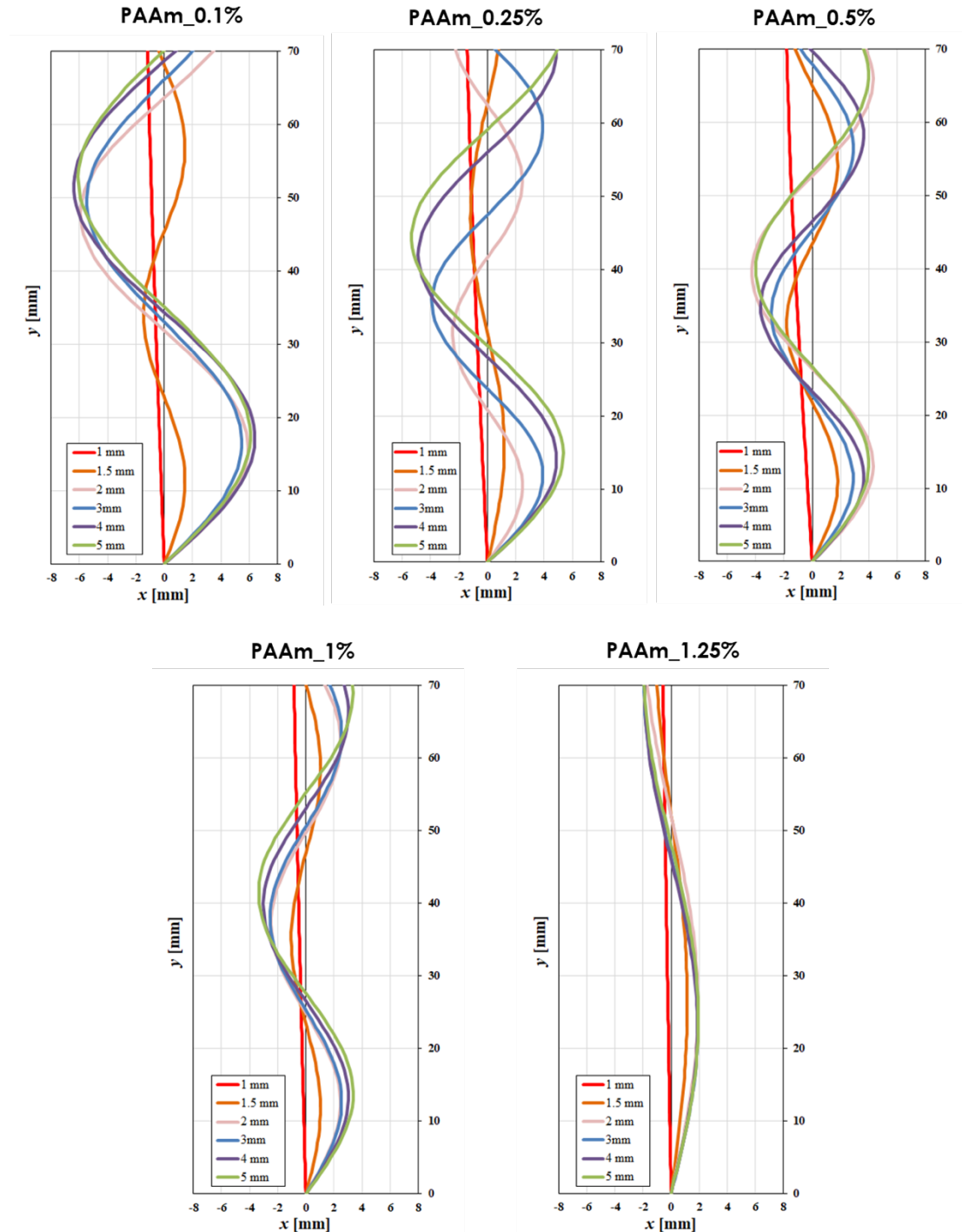


Figure 4-23 Trajectory of the bubbles in different size ($D_{eq}=1-5$ mm) rising in PAAm solutions

The result of the trajectory in Xanthan gum solutions is plotted in Figure 4-24. For the chosen concentration of the solute, all the bubble rises in a linear path even for big bubbles. When the bubble size changes, the trajectory is stable only with a slight deviation between each case. For concentrated solutions, the trajectory lines are overlapped and the impact of the bubble size on the trajectory is negligible. Particularly, the trajectory of a bigger bubble seems to more vertical (see the blue lines) than the others. That is because such a big bubble has a higher vertical velocity U_y . Regarding the impact of the bubble shape on the trajectory, although the bubble shape have more variation in Xanthan gum solutions (from spherical bubble to teardrop bubble), it seems that the bubble trajectory is independent on the bubble shape in these media since all the bubbles rise vertically.

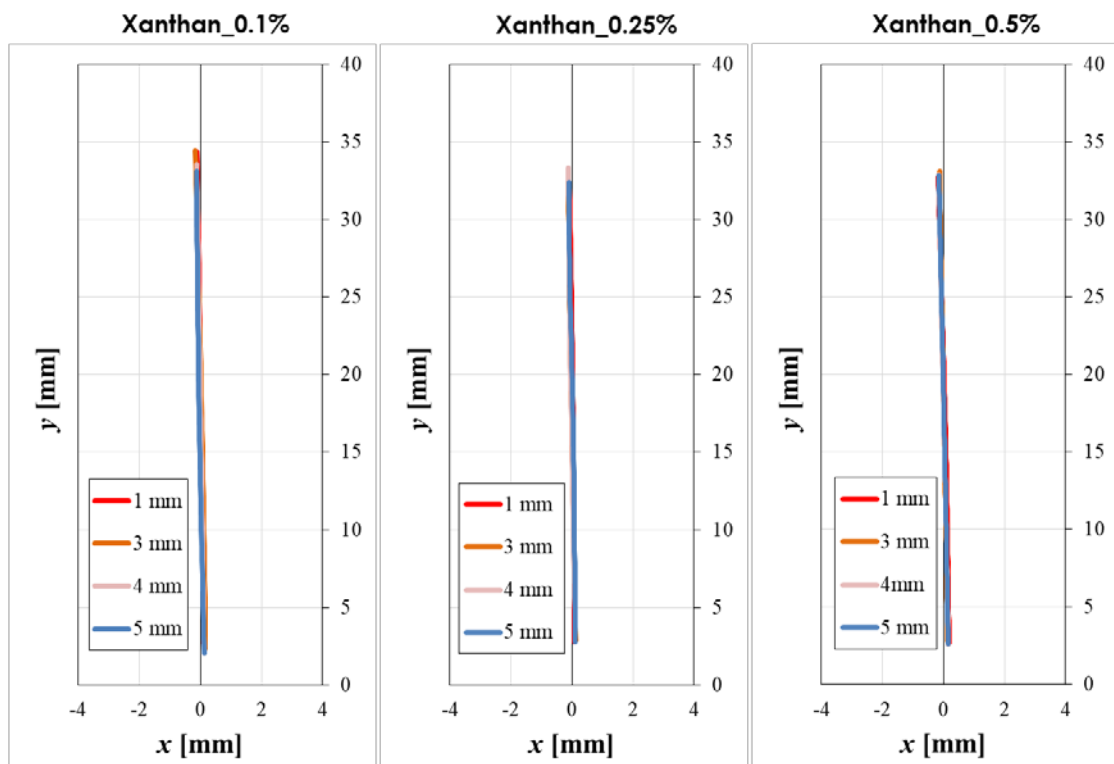


Figure 4-24 Trajectory of the bubble of different size ($D_{eq}=1-5$ mm) rising in Xanthan solutions

4.5 Conclusion

In this chapter, various single air bubbles (D_{eq} : 0.7-7 mm) rising in stagnant non-Newtonian fluids (polyacrylamide, Xanthan) are investigated by high-speed photography and image post-processing technologies. To characterize the bubble shape, an innovative model is proposed, which used parametric equations and contains the aspect ratio (E) and two shape parameters (α , β). The evolution of these three parameters has been investigated by considering the overall impact of multiple dimensionless numbers (Re , We , Ta , EO) and the fluid rheological index n . Based on the experimental results, several conclusions can be drawn:

1. Within the range investigated here ($-9 < \log Mo < -7$), the bubble shapes in PAAM solution cover the spherical bubble and the ellipsoidal bubble regime while, in Xanthan, the range of Mo is bigger ($-9 < \log Mo < 3$), and the data covers not only spherical and ellipsoidal bubbles but also prolate and teardrop ones.

2. In investigated non-Newtonian fluids, the aspect ratio of the bubble can be smaller than 1, indicating the appearance of an elongated bubble. To predict the aspect ratio, although it is still mainly related to the inertial force (for big oblate bubbles), simply considering one factor or one dimensionless number is insufficient. The aspect ratio of the bubble depends not only on the different forces applied to the bubble but also on the rheological properties of the fluid. An empirical correlation is then obtained for the aspect ratio by considering all the influencing factors, which are denoted by $Tn=We\cdot Ta\cdot n$.

3. The shapes of the bubbles from spherical to inverted teardrop can be characterized with good accuracy by adjusting three specific parameters (E , α , β) in the parametric shape equations. The parameter α correlates with the parameter β by a power-law function.

4. In non-Newtonian fluid, the cusp of the bubble (quantified by β) is related to the viscoelasticity as well as the shear-thinning level of the solutions. A correlation of

parameter β is obtained with the Deborah number (De , Eötvös number (Eo) and the shear-thinning index n . Along with the other correlations and the bubble equation, a complete system is established for bubble shape characterization and prediction, which will provide new ideas for future studies on bubble hydrodynamics.

5. Regarding the bubble trajectory, in PAAm solutions, the bubble path is linear for small spherical bubbles and is changed to a zigzag path for the ellipsoidal bubbles. On the other hand, the bubbles in Xanthan gum solution always rise vertically indicating that the trajectory is independent on the bubble shape and size.

With the knowledge of the bubble shape, the interfacial area for mass transfer can be calculated. The impact of the hydrodynamic property of bubble on the mass transfer is discussed in the next chapter.

Chapter 5

Mass transfer in polymer fluids

Abstract

Based on the planar laser-induced fluorescence with Inhibition (PLIF-I) experiments, the mass transfer and diffusion phenomena in the wake of single air bubbles (equivalent diameter~1-1.4 mm) rising in various aqueous polymer solutions (PAAm: 0.1 wt%-0.5 wt%; Breox: 2 wt%-9.1 wt%) are investigated. For each fluid medium, liquid-side mass transfer coefficient and the diffusion coefficient are determined and analyzed by considering multiple factors: the rheological properties of the fluid, the concentration of the solute, the hydrodynamics of the bubble, and the contamination effect. The results are compared with cases implemented in non-polymer solutions to clearly identify the characteristics of mass transfer in the polymer media. In addition, an extension study has been carried out for measuring the mass transfer from bigger bubbles ($D_{eq} = 1.5-5.5$ mm) in two types of solutions (PAAm 1 wt.% and Xanthan gum 0.1 wt.%). The impact of the deformation of the bubble shape on the mass transfer is investigated.

5.1 State of the art

5.1.1 Mass transfer quantification by visualization techniques

As introduced in Chapter 1, with the development of optical equipment such as high-resolution cameras, powerful lasers, and high-performance sensors, many visualization techniques are developed providing the feasibility to gain new insight into the local gas-liquid mass transfer. These techniques have been applied to the different systems and lots of achievements have been done giving a better quantification for the mass transfer.

(Roy and Duke, 2000) estimated local interfacial mass transfer coefficients for oxygen absorption from direct measurements of the concentration gradients and boundary layer thicknesses along the air bubble surface. The technique provides measurements of mass transfer coefficient that are uncoupled from the specific interfacial area. In the work of (Lee, 2002), oxygen concentration fields in a water body were visualized by the fluorescence oxygen visualization method. From image processing, the accurate pathway of oxygen-rich, cold water at the water surface was also visualized. The amount of oxygen transferred through the air-water interface during the experiment was measured and the oxygen transfer coefficient was determined. A novel calculation method for the measurement of mass transfer coefficients has been developed by (Kück et al., 2010). In the work of (François et al., 2011b), an original approach for accurately measuring the mass transfer of a single bubble rising in a liquid is reported. The approach consists of using PLIF technique at micro-scale to capture images of the released oxygen concentration field in the bubble wake. The applicability of the technique for determining mass transfer coefficients in different fluids ($1 < Re < 100$) is demonstrated and the relevance of the results is corroborated by established correlations. With the similar approach, (Dietrich et al., 2015) demonstrated that the oxygen concentration fields appear symmetric with a 3D Gaussian profile forming a concentric, rounded gradient of oxygen with the maximum concentrations at the center of the spot. The approach consists of capturing pictures of the concentration field at

micro-scale in the laminar bubble wake, which permits to accurately and quickly evaluate the gas-liquid diffusivity. In the work of (Jimenez et al., 2012b, 2012a), experiments based on a flat air-liquid interface were carried out in a Hele-Shaw cell. With assumptions of one-dimensional diffusion, a simplified mathematical approach is used to determine the diffusion coefficient of oxygen in the water then the method is extended to the wastewater cases (Jimenez et al., 2014). More recently, (Huang and Saito, 2017a) precisely calculated the instantaneous mass transfer coefficient of the bubble and discussed the influences of the bubble-surface contamination on the bubble motion and the mass transfer. (Roudet et al., 2017) measured the interfacial mass fluxes for pure confined oxygen bubbles of various shapes and paths rising in water and proposed a scaling law of the Sherwood number as a function of Peclet number. (Kong et al., 2018) obtained the evolution of CO₂ concentration for a rising bubble and the transfer from mass to the wake region by means of vortex shedding is determined. Several representative works for the bubble cases are listed in Table 5-1 with the gas-liquid types, the bubble size and the result of the quantification.

Table 5-1. Bibliography of the mass transfer quantification of a freely rising bubble by PLIF-I in the past decade

Author	Gas	Bubble Diameter [mm]	Liquid (aqueous solution)	Quantification result
(Dani et al., 2007)	O ₂	<1	water	image of [O ₂] distribution
(Stöhr et al., 2009)	CO ₂	0.5-5	water	image of [O ₂] distribution
(Hanyu and Saito, 2010)	CO ₂	2.9	water	image of [O ₂] distribution
(François et al., 2011a)	O ₂	0.72~1.88	water + glycerol (0-80 wt%) + ethanol (0-80 wt%)	k_L : 8.5×10^{-6} - 3.3×10^{-4} m/s
(Kück et al., 2012)	CO ₂	2.9	water	k_L : 1.5×10^{-4} - 3.5×10^{-4} m/s

(Valiorgue et al., 2013, 2014)	CO ₂	0.8~1.5	water ; water + ethanol (20 wt%) Na ₂ SO ₃	k_L for water case: $2.00 \times 10^{-4} - 4.64 \times 10^{-4}$ m/s
(Jimenez et al., 2013)	Air	0.9~2.24	water + ethanol (20 wt%); NaCl (1-5 g/L) ; glucose (0.5-1 g/L); glycerol (10-25 wt%);	k_L for water case: $2.49 \times 10^{-4} - 4.31 \times 10^{-4}$ m/s
(Jimenez et al., 2014)	O ₂	~1.20	Demineralized water, Treated water and wastewater + surfactant	D : $1.6 \times 10^{-9} - 2.03 \times 10^{-9}$ m ² /s k_L : $0.16 \times 10^{-4} - 3.95 \times 10^{-4}$ m/s
(Dietrich et al., 2015)	Air	0.72-1.88	glycerol (0-43 wt%)	D : $4 \times 10^{-11} - 2.09 \times 10^{-9}$ m ² /s
(Saito and Toriu, 2015b)	CO ₂	~1.16	water	[CO ₂]=1 - 2.5 mg/L in the bubble
(Huang and Saito, 2015, 2017a)	CO ₂	2.9	purified and contaminated water	k_L for purified water: $1.5 \times 10^{-4} - 3.5 \times 10^{-4}$ m/s contaminated water: $0.2 \times 10^{-4} - 0.4 \times 10^{-4}$ m/s
(Xu et al., 2017)	Air	0.90-1.23	water	D : $1.9 \times 10^{-9} - 2 \times 10^{-9}$ m/s
(Roudet et al., 2017)	O ₂	5.1-32	water + ethanol (20 wt%)	$Sh = 1.066 Pe^{1/2}$
(Kong et al., 2018)	CO ₂	1.9	water	[CO ₂] $< 2.5 \times 10^{-5}$ mol·L ⁻¹ in the core of the vortex.

In industrial application, most of the liquid media are polymers as in biological systems, cosmetic, food industries, etc. For wastewater treatment, polymers can play as flocculants, coagulants or emulsion breakers to remove the total suspended solids (TSS) and enhance the sedimentation process. It is believed that the presence of the molecule can affect the mass transfer (Levitsky and Shulman, 1995) and the rate of diffusion of oxygen through the polymer is a critical characteristic of the polymer's performance when the polymer used as medical implants, food containers, and sensor materials (Bowyer et al., 2004). It can be seen (in Table 5-1) that most of the previous research is implemented for bubbles rising in water and the study on the mass transfer of freely rising bubble in a complex liquid media like highly viscous fluid or polymer fluid are relatively rare. Therefore, this chapter contributes to study the effect of the polymer

solutions on the bubble-liquid mass transfer.

5.2 Mass transfer visualization and characterization

As shown in Table 5-1, the mass transfer of bubbles in polymer solutions has rarely been studied despite the fact that the properties of the polymer molecules may have an impact on the mass transfer (Levitsky and Shulman, 1995). To investigate this problem, the experiments have been implemented for single air bubbles rising in the different polymer solutions (PAAm: 0.1-0.5 wt%; Breox: 2-9.1 wt%) by using the technique of Planar Laser-Induced Fluorescence with Inhibition (PLIF-I). For each liquid medium, the properties of the liquid phase, such as viscosity, polymer type and concentration of the solute, as well as the hydrodynamics of the bubble, are taken into account and their impact on the mass transfer is estimated. The results are compared to some cases implemented in non-polymeric solutions mentioned in the literature.

5.2.1 Hydrodynamic result

Based on the two-camera experimental configuration (Chapter 2), the hydrodynamic behavior is recorded by the high-speed camera. The detailed results on the bubble size, rising velocity, and other parameters are shown in Table 5-2 for all the experimental cases.

Table 5-2 Hydrodynamics results of the bubble

Composition [wt.]		D_{eq} [mm]	U_b [mm/s]	\bar{E}	\bar{Re}	C_D
Water		1.02 ±0.02	268.54 ±1.69	1.13	273	0.18
+ Breox	2.00 %	1.16 ±0.01	113.15 ±1.02	1.02	66	1.19
	5.50 %	1.33 ±0.01	100.88 ±1.21	1.02	28	1.71
	9.10 %	1.40 ±0.01	86.58 ±0.71	1.02	11	2.44
+ PAAm	0.10 %	1.00 ±0.01	81.14±0.92	1.04	30	1.99
	0.25 %	1.00 ±0.01	69.83 ±0.77	1.00	18	2.66
	0.50 %	1.03 ±0.01	62.28±0.48	1.00	12	3.47

It can be seen that, although generated under the same conditions (identical nozzle, flow rate, etc.), the presence of polymer molecule changes the hydrodynamic properties of the bubble and the results depend on the type of solute.

In the Breox solutions (Newtonian fluid), the bubble has a larger size but rises much slower than the one in water. With a higher concentration of the solute, the velocity of the bubble decreases and the aspect ratio decreases and tend to be 1. The change of bubble behavior is related to the higher viscosity of the liquids (Chapter 2) which also leads to smaller Remolds number and larger drag coefficient.

In the PAAm solutions (non-Newtonian fluid), the equivalent diameter of the bubble stays close to 1 mm for three concentrations of the solute. The other results are similar to the ones in Breox except that the velocity of the bubble is even lower.

Since all the bubble in the experiment has a small size ($D_{eq} < 1.5$ mm), it is also found that the rising trajectories of all the bubbles are nearly rectilinear. Regarding the bubble shape, the aspect ratios are close to 1 for all the cases indicating the bubbles in this study can be assumed to be quasi-spherical. An example of the bubble shapes in the different types of the solution can be seen in Figure 5-1. In addition, the bubble rises

more slowly in polymer media, making it more reasonable to neglect the influence of the convection caused by the bubble motion on the mass transfer in the bubble wake.

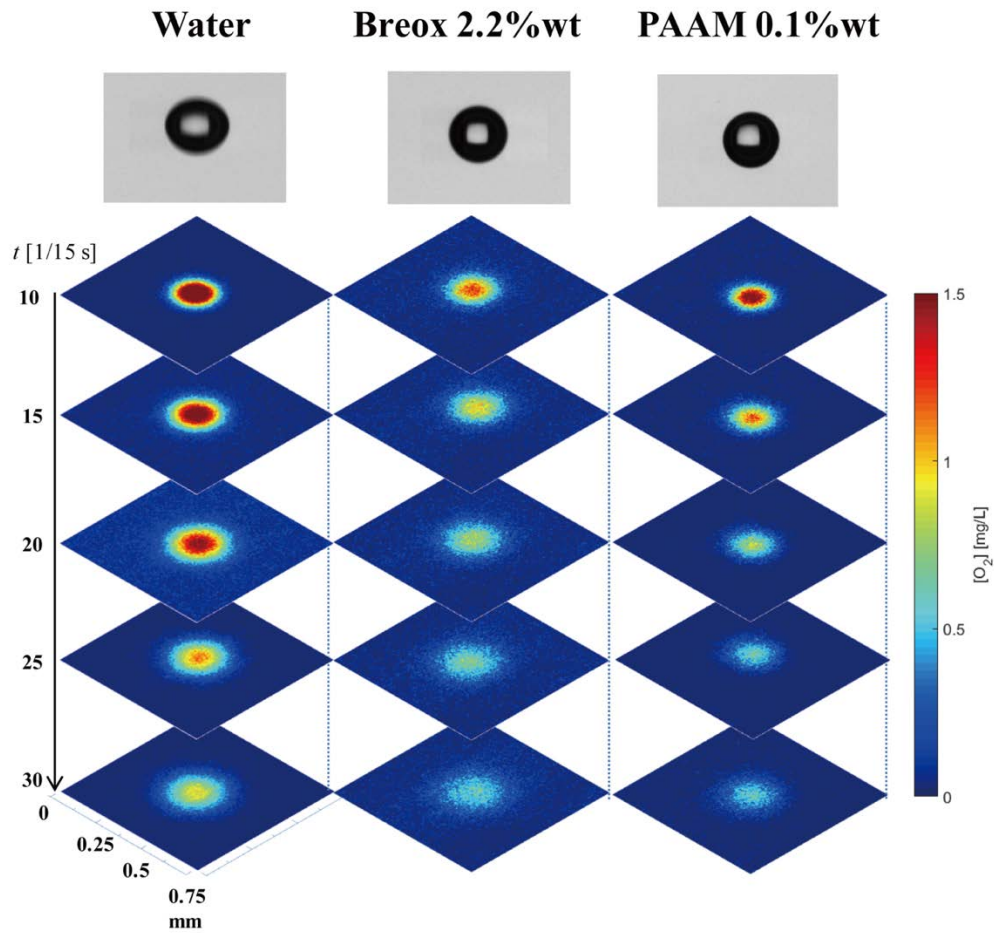


Figure 5-1 Examples of corrected images and shapes of a single bubble rising in water, Breox 2.2 wt% and PAAM 0.1 wt% solutions

5.2.2 Oxygen concentration field in the bubble wake

With the CCD camera located under the column (Chapter 2), the mass transfer is visualized in the bubble wake. The examples of the corrected images are given in Figure 5-1, which shows the evolution of the oxygen concentration field in the cross-section of the bubble wake (recorded every 5/15s as the laser frequency is 15 Hz) for three different fluids (water, Breox 2.2 wt%, and PAAM 0.1 wt%), with the corresponding

bubble shapes given at the top of the figure.

Some results are immediately visible on this figure. Since the bubble is small and quasi-spherical, the mass transfer or the oxygen concentration field is presented as a circular diffusion spot and the concentration distribution shows centrosymmetry. The oxygen concentration decreases with the distance from the spot center. As a function of time, the oxygen spot expands and the oxygen molecule diffuses from the spot center to the surroundings.

Comparing the mass transfer spots for the three cases, we can find that the transferred mass in polymer media is much less than that in water. Moreover, at the same moment, for the small concentration (Breox 2.2 wt%, and PAAm 0.1 wt%), the dissolved oxygen concentrates more at the center in the PAAm solution than in Breox solution even though the total mass transfer is basically the same in these two cases.

5.2.3 Characterization with Gaussian equation

In order to further quantify the mass transfer with the images as shown in Figure 5-1, a Gaussian model (Eq. (2-16)) is proposed for fitting the corrected oxygen concentration field. The fitting method is presented in Chapter 2. For each moment (each image), a set of the fitting parameters (ie. A , B , C) of the Gaussian model is obtained thus we can study the evolution of the concentration field by investigating the temporal evolution of the values of these three parameters. An example of the evolution curves is shown in Figure 5-2 for the PAAm 0.1 wt% case.

It can be seen that the parameter A , which refers to the peak value of the concentration field, has an exponential decay. The peak value decreases by 90% in the first 3 seconds. The mass transferred on the cross-section of the bubble wake seems to diffuse quickly from the point source to an infinite plane.

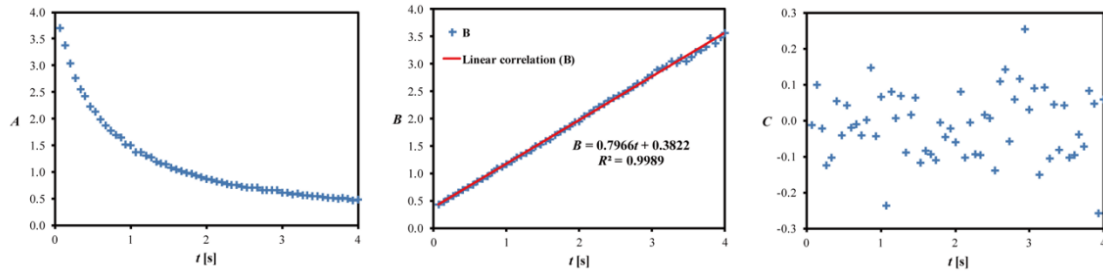


Figure 5-2 Evolution of the values of three parameters A , B , C as a function of time (Example of the PAAm 0.1 wt% case)

On the other hand, the parameter B increases linearly with time. When the B values are correlated with the linear function, the coefficient of determination is as high as 99%, showing the great linearity of the evolution of the parameter B . This property is believed to be related to the diffusion coefficient. As discussed in Chapter 2, for a total amount of transferred mass M diffusing from a point source on an infinite plane surface, the instantaneous concentration can be expressed as follows (for the oxygen diffusion in this study):

$$[O_2] = \frac{M}{4\pi Dt} \exp\left(-\frac{r^2}{4Dt}\right) \quad (5-1)$$

with r the distance from the spot center and D the diffusion coefficient.

By comparing Eq. (5-1) and the fitting Gaussian equation, it can be found that:

$$B = 4Dt \quad (5-2)$$

Thus, the slope of the curve $B-t$ (Figure 5-2-B) is equal to $4D$ leading to the knowledge of the diffusion coefficient. Aside from the method introduced in Chapter 2 which deduces the diffusion coefficient from the spot area, this provides an alternative way to estimate the diffusion coefficient from the fitting parameter B . The results by both methods are discussed in the next Section.

In addition, the value of parameter C scatters with time because it refers to the background noise. As expected, the parameter C can quantify the background impact,

caused by the remaining transferred mass or the instability of the laser. However, the majority of the values of C are between -0.1 mg/L and 0.1 mg/L, indicating the reliability of the image recording and acquisition system.

5.3 Result of mass transfer quantification

5.3.1 Mass flux

The mass flux can be calculated from the images of the oxygen concentration field. The images before and after the fitting with Gaussian equation are compared and shown in Figure 5-3. As discussed in Chapter 2, the flux of the oxygen J_{O_2} [$\text{mg}\cdot\text{s}^{-1}\cdot\text{m}^{-2}$] before fitting is regarded as a general oxygen spot that is calculated using the equation:

$$J_{O_2} = \frac{U_b \Sigma [O_2]_i \delta^2}{S_b} \quad (5-3)$$

where δ^2 is the area of a square pixel [m^2].

For the flux after fitting, the mass flux can be estimated with the fitting parameters A and B :

$$J_{O_2} = \frac{U_b \pi \cdot A \cdot B}{S_b} \quad (5-4)$$

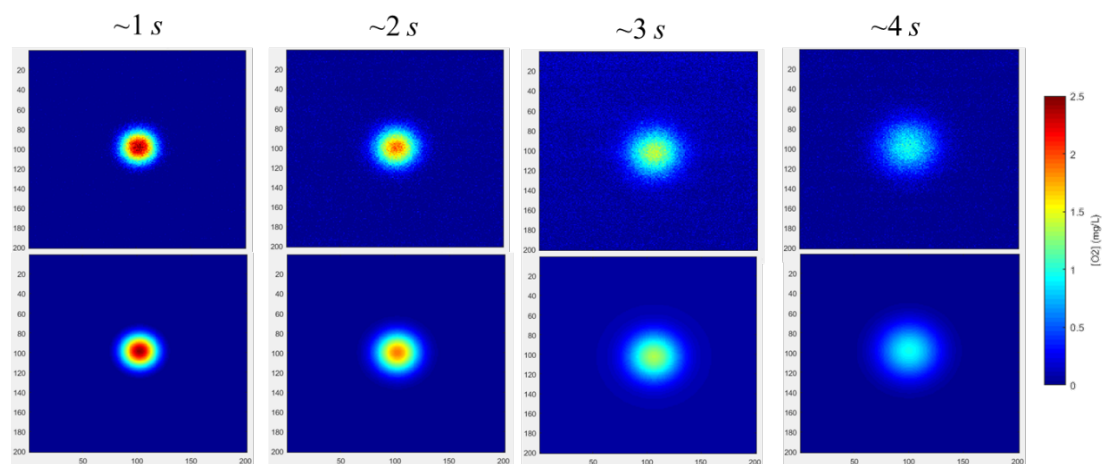


Figure 5-3 Oxygen concentration field before and after the fitting with Gaussian equation. (Example of PAAM_0.1 wt.%)

To estimate the impact of the fitting process on the mass transfer determination, the fluxes before and after fitting are calculated. The result is shown in Figure 5-4. The case of water was chosen as the example for its wider range of flux values. Good consistency can be seen between the fluxes before fitting and after fitting, with a deviation of less than 5%. In other solutions, since the flux value is more stable after the bubble passing, the deviation is even smaller, indicating that the dissolved oxygen spot on the bubble wake is more circular and can be better characterized by Gaussian equation.

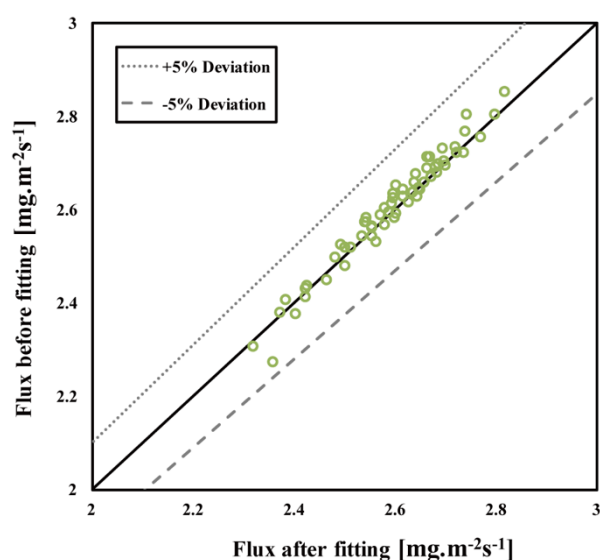


Figure 5-4. Comparison between flux before fitting and flux after fitting (Example of water case)

The evolution of the estimated flux (after fitting) is plotted versus time for different fluids in Figure 5-5. For the water case, the flux increases gradually in the first zone ($t < 0.8s$), which, experimentally, corresponds to the time necessary for the bubble to pass far enough to satisfy the non-convection hypothesis. Then, while the bubble continues to rise and the impact of the bubble passing tends to disappear in the second zone ($0.8 < t < 3s$), the flux value remains constant and the mathematical approach for

determining the mass transfer is applicable in this region. After a longer time (third zone: $t > 3$ s), the experimental points start to scatter. This distortion is due to the broad distribution of the oxygen and the relatively low oxygen concentration in each pixel. Thus it is difficult to distinguish the oxygen transferred by the bubble from the background noise, which is estimated to be in the order of $0.1 \text{ mg}\cdot\text{L}^{-1}$. This evolution result of the flux is consistent with the findings of (Jimenez et al., 2013) in the first two zones. In the third zone, a diminution of flux was visualized in their study due to the fixed threshold setting the limit between mass transfer and the background. This distortion is improved since the threshold is not applied in the present image processing.

For the polymer cases, the evolution of the flux is similar to the water case. However, the zone of increase ($t < 0.4$ s) is much shorter as the bubble rising velocity is lower in the polymer media. The long-chained molecules of the polymer are thought to be another factor that can maintain the stability of the fluid. Both factors can thus reduce the impact of the bubble motion on the fluid. When the Breox and PAAm cases are compared, the flux of the PAAm depends more on the concentration of the solute. For Breox solution at a different concentration, there is no obvious difference in the length of the first zone and the flux values of the second zone vary from 0.94 to $0.74 \text{ mg}\cdot\text{m}^{-2}\cdot\text{s}^{-1}$ when the solution becomes denser. On the other hand, for the PAAm cases, the length of the first zone is different for the three concentrations: it becomes shorter with higher concentration. The flux values of the second zone decrease from 0.85 to $0.43 \text{ mg}\cdot\text{m}^{-2}\cdot\text{s}^{-1}$ when the concentration increases from $0.1 \text{ wt}\%$ to $0.25 \text{ wt}\%$. This suggests that even a slight change of concentration will have an obvious impact on the mass transfer in PAAm solutions. The different results for these two polymer solutions are presumed to be related to their rheological properties.

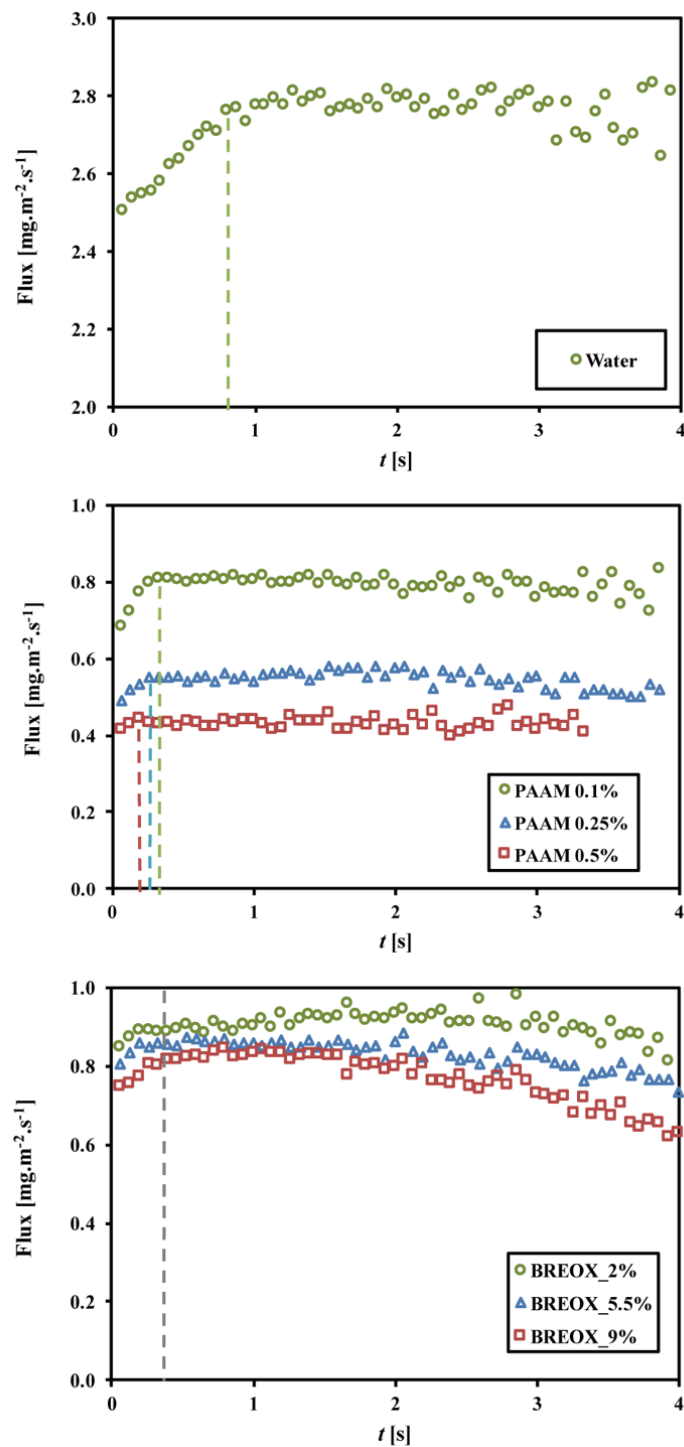


Figure 5-5 Evolution of the estimated flux as a function of time in different liquids (Water, PAAm and Breox)

5.3.2 Diffusion coefficient

The diffusion phenomenon on the cross-section of the bubble wake for each solution has been displayed in Figure 5-1. In order to quantify the diffusion, the profile of the dissolved concentration fields is investigated. Since the oxygen concentration field has a centrosymmetric distribution, only one profile containing the symmetry axis is plotted for each moment. The profile refers to the one-dimensional Gaussian equation:

$$[O_2](x) = A \exp \frac{-x^2}{B} \quad (5-5)$$

where the values A and B are obtained from the fitting result and the mass transfer spot center is moved to the origin ($x = 0$).

The results of six consecutive moments with the time interval $\Delta t = \frac{10}{15} s$ are shown in Figure 5-6 for Breox solutions and Figure 5-7 for PAAm cases. The total mass transfer of the spot $M [mg \cdot m^{-1}]$ defined by (2-36) is also given in the figures.

As discussed before, for the Breox solutions, the dissolved oxygen diffuses from the spot center to the surroundings. The peak value of the profile drops rapidly in the first two moments and the oxygen field tends to become uniform. With increasing concentration of the solute, total transfer mass M increases. For the PAAm solutions, a similar diffusion phenomenon is observed under the same concentration of solute except that the profiles look slimmer, indicating that the mass transfer is concentrated nearer the spot center. With the increasing concentration of the solute, the total transfer mass decreases, unlike the transfer in the Breox cases.

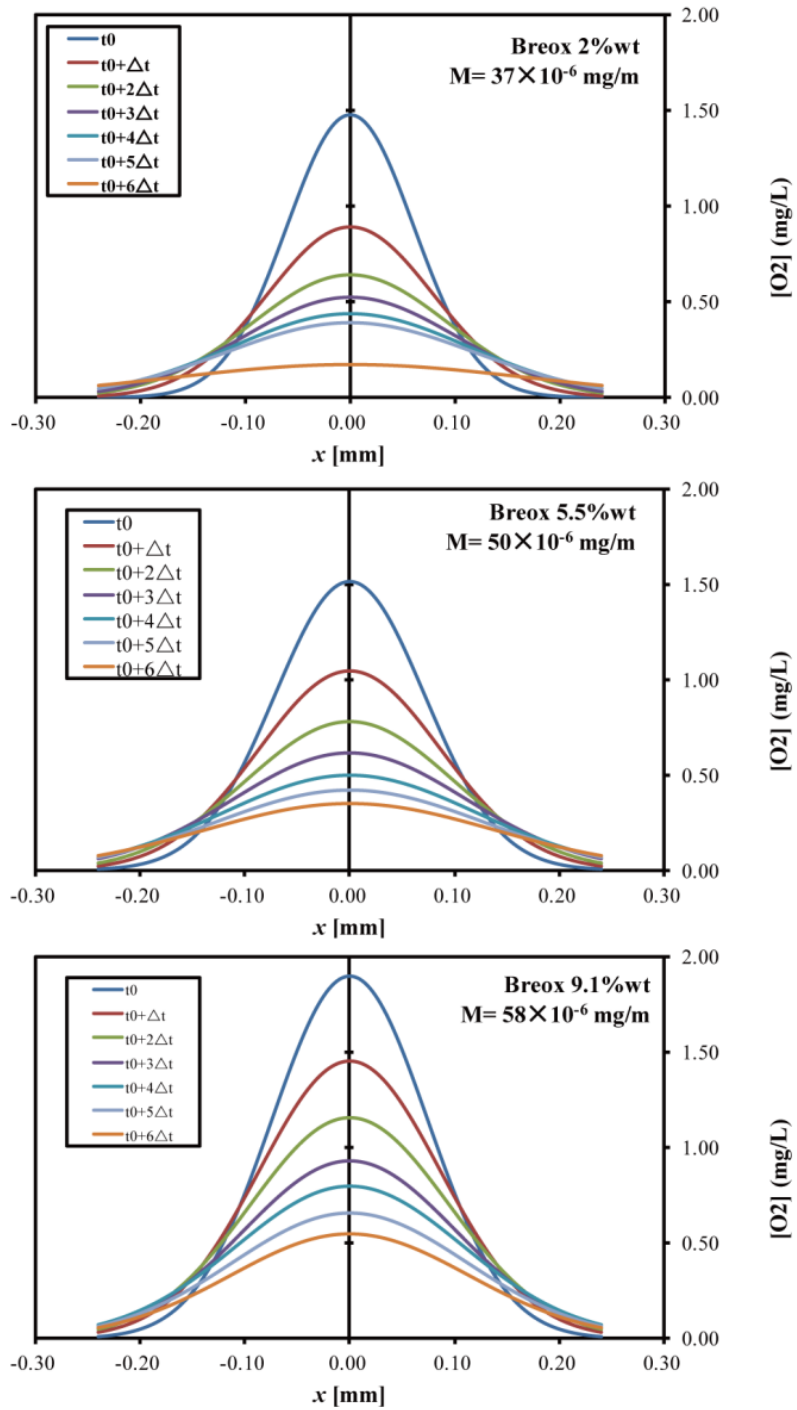


Figure 5-6 Profile of dissolved oxygen concentration fields in the bubble wake cross sections in Breox solutions ($\Delta t = 2/3$ s)

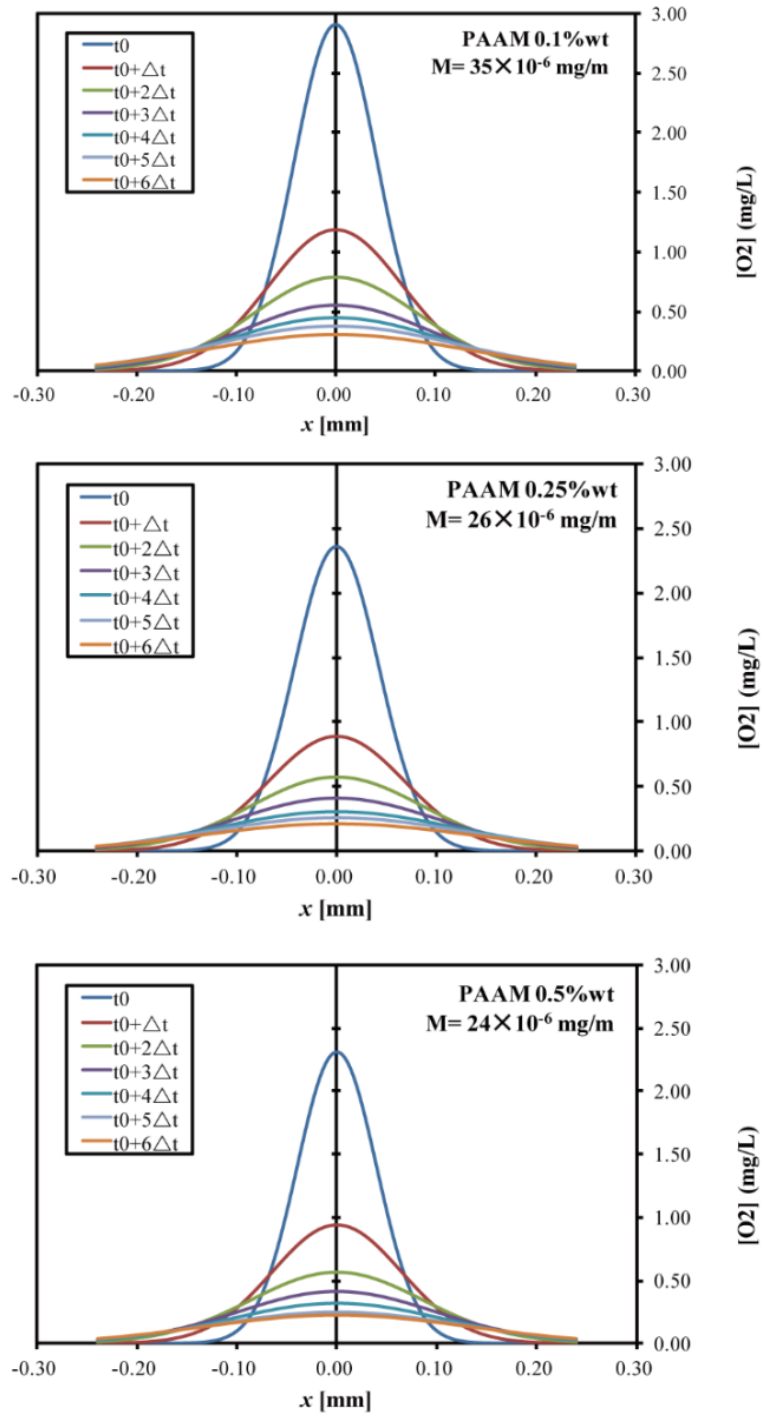


Figure 5-7 Profile of dissolved oxygen concentration fields in the bubble wake cross sections in PAAM solutions ($\Delta t=2/3$ s)

As explained in Section 2.5.3, the diffusion coefficient can be calculated from the evolution of the partial spot area as a function of time.

$$S_{spot} = \pi R^2 = 2\pi\eta Dt \quad (5-6)$$

In the study, the value of η is set to 1. It has already been proved that the choice of η does not affect the estimation of the diffusion coefficient (Xu et al., 2017). Thus the slope of the curve $S_{spot}-t$ is equal to $4\pi D$. The experimental data and the fitting curves are shown in Figure 5-8. The result of the water case and the highest concentrations of the two polymer solutions were chosen for plotting in order to indicate the difference between them. It is found that all three sets of data show good linearity as the coefficient of determination for each is higher than 95%. Moreover, the diffusion is reduced when the polymer solute is added.

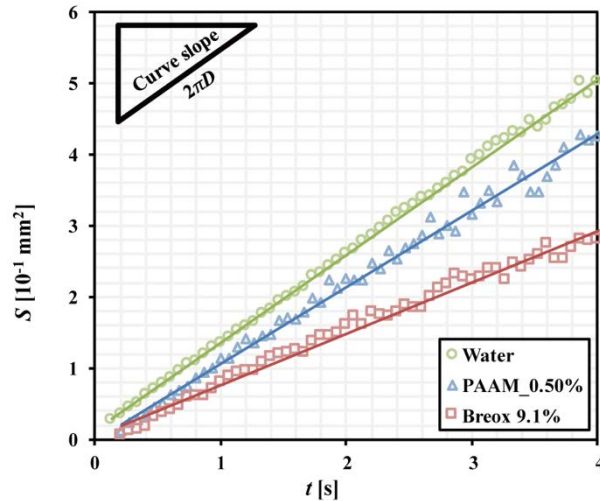


Figure 5-8 Evolution of the spot area as a function of time

The complete results on the diffusion coefficient are given in Table 5-3, in which the diffusion coefficient is calculated with Eq. (2-31) and Eq. (5-2). It can be seen that there is no great difference between the results of the two methods. For both polymer

solutions, the diffusion coefficient decreases with a higher concentration of the solute.

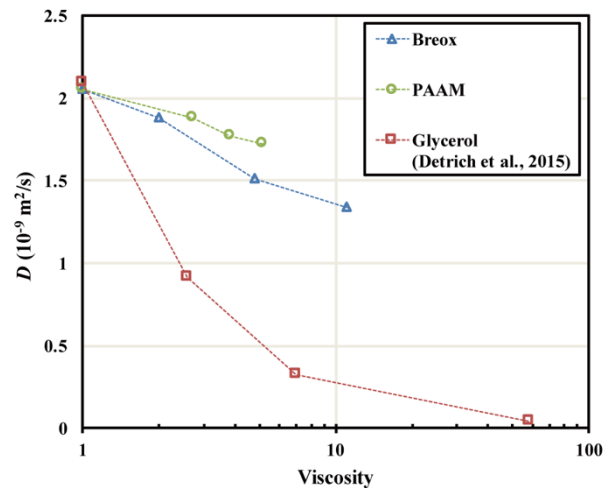
Table 5-3 Results for the diffusion coefficient

Solution	Concentration [wt.]	<i>D</i> by Eq. (2-31) [10⁻⁹ m²/s]	<i>D</i> by Eq. (5-2) [10⁻⁹ m²/s]
Water	-	1.99±0.05	2.00±0.15
	2.00%	1.88±0.02	1.86±0.09
Breox	5.50%	1.50±0.02	1.48±0.06
	9.10%	1.34±0.01	1.32±0.05
	0.10%	1.88±0.02	1.84±0.08
PAAm	0.25%	1.77±0.02	1.78±0.07
	0.50%	1.72±0.02	1.70±0.07

To investigate the effect of rheological properties on the diffusion, the result of the viscosity and averaged diffusion coefficient for each solution are listed in Table 5-4. It can be seen that diffusion is inhibited when the liquid media become more viscous. For the same viscosity, the diffusion coefficient is higher in PAAm solution than that in Breox solution and their difference tends to increase for higher viscosities. The diffusion coefficient is plotted versus viscosity (Figure 5-9). and compared with the work by (Dietrich et al., 2015) in which experiments were carried out to measure the diffusion coefficient of a bubble rising in glycerol, a non-polymer fluid. As can be seen in the figure, the diffusion is much more significant in the polymer than in non-polymer medium at the same viscosity.

Table 5-4 Result of the viscosity and diffusion coefficient for each solution

Solution	Concentration [wt.]	μ [10^{-3} Pa·s]	\bar{D} [10^{-9} m ² /s]
Water	-	1.00	2.00
	2.00%	1.99	1.87
Breox	5.50%	4.77	1.49
	9.10%	10.96	1.33
	0.10%	2.75	1.86
PAAm	0.25%	3.84	1.77
	0.50%	5.15	1.71

**Figure 5-9 Diffusion coefficient versus viscosity in different liquid media**

5.3.3 Mass transfer coefficient

With the knowledge of the flux, as driven in Chapter 2, the liquid side mass transfer coefficient k_L can be calculated with the flux density J_{O_2} divided by the driving force ($[O_2]^* - [O_2]_0$):

$$J_{O_2} = \frac{F_{O_2}}{S_b} \quad (5-7)$$

$$k_L = \frac{J_{O_2}}{[O_2]^* - [O_2]_0} \quad (5-8)$$

The results are shown in Table 5-5. It can be seen that when the polymer molecule is present, the mass transfer coefficient, k_L , decreases dramatically, from 3.47×10^{-4} m/s to less than 1×10^{-4} m/s. Like the mass flux, the mass transfer coefficient decreases with the higher concentration of solute.

Table 5-5 Results for the liquid side mass transfer coefficient and the contaminated angle

Composition [wt. %]		k_L [10^{-4} m·s $^{-1}$]	k_L Frössling [10^{-4} m·s $^{-1}$]	k_L Higbie [10^{-4} m·s $^{-1}$]
Water		4.47±0.22	1.70	8.20
+ Breox	2.00 %	1.16±0.09	0.90	4.84
	5.50 %	1.06±0.09	0.65	4.08
	9.10 %	0.95±0.07	0.43	3.25
+ PAAm	0.10 %	1.06±0.09	0.78	4.40
	0.25 %	0.78±0.05	0.67	3.98
	0.50 %	0.69±0.05	0.58	3.64

The experimental values are compared with the extreme cases of a clean bubble (Higbie, 1935) and a fully contaminated one (Frössling, 1938).

$$k_{L_{Higbie}} = \frac{D}{d_{eq}} (1.13 Re^{0.5} Sc^{0.5}) \quad (5-9)$$

$$k_{L_{Frössling}} = \frac{D}{d_{eq}} (2 + 0.66 Re^{0.5} Sc^{0.33}) \quad (5-10)$$

where Sc is the Schmidt Number, defined as $\mu_L / \rho_L D$. The results are listed in Table 5-5. Our experimental results lie between these two extreme cases. This implies that the bubble is partially contaminated, which makes sense since the water could hardly be considered as extra pure (Alves et al., 2005) and the dye or polymer molecule also alters the bubble contamination. It can also find that all the experimental k_L closer to

the value by Frössling model indicating that the bubble is at high contamination level.

5.3.3.1 Bubble velocity on the mass transfer

Regarding the influence of the hydrodynamics of the bubble on the mass transfer, the velocity is reduced in polymer mainly due to the high viscosity. The Re number of the bubble is much smaller in polymer solutions than in water so the flow field is more stable and less turbulent that will reduce the mass transfer. To some extent, this is believed to be the main reason for the mass transfer reduction.

On the other hand, in spite of the impact of velocity, we can estimate the mass transfer per unit area by dividing the total transferred mass M by the bubble surface area S_b (results given in Table 5-6). As given in Chapter 2, the total transferred mass M can be obtained by the equation:

$$M = \pi \cdot A \cdot B \quad (5-11)$$

It can be seen that the mass transfer per unit area for bubble rising in polymer solutions is smaller than the result in water (33%-38% decrease in Breox and 21%-49% decrease in PAAm). In particular, the bubble rises slower in more concentrated Breox solutions but the mass transfer per unit area is even bigger than the result in thinner solutions. Regarding this, the lower velocity is not the only reason why the mass transfer is reduced in polymer solutions.

Table 5-6 Impact of bubble velocity on the mass transfer

Composition [wt. %]		U_b [mm·s ⁻¹]	\bar{M} [10 ⁻⁶ mg·m ⁻¹]	\bar{M}/S_b [mg·m ⁻³]
Water		268.54 ±1.69	45.80	14.15
+ Breox	2.00 %	113.15 ±1.02	36.99	8.75
	5.50 %	100.88 ±1.21	49.58	8.92
	9.10 %	86.58 ±0.71	57.61	9.36
+ PAAm	0.10 %	81.14±0.92	35.06	11.09
	0.25 %	69.83 ±0.77	25.90	8.38
	0.50 %	62.28±0.48	24.08	7.23

5.3.3.2 Contamination effect on the mass transfer

To investigate the contamination properties, the cap angle was introduced. According to the stagnant cap model by (Sadhal and Johnson, 1983), for a bubble whose interface is partially covered by a stagnant layer of surfactant, a cap angle φ_{cap} can be proposed to denote this non-slip region as presented in Figure 5-10. Thus when $\varphi_{cap} = 0^\circ$ the bubble is clean and when $\varphi_{cap} = 180^\circ$, the bubble is fully contaminated. The cap angle can be calculated by the normalized drag coefficient:

$$C_D^*(\varphi_{cap}) = \frac{C_D - C_D^m}{C_D^{im} - C_D^m} = \frac{1}{2\pi} \left(2\varphi_{cap} + \sin(\varphi_{cap}) - \sin(2\varphi_{cap}) - \frac{1}{3}\sin(3\varphi_{cap}) \right) \quad (5-12)$$

where C_D is the drag coefficient of the bubble. C_D^m and C_D^{im} are the drag coefficients for a clean bubble and for a fully contaminated one, respectively.

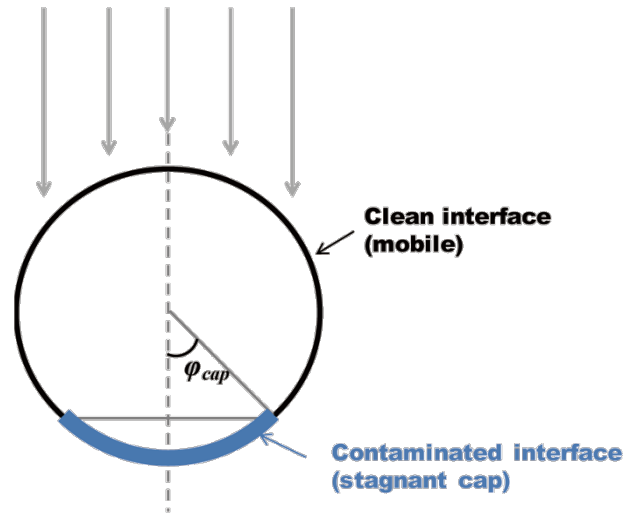


Figure 5-10 Stagnant cap model

Since the Reynolds numbers in our study are small ($Re < 100$), this equation is applicable by considering the correlations of (Schiller and Naumann, 1933) and (Mei et al., 1994):

$$C_D^{im} = \frac{24}{Re} (1 + 0.15Re^{0.687}) \quad (5-13)$$

$$C_D^m = \frac{16}{Re} \left(1 + \frac{Re}{8 + 0.5(Re + 3.315Re^{0.5})} \right) \quad (5-14)$$

The expression of the drag coefficient results from the buoyancy and drag force for an isolated bubble rising at terminal velocity has been deduced in Chapter 4:

$$C_D = \frac{4}{3} \frac{g \cdot D_{eq}}{U_b^2} \quad (5-15)$$

The equation above is valid for spherical bubbles. Although some bubbles in our study were ellipsoidal, their aspect ratios were relatively close to 1. So this approach can still be used for the contamination angle and drag coefficient calculation.

The result of drag coefficients is listed in Table 5-7. It can be seen that the drag

coefficients for all cases have the values between the extreme values for a clean bubble and for a fully contaminated one that is consistent with the result when the mass transfer coefficient is compared with the models of (Higbie, 1935) and (Frössling, 1938). With the normalized drag coefficient, the cap angles can be deduced by Eq. (5-12). The result is also given in the table.

Table 5-7 Results of normalized drag coefficient and cap angle

Solution	Concentration [wt.]	C_D^{im}	C_D	C_D^m	C_D^*	φ_{cap} [°]
Water	-	0.71	0.18	0.15	0.06	29
	2.00%	1.33	1.19	0.54	0.81	100
Breox	5.50%	2.11	1.71	1.08	0.61	81
	9.10%	3.83	2.44	2.26	0.11	39
	0.10%	2.06	1.99	1.05	0.93	117
PAAm	0.25%	2.79	2.66	1.55	0.90	112
	0.50%	3.56	3.47	2.08	0.94	119

It can be found that For PAAm cases, the cap angles are large which is consistent with high contamination level. However, for other cases, the cap angles are too small considering their relatively low mass transfer coefficients. It implies that the cap model, which is useful to characterize the hydrodynamics around the bubble, is not quite valid for characterizing the mass transfer to some extent. The explanation for this distortion is that, according to the cap model by (Sadhal and Johnson, 1983), the contaminant distributes only on the stagnant cap. Thus, for a little contaminated bubble with a small cap angle, there is no contaminant in most part of the bubble. However, for a real rising bubble, as depicted in Figure 5-11, away from the cap, the concentration of the contaminant decreases gradually along the bubble surface. There are also some contaminants outside the cap, and they will still affect the mass transfer. In this point of view, the cap angle is underestimated.

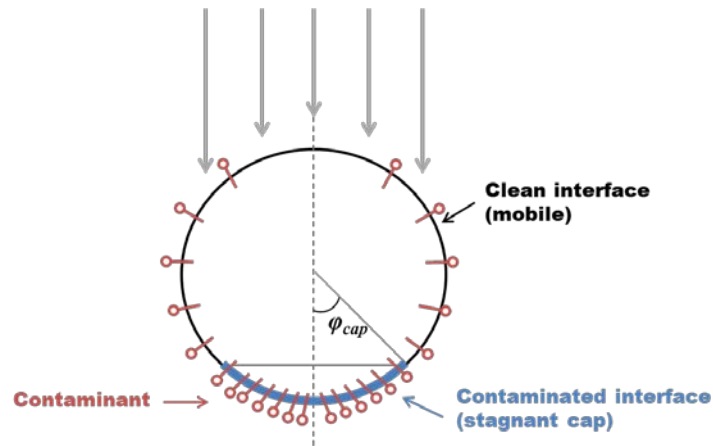


Figure 5-11 Cap angle and contamination on a real bubble.

In order to find a better contamination angle, from a point of view of mass transfer, a normalized Sherwood number is $Sh^*(\varphi_{cap})$ defined as follows:

$$Sh^* = \frac{Sh - Sh^m}{Sh^{im} - Sh^m} \quad (5-16)$$

with the Sherwood number:

$$Sh = \frac{k_L D_{eq}}{D} \quad (5-17)$$

The value Sh^m and Sh^{im} can be obtained from the Higbie model for a clean bubble and from Frössling model for a fully contaminated one.

According to the work of (Takemura and Yabe, 1999) which carried out a numerical analysis of the dissolution process of the stagnant cap model, a correlation between Sh^* and the cap angle was proposed:

$$Sh^* = 1 - [1 - C_D^*(\varphi_{cap_rec})]^{0.5} \quad (5-18)$$

The curve of the normalized drag coefficient (left y-axis) and Sherwood number (right y-axis) as a function of cap angle is shown in Figure 5-12.

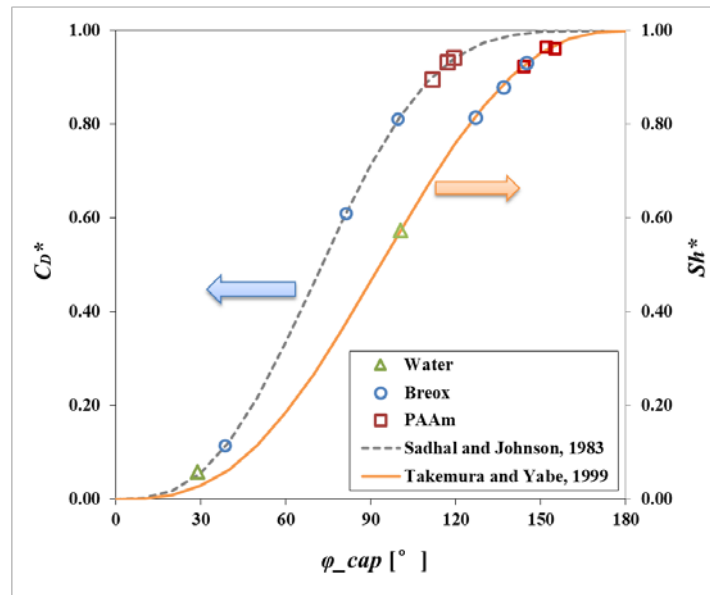


Figure 5-12 Normalized drag coefficient vs stagnant cap angle (Left y-axis); Normalized Sherwood number vs stagnant cap angle (Right y-axis)

By using the mass transfer coefficient and the diffusivity measured in this study, the rectified cap angles ϕ_{cap_rec} are calculated and given in Table 5-8. It can be found that rectified cap angles have a better agreement with the mass transfer result from the experiment. They are all larger than the original cap angles, especially for the water and Breox cases. Compared with the result in water, bubbles in polymer solutions always have a bigger cap angle. This suggests that the presence of polymer particles will enhance the contamination of the bubble surface from the mass transfer point of view and reduce the mass transfer. Moreover, when the concentration of the solute increases, the cap angle decreases for the Breox solutions but remains stable at high values for the PAAm cases. This can explain why k_L decreases less in Breox solutions than in the PAAm solutions when the solutions become thicker.

Table 5-8 Results of normalized Sherwood number and rectified cap angle

Solution	Concentration [wt.]	Sh_{im}	Sh	Sh_m	Sh^*	φ_{cap_rec} [°]
Water	-	87	228	418	0.57	101
Breox	2.00%	55	72	299	0.93	145
	5.50%	50	82	316	0.88	137
	9.10%	45	100	340	0.81	127
PAAm	0.10%	42	57	235	0.92	144
	0.25%	37	44	224	0.97	152
	0.50%	35	41	218	0.96	155

5.4 Extension to mass transfer from big bubbles

Based on the same experimental configuration, the measurement is extended for the mass transfer from bigger bubbles ($D_{eq} = 1.5-5.5$ mm) which are generated with stainless steel needles of different calibers (0.7-1 mm, see Chapter 2). According to the study of the bubble shapes in Chapter 4, two solutions are used in the section including PAAm 1 wt.% and Xanthan gum 0.1 wt.% in order to have stable bubble shapes. The visualization results of the mass transfer near the bubbles in different sizes are shown in Figure 5-13 for PAAm case and Figure 5-14 for the Xanthan case. The results of the bubble shapes are also given above each image involving the equivalent diameter, the aspect ratio and the shape parameters α , β (defined in Chapter 4). It should be noticed that the trajectory of the bubbles in this section are almostly vertical (see Chapter 4) and its impact on the mass transfer is not considered.

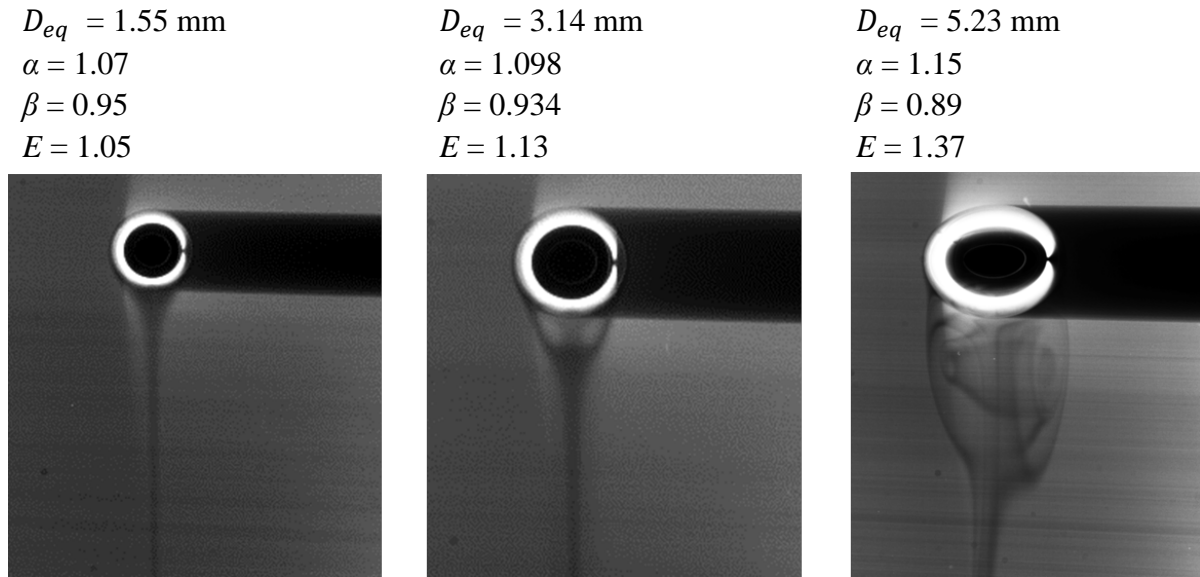


Figure 5-13 Visualisation result of the mass transfer of bubbles in different sizes rising in PAAM solutions (1.25 wt. %).

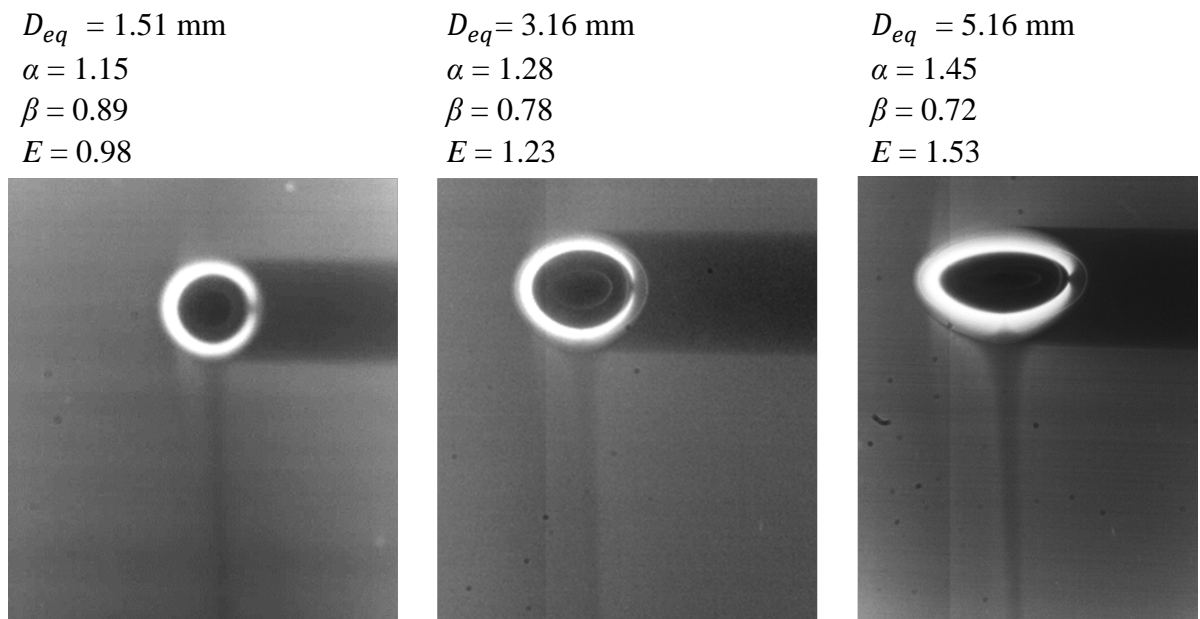


Figure 5-14 Visualisation result of the mass transfer of bubbles in different sizes rising in Xanthan gum solution (0.1% wt.).

For the PAAM case, when the bubble size increases, the aspect ratio has changed from 1.05 to 1.37 indicating the bubble gets more oblate. Meanwhile, the shape parameters are basically close to 1 thus the bubble shapes change from spherical to ellipsoidal. For

small bubble ($D_{eq} \approx 1.5$ mm), the mass transfer is concentrated at a small area in the rear of the bubble. When the bubble enlarges, it can be seen that the profile of mass transfer become more complex near the bubble surface. Two vortices are developed in the bubble wake and can be clearly visualized for the biggest bubble ($D_{eq} > 5$ mm).

For the Xanthan gum case, there is more variation in the bubble shape. When the bubble size increases, not only the aspect ratio changes from 0.98 to 1.53 but also the shape parameter β decreases to as low as 0.72. According to the discussion in Chapter 4, the small value of the parameter β leads to tip tail of the bubble. The property can be seen from the images (Figure 5-14) which are different from the ellipsoidal shape in PAAM case. Thanks to this bubble shapes, the profile of the mass transfer from the bubbles in all the investigated sizes are similar without vortices. Compared with the result of PAAM cases, it can be assumed that the more sharp shape can maintain the structure of the mass transfer.

The mass transfer in the cross-section of the bubble wake is also captured. The oxygen concentration fields are shown in Figure 5-15 for PAAM case and Figure 5-16 for the Xanthan case with the corresponding bubble shapes. It can be seen that the mass transfer spots on the image are circular for small bubbles in PAAM solution but when the bubble enlarges, the mass transfer spot is no longer circular. Compared to the study by (Jimenez et al., 2013) which has measured the mass transfer of the non-spherical bubbles in water, the behavior of the mass transfer spot is similar to the case of the bubble in equivalent diameter of 0.9 mm -2 mm. However, since the PAAM solution is much viscous than water, the mass transfer spot doesn't disperse while the mass transfer presents as two rotating filaments in water for the bubbles in the same size (Yamamoto et al., 2008).

On the other hand, the oxygen concentration field of Xanthan cases can maintain approximately circular even for a very big bubble ($D_{eq} > 5$ mm). This result is consistent with the visualization images, since the mass transfer structure is quite stable in Xanthan gum cases.

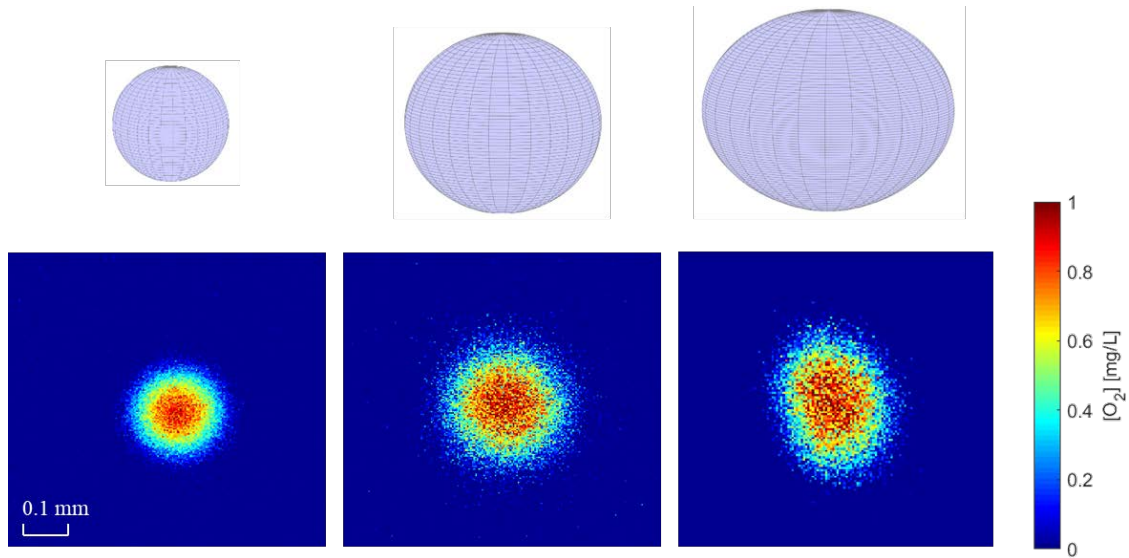


Figure 5-15 Oxygen concentration field in the wake of bubbles in different sizes rising in PAAm gum solution (1% wt.).

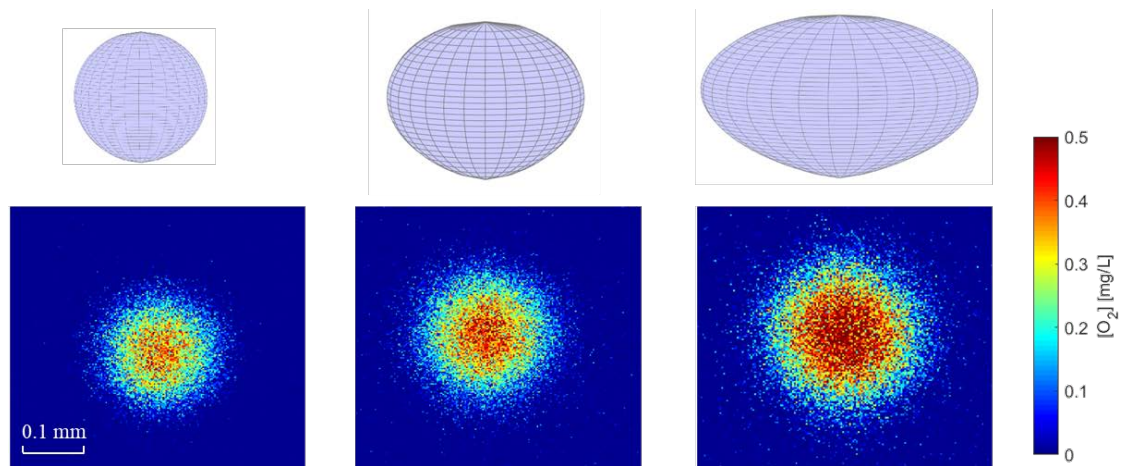


Figure 5-16 Oxygen concentration field in the wake of bubbles in different sizes rising in Xanthan gum solution (0.1% wt.).

To quantify the mass transfer, the transferred mass is estimated with images of oxygen concentration field. Since the mass transfer spot is not always circular, instead of using the Gaussian equation, the transferred mass, M [$\text{mg} \cdot \text{m}^{-1}$], is calculated as the sum of the oxygen concentrations $[O_2]_i$ in all pixels on the experimental image:

$$M = \sum [O_2]_i \delta_{pixel}^2 \quad (5-19)$$

where δ_{pixel}^2 is the area of a square pixel [m²].

The result is given in Table 5-9. There is more mass transfer for the bubbles rising in PAAm solutions than the ones in Xanthan gums. This is believed due to the properties of the polymer regarding that the molecule of Xanthan gum has a longer chain and its solutions are more visco-elastic and present as a colloid.

For the same solute, the mass transfer increase for the bigger bubbles which has a larger interfacial area for substance exchange. Nevertheless, if we compare the mass transfer per surface area for each case, it can be found that the small bubble has a high mass transfer efficiency than a big bubble.

Table 5-9 Total transferred mass on the oxygen concentration field

Solution	D_{eq} [mm]	S [mm ²]	\bar{M} [10 ⁻⁶ mg·m ⁻¹]	\bar{M}/S_b [mg·m ⁻¹]
PAAm 1 wt. %	1.55±0.01	7.55	60.16	7.97
	3.14±0.02	30.97	97.47	3.14
	5.23±0.03	85.93	166.23	1.93
Xanthan gum 0.1 wt. %	1.51±0.01	7.16	33.46	4.67
	3.16±0.01	31.37	45.63	1.45
	5.16±0.01	83.65	86.86	1.04

With the total transferred mass on the oxygen concentration field, the mass transfer coefficient can be calculated and the result is given in Table 5-10. It is found that although a bigger bubble rises faster and has a larger interfacial area, the mass transfer coefficients in both types of solutions decreases as a function of the bubble size. This property is different from the result in water. According to the study of (Sastaravet et al., 2014), the mass transfer coefficient increases with the air bubble size for small bubbles and tends to be constant for the bubble larger than 3.5 mm which is believed to behave as fluid particles with a mobile surface (Higbie, 1935). The increase of the mass

transfer coefficient is related to change of the bubble shape (from spherical bubble to cap bubble) which will enhance the bubble surface oscillation. Different from the water case, the bubbles rising in polymer solutions have a more trajectory and less shape variation ($D_{eq}=1-5$ mm) against the bubble size. This might lead to a decrease of the mass transfer coefficient that is also found in the literature (Barnett et al., 1966; Calderbank and Lochiel, 1964) for CO₂ bubbles. Moreover, under the investigated range, the mass transfer coefficients are smaller in Xanthan solutions than in PAAm.

Table 5-10 Result of the mass transfer coefficient

Solution	D_{eq} [mm]	U_b [mm·s ⁻¹]	k_L [10 ⁻⁴ m·s ⁻¹]
PAAm 1 wt.%	1.55±0.01	74.54 ±1.02	0.74
	3.14±0.02	171.61 ±1.21	0.67
	5.23±0.03	232.16 ±0.71	0.56
Xanthan gum 0.1 wt.%	1.51±0.01	72.84±0.92	0.43
	3.16±0.01	186.37 ±0.77	0.34
	5.16±0.01	245.66±0.48	0.32

5.5 Conclusion

Based on previous works (Dietrich et al., 2015; François et al., 2011a; Jimenez et al., 2013; Xu et al., 2017), the study of the mass transfer and the diffusion phenomenon in the wake of a bubble has been extended to aqueous polymer media here. By the technique of Planar Laser-Induced Fluorescence with Inhibition (PLIF-I), experiments were performed with air bubbles ($D_{eq}=1-1.4$ mm) rising in various aqueous polymer solutions (PAAm: 0.1-0.5 wt%; Breox: 2-9.1 wt%). The diffusion coefficient and liquid side mass transfer coefficient were calculated for each case. The experimental results have been analyzed considering multiple factors (polymer type, the concentration of the solute, hydrodynamics of the bubble, and rheological properties of the fluid) and compared with the literature. The several conclusions drawn from the study can be

summarized as follows:

1. As the bubble is quasi-spherical, the transferred mass is presented as a circular diffusion spot and the concentration field has a centrosymmetric distribution. Over time, the oxygen diffuses from the symmetric center to the surroundings. The diffusion is much more significant in the polymer than in the non-polymer viscous media with the same viscosity.
2. A new method is proposed to determine the diffusion coefficient by analyzing the evolution of the parameter B of the Gaussian equation as a function of time. The result is consistent with the calculations made by the previous method (Xu et al., 2017).
3. The presence of the polymer reduces the mass transfer in water (with mass transfer coefficient dramatically decreasing from 4.47×10^{-4} m/s in water to less than 1×10^{-4} m/s in polymer solutions). This is due to the low bubble velocity and the enhanced contamination effect under our investigated condition. For the Breox solution, the contamination angle decreases with the polymer concentration while for PAAm the contamination effect remains high with the polymer concentration.
4. The contamination effect can be quantified by the stagnant cap model but the result is then underestimated for the mass transfer modeling. By using the normalized Sherwood number, a rectified contamination angle is proposed which is found more consistent with the mass transfer result by the experiment. For the Breox solution, the total mass transferred increases with the polymer concentration (decreasing contamination) but the mass flux decreases due to viscous effects (decreasing slip velocity). For the PAAm solution, the total mass transferred decreases with the polymer concentration (higher contamination) and the mass flux decreases more drastically than with the Breox solution.

In addition, a preliminary extension study has been carried out for measuring the mass transfer from bigger bubbles ($D_{eq} = 1.5-5.5$ mm) in two types of solutions (PAAm 1 wt.% and Xanthan gum 0.1 wt.%). The impact of the bubble size and the deformation

of the bubble shape on the mass transfer is investigated. Compared the visualization result of the PAAM cases with Xanthan ones, it is found that the sharp bubble shape (with a more pointed tail of the bubble) can maintain the structure of the mass transfer. The mass transfer coefficients are smaller in Xanthan solutions than in PAAM solutions and the smaller bubble ($D_{eq} \approx 1.5$ mm) has a higher mass transfer efficiency than bigger bubbles.

Conclusion and Perspective

The study on the gas-liquid mass transfer is of great significance since the realization of the control of the mass transfer rate is very critical for many chemical and biological processes. With the development of the experimental equipment, new techniques by using optical instruments and soluble dyes are developed which are capable to visualize and quantify local gas-liquid mass transfer. However, the mechanism of the gas-liquid mass transfer is still required further investigations, especially for mass transfer in the complex fluids (e.g. non-Newtonian fluids, polymer solutions, etc.). For this purpose, this Ph.D. manuscript has implemented an experimental investigation of single air bubbles rising in water and various polymer solutions (Brex, Polyacrylamide (PAAm) and Xanthan gum) which can simulate the property of the sewage and have a wide application in the industry (Duran Quintero, 2015). It is found that the presence of the polymer molecules will affect bubble hydrodynamics (velocity, bubble shape, interfacial area), as well as the total transferred mass and diffusion from bubble to the liquid, leading to a reduction of the mass transfer rate. The detail conclusions can be summarized in the following aspects:

Firstly, three visualization techniques: Planar laser-induced fluorescence (PLIF, dye: fluorescent resorufin), PLIF with Inhibition (PLIF-I, dye: ruthenium complex), and colorimetric techniques (dye: pink resorufin) are compared focusing on their application to characterize the mass transfer around a single rising bubble in a column. The experimental setup and procedure for different techniques are basically the same except that the colorimetric technique is carried out without the laser. Once a single bubble is injected, the images of mass transfer and the movement of the bubble are captured by the two-camera system (CCD camera and high-speed camera). While the hydrodynamic results of the bubble are obtained with the high-speed camera, the images from the CCD camera are used for mass transfer characterization, based on a

calibration which establishes the relationship between the gray level on the image and the actual dissolved oxygen concentration. To calculate the diffusion coefficient, the probability density function of the chi-squared distribution in statistics is introduced to describe the diffusing oxygen concentration field. It found that the ratio between the oxygen diffusing within the specific area S_{spot} and the total transferred mass M refers to the diffusion coefficient. The diffusion coefficient can thus be determined from the slope of the curve S_{spot} as a function time. To calculate the mass transfer coefficient, it is assumed that, when the bubble has passed far enough from the investigated plane, the convection induced by the bubble passing or the convection can be neglected. Thus the oxygen is transferring only within the cross-section of the bubble wake and the transferred mass equals to the sum of the oxygen concentrations in all pixels on the experimental image. With the bubble velocity and surface area of the bubble, and the driving force measured by the probe, the mass transfer coefficient can be determined.

According to the result of the bubble rising in water, it is found that the PLIF and colorimetric technique with resorufin are both effective for tracking the local mass transfer. However, these two techniques cannot be used to characterize the oxygen diffusion process. The reason is that these two techniques are based on the tracking of a different molecule (resorufin) instead of the oxygen molecule. Regardless of the relatively rigorous treatment to remove the noise in the image background, PLIF-I is more accurate for the quantification of the diffusion coefficient and mass transfer coefficient. For the above reason, the PLIF-I technique is selected for the study to characterize the mass transfer in polymer solutions.

Secondly, based on the same experimental configuration, various single air bubbles (D_{eq} : 0.7-7 mm) rising in stagnant non-Newtonian fluids (polyacrylamide, Xanthan) have been investigated by high-speed photography and image post-processing technologies. To characterize the bubble shape, an innovative model is proposed, which used parametric equations and contains the aspect ratio (E) and two shape parameters (α, β).

Within the range investigated here ($-9 < \log Mo < -7$), the bubble shapes in PAAM solution cover the spherical bubble and the ellipsoidal bubble regime while, in Xanthan gum solutions, the range of Mo is bigger ($-9 < \log Mo < 3$), and the data covers not only spherical and ellipsoidal bubbles but also prolate and teardrop ones. Compared with the bubble shapes in Newtonian fluids, the aspect ratio of the bubble can be smaller than 1, indicating the appearance of an elongated bubble. To predict the aspect ratio, although it is still mainly related to the inertial force (for big oblate bubbles), simply considering one factor or one dimensionless number is insufficient. The aspect ratio of the bubble depends not only on the different forces applied to the bubble but also on the rheological properties of the fluid. An empirical correlation is then obtained for the aspect ratio by considering all the influencing factors, which are denoted by $Tn = We Ta \cdot n$. Moreover, the shapes of the bubbles from spherical to inverted teardrop can be characterized with good accuracy by adjusting three specific parameters (E, α, β). The parameter α correlates with the parameter β by a power-law function. It is also found that the cusp of the bubble (quantified by β) is related to the viscoelasticity as well as the shear-thinning level of the solutions. A correlation of parameter β is obtained with the Deborah number (De , Eötvös number (Eo) and the shear-thinning index n . Along with the other correlations and the bubble equation, a complete system is established for bubble shape characterization and prediction, which will provide new ideas for future studies on bubble hydrodynamics.

Thirdly, the mass transfer and the diffusion phenomenon in the wake of a bubble in aqueous polymer media have been investigated by the PLIF-I technique. The experiments have been performed with air bubbles ($D_{eq} = 1-1.4$ mm) rising in various aqueous polymer solutions (PAAm: 0.1-0.5 wt. %; Breox: 2-9.1 wt. %). It is found that as the bubble is quasi-spherical, the transferred mass is presented as a circular diffusion spot and the concentration field has a centrosymmetric distribution. Over time, the oxygen diffuses from the symmetric center to the surroundings. The diffusion is much

more significant in the polymer than in the non-polymer viscous media with the same viscosity. The presence of the polymer reduces the mass transfer in water (with mass transfer coefficient dramatically decreasing from 4.47×10^{-4} m/s in water to less than 1×10^{-4} m/s in polymer solutions). This is due to the low bubble velocity and the enhanced contamination effect under our investigated condition. For the Breox solution, the contamination angle decreases with the polymer concentration while for PAAm the contamination effect remains high with the polymer concentration. The contamination effect can be quantified by the stagnant cap model but the result is then underestimated for the mass transfer modeling. It is not sufficient to simply use the effect of rigid or mobile bubble interface to explain the reduction of the observed mass transfer in polymer solutions. By using the normalized Sherwood number, a rectified contamination angle is proposed which is found more consistent with the mass transfer result by the experiment. For the Breox solution, the total mass transferred increases with the polymer concentration (decreasing contamination) but the mass flux decreases due to viscous effects (decreasing slip velocity). For the PAAm solution, the total mass transferred decreases with the polymer concentration (higher contamination) and the mass flux decreases more drastically than with the Breox solution.

Finally, an extension study has been carried out for measuring the mass transfer from bigger bubbles ($D_{eq} = 1.5-5.5$ mm) in two types of solutions (PAAm 1 wt.% and Xanthan gum 0.1 wt.%). The impact of the bubble size and the deformation of the bubble shape on the mass transfer is investigated. Compared the visualization result of the PAAm cases with Xanthan ones, it is found that the sharp bubble shape (with a more pointed tail of the bubble) can maintain the structure of the mass transfer. The mass transfer coefficients are smaller in Xanthan solutions than in PAAm solutions and the smaller bubble ($D_{eq} \approx 1.5$ mm) has a higher mass transfer efficiency than bigger bubbles.

Perspective

The following perspectives have been identified to improve the understanding and the mechanism of the mass transfer of freely rising bubble.

1. Impact of the surfactant on the mass transfer

One of the interesting extensive research is on the surfactant impact. A tentative result is obtained (Table C-1) for the mass transfer of single bubbles rising in solutions containing the surfactant: Triton (X-100, linear formula: t-Oct-C₆H₄-(OCH₂CH₂)_xOH, x= 9-10, Sigma-Aldrich, USA). It is found that the presence of the surfactant molecule will reduce the bubble rising velocity and the mass transfer coefficient. When the surfactant is added into the polymer solutions, the mass transfer is further inhibited with a mass transfer coefficient about 10 times lower than the value in pure water case. Further investigation has been launched by the Ph.D. student Gaëlle LEBRUN in the laboratory (2018-2021).

Table C-1 Impact of the surfactant (20 mg·L⁻¹) on the result of mass transfer

Solution	D_{eq} [mm]	U_b [mm·s⁻¹]	k_L [10⁻⁴ m·s⁻¹]
Pure water	1.44	321	1.89
Pure water + Triton	1.41	164	0.35
Pure water + PAAM 0.1%	1.55	74	0.74
Pure water + Triton+ PAAM 0.1 %wt.	1.74	120	0.23

2. Extension to large bubbles with complex shape and multiple bubbles

Due to the rheological property of the complex liquid phase (e.g. polymer solution in this study), the large bubbles can present more complex shape instead of spherical or ellipsoidal bubbles. Although the mass transfer has been investigated for bubbles with slight deformation, it is interesting to extend the study to characterize the mass transfer

phenomena of bubbles in more complex shape like tear-drop. Particle image velocimetry (PIV) can be used to investigate the flow field around the bubble (Böhm et al., 2016), which may give rise to a deep understanding of the impact of the hydrodynamics of the bubble (e.g. negative wake, vorticity, strain, etc.) on the mass transfer. In addition, it is also significant to study the mass transfer phenomena of multiple bubbles by taking account of the impact of bubble interactions and coalescence (Li et al., 2001; Sun et al., 2017).

3. Three-dimensional characterization of the mass transfer

Since the bubble has a good reproducibility of the bubble shape and trajectory in the investigated polymer solutions, it is possible to implement a three-dimensional characterization of the mass transfer. By taking images of multiple cross-sections of the mass transfer of the bubble, the mass transfer can be reconstructed that will be useful to study mass transfer in more complex structure (Huang and Saito, 2017b).

4. Mass transfer visualization by coupling PLIF with colorimetric technique

Based on the investigation in Chapter 3, the resorufin molecule can be used as both colorimetric dye and fluorescence dye. Thanks to this property, the experimentation coupling the PLIF technique with the colorimetric technique can be driven to visualize the mass transfer in two aspects: near the bubble surface and in the bubble wake. The experimental setup is shown in Figure C-1. This configuration adopts the advantage of each technique that there is no reflection around the bubble surface and clear mass transfer spot in the bubble wake.

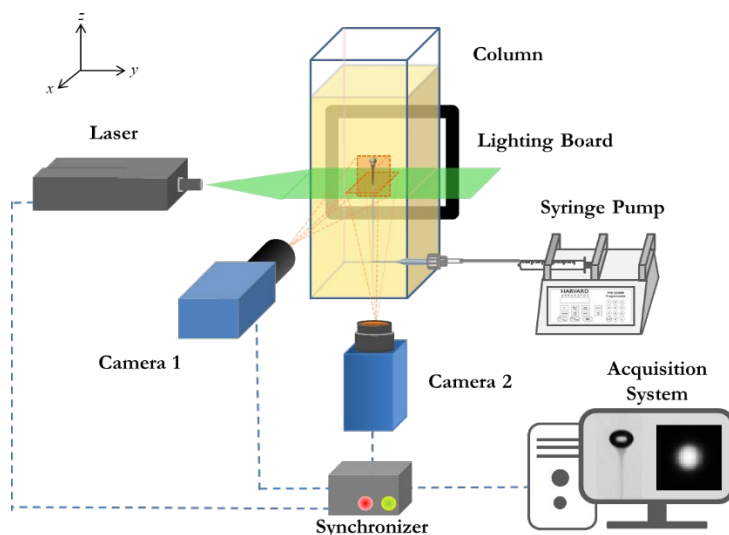


Figure C-1 Experimental setup for the experimentation coupling the PLIF technique with the colorimetric technique

5. “Two-color” method

Regarding the experimental configuration, in order to reduce the reflection effect around the bubble surface, one promising solution is “two-color” method (Kováts et al., 2018; Lacassagne et al., 2018). The principle is based on the application of a specific dye or two dyes that the fluorescent light emitted at two different wavelengths while the one emitted light for quantification and the other one used as a reference. Dividing the first wavelength intensity field by the second one, the heterogeneous excitation effects can be corrected. This method may improve the image quality leading to a better characterization of the mass transfer in complex media.

List of publications

JOURNAL ARTICLES:

- **Xu, Feishi**, Arnaud Cockx, Gilles Hébrard, and Nicolas Dietrich, 2018. Mass Transfer and Diffusion of a Single Bubble Rising in Polymer Solutions. *Industrial & Engineering Chemistry Research* 57(44): 15181–15194. DOI: 10.1021/acs.iecr.8b03617
- **Xu, Feishi**, Mélanie Jimenez, Nicolas Dietrich, and Gilles Hébrard, 2017. Fast Determination of Gas-Liquid Diffusion Coefficient by an Innovative Double Approach. *Chemical Engineering Science* 170 (Supplement C): 68–76. DOI: 10.1016/j.ces.2017.02.043

CONFERENCE PAPER:

- **Xu, Feishi**, Nicolas Dietrich, Arnaud Cockx, and Gilles Hebrard, 2018. Comparison of Three Different Visualization Techniques for Local Mass Transfer Characterization around Single Bubble Rising in Water. *Proceeding of 19th International Symposium on the Application of Laser and Imaging Techniques to Fluid Mechanics*.

CONFERENCE PRESENTATIONS:

- Oral presentation: Comparison of different visualization techniques for local mass transfer characterization around single bubble rising in water, 19th International Symposium on Applications of Laser and Imaging Techniques to Fluid Mechanics. 18 July 2018. Lisbon, Portugal.
- Oral presentation: Comparison of different visualization techniques for local mass transfer characterization, 2nd Franco-Germany international workshop: Non-Invasive Experimental Tools and Numerical Methods for the Investigation of Non-Reactive and Reactive Gas-Liquid Flows. 21 June 2018. Hamburg, Germany.
- Oral presentation: Fast determination of gas-liquid diffusion coefficient by an innovative double approach, 13th International Conference on Gas-Liquid and Gas-Liquid-Solid Reactor Engineering (GLS-13). 23 August 2017. Brussels, Belgium.

-
- Oral presentation: Visualization of mass transfer around rising bubble in non-Newtonian fluids, 13th International Conference on Gas-Liquid and Gas-Liquid-Solid Reactor Engineering (GLS-13). 21 August 2017. Brussels, Belgium.

References

- Aguirre, V.A., Castillo, B.A., and Narvaez, C.P. (2017). Numerical simulation of a bubble rising in an environment consisting of Xanthan gum. *AIP Conf. Proc.* 1872, 020022.
- Alm eras, E., Cazin, S., Roig, V., Risso, F., Augier, F., and Plais, C. (2016). Time-resolved measurement of concentration fluctuations in a confined bubbly flow by LIF. *Int. J. Multiph. Flow* 83, 153–161.
- Alves, S.S., Orvalho, S.P., and Vasconcelos, J.M.T. (2005). Effect of bubble contamination on rise velocity and mass transfer. *Chem. Eng. Sci.* 60, 1–9.
- Amirmia, S., de Bruyn, J.R., Bergougnou, M.A., and Margaritis, A. (2013). Continuous rise velocity of air bubbles in non-Newtonian biopolymer solutions. *Chem. Eng. Sci.* 94, 60–68.
- Anderson, K., Cooper, J.M., Haswell, S.J., Marshall, D., Yin, H., and Zhang, X. (2010). Microfluidic-based measurements of cytochrome P450 enzyme activity of primary mammalian hepatocytes. *Analyst* 135, 1282–1287.
- Anderson, L., Wittkopp, S.M., Painter, C.J., Liegel, J.J., Schreiner, R., Bell, J.A., and Shakhshiri, B.Z. (2012). What is happening when the blue bottle bleaches: an investigation of the methylene blue-catalyzed air oxidation of glucose. *J. Chem. Educ.* 89, 1425–1431.
- Annesini, M.C., Marrelli, L., Piemonte, V., and Turchetti, L. (2017). Mass transfer coefficient. In *Artificial Organ Engineering*, (London: Springer-Verlag), pp. 23–31.
- Anwar, S. (2013). Lattice Boltzmann modeling of buoyant rise of single and multiple bubbles. *Comput. Fluids* 88, 430–439.
- Aoyama, S., Hayashi, K., Hosokawa, S., and Tomiyama, A. (2016). Shapes of ellipsoidal bubbles in infinite stagnant liquids. *Int. J. Multiph. Flow* 79, 23–30.
- Asher, W.E. (2009). The effects of experimental uncertainty in parameterizing air-sea gas exchange using tracer experiment data. *Atmos Chem Phys* 9, 131–139.
- Asher, W.E., and Litchendorf, T.M. (2009). Visualizing near-surface concentration fluctuations using laser-induced fluorescence. *Exp. Fluids* 46, 243–253.
- Axelrod, D., Koppel, D.E., Schlessinger, J., Elson, E., and Webb, W.W. (1976). Mobility measurement by analysis of fluorescence photobleaching recovery kinetics. *Biophys. J.* 16, 1055–1069.
- Barnett, S.M., Humphrey, A.E., and Litt, M. (1966). Bubble motion and mass transfer in non-Newtonian fluids. *AIChE J.* 12, 253–259.
- B ohm, L., Kurita, T., Kimura, K., and Kraume, M. (2014). Rising behaviour of single bubbles in narrow rectangular channels in Newtonian and non-Newtonian liquids. *Int. J. Multiph. Flow* 65, 11–23.

- Böhm, L., Brehmer, M., and Kraume, M. (2016). Comparison of the Single Bubble Ascent in a Newtonian and a Non-Newtonian Liquid: A Phenomenological PIV Study. *Chem. Ing. Tech.* 88, 93–106.
- Bork, O., Schlueter, M., and Raebiger, N. (2005). The Impact of Local Phenomena on Mass Transfer in Gas-Liquid Systems. *Can. J. Chem. Eng.* 83, 658–666.
- Bouche, E., Cazin, S., Roig, V., and Risso, F. (2013). Mixing in a swarm of bubbles rising in a confined cell measured by mean of PLIF with two different dyes. *Exp. Fluids* 54, 1552.
- Bowyer, W.J., Xu, W., and Demas, J.N. (2004). Determining oxygen diffusion coefficients in polymer films by lifetimes of luminescent complexes measured in the frequency domain. *Anal. Chem.* 76, 4374–4378.
- Bruchhausen, M., Guillard, F., and Lemoine, F. (2005). Instantaneous measurement of two-dimensional temperature distributions by means of two-color planar laser induced fluorescence (PLIF). *Exp. Fluids* 38, 123–131.
- Butler, C., Cid, E., and Billet, A.-M. (2016). Modelling of mass transfer in Taylor flow: Investigation with the PLIF-I technique. *Chem. Eng. Res. Des.* 115, 292–302.
- Butler, C., Lalanne, B., Sandmann, K., Cid, E., and Billet, A.-M. (2018). Mass transfer in Taylor flow: Transfer rate modelling from measurements at the slug and film scale. *Int. J. Multiph. Flow* 105, 185–201.
- Byron Bird, R., and Carreau, P.J. (1968). A nonlinear viscoelastic model for polymer solutions and melts-I. *Chem. Eng. Sci.* 23, 427–434.
- Calderbank, P.H., and Lochiel, A.C. (1964). Mass transfer coefficients, velocities and shapes of carbon dioxide bubbles in free rise through distilled water. *Chem. Eng. Sci.* 19, 485–503.
- Cao, X., Zhao, Z., Cheng, L., and Yin, W. (2016). Evaluation of a Transparent Analog Fluid of Digested Sludge: Xanthan Gum Aqueous Solution. *Procedia Environ. Sci.* 31, 735–742.
- Carreau, P.J., MacDonald, I.F., and Bird, R.B. (1968). A nonlinear viscoelastic model for polymer solutions and melts-II. *Chem. Eng. Sci.* 23, 901–911.
- Charogiannis, A., An, J.S., and Markides, C.N. (2015). A simultaneous planar laser-induced fluorescence, particle image velocimetry and particle tracking velocimetry technique for the investigation of thin liquid-film flows. *Exp. Therm. Fluid Sci.* 68, 516–536.
- Chhabra, R. (2010). *Non-Newtonian Fluids: An Introduction*. Rheol. Complex Fluids.
- Chhabra, R.P. (2006). *Bubbles, Drops, and Particles in Non-Newtonian Fluids*, Second Edition (CRC Press).
- Chu, C.R., and Jirka, G.H. (1992). Turbulent gas flux measurements below the air-water interface of a grid-stirred tank. *Int. J. Heat Mass Transf.* 35, 1957–1968.

- Clift, R., Grace, J.R., and Weber, M.E. (1978). *Bubbles, Drops, and Particles* (New York: Dover Publications).
- Colombet, D., Legendre, D., Cockx, A., Guiraud, P., Risso, F., Daniel, C., and Galinat, S. (2011). Experimental study of mass transfer in a dense bubble swarm. *Chem. Eng. Sci.* *66*, 3432–3440.
- Coppeta, J., and Rogers, C. (1998). Dual emission laser induced fluorescence for direct planar scalar behavior measurements. *Exp. Fluids* *25*, 1–15.
- Crank, J. (1975). *The Mathematics of Diffusion* (Clarendon Press).
- Crimaldi, J.P. (2008). Planar laser induced fluorescence in aqueous flows. *Exp. Fluids* *44*, 851–863.
- Dani, A., Guiraud, P., and Cockx, A. (2007). Local measurement of oxygen transfer around a single bubble by planar laser-induced fluorescence. *Chem. Eng. Sci.* *62*, 7245–7252.
- Davidson, R.L. (1980). *Handbook of water-soluble gums and resins* (McGraw-Hill).
- DeGraff, B.A., and Demas, J.N. (2005). Luminescence-Based Oxygen Sensors. In *Reviews in Fluorescence*, pp. 125–151.
- Dekée, D., and Chhabra, R.P. (1988). A photographic study of shapes of bubbles and coalescence in non-Newtonian polymer solutions. *Rheol. Acta* *27*, 656–660.
- Dekée, D., Carreau, P.J., and Mordarski, J. (1986). Bubble velocity and coalescence in viscoelastic liquids. *Chem. Eng. Sci.* *41*, 2273–2283.
- Dewsbury, K., Karamanev, D., and Margaritis, A. (1999). Hydrodynamic characteristics of free rise of light solid particles and gas bubbles in non-Newtonian liquids. *Chem. Eng. Sci.* *54*, 4825–4830.
- Dietrich, N. (2008). *Étude locale et expérimentale des phénomènes interfaciaux*. Vandoeuvre-les-Nancy, INPL.
- Dietrich, N., and Hébrard, G. (2018). Visualisation of gas-liquid mass transfer around a rising bubble in a quiescent liquid using an oxygen sensitive dye. *Heat Mass Transf.* 1–9.
- Dietrich, N., Loubière, K., Jimenez, M., Hébrard, G., and Gourdon, C. (2013). A new direct technique for visualizing and measuring gas-liquid mass transfer around bubbles moving in a straight millimetric square channel. *Chem. Eng. Sci.* *100*, 172–182.
- Dietrich, N., Francois, J., Jimenez, M., Cockx, A., Guiraud, P., and Hébrard, G. (2015). Fast measurements of the gas-liquid diffusion coefficient in the gaussian wake of a spherical bubble. *Chem. Eng. Technol.* *38*, 941–946.
- Dong, H., Wang, X., Liu, L., Zhang, X., and Zhang, S. (2010). The rise and deformation of a single bubble in ionic liquids. *Chem. Eng. Sci.* *65*, 3240–3248.
- Duke, S.R., and Hanratty, T.J. (1995). Measurement of the concentration field resulting from oxygen absorption at a wavy air-water interface. *Air-Water Gas Transf.* 627–635.

Duran Quintero, C. (2015). Comportement rhéologique des boues activées : Mesures, modélisation et impact sur le transfert d'oxygène dans les bioréacteurs aérés. Toulouse, INSA.

Dziubiński, M., Orzykowska, M., and Budzyński, P. (2003). Comments on bubble rising velocity in non-Newtonian liquids. *Chem. Eng. Sci.* 58, 2441–2443.

Eftink, M.R. (1991). Fluorescence Quenching Reactions. In *Biophysical and Biochemical Aspects of Fluorescence Spectroscopy*, T.G. Dewey, ed. (Boston, MA: Springer US), pp. 1–41.

Erb, R.E., and Ehlers, M.H. (1950). Resazurin Reducing Time as an Indicator of Bovine Semen Fertilizing Capacity. *J. Dairy Sci.* 33, 853–864.

Fan, L.-S., and Tsuchiya, K. (1990). *Bubble Wake Dynamics in Liquids and Liquid-Solid Suspensions* (Boston, Mass: Butterworth-Heinemann).

Fedrizzi, M., and Soria, J. (2014). Planar laser fluorescence imaging of bubble detachment. (RMIT University), pp. 1–4.

Felis, F., Dietrich, N., Billet, A.-M., Strassl, F., Herres-Pawlis, S., Roig, V., and Loubière, K. (2018). Experiments on reactive mass transfer around an oxygen bubble rising freely in a confined cell using colourimetric methods. (Lisbon, Portugal), pp. 121–130.

Fenner, A., and Stephan, P. (2017). Two dye combinations suitable for two-color/two-dye laser-induced fluorescence thermography for ethanol. *Exp. Fluids* 58, 65.

Fick, A. (1855). Ueber Diffusion. *Ann. Phys.* 170, 59–86.

Fraggedakis, D., Pavlidis, M., Dimakopoulos, Y., and Tsamopoulos, J. (2016). On the velocity discontinuity at a critical volume of a bubble rising in a viscoelastic fluid. *J. Fluid Mech.* 789, 310–346.

François, J., Dietrich, N., Guiraud, P., and Cockx, A. (2011a). Direct measurement of mass transfer around a single bubble by micro-PLIFI. *Chem. Eng. Sci.* 66, 3328–3338.

François, J., Dietrich, N., and Cockx, A. (2011b). A novel methodology to measure mass transfer around a bubble. *Mod. Phys. Lett. B* 25, 1993–2000.

Frank, X., Li, H.Z., Funfschilling, D., Burdin, F., and Ma, Y. (2003). Bubble Motion in Non-Newtonian Fluids and Suspensions. *Can. J. Chem. Eng.* 81, 483–490.

Frank, X., Charpentier, J.-C., Ma, Y., Midoux, N., and Li, H.Z. (2012). A Multiscale Approach for Modeling Bubbles Rising in Non-Newtonian Fluids. *Ind. Eng. Chem. Res.* 51, 2084–2093.

Frössling, N. (1938). Über die Verdunstung fallender Tropfen. *Beitr Geophys Gerlands* 52, 170–216.

Funfschilling, D., and Li, H.Z. (2006). Effects of the Injection Period on the Rise Velocity and Shape of a Bubble in a Non-Newtonian Fluid. *Chem. Eng. Res. Des.* 84, 875–883.

- Garbe, C.S., Handler, R.A., and Jähne, B. (2008). *Transport at the Air-Sea Interface: Measurements, Models and Parametrizations* (Springer Science & Business Media).
- Golnabi, H., and Razani, M. (2007). Oxygen sensing based on the oxidation process in resorufin dye. *Sens. Actuators B Chem.* *122*, 109–117.
- Grace, J., Wairegi, T., and Nguyen, T.H. (1976). Shapes and Velocities of Single Drops and Bubbles Moving Freely Through Immiscible Liquids. *Trans Inst Chem Eng* *54*, 167–173.
- Guet, S., and Ooms, G. (2006). Fluid Mechanical Aspects of the Gas-Lift Technique. *Annu. Rev. Fluid Mech.* *38*, 225–249.
- Hadamard, J.S. (1911). Movement permanent lent d'une sphere liquide et visqueuse dans un liquide visqueux. *Comptes Rendus Académie Sci.* *152*, 1735–1752.
- Hammad, K.J. (2015). The Flow Behavior of a Biofluid in a Separated and Reattached Flow Region. *J. Fluids Eng.* *137*, 061104–061112.
- Hanyu, K., and Saito, T. (2010). Dynamical mass-transfer process of a CO₂ bubble measured by using LIF/HPTS visualisation and photoelectric probing. *Can. J. Chem. Eng.* *88*, 551–560.
- Hassan, N.M.S., Khan, M.M.K., and Rackemann, D.W. (2007). An experimental study of bubble rise characteristics in non-Newtonian (power-law) fluids. 16th Australas. Fluid Mech. Conf. AFMC.
- Hassan, N.M.S., Khan, M.M.K., Rasul, M.G., and Rackemann, D.W. (2010). Bubble Rise Velocity and Trajectory in Xanthan Gum Crystal Suspension. *Appl. Rheol.* *20*, 65102.
- Hébrard, G. (1995). Etude de l'influence du distributeur de gaz sur l'hydrodynamique et le transfert de matière gaz-liquide des colonnes à bulles. thesis. Toulouse, INSA.
- Hébrard, G., Destrac, P., Roustan, M., Huyard, A., and Audic, J.M. (2000). Determination of the water quality correction factor α using a tracer gas method. *Water Res.* *34*, 684–689.
- Hébrard, G., Zeng, J., and Loubière, K. (2009). Effect of surfactants on liquid side mass transfer coefficients: A new insight. *Chem. Eng. J.* *148*, 132–138.
- Herlina, and Jirka, G.H. (2004). Application of LIF to investigate gas transfer near the air-water interface in a grid-stirred tank. *Exp. Fluids* *37*, 341–349.
- Higbie, R. (1935). The Rate of Absorption of a Pure Gas Into a Still Liquid During Short Periods of Exposure. *Trans. AIChE* *31*, 365–389.
- Hlawitschka, M.W., Kováts, P., Zähringer, K., and Bart, H.-J. (2017). Simulation and experimental validation of reactive bubble column reactors. *Chem. Eng. Sci.* *170*, 306–319.
- Hua, J., Stene, J.F., and Lin, P. (2008). Numerical simulation of 3D bubbles rising in viscous liquids using a front tracking method. *J. Comput. Phys.* *227*, 3358–3382.
- Huang, J., and Saito, T. (2015). Influence of Bubble-Surface Contamination on Instantaneous Mass

- Transfer. Chem. Eng. Technol. 38, 1947–1954.
- Huang, J., and Saito, T. (2017a). Influences of gas–liquid interface contamination on bubble motions, bubble wakes, and instantaneous mass transfer. Chem. Eng. Sci. 157, 182–199.
- Huang, J., and Saito, T. (2017b). Discussion about the differences in mass transfer, bubble motion and surrounding liquid motion between a contaminated system and a clean system based on consideration of three-dimensional wake structure obtained from LIF visualization. Chem. Eng. Sci. 170, 105–115.
- Jamnongwong, M., Loubière, K., Dietrich, N., and Hébrard, G. (2010). Experimental study of oxygen diffusion coefficients in clean water containing salt, glucose or surfactant: Consequences on the liquid-side mass transfer coefficients. Chem. Eng. J. 165, 758–768.
- Jimenez, M. (2013). Etude du transfert de matière gaz/liquide en milieux complexes: quantification du transfert d'oxygène par techniques optiques. INSA.
- Jimenez, M., Dietrich, N., Cockx, A., and Hébrard, G. (2012a). Experimental study of O₂ diffusion coefficient measurement at a planar gas-liquid interface by planar laser-induced fluorescence with inhibition. AIChE J. 59, 325–333.
- Jimenez, M., Dietrich, N., and Hébrard, G. (2012b). A New Method for Measuring Diffusion Coefficient of Gases in Liquids by Plif. Mod. Phys. Lett. B 26, 1150034.
- Jimenez, M., Dietrich, N., and Hébrard, G. (2013). Mass transfer in the wake of non-spherical air bubbles quantified by quenching of fluorescence. Chem. Eng. Sci. 100, 160–171.
- Jimenez, M., Dietrich, N., Grace, J.R., and Hébrard, G. (2014). Oxygen mass transfer and hydrodynamic behaviour in wastewater: determination of local impact of surfactants by visualization techniques. Water Res. 58, 111–121.
- Jung, J., Jang, J., and Ahn, J. (2016). Characterization of a Polyacrylamide Solution Used for Remediation of Petroleum Contaminated Soils. Materials 9, 16.
- Kapoustina, V., Ross-Jones, J., Hitschler, M., Raedle, M., and Repke, J.-U. (2015). Direct spatiotemporally resolved fluorescence investigations of gas absorption and desorption in liquid film flows. Chem. Eng. Res. Des. 99, 248–255.
- Kastens, S., Timmermann, J., Strassl, F., Rampmaier, R.F., Hoffmann, A., Herres-Pawlis, S., and Schlüter, M. (2017). Test System for the Investigation of Reactive Taylor Bubbles. Chem. Eng. Technol. 40, 1494–1501.
- Kelbaliyev, G., and Ceylan, K. (2007). Development of New Empirical Equations for Estimation of Drag Coefficient, Shape Deformation, and Rising Velocity of Gas Bubbles or Liquid Drops. Chem. Eng. Commun. 194, 1623–1637.
- Kim, J., Kim, K.C., and Kim, H.D. (2016). Quantitative visualization study on diffusion of oxygen using UV-LED induced phosphorescence. J. Vis. 19, 591–601.

- Kong, G., Buist, K.A., Peters, E.A.J.F., and Kuipers, J.A.M. (2018). Dual emission LIF technique for pH and concentration field measurement around a rising bubble. *Exp. Therm. Fluid Sci.* *93*, 186–194.
- Kováts, P., Thévenin, D., and Zähringer, K. (2017). Investigation of Mass Transfer and Hydrodynamics in a Model Bubble Column. *Chem. Eng. Technol.* *40*, 1434–1444.
- Kováts, P., Pohl, D., Thévenin, D., and Zähringer, K. (2018). Optical determination of oxygen mass transfer in a helically-coiled pipe compared to a straight horizontal tube. *Chem. Eng. Sci.* *190*, 273–285.
- Kramer, A., Gaulocher, S., Martins, M., and Filho, L.S.L. (2012). Surface Tension Measurement for Optimization of Flotation Control. *Procedia Eng.* *46*, 111–118.
- Kreft, S., and Kreft, M. (2009). Quantification of dichromatism: a characteristic of color in transparent materials. *J. Opt. Soc. Am. A Opt. Image Sci. Vis.* *26*, 1576–1581.
- Kreiba, A. (2000). *The Rheological Properties of Aqueous Polyacrylamide Solutions*. Concordia University.
- Krieger, W., Lamsfuß, J., Zhang, W., and Kockmann, N. (2017). Local Mass Transfer Phenomena and Chemical Selectivity of Gas-Liquid Reactions in Capillaries. *Chem. Eng. Technol.* *40*, 2134–2143.
- Kück, U.D., Schlüter, M., and Rübiger, N. (2010). Investigation on Reactive Mass Transfer at Freely Rising Gas Bubbles. (Tampa, Florida, USA), pp. 1–5.
- Kück, U.D., Schlüter, M., and Rübiger, N. (2012). Local Measurement of Mass Transfer Rate of a Single Bubble with and without a Chemical Reaction. *J. Chem. Eng. Jpn.* *45*, 708–712.
- Lacassagne, T., Hajem, M.E., Morge, F., Simoens, S., and Champagne, J.-Y. (2017). Study of Gas Liquid Mass Transfer in a Grid Stirred Tank. *Oil Gas Sci Technol – Rev IFP Energ. Nouv.* *72*, 7.
- Lacassagne, T., Simoëns, S., Hajem, M.E., and Champagne, J.-Y. (2018). Ratiometric, single-dye, pH-sensitive inhibited laser-induced fluorescence for the characterization of mixing and mass transfer. *Exp. Fluids* *59*, 21.
- Larsen, L.G., and Crimaldi, J.P. (2006). The effect of photobleaching on PLIF. *Exp. Fluids* *41*, 803–812.
- Lee, M. (2002). Visualization of oxygen transfer across the air–water interface using a fluorescence oxygen visualization method. *Water Res.* *36*, 2140–2146.
- Legendre, D., Zenit, R., and Velezcordero, J.R. (2012). On the deformation of gas bubbles in liquids. *Phys. Fluids* *24*, 043303.
- Levitsky, S.P., and Shulman, Z.P. (1995). *Bubbles in Polymeric Liquids: Dynamics and Heat-Mass Transfer* (Lancaster: Technomic Publishing Co.).

- Li, S. (2011). Study on the bubble motion and mass transfer in non-Newtonian fluids.
- Li, H.Z., Frank, X., Funfschilling, D., and Mouline, Y. (2001). Towards the understanding of bubble interactions and coalescence in non-Newtonian fluids: a cognitive approach. *Chem. Eng. Sci.* *56*, 6419–6425.
- Li, S., Ma, Y., Jiang, S., Fu, T., Zhu, C., and Li, H. (2012). The Drag Coefficient and the Shape for a Single Bubble Rising in Non-Newtonian Fluids. *J. Fluids Eng.* *134*, 084501.
- Liu, L., Yan, H., and Zhao, G. (2015). Experimental studies on the shape and motion of air bubbles in viscous liquids. *Exp. Therm. Fluid Sci.* *62*, 109–121.
- Ma, Y., Cheng, H., and Xu, G. (1999). Measurement of concentration fields near the interface of a rising bubble by holographic interference technique. *Chin. J. Chem. Eng.* *7*, 363–367.
- Margaritis, A., Bokkel, D.W. te, and Karamanev, D.G. (1999). Bubble rise velocities and drag coefficients in non-Newtonian polysaccharide solutions. *Biotechnol. Bioeng.* *64*, 257–266.
- Mayerhöfer, T.G., Mutschke, H., and Popp, J. (2016). Employing Theories Far beyond Their Limits-The Case of the (Boguer-) Beer-Lambert Law. *ChemPhysChem* *17*, 1948–1955.
- Mei, R., Klausner, J.F., and Lawrence, C.J. (1994). A note on the history force on a spherical bubble at finite Reynolds number. *Phys. Fluids* *6*, 418–420.
- Mezger, T.G. (2014). *The Rheology Handbook*, 4th Edition (Hannover: Vincentz Network).
- Moghaddas, J., Trägårdh, C., Kovacs, T., and Östergren, K. (2002). A new method for measuring concentration of a fluorescent tracer in bubbly gas–liquid flows. *Exp. Fluids* *32*, 728–729.
- Moore, D.W. (1959). The rise of a gas bubble in a viscous liquid. *J. Fluid Mech.* *6*, 113–130.
- Myint, W., Hosokawa, S., and Tomiyama, A. (2007). Shapes of Single Drops Rising Through Stagnant Liquids. *J. Fluid Sci. Technol.* *2*, 184–195.
- Nagami, Y., and Saito, T. (2013). An Experimental Study of the Modulation of the Bubble Motion by Gas–Liquid-Phase Interaction in Oscillating-Grid Decaying Turbulence. *Flow Turbul. Combust.* *92*, 147–174.
- Najafpour, G. (2006). *Biochemical Engineering and Biotechnology* (Amsterdam ; Boston, MA: Elsevier Science).
- du Noüy, P.L. (1925). AN INTERFACIAL TENSIO METER FOR UNIVERSAL USE. *J. Gen. Physiol.* *7*, 625–631.
- Paul, M., Strassl, F., Hoffmann, A., Hoffmann, M., Schlüter, M., and Herres-Pawlis, S. (2018). Reaction Systems for Bubbly Flows. *Eur. J. Inorg. Chem.* *2018*, 2101–2124.
- Piccione, P.M., Rasheed, A.A., Quarmby, A., and Dionisi, D. (2017). Direct Visualization of Scale-Up Effects on the Mass Transfer Coefficient through the “Blue Bottle” Reaction. *J. Chem. Educ.* *94*,

726–729.

Raymond, F., and Rosant, J.-M. (2000). A numerical and experimental study of the terminal velocity and shape of bubbles in viscous liquids. *Chem. Eng. Sci.* *55*, 943–955.

Reiner, M. (1964). The Deborah Number. *Phys. Today* *17*, 62.

Riethues, M., Buchholz, R., Onken, U., Baumgärtl, H., and Lübbers, D.W. (1986). Determination of oxygen transfer from single air bubbles to liquids by oxygen microelectrodes. *Chem. Eng. Process. Process Intensif.* *20*, 331–337.

Rodrigue, D. (2001). Drag coefficient—reynolds number transition for gas bubbles rising steadily in viscous fluids. *Can. J. Chem. Eng.* *79*, 119–123.

Rodrigue, D. (2002). A simple correlation for gas bubbles rising in power-law fluids. *Can. J. Chem. Eng.* *80*, 289–292.

Rodrigue, D. (2004). A General Correlation for the Rise Velocity of Single Gas Bubbles. *Can. J. Chem. Eng.* *82*, 382–386.

Roudet, M., Billet, A.-M., Cazin, S., Risso, F., and Roig, V. (2017). Experimental investigation of interfacial mass transfer mechanisms for a confined high-reynolds-number bubble rising in a thin gap. *AIChE J.* *63*, 2394–2408.

Roustan, M. (2003). *Transferts gaz-liquide dans les procédés de traitement des eaux et des effluents gazeux* (Paris; Londres; New York: Tec & Doc Lavoisier).

Roy, S., and Duke, S.R. (2000). Laser induced fluorescence measurements of dissolved oxygen concentration fields near air bubble surfaces. *Rev. Sci. Instrum.* *71*, 3494–3501.

Roy, S., and Duke, S.R. (2004). Visualization of oxygen concentration fields and measurement of concentration gradients at bubble surfaces in surfactant-contaminated water. *Exp. Fluids* *36*, 654–662.

Rüttinger, S., Spille, C., Hoffmann, M., and Schlüter, M. (2018). Laser-Induced Fluorescence in Multiphase Systems. *ChemBioEng Rev.* *5*, 253–269.

Sadhal, S.S., and Johnson, R.E. (1983). Stokes flow past bubbles and drops partially coated with thin films. Part 1. Stagnant cap of surfactant film – exact solution. *J. Fluid Mech.* *126*, 237–250.

Saito, T., and Toriu, M. (2015a). Effects of a bubble and the surrounding liquid motions on the instantaneous mass transfer across the gas–liquid interface. *Chem. Eng. J.* *265*, 164–175.

Saito, T., and Toriu, M. (2015b). Effects of a bubble and the surrounding liquid motions on the instantaneous mass transfer across the gas–liquid interface. *Chem. Eng. J.* *265*, 164–175.

Sastaravet, P., Chuenchaem, C., Thaphet, N., Chawaloesphonsiya, N., and Painmanakul, P. (2014). Comparative Study of Mass Transfer and Bubble Hydrodynamic Parameters in Bubble Column

- Reactor: Physical Configurations and Operating Conditions. *Environ. Eng. Res.* *19*, 345–354.
- Schiller, L., and Naumann, A. (1933). Ueber die grundlegenden Berechnungen bei der Schwerkraftaufbereitung. *Ver Deut Ing* *77*, 318–320.
- Schladow, S.G., Lee, M., Hürzeler, B.E., and Kelly, P.B. (2002). Oxygen transfer across the air-water interface by natural convection in lakes. *Limnol. Oceanogr.* *47*, 1394–1404.
- Shao, T., Feng, X., Wang, W., Jin, Y., and Cheng, Y. (2012). Visualization of coupled mass transfer and reaction between gas and a droplet using a novel reactive-PLIF technique. *Chem. Eng. J.* *200–202*, 549–558.
- Shulman, Z.P., and Levitskiy, S.P. (1992). Heat/mass transfer and dynamics of bubbles in high-polymer solutions—I. Free oscillations. *Int. J. Heat Mass Transf.* *35*, 1077–1084.
- Someya, S., Bando, S., Song, Y., Chen, B., and Nishio, M. (2005). DeLIF measurement of pH distribution around dissolving CO₂ droplet in high pressure vessel. *Int. J. Heat Mass Transf.* *48*, 2508–2515.
- Soto, E., Goujon, C., Zenit, R., and Manero, O. (2006). A study of velocity discontinuity for single air bubbles rising in an associative polymer. *Phys. Fluids* *18*, 121510.
- Stern, O., and Volmer, M. (1919). On the quenching time of fluorescence. *Phys. Z* *20*, 183–188.
- Stöhr, M., Schanze, J., and Khalili, A. (2009). Visualization of gas-liquid mass transfer and wake structure of rising bubbles using pH-sensitive PLIF. *Exp. Fluids* *47*, 135–143.
- Sugihara, K., Sanada, T., Shirota, M., and Watanabe, M. (2007). Behavior of single rising bubbles in superpurified water. *KAGAKU KOGAKU RONBUNSHU* *33*, 402–408.
- Sun, B., Guo, Y., Wang, Z., Yang, X., Gong, P., Wang, J., and Wang, N. (2015). Experimental study on the drag coefficient of single bubbles rising in static non-Newtonian fluids in wellbore. *J. Nat. Gas Sci. Eng.* *26*, 867–872.
- Sun, W., Zhu, C., Fu, T., Yang, H., Ma, Y., and Li, H. (2017). The minimum in-line coalescence height of bubbles in non-Newtonian fluid. *Int. J. Multiph. Flow* *92*, 161–170.
- Tadaki, T., and Maeda, S. (1961). On the Shape and Velocity of Single Air Bubbles Rising in Various Liquids. *Chem. Eng.* *25*, 254–264.
- Takemura, F., and Yabe, A. (1999). Rising speed and dissolution rate of a carbon dioxide bubble in slightly contaminated water. *J. Fluid Mech.* *378*, 319–334.
- Taylor, T.D., and Acrivos, A. (1964). On the deformation and drag of a falling viscous drop at low Reynolds number. *J. Fluid Mech.* *18*, 466–476.
- Timmermann, J., Hoffmann, M., and Schlüter, M. (2016). Influence of Bubble Bouncing on Mass Transfer and Chemical Reaction. *Chem. Eng. Technol.* *39*, 1955–1962.

- Tomiyama, A., Celata, G.P., Hosokawa, S., and Yoshida, S. (2002). Terminal velocity of single bubbles in surface tension force dominant regime. *Int. J. Multiph. Flow* 28, 1497–1519.
- Vakhrushev, I.A., and Efremov, G.I. (1970). Interpolation formula for computing the velocities of single gas bubbles in liquids. *Chem. Technol. Fuels Oils* 6, 376–379.
- Valiorgue, P., Souzy, N., Hajem, M.E., Hadid, H.B., and Simoëns, S. (2013). Concentration measurement in the wake of a free rising bubble using planar laser-induced fluorescence (PLIF) with a calibration taking into account fluorescence extinction variations. *Exp. Fluids* 54, 1501.
- Valiorgue, P., Souzy, N., Hajem, M.E., Hadid, H.B., and Simoëns, S. (2014). Erratum to: Concentration measurement in the wake of a free rising bubble using planar laser-induced fluorescence (PLIF) with a calibration taking into account fluorescence extinction variations. *Exp. Fluids* 55, 1700.
- Vaughn, W.M., and Weber, G. (1970). Oxygen quenching of pyrenebutyric acid fluorescence in water. Dynamic probe of the microenvironment. *Biochemistry* 9, 464–473.
- Walker, J.W., and Peirson, W.L. (2008). Measurement of gas transfer across wind-forced wavy air–water interfaces using laser-induced fluorescence. *Exp. Fluids* 44, 249–259.
- Warshay, M., Bogusz, E., Johnson, M., and C. Kintner, R. (1959). Ultimate velocity of drops in stationary liquid media. *Can. J. Chem. Eng.* 37, 29–36.
- Weisstein, E.W. (2002). Gamma Function. From Math World-A Wolfram Web Resource, <http://mathworld.wolfram.com/GammaFunction.html>
- Wellek, R.M., Agrawal, A.K., and Skelland, A.H.P. (1966). Shape of liquid drops moving in liquid media. *AIChE J.* 12, 854–862.
- Wolff, L.M., and Hanratty, T.J. (1994). Instantaneous concentration profiles of oxygen accompanying absorption in a stratified flow. *Exp. Fluids* 16, 385–392.
- Wolff, L.M., Liu, Z.-C., and Hanratty, T.J. (1991). A Fluorescence Technique to Measure Concentration Gradients near an Interface. (ASCE), pp. 210–218.
- Woodrow, P.T., and Duke, S.R. (2001). Laser-Induced Fluorescence Studies of Oxygen Transfer Across Unsheared Flat and Wavy Air–Water Interfaces. *Ind. Eng. Chem. Res.* 40, 1985–1995.
- Wylock, C., Dehaeck, S., Cartage, T., Colinet, P., and Haut, B. (2011). Experimental study of gas–liquid mass transfer coupled with chemical reactions by digital holographic interferometry. *Chem. Eng. Sci.* 66, 3400–3412.
- Xie, X., Le Men, C., Dietrich, N., Schmitz, P., and Fillaudeau, L. (2017). Local hydrodynamic investigation by PIV and CFD within a Dynamic filtration unit under laminar flow. *Sep. Purif. Technol.*
- Xu, F., Jimenez, M., Dietrich, N., and Hébrard, G. (2017). Fast determination of gas-liquid diffusion

- coefficient by an innovative double approach. *Chem. Eng. Sci.* *170*, 68–76.
- Yamamoto, M., Yamada, M., Morikawa, K., Sanada, T., and Saito, T. (2008). Coupling mechanism between liquid phase motion and mass transfer around single rising bubbles by using PIV/LIF. (Lisbon, Portugal).
- Yan, H., and Zhao, J. (2016). Experimental study on shape and rising behavior of single bubble in stagnant water. *J. Cent. South Univ. Sci. Technol.* *47*, 2513–2520.
- Yan, X., Jia, Y., Wang, L., and Cao, Y. (2017). Drag coefficient fluctuation prediction of a single bubble rising in water. *Chem. Eng. J.* *316*, 553–562.
- Yang, L., Dietrich, N., Loubière, K., Gourdon, C., and Hébrard, G. (2016). Visualization and characterization of gas–liquid mass transfer around a Taylor bubble right after the formation stage in microreactors. *Chem. Eng. Sci.* *143*, 364–368.
- Yang, L., Dietrich, N., Hébrard, G., Loubière, K., and Gourdon, C. (2017a). Optical methods to investigate the enhancement factor of an oxygen-sensitive colorimetric reaction using microreactors. *AIChE J.* *63*, 2272–2284.
- Yang, L., Loubière, K., Dietrich, N., Le Men, C., Gourdon, C., and Hébrard, G. (2017b). Local investigations on the gas-liquid mass transfer around Taylor bubbles flowing in a meandering millimetric square channel. *Chem. Eng. Sci.* *165*, 192–203.
- Yu, Z., Yang, H., and Fan, L.-S. (2011). Numerical simulation of bubble interactions using an adaptive lattice Boltzmann method. *Chem. Eng. Sci.* *66*, 3441–3451.
- Zenit, R., and Feng, J.J. (2018). Hydrodynamic Interactions Among Bubbles, Drops, and Particles in Non-Newtonian Liquids. *Annu. Rev. Fluid Mech.* *50*, 505–534.
- Zhang, L., Yang, C., and Mao, Z.-S. (2008). An Empirical Correlation of Drag Coefficient for a Single Bubble Rising in Non-Newtonian Liquids. *Ind. Eng. Chem. Res.* *47*, 9767–9772.
- Zhang, L., Yang, C., and Mao, Z.-S. (2010). Numerical simulation of a bubble rising in shear-thinning fluids. *J. Non-Newton. Fluid Mech.* *165*, 555–567.

